# Crystal Plasticity Due to Slip and Twinning

by

**Alexander V. Staroselsky**

B.S. in Electrical Engineering, Moscow Mining Institute, Russia (1984)
M.S. in Applied Mathematics, Moscow Institute of Electronics Engineering, Russia (1990)

Submitted to the Department of Mechanical Engineering
in partial fulfillment of the requirements for the degree of

Doctor of Philosophy

at the

MASSACHUSETTS INSTITUTE OF TECHNOLOGY

February 1998



Author .....
Department of Mechanical Engineering
September 12, 1997

Certified by .....
Lallit Anand
Professor of Mechanical Engineering
Thesis Supervisor

Accepted by .....
Ain A. Sonin
Chairman, Departmental Committee on Graduate Students

# Crystal Plasticity Due to Slip and Twinning

by

**Alexander V. Staroselsky**

Submitted to the Department of Mechanical Engineering
on September 12, 1997, in partial fulfillment of the
requirements for the degree of
Doctor of Philosophy

## Abstract

A new constitutive model for plastic deformation of crystalline materials deforming by slip and twinning has been formulated, and implemented in a finite-element program. The overall plastic deformation of a crystal is always inhomogeneous at length scales associated with slip and twinning, and is defined as an average over a representative-volume element (RVE) that contains enough dislocation loops and twins to result in an acceptably smooth process at the continuum level. We have simulated three different structural levels by choosing RVEs as *(i)* a small part of a single crystal for the analysis of single crystals, *(ii)* a whole single crystal for polycrystal simulations, and *(iii)* a group of crystals for a Taylor-type model of polycrystals.

By using comparisons between model predictions and macroscopically-measured stress-strain curves and texture evolution we have deduced information about the values of the single-crystal parameters. With the model so calibrated, we show that the predictions for the texture and stress-strain curves from the model are in reasonably good agreement with experiments in plane strain compression for differently oriented Co-8%Fe single crystals and $\alpha$-brass polycrystals. Our calculations also show that for the high-symmetry f.c.c. brass, a Taylor-type model for crystals deforming by combined slip and twinning is able to reasonably well predict the macroscopic stress-strain curves and crystallographic texture evolution.

The theory of finite plastic deformation due to crystallographic slip and twinning in materials with hexagonal close packed (h.c.p.) structure is in its beginning stages. We have modified the constitutive model developed for f.c.c. materials and applied it to analyze the inelastic deformation of magnesium. Results of full three-dimensional finite element simulations are shown to be in a good accord with obtained experimental data. Our calculations and experiments showed that basal slip and pyramidal twinning play the dominant role in the deformation of magnesium at room temperature. The macroscopic strain hardening observed in magnesium may for the most part be attributed to the fast twin-induced texture evolution.

Thesis Supervisor: Lallit Anand
Title: Professor of Mechanical Engineering

# Acknowledgments

I wish to express my sincere gratitude to my advisor, Professor Lallit Anand, for his guidance, patience, encouragement and support without which this work would not have been possible. He has exposed me to new, extremely interesting areas of solid mechanics and helped to feel confident in them.

I would like to thank Professors Rohan Abeyaratne, Mary Boyce, and David Parks for serving on my thesis committee. The discussions which took place at my committee meetings were always very interesting and useful.

I also wish to thank my colleague Dr. Maxim Seleznev for introducing me to the art of microanalysis. Dr. Zbignew Bartczak shared with me a small part of his knowledge and skills in x-ray diffraction technique. Without them, the experimental part of this thesis would be very poor. Special thanks to Dr. Vasily Bulatov for the hours he spent with me sharing his enthusiasm to understand the physical nature of metal plasticity. I also thank Ray Hardin for taking care of all the administrative details as well as helping me in my struggle with the English language. Thanks also to Leslie Regan and the staff of the graduate office, who were always there with all needed information.

All my past and present office mates are extraordinary people, and it has been a great pleasure and privilege to be a part of the Mechanics and Materials group at MIT. Thanks to all of them for warm and creative atmosphere. Special thanks to Leonid Lev, John Zaroulis, Clarence Chui, Andrew Parris, Srihari Balasubramanian, and Suryaprakash Ganti for many fruitful discussions.

I was very happy to be a resident graduate tutor for the last three years in an undergraduate dormitory (Russian House). I thank all past and present residents of this dorm with whom we built a community. Special thanks to my friends and colleagues Vadim Khayms and Gregory Golberg for their help in work on this project.

I could not possibly have finished this work without constant moral and financial support from my parents. My father, Vladimir, stepmother, Bronislava, and young brother Dennis made my graduate study possible. Special thanks to my mother, Maria Khayn, who supported me and persevered through my work on two doctoral dissertations.

Finally, I thank my beloved wife Svetlana for being a great wife, mother, and friend. I am forever indebted to her for all the work she did to help me to get this manuscript written, for strengthing me when I lost hope to do this work, for her constant faith in me, and for her friendship and love.

This work was supported by US Army Research Office Grant DAAH04-94-G-0060 and by National Science Foundation Grant CMS-9610130.

# Contents

# List of Figures

# List of Tables

# Chapter 1

# Introduction

The purpose of the present dissertation to understand and model the deformation processes of different polycrystalline materials, in which each grain can deform by crystallographic slip and/or mechanical twinning. The nature of the structure and anisotropy is very important for the properties of materials. In polycrystalline metals the major cause of the anisotropic plastic response is crystallographic texture resulting from the reorientation of the crystal lattices of grains during deformation. In this work we intend to relate the macroscopic texture evolution and deformation modes and structural transformations of single crystals.

There have been considerable recent advances in the understanding of anisotropy due to crystallographic texturing, and a reasonably successful, physically-based elasto-viscoplasticity theory for the deformation of face-centered-cubic single crystals and polycrystals with high stacking fault energies at low homologous temperatures ($<$ 0.3 of the melting temperature) and low strain rates ($10^{-3}$ — $10^{1}$ $s^{-1}$) is now well established. The theory is able to predict the macroscopic anisotropic stress-strain response, shape changes and the evolution of crystallographic texture in complex deformation modes. It is also beginning to be applied to the analysis of deformation-processing problems under isothermal and quasi-static conditions (e.g., Mathur and Dawson, [1989], [1990]; Kalidindi et al., [1992]; Bronkhorst et al., [1992]; Anand and Kalidindi, [1994]; Beaudoin et al., [1994]; Balasubramanian and Anand, [1996]).

The high stacking fault energy f.c.c. materials (e.g. Al, Cu) deform predominantly

by crystallographic slip, and the recent progress in the formulation of a mathematical theory of polycrystalline plasticity has occurred primarily for materials with cubic crystals which do not twin. In contrast, for f.c.c. materials with low stacking energies, e.g. copper, cobalt and several other *alloys* in addition to crystallographic slip, *deformation twinning* plays an important role in maintaining generalized plastic flow[1]. The deviation between these model predictions and experimental observations increases with growing of strain and decreasing of the stacking fault energy. Such deformation can no be longer explained by slip theories and models based on the mechanism that strongly depends on stacking fault energy, such as twinning, have to be considered.

The overall plastic deformation of a crystal is always inhomogeneous at length scales associated with slip and twinning. Although twinning is very strong source of a crystal inhomogeneous deformation, no crystal-plasticity based models for the twinning-related large inhomogeneous plastic deformations of single crystals have been reported.

The theory of finite plastic deformation due to crystallographic slip and mechanical twinning in materials with hexagonal close packed (h.c.p.) structure, such as magnesium, is less developed[2]. The development of constitutive models and attendant computational procedures for these materials are of substantial technological importance, because these lightweight materials can be used to create lighter weight vehicles with improved fuel economy and reduced emissions, resulting in environmental benefits. The reason for the lack of progress for h.c.p. materials is the complexity of the deformation modes present in these materials. In f.c.c. metals in addition to the dominant mode of deformation which is slip on twelve $\{111\} < 110 >$ slip systems, there also exist additional twelve $\{111\} < 11\bar{2} >$ twin systems. Unlike

[1]Venables [1964] first recognized the relationship between the susceptibility of a metal to twin and the value of its stacking fault energy. He showed that the critical resolved shear stress for twinning decreased with decreasing stacking fault energy, as occurs for example in Cu-Zn alloys with increasing amounts of zinc.

[2]Even a slip-based theory applicable to high temperature deformation of h.c.p. materials has not been properly formulated yet. Some progress in numerical texture prediction was obtained by D. M. Parks and S. Ahzi [1990], by S. Schoenfeld et al. [1995], and recently by S. Balasubramanian [1998].

the f.c.c. materials, inelastic deformation of a h.c.p. crystal is highly anisotropic: the deformation resistances of different slip systems are substantially different. Furthermore, deformation twinning plays an important role in maintaining plastic flow. Since twinning is sensitive to the sign of the applied stress, the yield strengths in tension and compression are different (Kelley and Hosford [1968]). Our review of the literature shows that the crystal mechanics–based treatments of plasticity of magnesium are incomplete and scattered. There does not exist a coherent set of data - stress-strain curves, microstructure, and crystallographic texture evolution under controlled basic modes of loading at different temperatures, where different slip and twinning systems are known to be operative. Clearly there is a need for a complete experimental-theoretical-computational study of plastic deformation of h.c.p. metals due to slip and twinning.

While there is a considerable amount of research aimed at describing the twinning patterns which exist in grains after transformation, (see I. Lifshiz [1948], J. M. Ball and R. D. James [1987], R. V. Kohn [1991], Khachaturyan [1983], etc.) the role of twinning in polycrystalline plasticity has not been extensive studied. Very little is known about plastic deformation caused by combined slip and twinning modes. The understanding of the development of textures related to both deformation mechanisms, slip and twinning, is very limited. The analytical modeling and computational accounting for twinning as a mechanism of inelastic deformation, texture evolution, and strain hardening is in its nascent stages. Some of the early considerations of twinning in texture development are those of Chin et al. [1969] Chin and Mammel [1969]. For a brief review of this early work on twinning, see Chin [1975] and in correspondent chapters of [1979]. Twinning is a more complicated deformation mode than slip because, in addition to the sudden large twinning shear, it produces a volume fraction of the grain with a very different orientation than that of the rest of the grain; in a sense, it produces new grains. The two major kinematic issues in modeling twinning are: (*i*) The reorientation of the crystal lattice due to twinning. (*ii*) Since splitting a grain and treating the twinned fractions as new orientations quickly lead to a numerically unmanageable number of grains, clever ways to handle twinning are needed. Van

Houtte [1978]; appears to have been the first to propose a simple tractable scheme for reorientation of grains due to twinning during simulation of texture development in a polycrystal. His scheme does not increase the number of crystals. In his approach, if a grain twins, then the shear due to twinning is first treated as a "pseudo-slip," and the crystal lattice is given the twinning-related orientation only if a probabilistic criterion, based on the relative volume fractions of the twinned and non-twinned parts of a crystal, is met. Recently, Tome et al. [1991] and Lebensohn and Tome [1994] have discussed some limitations of Van Houtte's proposal, and have proposed two new schemes of their own; however, their schemes are only applicable in the context of Taylor-type and self-consistent polycrystal models. In this thesis we shall carry out full finite-element modeling of polycrystalline aggregates deforming by slip and twinning, and we will explore the applicability of Van Houtte's scheme in predicting the crystallographic texture of f.c.c. 70-30 brass and h.c.p. magnesium alloy AZ31B.

Finite element modeling of crystalline materials is a powerful simulation technique. In finite element models of polycrystals (e.g. Bronkhorst et al. [1992], Kalidindi et al., [1992], Anand and Kalidindi, [1994], and several others) both compatibility and equilibrium are satisfied, and there is no need for the the Taylor [1938], Sachs [1928] or other such hypotheses (see Gill Sevillano et al. [1981] for a review of these works), which have been classically used to obtain the response of a polycrystalline aggregate. The finite element procedure also permits us to simulate the heterogeneity of plastic deformation in individual grains by subdividing the grains into small finite elements. The calculations in which each finite element quadrature point represents a single grain permit verification and calibration of constitutive models for polycrystals. The results obtained at this structural level can be used for verification of the scheme at the next structural level, where each element quadrature point represents a group of grains. Such a calibrated averaging scheme (Taylor, Sachs, etc) provides computationally inexpensive first order approximate solutions for polycrystalline behavior.

The broad objective of this thesis has been to study the evolution of the crystallographic textures and the flow stress in f.c.c. and h.c.p. materials. The present work focuses on:

- Experimental and theoretical study of inelastic deformation of Polycrystalline f.c.c. $Cu - Zn$ 70-30 brass by slip and twinning.
- Computational study of inhomogeneous deformation of Single Crystalline f.c.c. materials. We compare our model predictions against experiments of Chin et al. [1969] on single $Co - 8\%Fe$ crystals.
- Experimental and theoretical study of inelastic deformation of Polycrystalline h.c.p. magnesium alloy AZ31B due to both slip and twinning at low homologous temperatures.
- Experimental study of inelastic deformation of Polycrystalline h.c.p. magnesium alloy AZ31B by slip alone at high homologous temperatures.

Currently the most important trend in crystal plasticity is to simulate the processes of texture evolution, and to develop adequate constitutive models suitable for texture evolution and stress- strain response prediction of different classes of materials in different material processing operations. The results of the studies mentioned above motivated further development of constitutive models for single and poly- crystal plasticity caused by both mechanisms: crystallographic slip and mechanical twinning.

Specifically, the purpose of the present study is to conduct a combined analytical-experimental-computational research program to develop physically based constitutive models and computational procedures for large anisotropic inelastic deformations of f.c.c. low stacking fault energy alloys such as brass 70-30 and Co-8%Fe and of h.c.p magnesium alloy. We validate our numerical simulation capabilities by comparison against measurements from physical experiments.
With this as background, the following have been accomplished in the present dissertation:

1. In Chapter 2 we set down a constitutive model which accounts for both slip and twinning. Since twinning occurs very rapidly, and visco-plastic models of twinning are nebulous, we have formulated a *rate-independent* model to account for twinning. In this chapter we also describe our scheme to determine the active systems and the shear increments on the active slip and twin systems.

We set down this model in an incremental form to emphasize the computational procedure. The rate form of this model can be found in Appendix A.

We have implemented our constitutive equations in the finite element program ABAQUS/Explicit [1995]. This computational capability allows us to perform two types of finite element calculations: (*i*) where a finite element quadrature point represents a material point in a single grain and the constitutive response is given through a single-crystal constitutive model, and (*ii*) where a finite element quadrature point represents a material point in a polycrystalline sample and the constitutive response is given through a Taylor-type polycrystal model.

2. The finite element procedure permits us to simulate the heterogeneity of plastic deformation in individual grains by subdividing the grains into small finite elements. We have performed an evaluation of the constitutive model for plane deformation of a single f.c.c. crystal by comparing predictions of texture evolution, mechanical twinning, and stress-strain response in the deformed specimen against known experimental data (Chin et al., [1969]). These results are presented in Chapter 3.

3. In Chapter 4 we simulate "nominally-homogeneous" deformations of plane-strain compression and simple compression of a polycrystalline aggregate, using a multitude of single crystals. Important ingredients in the theory are the slip and twin resistances, and their interaction and evolution.

    a. Direct measurements of the hardening interactions are difficult, if not impossible. Accordingly, we first perform our finite-element simulations for the non-hardening case. That is, with $s_{sl}$ denoting a constant shear resistance for slip and $s_{tw}$ denoting a constant shear resistance for twinning, we examine the capability of the model based on Van Houtte's [1978] scheme to handle the reorientation of the individual grains due to twinning, in order to predict the evolution of crystallographic texture for three different values of the ratio $R = s_{tw}/s_{sl}$, equal to 4, 1.1, and 0.8. A value of $R = 4$

activates only the slip systems, and we obtain the well-known "copper-type" pole figures. A value of $R = 0.8$ activates both twinning and slip, and this produces a "brass-type" texture, whereas a value $R = 1.1$ activates small amounts of twinning, which produces a "transition" texture. These calculations show the important role of lattice reorientation due to twinning in producing the experimentally-observed brass-type textures.

b. Representation of slip-twin hardening and hardening interactions is one of the major uncertainties, and much work needs to be done to improve our understanding of these hardening interactions and their mathematical representation. In this context, Hirsch et al., [1988], Leffers and Bilde-Sorensen [1990], Leffers and Jensen [1991], and Leffers [1993] point out that in rolled brass $\{111\} < 11\bar{2} >$ twins form as thin lamellae which are not homogeneously distributed, but cluster to form bundles in grains. These bundles are usually parallel to one plane of the $\{111\}$ family. Subsequent slip in grains containing such twin clusters occurs predominantly on $\{111\} < 110 >$ slip systems with slip planes parallel to the plane of the twin bundles, and slip on other systems is restricted. Based on these experimental observations, in Chapter 4 we make plausible assumptions concerning the hardening part of the model, and use comparisons between model predictions and macroscopically-measured stress-strain curves and texture evolution to deduce information about the values of the single-crystal parameters associated with slip and twin system deformation resistances and hardening due to slip and twinning. We show that our model is able to reproduce both the experimentally-measured pole figures and the stress-strain curves in plane strain compression. Next, with the model so calibrated, we show that the predictions for the texture and stress-strain curves from the model are also in reasonably good agreement with experiments in simple compression.

c. We also evaluate the applicability of a Taylor-type model for combined slip and twinning. Our calculations show that for the high-symmetry f.c.c.

brass, a Taylor-type model for crystals deforming by combined slip and twinning is able to predict reasonably well the macroscopic stress-strain curves and crystallographic texture evolution, in both plane-strain compression and simple compression.

4. The combined experimental-theoretical study of the deformation of h.c.p. magnesium alloy have been conducted at room temperature. Results of this research is presented in Chapter 5. We performed a series of experiments to measure the stress-strain response and texture evolution of polycrystalline magnesium (magnesium alloy AZ31B) during different modes of deformation to large strain. These were simple tension, simple compression, and a set of three plane strain compression tests in different directions. A modified constitutive model suitable for the analysis of deformation of magnesium and its alloys at room temperature is developed and implemented in the finite-element program ABAQUS/Explicit [1995]. Our numerical results have been verified by comparison against experimental data.

    a. The amount of shear produced by twinning is small in comparison with slip, and, because of lack of activity of $< \mathbf{c} + \mathbf{a} >$ pyramidal slip systems, the individual grains are essentially inextensible in $c$-direction. To maintain generalized plastic flow, additional important features are shown to be operative in the deformation of polycrystalline magnesium (G. V. Raynor [1959]): grain boundary sliding and prolific twinning and non-basal slipping in grain boundary region. These features are localized in thin layers around the grain boundary (Hauser et al., [1955]) only value a small contribution to crystallographic texture. In order to account for these phenomena we have constructed a combined crystal plasticity and isotropic plasticity model, in which all non-crystallographic effects are localized in a thin isotropic "boundary layer" next to grain boundary.

    b. The predicted crystallographic textures and stress-strain curves are in good agreement with experimentally observed curves. We demonstrate both

numerically and experimentally that the main mechanisms of plastic deformation of magnesium at room temperature are basal $< a >$ slip and $\{10\bar{1}2\} < \bar{1}011 >$ twinning.

c. We have shown that texture evolution and stress-strain curves of magnesium at room temperature can be predicted by this non-hardening model. Polycrystalline strain hardening can be explained mostly by grain reorientation during the deformation process. Our simulations demonstrate that dominant mechanism contributing to the fast crystal lattice reorientation is mechanical twinning.

5. In the high temperature deformation of magnesium, twinning is suppressed, and number of $< \mathbf{c} + \mathbf{a} >$ pyramidal slip systems are expected to be active in addition to the dominant basal plane slip. The experimental data of polycrystalline magnesium deformation at elevated temperature is scattered. In Chapter 6 we present our experimental results for simple tension and compression, and plane strain compression to large strains. We measure the macroscopic stress – strain behavior and the corresponding evolution of crystallographic texture, and present these results together with microstructural analysis. Our numerical estimations permit us to choose the most important slip systems and evaluate deformation resistances for different systems in magnesium at high temperature. This numerical data is given in Appendix D.

6. Chapter 7 gives some suggestions for future work. The present study builds the foundation for detailed study of twin caused local inhomogeneity in polycrystalline aggregate. The single crystal model developed in Chapter 3 can be generalized for polycrystalline aggregate by merging a number of initially different oriented single grains subdivided for small finite elements. That is the next "meso-scale" structural level of crystal plasticity. Nobody doubts that the larger the number of mesh elements the better the approximation we have. We briefly discuss one possible approach to increase the number of elements based on thermoactivation mechanisms and a stochastic self-consistent model. Also,

some other suggestions for future research are presented.

We close in Chapter 8 with some conclusions and final remarks.

# Chapter 2

# Constitutive model

## 2.1 Manifistation of the twinning in the f.c.c. $\alpha$-brass deformation process.

A direct manifestation of twinning is the different crystallographic texture that is observed in 70-30 brass as compared to commercially pure copper, and this is one of the classsical problems in texture research (e.g., Wasserman, [1963]; Dillamore and Roberts, [1964]; Smallman and Green, [1964]; Goodman and Hu, [1968]). Fig. 2-1 shows a comparison of our measurements of the {111}, {100} and {110} pole figures in brass and copper after plane strain compression of 100%. The differences betweeen the {111} and {100} pole figures of brass and copper are quite pronounced.

Another material response characteristic which is different for $\alpha$-brass as compared to that for copper is the variation of the rate of strain hardening with strain. Experimentally measured stress-strain curves and the corresponding relation between the strain hardening rate $d|\sigma|/d|\epsilon|$ and true strain $|\epsilon|$ in plane-strain compression are shown in Fig. 2-2 For copper the rate of strain hardening decreases continuously with increasing strain (for the level of strains examined), while the rate of strain hardening for the brass exhibits a plateau at intermediate strain levels. Extensive microscopic observations by Asgari et al., [1997] show that the plateau in strain hardening rate can be correlated with the onset of twinning, and it is the twin-twin and twin-slip

hardening interactions which arrest the decrease in the strain hardening rate in brass at these intermediate strain levels.

Hirsch et al. [1988], [1988a] have conducted detailed metallographic and x-ray texture investigations on the mechanisms of deformation and texture evolution during rolling of f.c.c. polycrystalline materials. With respect to their metallographic observations, in their Fig. 2 they report that copper exhibits relatively homogeneous slip and an equi-axed subgrain structure at low strains. Subsequently, superimposed on this structure, long band-like features of $\sim 0.2\,\mu$m width form in individual grains, at strains as low as 5%. They call these microstructural features "microbands." The orientation difference of the microbands with respect to the surrounding matrix is usually only $\sim 2°$. They suggest that these microbands are formed by a process of dislocation channeling on active slip systems, and represent strong locally concentrated dislocation glide. These microbands are not restricted to special crystal orientations, and they may occur on all active slip planes. The number of these microbands increases with strain, and at moderate strains the dislocation microstructure in individual flattened grains consists mainly of these features. At strains $\epsilon > \sim 1$, macroscopic "shear bands" develop at $\sim \pm 35°$ to the rolling plane. These shear bands cut through the microbands in a grain, and also across grain boundaries. In contrast, they report that for 70-30 brass the dislocations are dissociated into partials, and neither cell structures nor microbands develop. At $\epsilon \sim 0.20$, fine deformation twins are observed in some suitably oriented grains, and by $\epsilon \sim 0.70$ profuse twinning is present in most grains (their Fig. 3a). As deformation progresses, the lamellar twin-parent structure becomes progressively aligned with the rolling plane, and they attribute this to preferential shearing of both the matrix and the twin components on the common $\{111\}$ planes. At high strains, $\epsilon > 1$, after the twins have become strongly aligned, macrospic shear bands form. The shear bands form as sheet-like structures at $\sim \pm 35°$ to the rolling plane. The width of these sheets is $\sim 0.5 - 2\,\mu$m, and they divide the microstructure into rhomboidal shaped packets of twinned material (their Fig. 3d). Hirch em et al. [1988] also describe the microstructure and texture evolution to strains as large as $\epsilon \sim 3$, in which case the microstructural features become very complex,

and numerous new shear bands form as deformation progresses (their Fig. 3e).

Hirsch et al. [1988] conclude that the microband and shear bands in copper only affect small localized volumes, and that these features do not have a significant influence on the averaged macroscopic texture evolution at strains up to $\sim 1$. In contrast, for 70-30 brass, mechanical twinning and shear band formation have a much larger influence on rolling texture. In this paper, to isolate the effects of crystallographic slip and twinning on texture evolution, we restrict our study to strains less than $\sim 1$ in plane strain compression, so that the contributions of shear bands to texture evolution are minimal.

The analytical modeling and computational accounting for twinning as a mechanism of inelastic deformation, texture evolution, and strain hardening is in its nascent stages. We note that all previous attempts to model polycrystalline plasticity due to both slip and twinning have been for the rigid-plastic, non-hardening case, and have been limited to the Taylor [e.g. Van Houtte [1978]] or the "self-consistent" (e.g. Lebensohn and Tome [1994]) averaging schemes for polycrystalline materials. In this chapter we present our formulation of an elastic-plastic model, which also attempts to capture the major features of strain hardening due to slip-twin interactions. We present the model in an *incremental* form, suitable for numerical implementation. The rate formulation of the constitutive equations is given in Appendix A.

## 2.2 Deformation of f.c.c. Single Crystals by Slip and Twinning

The deformation of a single crystal is taken as the sum of contributions from two independent atomic mechanisms: (*i*) an overall "elastic" distortion of the lattice, and (*ii*) a "plastic" deformation due to slip and/or twinning that does not distort the lattice geometry.

Slip in f.c.c. crystals occurs on twelve $\{111\} < 110 >$ slip systems listed in Table 2.1. Note that on a given slip system, slip can occur in either the positive or negative

$< 110 >$ slip direction in a $\{111\}$ plane.

Table 2.1: The Twelve $\{111\} < 110 >$ Slip Systems

| $(111)$ | | | $(\bar{1}\bar{1}1)$ | | | $(\bar{1}11)$ | | | $(1\bar{1}\bar{1})$ | | |
|---|---|---|---|---|---|---|---|---|---|---|---|
| $[01\bar{1}]$ | $[\bar{1}01]$ | $[1\bar{1}0]$ | $[0\bar{1}\bar{1}]$ | $[101]$ | $[\bar{1}10]$ | $[01\bar{1}]$ | $[101]$ | $[\bar{1}\bar{1}0]$ | $[0\bar{1}\bar{1}]$ | $[\bar{1}01]$ | $[110]$ |

It is well known that an increment of plastic deformation due to slip does not change the lattice orientation. Figure 2-3 shows an idealized scheme for uniform slip; the lattice is not changed, but the slip gives rise to steps on the crystal surface. Twinning rotates the lattice in the region of the crystal that has twinned (e.g., Kelly and Groves [1970]; Pitteri [1985], [1986]). Fig. 2-4a schematically shows the local description of a twinned crystal, where we have two regions $R_1$ and $R_2$ which are separated by a plane $P$ with unit normal $\mathbf{n}$.

For the case where the crystalline structure in $R_2$ can be obtained from the one in $R_1$ by means of a rotation of $\pi$ about an axis parallel to $\mathbf{n}$,

$$\mathbf{R}^{tw}_{(1)} = 2\mathbf{n} \otimes \mathbf{n} - \mathbf{1},$$

the twin is called a *Type-1* twin[1]. Another possibility is that $R_2$ is obtained from $R_1$ by means of rotation of $\pi$ about a crystallographic direction parallel to $\mathcal{P}$, say $\mathbf{m}$:

$$\mathbf{R}^{tw}_{(2)} = 2\mathbf{m} \otimes \mathbf{m} - \mathbf{1};$$

such a twin is called *Type-2* twin. For either type of twin in simple crystal structures, $R_2$ can also be obtained from $R_1$ by means of a *simple shear of the Bravais Lattice*, and the reorientation due to deformation twinning is classically described in terms of such a simple shear. Fig. 3b summarizes the standard crystallographer's description of the twinning shear. All points in the lattice on the upper side of the plane $K_1$ are displaced in the $\eta_1$ direction by amount $u_1$, proportional to their distance above $K_1$.

[1]A *Type-1* twin may alternatively be described by a reflection across $\mathcal{P}$, $\mathbf{Q} = \mathbf{1} - 2\mathbf{n} \otimes \mathbf{n}$, in which case it is called a *reflection twin*.

Thus $u_1 = \gamma_0 x_2$, where $\gamma_0$ is the amount of simple shear. The plane $K_1$, which is neither distorted nor rotated during the shear, is called the *twinning plane*, and $\eta_1$ is the *direction of shear*. The plane containing $\eta_1$ and the normal $\mathbf{n}$ to the twinning plane is called the *plane of shear* $S$. It is easy to show that a vector parallel to a direction $\eta_2$ in $S$ will be of the same length after the shear has been applied, if the angle $\alpha$ that it makes with the normal to $K_1$ is given by $\gamma_0 = 2\tan\alpha$. Clearly, all vectors in the plane through $\eta_2$ which is normal to $S$ are unchanged in length, although rotated; this plane, AOB in Fig. 2-4b, is conventionally labelled $K_2$, and is called the second undistorted plane. The quantities $\{K_1, K_2, \eta_1, \eta_2\}$ are called the twinning elements. Twins whose shear elements $K_1$ and $\eta_2$ are rational, that is if the directions associated with these elements pass through sets of points of the Bravais lattice, while $K_2$ and $\eta_1$ are irrational, form Type-1 twins. Alternatively, if $K_2$ and $\eta_1$ are rational, while $K_1$ and $\eta_2$ are irrational, then the twins are of Type-2. Very commonly, all four elements $K_1, K_2, \eta_1, \eta_2$ are rational, the two types merge, and such twins are called *compound*. In a cubic lattice, only compound twins are possible.

Fig. 2-5a shows the structure of a twin in a f.c.c. metal. In this case, the equivalent symmetry rules connecting the differently-oriented parts are: (*i*) that $R_2$ is obtained by a rotation of $\pi$ about the [111] direction, or (*ii*) that $R_2$ is obtained by a rotation of $\pi$ about the $[11\bar{2}]$ direction. It can be seen in Fig. 2-5b that the nearest neighbor relations are preserved at the boundary, but an error in the stacking of the (111) planes occurs, such that the stacking sequence ABCABC is turned into ABCBAC. Fig. 2-5c shows how the twinned crystal could have been produced by homogeneously shearing part of a single crystal. The twinning elements for f.c.c. materials are

$$K_1 = (111), \quad \eta_1 = [11\bar{2}], \quad K_2 = (11\bar{1}), \quad \eta_2 = [112]. \tag{2.1}$$

The twinning shear corresponding to these elements may be written as

$$\mathbf{S} = \mathbf{1} + \gamma_0\, \mathbf{m} \otimes \mathbf{n}, \quad \mathbf{m} \cdot \mathbf{n} = 0, \quad \gamma_0 = 1/\sqrt{2}, \tag{2.2}$$

where $\mathbf{m}$ is a unit vector in the $\eta_1 = [11\bar{2}]$ direction, and $\mathbf{n}$ the unit normal to the

$K_1 = (111)$ plane. The rotations which carry $R_1$ to $R_2$ are given by

$$\mathbf{R}^{tw}_{(1)} = 2\mathbf{n} \otimes \mathbf{n} - \mathbf{1}, \tag{2.3}$$

$$\mathbf{R}^{tw}_{(2)} = 2\mathbf{m} \otimes \mathbf{m} - \mathbf{1}. \tag{2.4}$$

That is, if $\mathbf{e}_a$ are the lattice vectors which generate the crystal in $R_1$, then the lattice vectors which generate the lattice in $R_2$ are given by $\tilde{\mathbf{e}}_a = \mathbf{R}^{tw}\mathbf{e}_a$. In all cases $(\mathbf{R}^{tw})^2 = \mathbf{1}$, that is, successive application of $\mathbf{R}^{tw}$ on any lattice vector returns it to its original orientation.

The twelve $\{111\} < 11\bar{2} >$ twin systems are listed in Table 2.2. Note that unlike the slip systems listed in Table 2.1 for which slip can occur in either the positive or negative $< 110 >$ slip direction in a $\{111\}$ plane, twinning, because the underlying atomic arrangement is polar in nature, can occur in only one $< 11\bar{2} >$ type direction on a $\{111\}$ plane, and the twin systems listed in Table 2.2 correspond to the easy direction of twinning. We do not consider the possibility of "de-twinning" in this thesis.

Table 2.2: The Twelve $\{111\} < 11\bar{2} >$ Twin Systems

| $(111)$ | | | $(\bar{1}\bar{1}1)$ | | | $(\bar{1}11)$ | | | $(1\bar{1}1)$ | | |
|---|---|---|---|---|---|---|---|---|---|---|---|
| $[\bar{2}11]$ | $[1\bar{2}1]$ | $[11\bar{2}]$ | $[2\bar{1}1]$ | $[\bar{1}21]$ | $[\bar{1}\bar{1}\bar{2}]$ | $[211]$ | $[\bar{1}\bar{2}1]$ | $[\bar{1}1\bar{2}]$ | $[\bar{2}\bar{1}1]$ | $[121]$ | $[1\bar{1}\bar{2}]$ |

We assume that plastic deformation of a crystal due to slip and twinning arises from a set of uniform shear increments occurring in small discrete volume-elements. The overall plastic deformation of a crystal is always inhomogeneous at length scales associated with slip and twinning, and should be defined as an average over a volume element that must contain enough dislocation loops and twins to result in an acceptably smooth process at the continuum level of interest here. The smallest such volume element above which the plastic response can be considered smooth, is labeled as a representative-volume element (RVE), and its volume denoted by $V$. We shall take *a small part of a crystal* as a representative-volume element in our simulations of

single crystal deformation, and the *whole crystal* as a representative-volume element for polycrystalline simulations.

Consider a single slip system characterized by a pair of orthonormal unit vectors $\mathbf{m}_0$ and $\mathbf{n}_0$ which define, respectively, the slip direction and the slip plane normal of a slip system. At any given time, let there be $n$ dislocation loops on such a slip system, and let $a_k$ denote the area of the $k$-th dislocation loop, and let $h$ = const. denote the spacing between the slip planes. Then, at a given time, there exist $n$ disk-like volume elements with principal planes normal to the unit vector $\mathbf{n}_0$, each of volume $v_k = h \times a_k$, which can potentially slip. The total volume of these disk-like volume elements is $v_{sl} = h \times \sum_{k=1}^{n} a_k$. Let $\gamma_{\text{tr}} = b/h$, with $b$ denoting the magnitude of the Burgers vector in the slip direction $\mathbf{m}_0$, be the transformation shear strain associated with each such volume element. Then, an increment of plastic deformation resulting from slip may be visualized as being produced by an increment $\Delta v_{sl} = h \times \sum_{k}^{n} \Delta a_k$ of the volume of the disk-like elements, and the volume-averaged incremental plastic deformation gradient for the crystal may be written as

$$\mathbf{F}^p{}_t(\tau) = \mathbf{1} + \Delta\gamma_{sl}\, \mathbf{m}_0 \otimes \mathbf{n}_0, \qquad \text{with} \qquad \Delta\gamma_{sl} = \frac{\Delta v_{sl}}{V}\,\gamma_{\text{tr}} = \frac{b \sum_{k=1}^{n} \Delta a_k}{V}, \tag{2.5}$$

where $\Delta\gamma_{sl}$ is the incremental shear due to slip which arises from the change in the entire area of the slip planes swept by mobile segments of the dislocation loops (Fig. 2-6).

Next, consider a single twin system characterized by a pair of orthonormal unit vectors $\mathbf{m}_0$ and $\mathbf{n}_0$ which define, respectively, the twin direction and the twin plane normal of a twin system, and let $\gamma_0$ be the twinning shear associated with this twin system. At a given time we assume that there exist $n$ lenticular volume elements with principal planes normal to the unit vector $\mathbf{n}_0$, which can potentially twin. The total volume of such lenticules is $v_{tw} = \sum_{l=1}^{n} v_l$, and their volume fraction in $V$ is $f = v_{tw}/V$. Then, an increment of plastic deformation resulting from twinning may be visualized as being produced by an increment $\Delta v_{tw}$ of the volume of the lenticular elements, and the volume averaged incremental plastic deformation gradient for the

crystal may be written as

$$\mathbf{F}^p{}_t(\tau) = \mathbf{1} + \Delta\gamma_{tw}\,\mathbf{m}_0 \otimes \mathbf{n}_0, \qquad \text{with} \qquad \Delta\gamma_{tw} = \Delta f\,\gamma_0, \quad \text{and} \quad \Delta f = \frac{\Delta v_{tw}}{V}, \tag{2.6}$$

where $\Delta\gamma_{tw}$ is the incremental shear due to twinning, and $\Delta f$ is the incremental volume fraction of the crystal that has undergone twinning (Fig. 2-7).

For combined slip and twin on multiple slip and twin systems, labeled by integers $i$ and $\alpha$, respectively, the kinematic expression generalizes to

$$\mathbf{F}^p{}_t(\tau) = \mathbf{1} + \sum_i \Delta\gamma^i\,\mathbf{S}_0^i + \sum_\alpha \Delta\gamma^\alpha\,\mathbf{S}_0^\alpha, \quad \mathbf{S}_0^i \equiv \mathbf{m}_0^i \otimes \mathbf{n}_0^i, \quad \mathbf{S}_0^\alpha \equiv \mathbf{m}_0^\alpha \otimes \mathbf{n}_0^\alpha, \tag{2.7}$$

where $\mathbf{S}_0^i$ is the Schmid tensor for the $i$-th slip system, and $\mathbf{S}_0^\alpha$ is the Schmid tensor for the $\alpha$-th twin system. Also,

$$\Delta\gamma^i = \frac{b\left(\sum_{k=1}^M \Delta a_k\right)^i}{V}, \quad \text{and} \quad \Delta\gamma^\alpha = \Delta f^\alpha\,\gamma_0, \tag{2.8}$$

are the plastic shearing increments on the $i$-th slip system and the $\alpha$-th twin system, respectively. In writing the above, we have used the fact that the magnitude of the Burgers' vector $b$ is the same for all the slip systems, and the twinning shear has the same value $\gamma_0 = 1/\sqrt{2}$ for all the twin systems in a f.c.c. crystal. For later use we define the twin fraction $f^\alpha(\tau)$ of the crystal at time $\tau$, which has deformed by twinning on system $\alpha$, by

$$f^\alpha(\tau) \equiv \frac{\Gamma^\alpha(\tau)}{\gamma_o}, \qquad \text{where} \quad \Gamma^\alpha(\tau) = \int_0^\tau \Delta\gamma^\alpha(\xi)\mathrm{d}\xi. \tag{2.9}$$

We have yet to specify under what conditions the shearing rates $\dot\gamma^i$ and $\dot\gamma^\alpha$ on the slip and twin systems are non-zero. We shall do that once we define the resolved shear stresses on the slip and twin systems, compare the values of these quantities to the slip and twin system shear resistances $s^i > 0$ and $s^\alpha > 0$, respectively, and more completely formulate the flow rule.

For the development of elastic-plastic constitutive equations for a single crystal,

we affix an orthonormal basis $\left\{\mathbf{e}_i^{(c)}\right\}$ $(i = 1, 2, 3)$ to the atomic lattice of the crystal to determine the orientation of a material neighborhood of the crystal. The reference configuration of such a material neighborhood is assumed to be stress free. The current configuration has deformation gradient $\mathbf{F}(t)$ and Cauchy stress $\mathbf{T}(t)$. Suppose for the moment that the operative plastic mechanism up to this point is only crystallographic slip. Then, associated with each material neighborhood we introduce a conceptual local configuration which is intermediate between the reference configuration and the current deformed configuration of the material neighborhood. Such a local intermediate configuration is assumed to be obtained by unloading a material neighborhood by reducing the stress to zero. The unloading process is again conceptual in nature, in that we assume: $(i)$ that it is possible to fix the current arrangement of the material neighborhoods on the microscale so as not to allow any rearrangements of the microstructure by slip or twinning as we reduce the stress to zero, thereby undistorting the lattice; and $(ii)$ that it is possible to orient the unloaded configuration such that $\left\{\mathbf{e}_i^{(c)}\right\}$ in this configuration has the same orientation with respect to a fixed orthonormal basis $\left\{\mathbf{e}_i^{(g)}\right\}$ in space, as it did in the reference configuration. Following Mandel [1974], such a relaxed configuration is referred to as *isoclinic*. The deformation gradient associated with this specially-oriented relaxed configuration is denoted by $\mathbf{F}^p(t)$, it has $\det \mathbf{F}^p(t) = 1$, and is called the plastic deformation gradient. The elastic deformation gradient may then be defined by $\mathbf{F}^e(t) \equiv \mathbf{F}(t)\,\mathbf{F}^p(t)^{-1}$ with $\det \mathbf{F}^e(t) > 0$. The plastic part $\mathbf{F}^p(t)$ in this multiplicative decomposition of $\mathbf{F}(t) = \mathbf{F}^e(t)\,\mathbf{F}^p(t)$ represents the cumulative effect of plastic deformation mechanisms in the crystal, and the elastic part $\mathbf{F}^e(t)$ describes the elastic distortion of the lattice; it is this distortion that gives rise to the stress $\mathbf{T}(t)$.

Now consider an incremental deformation occurring over an infinitesimal time increment $\Delta t = \tau - t$, with relative deformation gradient $\mathbf{F}_t(\tau)$, so that $\mathbf{F}(\tau) = \mathbf{F}_t(\tau)\,\mathbf{F}(t)$. If the plastic part of the incremental deformation is due to slip alone, then $\mathbf{F}^p(\tau) = \mathbf{F}_t^p(\tau)\,\mathbf{F}^p(t)$, with $\mathbf{F}_t^p(\tau) = \mathbf{1} + \sum_i \Delta\gamma^i\,\mathbf{S}_0^i(t)$, the lattice in the relaxed configuration maintains the same orientation as it had at time $t$, and the elastic deformation gradient which determines the stress $\mathbf{T}(\tau)$ is given by $\mathbf{F}^e(\tau) = \mathbf{F}(\tau)\mathbf{F}^p(\tau)^{-1}$,

Fig. 2-8. In contrast, if the plastic part of the incremental deformation is due to twinning alone, then $\mathbf{F}_t^p(\tau) = \mathbf{1} + \sum_\alpha \Delta\gamma^\alpha \mathbf{S}_0^\alpha(t)$, and twin fractions $\Delta f^\alpha = \Delta\gamma^\alpha/\gamma_0$ of the crystal have to be reoriented according to the appropriate rotations associated with the new twin orientations. Treating the twinned fractions as new orientations essentially involves introducing new crystals, and this quickly leads to a numerically-unmanageable number of crystals in a calculation of the response of a polycrystal. In Van Houtte's [1978] approach, if a crystal twins, then the twin is first treated as a "pseudo-slip," and its lattice is given a twinning-related orientation only if a probabilistic criterion, based on the relative twin fractions of the twinned and non-twinned parts of a crystal, is met. Specifically, during the "pseudo-slip" phase, with $f^\alpha(\tau) \equiv \Gamma^\alpha(\tau)/\gamma_0$ denoting the "twin fraction" corresponding to a twin system, Van Houtte suggests that we compare the twin fraction $f(\tau) = \max\{f^\alpha(\tau)\}$ with a random number $\xi \in [0.2, 1]$; if $f > \xi$, then the orientation of the RVE is replaced by the orientation of the twinned part of the grain corresponding to the system $\alpha$. That is, if $\bar{\mathbf{Q}}(t)$ denotes a rotation tensor[2] which brings the orthonormal crystal basis $\left\{\mathbf{e}_i^{(c)}(t)\right\}$ to be in correspondence with the fixed orthonormal global basis $\left\{\mathbf{e}_i^{(g)}\right\}$, $\mathbf{e}_i^{(g)} = \bar{\mathbf{Q}}(t)\,\mathbf{e}_i^{(c)}(t)$, then for the reoriented crystal, for which the orientation of the crystal basis after twinning is $\mathbf{e}_i^{(c)}(\tau) = \mathbf{R}^{tw}(t)\mathbf{e}_i^{(c)}(t)$, the corresponding relationship between the global basis and the reoriented crystal basis is $\mathbf{e}_i^{(g)} = \left(\bar{\mathbf{Q}}(t)\,(\mathbf{R}^{tw}(t))^T\right)\,\mathbf{e}_i^{(c)}(\tau)$. Once a grain is given a new twin-related orientation, the accumulated strain $\Gamma^\alpha$ on all twin systems in that grain is set to zero, $\bar{\mathbf{Q}}(\tau)$ is set equal $\bar{\mathbf{Q}}(\tau) = \bar{\mathbf{Q}}(t)\,(\mathbf{R}^{tw}(t))^T$, and the algorithm continued.

## 2.3 Governing Equations and Time-Integration Procedure

The governing variables of the model are: (*i*) The Cauchy stress, $\mathbf{T}$. (*ii*) The deformation gradient, $\mathbf{F}$. (*iii*) Crystal slip systems and twin systems, labeled by integers $i$

[2]Deriviation of the rotation tensor form is presented in Appendix B.

and $\alpha$. Each slip system is specified by a unit normal $\mathbf{n}_o^i$ to the slip plane, and a unit vector $\mathbf{m}_o^i$ denoting the slip direction; and each twin system is specified by a unit normal $\mathbf{n}_o^\alpha$ to the twin plane, and a unit vector $\mathbf{m}_o^\alpha$ denoting the twin direction. $(iv)$ The plastic deformation gradient, $\mathbf{F}^p$, with $\det\mathbf{F}^p = 1$. The local configuration defined by $\mathbf{F}^p$ is relaxed, that is, $\mathbf{T} = \mathbf{0}$. $(v)$ The slip and twin systems have deformation resistances $s^i > 0$ and $s^\alpha > 0$, respectively, in units of stress.

We take as given $\{\mathbf{F}(t), \mathbf{F}(\tau)\}$, $\{\mathbf{T}(t), \mathbf{F}^p(t)\}$, $\{\mathbf{m}_o^i(t), \mathbf{n}_o^i(t), s^i(t)\}$, and $\{\mathbf{m}_o^\alpha(t), \mathbf{n}_o^\alpha(t), s^\alpha(t)\}$. Then the incremental problem is to calculate $\{\mathbf{T}(\tau), \mathbf{F}^p(\tau)\}$, $\{\mathbf{m}_o^i(\tau), \mathbf{n}_o^i(\tau), s^i(\tau),\}$, $\{\mathbf{m}_o^\alpha(\tau), \mathbf{n}_o^\alpha(\tau), s^\alpha(\tau),\}$, and the orientation of the slip systems in the deformed configuration at time $\tau$ from

$$\mathbf{m}_\tau^i = \mathbf{F}^e(\tau)\mathbf{m}_o^i(\tau), \qquad \mathbf{n}_\tau^i = \mathbf{F}^e(\tau)^{-T}\mathbf{n}_o^i(\tau), \tag{2.10}$$

$$\mathbf{m}_\tau^\alpha = \mathbf{F}^e(\tau)\mathbf{m}_o^\alpha(\tau), \qquad \mathbf{n}_\tau^\alpha = \mathbf{F}^e(\tau)^{-T}\mathbf{n}_o^\alpha(\tau), \tag{2.11}$$

and march forward in time.

For metallic materials the elastic stretch is usually infinitesimal, and accordingly the constitutive equation for stress may be taken as a linear relation

$$\mathbf{T}^*(\tau) = \boldsymbol{\mathcal{C}}\left[\mathbf{E}^e(\tau)\right], \tag{2.12}$$

where $\boldsymbol{\mathcal{C}}$ is a fourth order anisotropic elasticity tensor. With

$$\mathbf{C}^e(\tau) = (\mathbf{F}^e(\tau))^T\mathbf{F}^e(\tau), \tag{2.13}$$

defining an elastic right Cauchy-Green tensor,

$$\mathbf{E}^e(\tau) = (1/2)\,\{\mathbf{C}^e(\tau) - \mathbf{1}\} \tag{2.14}$$

is an elastic strain measure, and

$$\mathbf{T}^*(\tau) = \mathbf{F}^e(\tau)^{-1}\,\{(\det\mathbf{F}^e(\tau))\;\mathbf{T}(\tau)\}\;\mathbf{F}^e(\tau)^{-T} \tag{2.15}$$

is a stress measure conjugate to the strain measure (2.14).

The scalar

$$\tau(\tau) = \{\mathbf{C}^e(\tau)\,\mathbf{T}^*(\tau)\} \cdot \mathbf{S}_0(t) \tag{2.16}$$

is the resolved shear stress, or the Schmid stress, on a slip or twin system at time $\tau$. For infinitesimal elastic stretches the resolved shear stress $\tau(\tau)$ may be approximated by

$$\tau(\tau) \doteq \mathbf{T}^*(\tau) \cdot \mathbf{S}_0(t). \tag{2.17}$$

Next, we define a *trial* elastic strain and stress at time $\tau$ as follows. We fix the value of $\mathbf{F}^p$ at time $t$, and define a trial elastic deformation gradient by

$$\mathbf{F}^e(\tau)^{\mathrm{tr}} = \mathbf{F}(\tau)\,\mathbf{F}^p(t)^{-1}, \tag{2.18}$$

in terms of which we define a trial elastic right Cauchy-Green tensor by

$$\mathbf{C}^e(\tau)^{\mathrm{tr}} = (\mathbf{F}^e(\tau)^{\mathrm{tr}})^T \mathbf{F}^e(\tau)^{\mathrm{tr}}, \tag{2.19}$$

a trial elastic strain by

$$\mathbf{E}^e(\tau)^{\mathrm{tr}} = (1/2)\left\{\mathbf{C}^e(\tau)^{\mathrm{tr}} - \mathbf{1}\right\}, \tag{2.20}$$

a trial stress by

$$\mathbf{T}^*(\tau)^{\mathrm{tr}} = \boldsymbol{\mathcal{C}}\left[\mathbf{E}^e(\tau)^{\mathrm{tr}}\right], \tag{2.21}$$

and trial resolved shear stresses on the slip and twin systems by

$$\tau^i(\tau)^{\mathrm{tr}} = \mathbf{T}^*(\tau)^{\mathrm{tr}} \cdot \mathbf{S}_0^i(t), \quad \tau^\alpha(\tau)^{\mathrm{tr}} = \mathbf{T}^*(\tau)^{\mathrm{tr}} \cdot \mathbf{S}_0^\alpha(t). \tag{2.22}$$

For active slip and twin systems, both the trial and actual values of the resolved shear stresses are well separated from zero, and it is reasonable to expect that

$$\mathrm{sign}\left(\tau^i(\tau)\right) \equiv \mathrm{sign}\left(\tau^i(\tau)^{\mathrm{tr}}\right), \quad \mathrm{sign}\left(\tau^\alpha(\tau)\right) \equiv \mathrm{sign}\left(\tau^\alpha(\tau)^{\mathrm{tr}}\right). \tag{2.23}$$

With these definitions, the incremental flow rule is taken as

$$\mathbf{F}^p(\tau) = \left\{ \mathbf{1} + \sum_i \Delta\gamma^i \operatorname{sign}\left(\tau^i(\tau)^{\mathrm{tr}}\right) \mathbf{S}_0^i(t) + \sum_\alpha \Delta\gamma^\alpha \mathbf{S}_0^\alpha(t) \right\} \mathbf{F}^p(t)\,, \tag{2.24}$$

with

$$\Delta\gamma^i = \left\{ \begin{array}{lll} 0 & \text{if} & \left|\tau^i(\tau)^{\mathrm{tr}}\right| \leq s^i(t), \\ \\ \geq 0 & \text{if} & \left|\tau^i(\tau)^{\mathrm{tr}}\right| > s^i(t), \end{array} \right\} \tag{2.25}$$

and

$$\Delta\gamma^\alpha = \left\{ \begin{array}{lll} 0 & \text{if} & \tau^\alpha(\tau)^{\mathrm{tr}} \leq s^\alpha(t), \\ \\ \geq 0 & \text{if} & \tau^\alpha(\tau)^{\mathrm{tr}} > s^\alpha(t). \end{array} \right\} \tag{2.26}$$

Systems for which

$$\left|\tau^i(\tau)^{\mathrm{tr}}\right| \leq s^i(t), \quad \tau^\alpha(\tau)^{\mathrm{tr}} \leq s^\alpha(t),$$

are *inactive*, and those for which

$$\left|\tau^i(\tau)^{\mathrm{tr}}\right| > s^i(t), \quad \tau^\alpha(\tau)^{\mathrm{tr}} > s^\alpha(t),$$

are *potentially active*. We denote by

$$\mathcal{PA}^{sl} = \{i \,|i = 1, \cdots, m\}\,, \quad \mathcal{PA}^{tw} = \{\alpha \,|\alpha = 1, \cdots, n\}$$

the *potentially active* slip and twin systems. The set of all potentially active slip and twin systems is denoted simply by $\mathcal{PA}$. Of the potentially active systems, the $p \leq m$ slip systems, and the $q \leq n$ twin systems for which the shear increments are actually non-zero are the *active* systems, and we denote the set of active systems by $\mathcal{A}^{sl}$ and $\mathcal{A}^{tw}$, respectively. The set of all active slip and twin systems is denoted by $\mathcal{A}$.

Since the twin systems have been defined such that both $\tau^\alpha(\tau)^{\mathrm{tr}}$ and $\tau^\alpha(\tau)$ are positive valued on the potentially active as well as the active twin systems, to simplify notation we let the index $i$ extend over all slip and twin systems and write the

incremental flow rule as

$$\mathbf{F}^p(\tau) = \left\{ \mathbf{1} + \sum_{i \in \mathcal{PA}} \Delta\gamma^i \, \mathrm{sign}\left(\tau^i(\tau)^{\mathrm{tr}}\right) \, \mathbf{S}_0^i(t) \right\} \mathbf{F}^p(t). \tag{2.27}$$

Also, the slip and twin systems resistances are denoted simply by $s^i$; the evolution equation for these resistances is taken in a generic form as

$$s^i(\tau) = s^i(t) + \sum_{j \in \mathcal{PA}} h^{ij}(t) \, \Delta\gamma^j, \quad i = 1, \cdots, N, \tag{2.28}$$

where $h^{ij}$ are the hardening moduli, and $N$ is the total number of slip and twin systems. The nature of the slip/twin hardening moduli is the least well understood part of the theory. Accordingly, in the following section we will first examine texture evolution in a non-hardening model, and then we will construct an approximate hardening model to also match the macroscopic strain hardening response of the brass under study.

During plastic flow the active systems must satisfy the consistency condition

$$\left|\tau^i(\tau)\right| = s^i(\tau). \tag{2.29}$$

The calculation of $|\tau^i(\tau)|$ proceeds as follows. Using (2.27), $\mathbf{F}^e(\tau) = \mathbf{F}(\tau)\,\mathbf{F}^{p-1}(\tau)$, equations (2.18, 2.19, 2.20 ), and retaining terms of first order in $\Delta\gamma^j$, we obtain

$$\mathbf{E}^e(\tau) = \mathbf{E}^e(\tau)^{\mathrm{tr}} - \sum_{j \in \mathcal{PA}} \Delta\gamma^j \mathrm{sign}\left(\tau^j(\tau)^{\mathrm{tr}}\right) \mathrm{sym}\left(\mathbf{C}^e(\tau)^{\mathrm{tr}} \mathbf{S}_0^j(t)\right), \tag{2.30}$$

and then using (2.30) in (2.12), together with (2.17,2.21,2.23), gives

$$\begin{aligned} \left|\tau^i(\tau)\right| \;=\; & \left|\tau^i(\tau)^{\mathrm{tr}}\right| - \\ & \sum_{j \in \mathcal{PA}} \left\{ \mathrm{sign}\left(\tau^i(\tau)^{\mathrm{tr}}\right) \mathrm{sign}\left(\tau^j(\tau)^{\mathrm{tr}}\right) \right. \\ & \left. \mathbf{S}_0^i(t) \cdot \boldsymbol{\mathcal{C}} \left[ \mathrm{sym}\left(\mathbf{C}^e(\tau)^{\mathrm{tr}} \mathbf{S}_0^j(t)\right) \right] \right\} \Delta\gamma^j . \end{aligned} \tag{2.31}$$

Use of (2.31) in the consistency condition (2.29) gives

$$\sum_{j \in \mathcal{PA}} A^{ij}\, x^j = b^j\,, \qquad i \in \mathcal{PA}, \tag{2.32}$$

with

$$A^{ij} = h^{ij} + \text{sign}\left(\tau^i(\tau)^{\text{tr}}\right) \text{sign}\left(\tau^j(\tau)^{\text{tr}}\right) \mathbf{S}_0^i(t) \cdot \mathcal{C}\left[\text{sym}\left(\mathbf{C}^e(\tau)^{\text{tr}} \mathbf{S}_0^j(t)\right)\right] \tag{2.33}$$

$$b^i = \left|\tau^i(\tau)^{\text{tr}}\right| - s^i(t) > 0, \tag{2.34}$$

$$x^j \equiv \Delta\gamma^j \geq 0. \tag{2.35}$$

Equation (2.32) is a system of linear equations for $x^j \equiv \Delta\gamma^j \geq 0$.

For the case of slip alone, Anand and Kothari [1996] have recently proposed an iterative solution procedure based on the Singular Value Decomposition (SVD) of the matrix $A$, to determine the active slip systems and the corresponding shear increments. In their procedure the shear increments are calculated as

$$x^+ = A^+ b,$$

where $A^+$ is the pseudo-inverse of the matrix $A$, defined over all the potentially active slip and twin systems. If $A$ is singular, then from the set of non-unique solutions to $Ax = b$, the chosen solution is the one which has the minimum length $||x||_2$. If for any system the solution $x^j = \Delta\gamma^j \leq 0$, then this system is inactive, and it is removed from the set of potentially active systems. The reduced system $Ax = b$ is solved again using the pseudo-inverse of the new $A$. This iterative procedure is continued until all $x^j = \Delta\gamma^j > 0$. An alternate procedure which does not involve iterations, and which is based on a constrained quadratic minimization statement of the problem, is given in the next section. The solutions obtained by either method are identical.

To summarize, with $t$ denoting the current time, $\Delta t$ is an infinitesimal time increment, and $\tau = t + \Delta t$. The algorithm is as follows:

**Given**: (1) $\{\mathbf{F}(t), \mathbf{F}(\tau)\}$; (2) $\{\mathbf{T}(t), \mathbf{F}^p(t)\}$; (3) the rotation tensor $\bar{\mathbf{Q}}(t)$, which brings

the orthonormal crystal basis $\left\{\mathbf{e}_i^{(c)}(t)\right\}$ to be in correspondence with a fixed orthonormal basis $\left\{\mathbf{e}_i^{(g)}\right\}$ in space; (4) $\{\mathbf{m}_o^i(t), \mathbf{n}_o^i(t), s^i(t)\}$; and (5) the accumulated shears due to twinning $\Gamma^i(t)$, where the index $i$ ranges over the previously active twin systems since the last reorientation of the lattice.

**Calculate:** (a) $\{\mathbf{T}(\tau), \mathbf{F}^p(\tau)\}$; (b) the accumulated shears due to twinning $\Gamma^i(\tau)$, where the index $i$ ranges over the previously active twin systems since the last reorientation of the lattice; (c) the rotation tensor $\bar{\mathbf{Q}}(\tau)$, which brings the orthonormal crystal basis $\left\{\mathbf{e}_i^{(c)}(\tau)\right\}$ to be in correspondence with a fixed orthonormal basis $\left\{\mathbf{e}_i^{(g)}\right\}$ in space; (d) $\{\mathbf{m}_o^i(\tau), \mathbf{n}_o^i(\tau), s^i(\tau), \}$; and (e) the orientation of the slip and systems in the deformed configuration at time $\tau$ from

$$\mathbf{m}_\tau^i = \mathbf{F}^e(\tau)\mathbf{m}_o^i(\tau), \qquad \mathbf{n}_\tau^i = \mathbf{F}^e(\tau)^{-T}\mathbf{n}_o^i(\tau),$$

and march forward in time.

The steps used in the calculation procedure are:

**Step 1.** Calculate the trial elastic strain $\mathbf{E}^e(\tau)^{tr}$ :

$$\begin{aligned}
\mathbf{F}^e(\tau)^{\mathrm{tr}} &= \mathbf{F}(\tau)\,\mathbf{F}^p(t)^{-1}, \\
\mathbf{C}^e(\tau)^{\mathrm{tr}} &= (\mathbf{F}^e(\tau)^{\mathrm{tr}})^T\mathbf{F}^e(\tau)^{\mathrm{tr}}, \\
\mathbf{E}^e(\tau)^{\mathrm{tr}} &= (1/2)\{\mathbf{C}^e(\tau)^{\mathrm{tr}} - \mathbf{1}\}.
\end{aligned} \tag{2.36}$$

**Step 2.** Calculate the trial stress $\mathbf{T}^*(\tau)^{\mathrm{tr}}$ :

$$\mathbf{T}^*(\tau)^{\mathrm{tr}} = \boldsymbol{\mathcal{C}}[\mathbf{E}^e(\tau)^{\mathrm{tr}}].$$

**Step 3.** Calculate the trial resolved shear stress $\tau^i(\tau)^{\mathrm{tr}}$ on each slip system :

$$\begin{aligned}
\mathbf{S}_o^i &= \mathbf{m}_0^i \otimes \mathbf{n}_0^i, \\
\tau^i(\tau)^{\mathrm{tr}} &= \mathbf{T}^*(\tau)^{\mathrm{tr}} \cdot \mathbf{S}_o^i.
\end{aligned}$$

**Step 4.** Determine the set $\mathcal{PA}$ of the potentially active slip and twin systems which satisfy

$$|\tau^i(\tau)^{\mathrm{tr}}| - s^i(t) > 0, \tag{2.37}$$

for the slip systems, and

$$\tau^i(\tau)^{\mathrm{tr}} - s^i(t) > 0 \tag{2.38}$$

for the twin systems.

**Step 5.** Calculate the shear increments from the consistency condition:

$$Ax = b,$$

where $A$ is the possibly singular matrix defined over all the potentially active slip and twin systems, with elements

$$\begin{aligned} A^{ij} &= h^{ij} + \text{sign}\ (\tau^i(\tau)^{\mathrm{tr}})\ \text{sign}\ (\tau^j(\tau)^{\mathrm{tr}})\ \mathbf{S}_o^i(t) \cdot \boldsymbol{\mathcal{C}}[\text{sym}\ (\mathbf{C}^e(\tau)^{\mathrm{tr}}\mathbf{S}_o^j(t))], \\ b^i &= |\tau^i(\tau)^{\mathrm{tr}}| - s^i(t), \\ x^j &\equiv \Delta\gamma^j \geq 0. \end{aligned}$$

This calculation may be performed by using either the iterative method based on the pseudo-inverse of $A$ (Anand and Kothari, 1996), or the quadratic-minimization method detailed in the next section.

**Step 6.** Update the plastic deformation gradient $\mathbf{F}^p(\tau)$ :

$$\mathbf{F}^p(\tau) = \mathbf{1} + \sum_{i \in \mathcal{A}} \text{sign}\,(\tau^i(\tau)^{\mathrm{tr}}) \Delta\gamma^i \mathbf{S}_o^i(t)\} \mathbf{F}^p(t).$$

**Step 7.** Check if $\det \mathbf{F}^p(\tau) = 1$. If not, normalize $\mathbf{F}^p(\tau)$ as :

$$\mathbf{F}^p(\tau) = [\det \mathbf{F}^p(\tau)]^{-1/3}\ \mathbf{F}^p(\tau).$$

**Step 8.** Compute the elastic deformation gradient $\mathbf{F}^e(\tau)$ and the stress $\mathbf{T}^*(\tau)$:

$$\begin{aligned} \mathbf{F}^e(\tau) &= \mathbf{F}(\tau)\mathbf{F}^{p^{-1}}(\tau) \\ \mathbf{T}^*(\tau) &= \boldsymbol{\mathcal{C}}[\mathbf{E}^e(\tau)]. \end{aligned}$$

**Step 9.** Update the variables $\{\mathbf{T}(\tau), s^i(\tau)\}$ :

$$\begin{aligned} \mathbf{T}(\tau) &= \mathbf{F}^e(\tau)\left\{[\det\mathbf{F}^e(\tau)]^{-1}\,\mathbf{T}^*(\tau)\right\}\mathbf{F}^{e^T}(\tau) \\ s^i(\tau) &= s^i(t) + \sum_{j\in\mathcal{A}}^{r} h^{ij}\,\Delta\gamma^j, \quad i = 1,\cdots,N \end{aligned}$$

Here, $N$ denotes the total number of slip and twin systems. For example, $N = 24$, for a f.c.c. crystal.

**Step 10.** Update the twin fractions $f^i(\tau)$:

$$f^i(\tau) = f^i(t) + \frac{\Delta\gamma^i}{\gamma_0} \tag{2.39}$$

where the index $i$ ranges over all the active twin systems.

**Step 11.** Rotate the lattice if a sufficiently large fraction of the grain has twinned. Let $f(\tau) = \max\{f^i(\tau)\}$ denote the maximum value of the twin fraction, and let $\xi \in [0.2, 1]$ denote a random number. If $f > \xi$ set $\bar{\mathbf{Q}}(\tau) = \bar{\mathbf{Q}}(t)\,(\mathbf{R}^{tw}(t))^T$. Update the deformation resistances.

**Step 12.** Calculate the "texture" $(\mathbf{m}^i_\tau, \mathbf{n}^i_\tau)$ :

$$\begin{aligned} \mathbf{m}^i_\tau &= \mathbf{F}^e(\tau)\mathbf{m}^i_0(\tau), \\ \mathbf{n}^i_\tau &= \mathbf{F}^{e^{-T}}(\tau)\mathbf{n}^i_0(\tau). \end{aligned}$$

The single-crystal constitutive equations and the time-integration procedures described in this section have been implemented in the finite-element program ABAQUS/Explicit [1995] by writing a "user material" subroutine. The polycrystal calculations shown in

the following chapter were carried out by modeling each crystal in a polycrystalline aggregate as a single finite element quadroture point.

## 2.4 Determination of Active Systems and the Amount of Shear

To find the active systems and the corresponding shear increments we need to solve the linear problem

$$Ax = b, \tag{2.40}$$

subject to constraints

$$x_i \geq 0. \tag{2.41}$$

We may solve this problem using a minimization scheme as follows. First, we construct a convex scalar function as a sum of discrepancy and penalty functions. The discrepancy function is defined as

$$U = (Ax - b)^T(Ax - b), \tag{2.42}$$

minimizing of which gives a solution of the linear system in the sense of least squares. To take into account the constraints (2.41), we must add to the function $U$ a penalty function which helps in the satisfaction of the constraints. The form of penalty functions depends on the iterative minimization procedure. We chose the conjugate gradient method. This method converges to the minimum of the quadratic function in a finite number of steps. The main idea of the method is to choose a secant search direction in the subspace orthogonal to all the previous search directions. Two variants of this approach are the Fletcher-Powell [1963], and the Fletcher-Reeves [1964] algorithms. One of the simplest and most effective classes of penalty functions

is the "cut-type":

$$F(x) = \begin{cases} 0 & \text{if condition is satisfied,} \\ g(x) & \text{otherwise,} \end{cases}$$

where $g(x)$ is a positive function increasing with $x$ moving away from the domain where the condition is satisfied. We choose our penalty functions corresponding to the constraint (2.41) in the following form:

$$\Psi_i^2 = [\min(x_i, 0)]^2.$$

Together, the discrepancy and the penalty functions may be written as

$$\tilde{U} = U + C \sum \Psi_i^2, \tag{2.43}$$

where $C$ is a scalar weighting coefficient. Provided that the system (2.40) is not singular, the minimum of this function gives us the least square solution of the system (2.40) subject to the constraints (2.41). If $A$ is singular, the paraboloid degenerates to a plane, and the system has an infinite number of solutions. Guided by the SVD method outlined in the main body of the paper, we add another penalty term which guarantees a *minimum length* solution. With this, the minimization function becomes

$$U^* = U + C \sum \Psi_i^2 + W \sum (x_i)^2, \tag{2.44}$$

with gradient

$$G = 2A^T(Ax - b) + 2\,C\,\Psi + 2\,W\,x. \tag{2.45}$$

Here $W$ is another scalar weight coefficient. Since the last term should play a role only at the end of the solution process, and since it does not affect the solution if the matrix A is not singular, the weight $W$ should be small in contrast to the weight $C$. The weight coefficients $C$ and $W$, and the desired minimum value of the gradient $||G||$ are used to control the solution process.

The solutions obtained by either the minimization method outlined above, or the method based on the SVD decomposition of $A$, are identical. The advantage of the method outlined in this section is that it avoids the iterative and repeated solution of the system $Ax = b$, using the SVD method to ensure that the constraints $x_i \geq 0$ are satisfied.

This procedure explains the loss of uniqueness of the solution if one were to adopt an assumption of selecting the operative slip systems by minimizing the sum of shears. It can be understood from the point of view of convexity of objective function. We can write the last term in the expression (2.44) as $W(\sum_{i=1}^{i=N} |x_i|)$. If matrix [**A**] is singular i.e., the system of equations is linearly dependent, then there exist the whole domain each point of which satisfies to the minimum of the first two terms of (2.44). A small variation of the variables does not change the gradient[3]. Subsequently, any point of the domain is the solution of the problem. To obtain a unique solution, the last term in the expression (2.44) should be a convex function.

We have evaluated this model by comparing the predictions of the stress-strain response, the slip system activity and the evolution of the crystal lattice against corresponding predictions of the rate-dependent models of Kalidindi et al., [1992] and Anand and Kothari [1996]. Some results of our calculations are shown in Fig. 2-9. We analyzed simple tension of a single [$\bar{2}$36] oriented copper crystal. It deforms by two slip systems, first A3=(111)[$\bar{1}$01], than, when the crystal orientation of the tensile axis reaches the [001]-[$\bar{1}$11] boundary of the stereographic triangle, the conjugate slip system B5=(11$\bar{1}$)[011] becomes active. There are six slip systems activated in the [$\bar{1}$11] orientation. The slip activity on all the systems is equal, and the crystal orientation is stable, Fig. 2-10. This is very important case from the calculation point of view. The matrix **A** here is singular and the last term in 2.44 played the principal role in the obtaining of the solution. The results obtained by gradient method are not

[3]In matrix form the gradient of the function $U^*$ with non-convex penalty functions has a form:

$$\mathbf{G} = 2\mathbf{A}^T(\mathbf{Ax} - \mathbf{b}) + 2\,C\,\mathbf{\Psi} + W\,\mathbf{SIGN(x)} \qquad (2.46)$$

$\mathbf{\Psi}$ is a vector with coordinats $\Psi_i$ and $\mathbf{SIGN(x)}$ is a vector with coordinates sign$x_i$.

distinguishable from the results of SVD calculations[4].

[4]It is important to note that SVD method is made for solving linear systems and cannot be used for nonlinear ones. For example, if one derives the incremental model using the two first terms of the Taylor expansion of deformation gradient, the final system will be nonlinear. There is no difference in the gradient method application if linear or nonlinear system is.

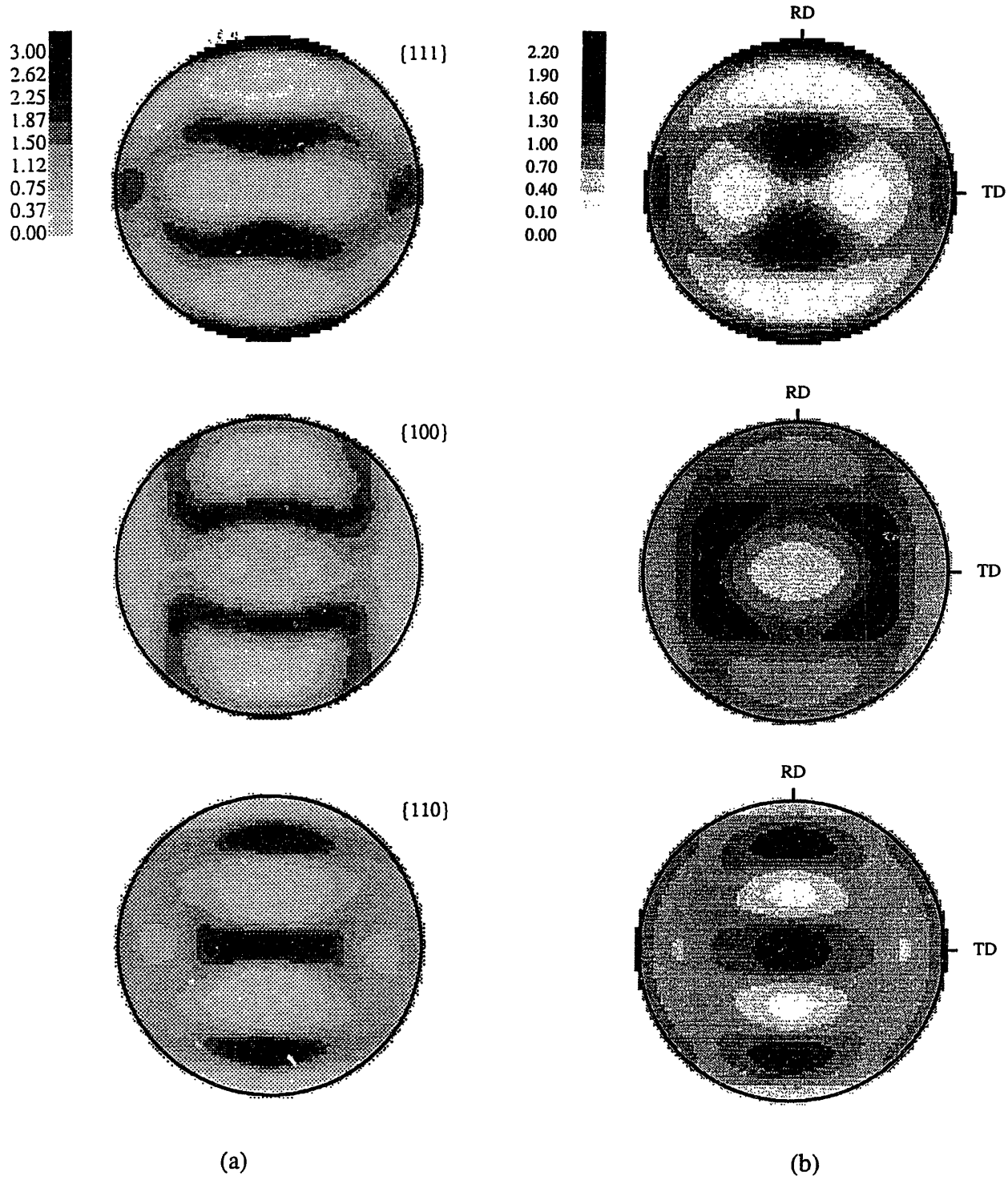


Figure 2-1: Experimentally-measured crystallographic texture for (a) copper (Bronkhorst *et al.*, 1992), and (b) 70-30 brass after plane strain compression of 100%.

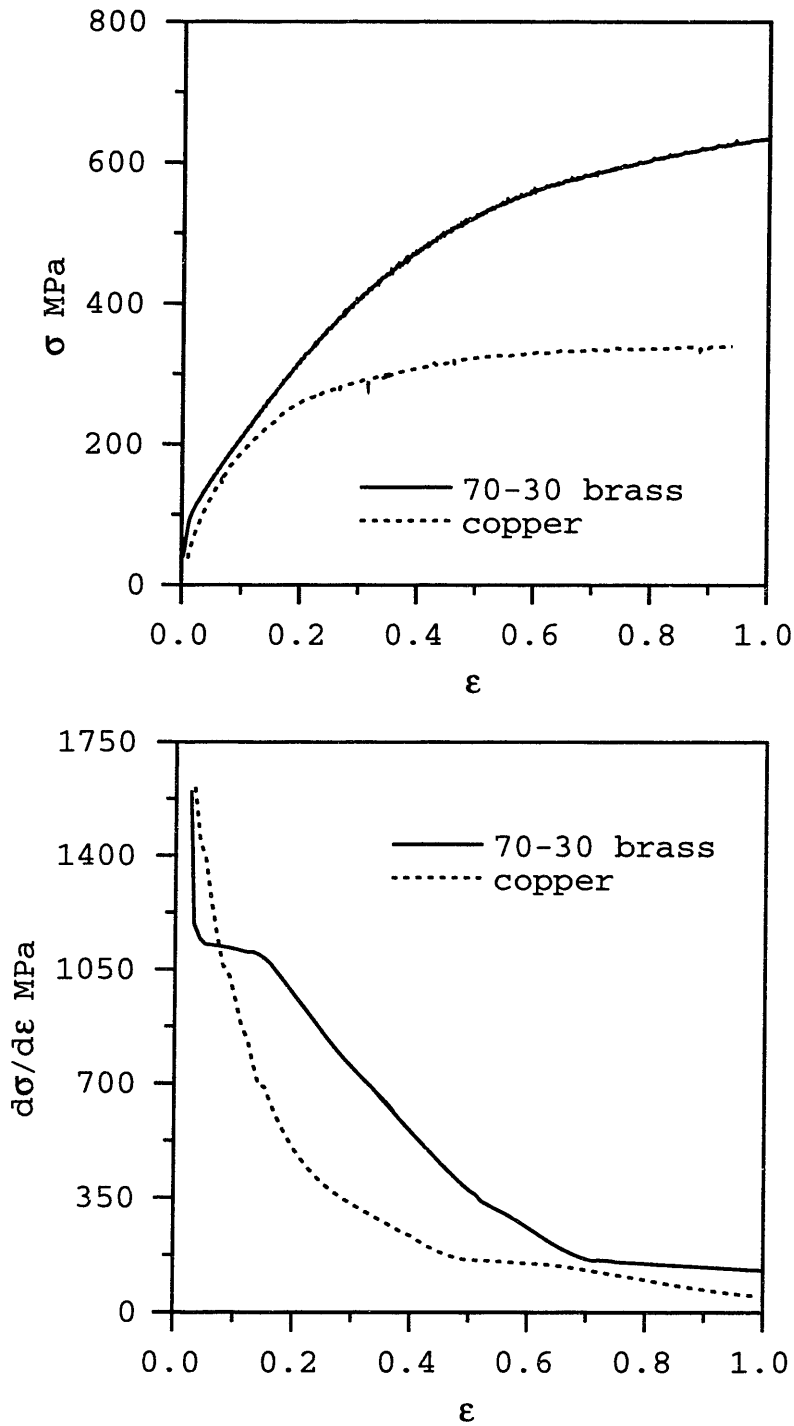


Figure 2-2: (a) Stress-strain curves, and (b) rate of strain-hardening versus strain in plane strain compression for 70-30 brass and copper.

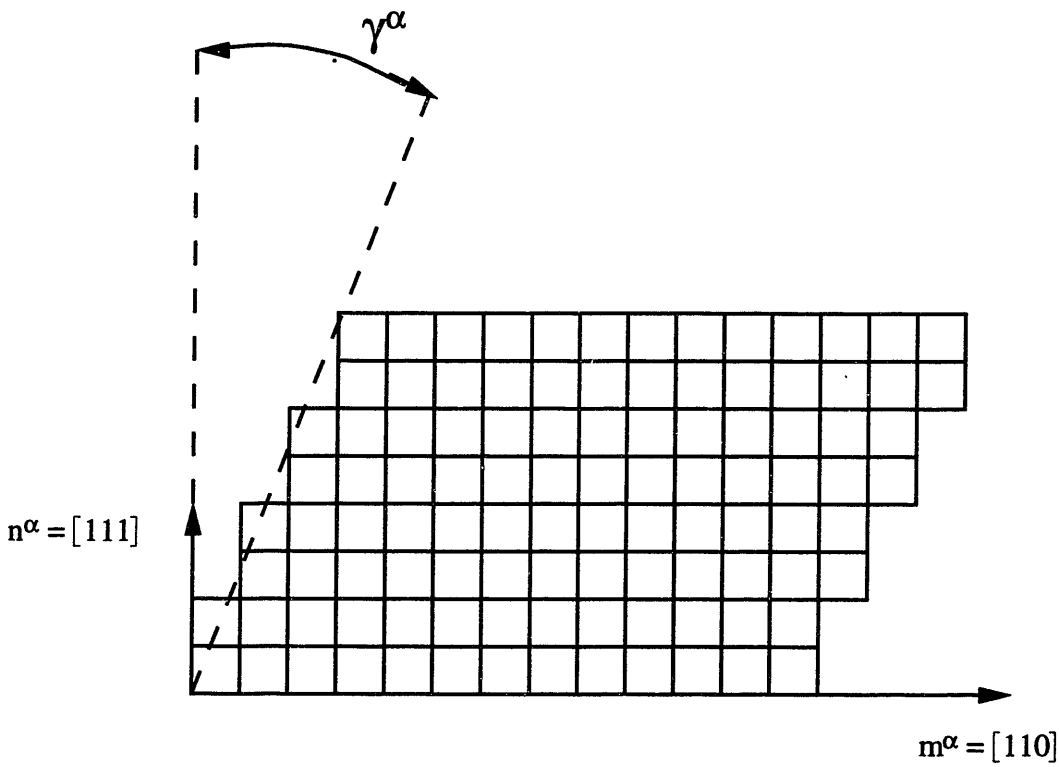


Figure 2-3: Deformation of crystallographic lattice by slip

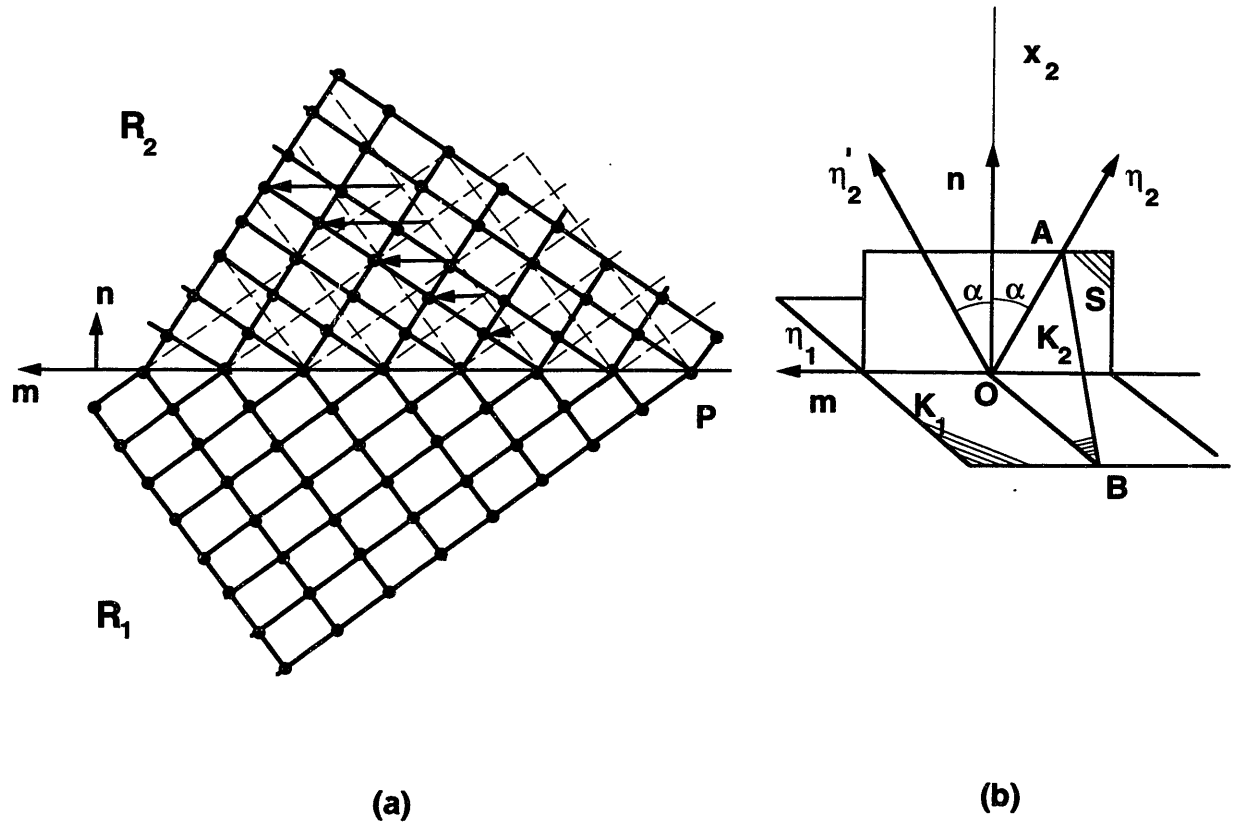


Figure 2-4: (a) Depiction of twinning in a local region of a crystal. (b) Crystallographic twinning elements $\{K_1, K_2, \eta_1, \eta_2\}$.

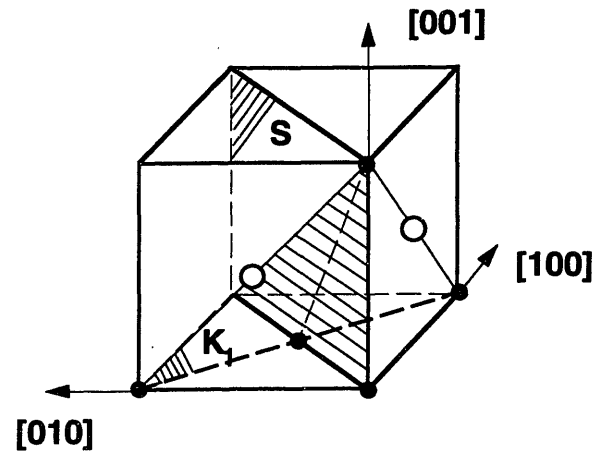


(a)

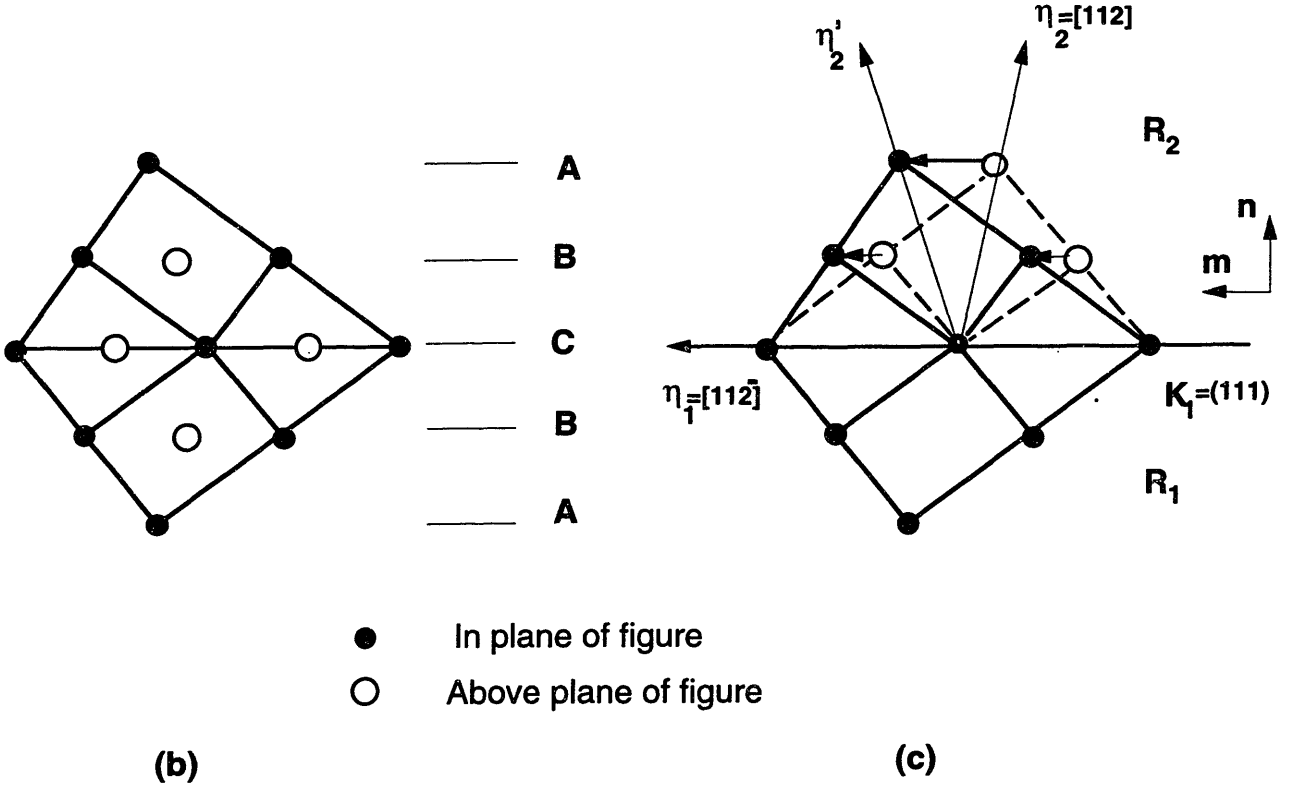


(b) (c)

Figure 2-5: (a) A twinning plane $K_1$ and a shear plane $S$ in a f.c.c. crystal. (b) Error in stacking sequence of (111) planes at the twinning plane. The stacking sequence ABCABC is turned into ABCBAC. (c) The twinning elements $\{K_1, K_2, \eta_1, \eta_2\}$ in a f.c.c. crystal.

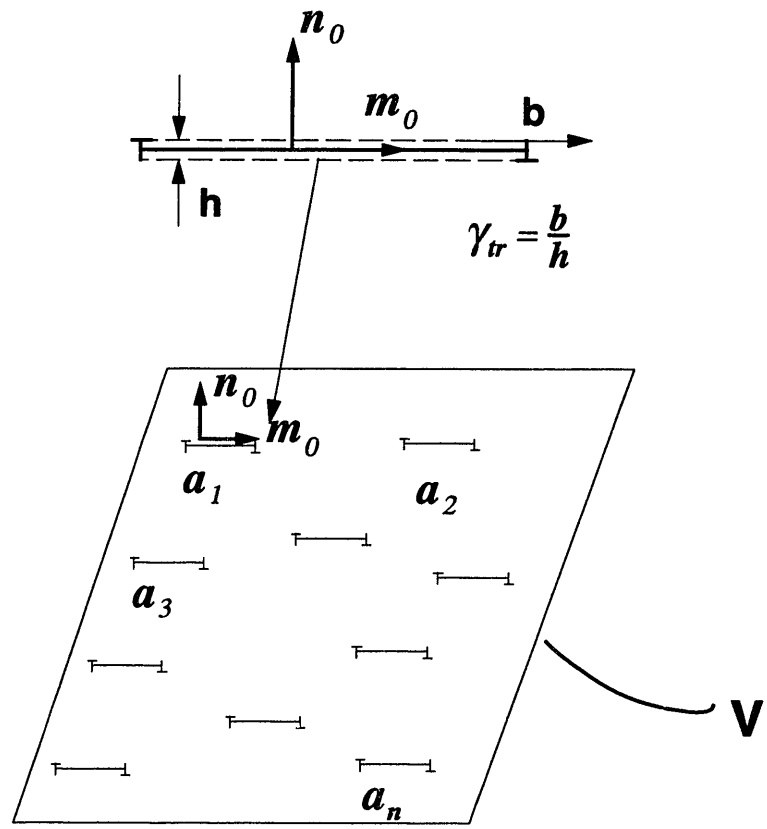


$$v_{sl} = h \times \sum_{k=1}^{n} a_k \qquad \gamma_{tr} = \frac{b}{h}$$

$$\Delta\gamma_{sl} = \frac{\Delta v_{sl}}{V}\gamma_{tr} = \frac{b\sum_{k=1}^{n}\Delta a_{\kappa}}{V}$$

$$F^{p}{}_{t}(\tau) = 1 + \Delta\gamma_{sl}\, m_0 \otimes n_0$$

Figure 2-6: Schematic of volume-averaged incremental plastic gradient in a crystal due to slip.

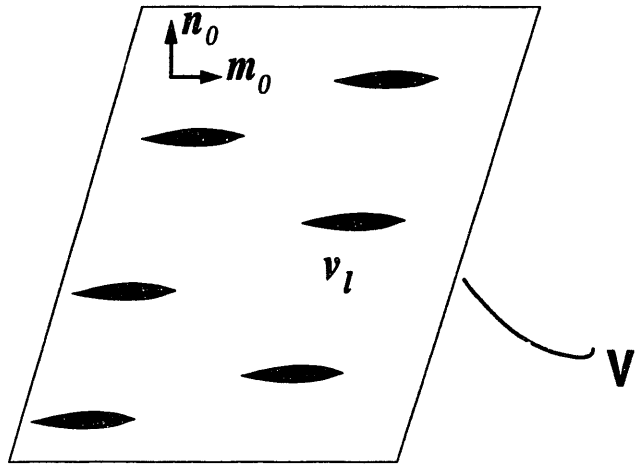


$$v_{tw} = \sum_{l=1}^{m} v_l$$

$$f = \frac{v_{tw}}{V} \qquad \gamma_0 = \textit{twinning shear}$$

$$\Delta\gamma_{tw} = \Delta f \ \gamma_0 \qquad \Delta f = \frac{\Delta v_{tw}}{V}$$

$$F^p{}_t(\tau) = 1 + \Delta\gamma_{sl}\, m_0 \otimes n_0$$

Figure 2-7: Schematic of volume-averaged incremental plastic gradient in a crystal due to twinning.

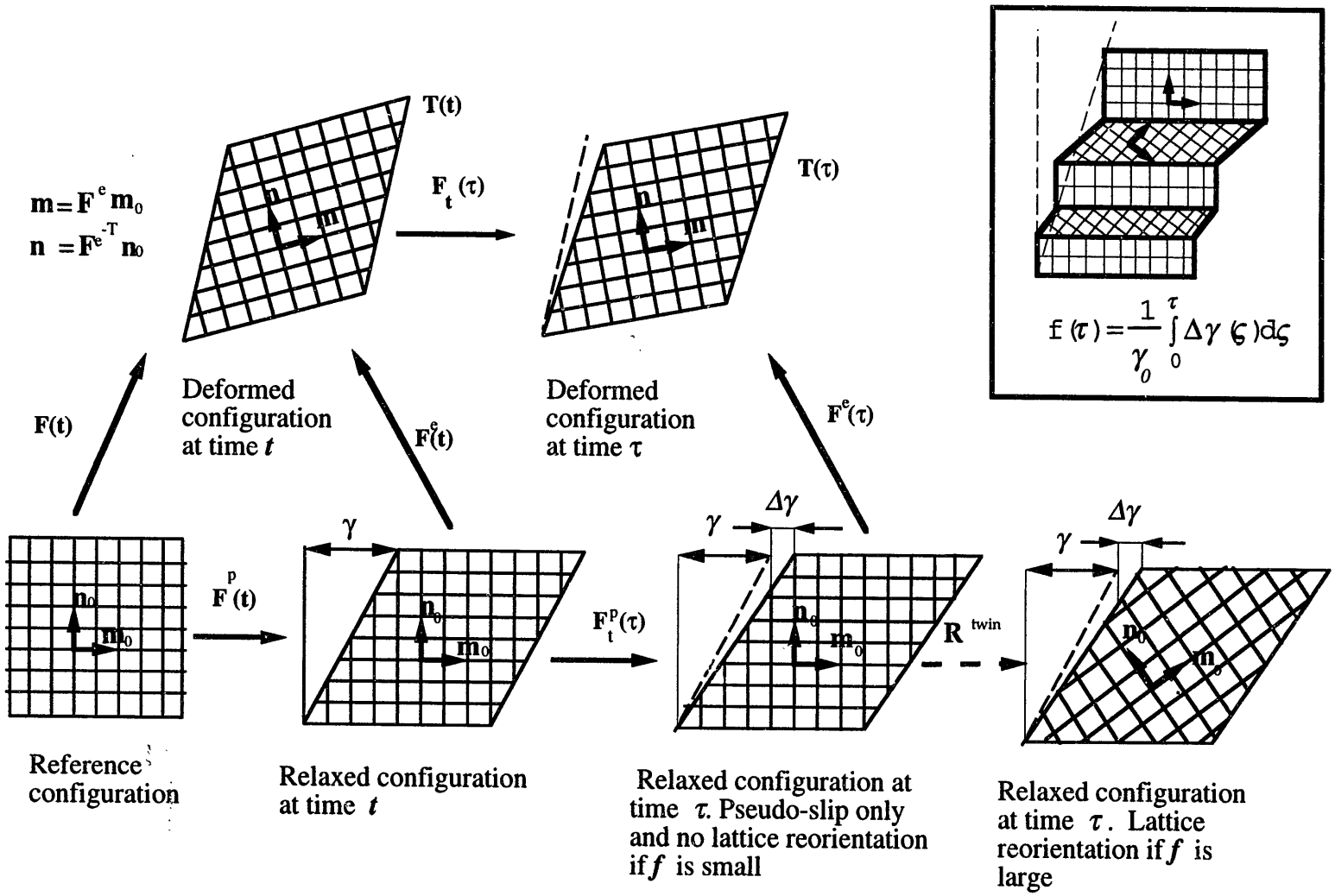


Figure 2-8: Schematic of the incremental kinematics of slip and twinning.

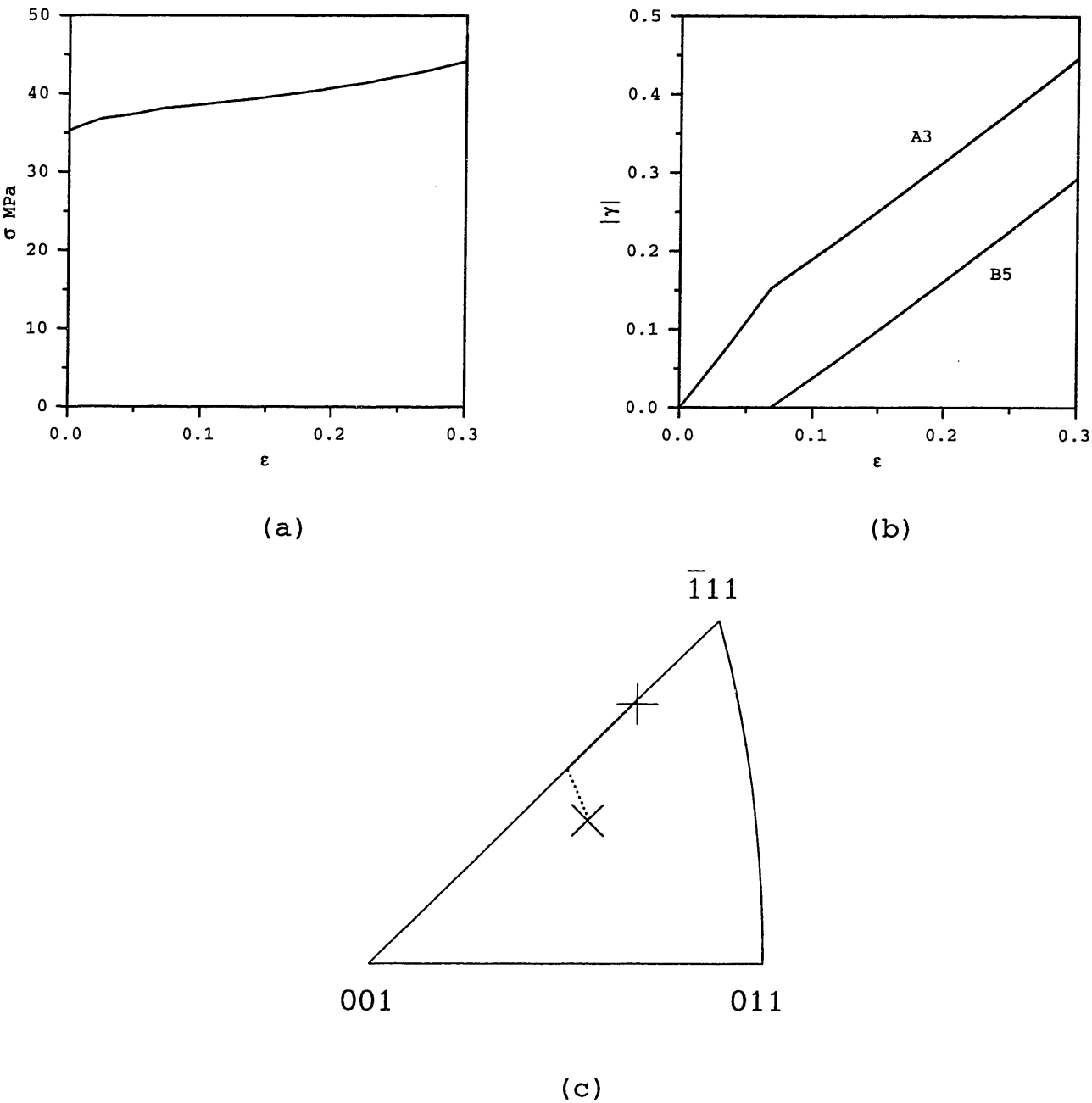


Figure 2-9: Simple tension of a non-hardening crystal initially oriented in the $[\bar{2}36]$ direction. (a) Stress-strain curve; (b) slip shears; (c) inverse pole figure of the change in the orientation of the tensile axis.

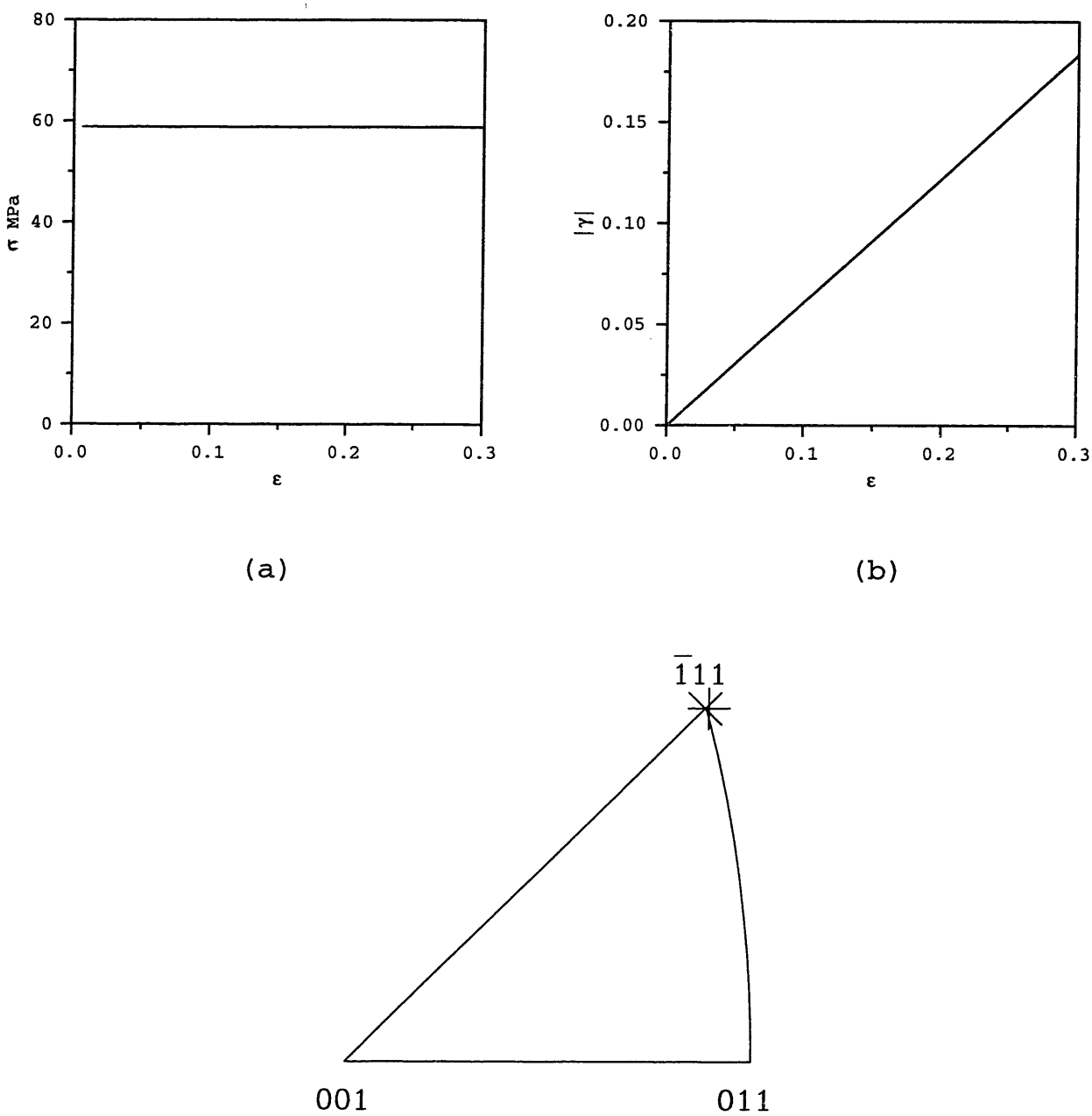


Figure 2-10: Simple tension of a non-hardening crystal initially oriented in the $[\bar{1}11]$ direction. (a) Stress-strain curve; (b) slip shears; (c) inverse pole figure of the change in the orientation of the tensile axis.

# Chapter 3

# Inelastic Deformation of Face Centered Cubic Single Crystals by Slip and Twinning.

## 3.1 Background

In the present chapter we report on our computational experiments on texture evolution and twin bands formation in plane strain compression of single crystals of f.c.c. materials.

There appears to be very little work devoted to detailed modeling of single crystal inelastic deformation due to slip and twinning. The study of deformation twinning in single crystals is in its nascent stage. Wassermann et al. [1963] and Narita and Takamura [1974]; reported mostly experimental results. I. Lifshiz [1948], Khachaturyan [1983], J. M. Ball and R. D. James [1987], Rosakis [1992] and several others investigated the twinn-lamellae structure in a grain by minimization of elastic energy. In their analysis, the effects of large plastic deformation and texture evolution were neglected. Some of the early considerations of twinning in crystal plasticity models are those of Chin et al. [1969]. In this early model the shear due to twinning was treated as pseudo-slip, but the rotation due to twinning was not accounted for, and

hence the model was not capable of predicting crystallographic texture evolution. Evolution of texture due to slip and twinning has been considered by Van Houtte [1978], and more recently by Tome and co-workers [1991] and [1994]. However, their considerations have been for the rigid-plastic, non-hardening case, and have been limited to the Taylor (e.g., Van Houtte 1978) or the "self-consistent" (e.g., Lebensohn and Tome, 1994) averaging schemes for *polycrystalline* materials.

Here, we shall explore the applicability of Chin's and Van Houtte's ideas to model the response of single crystals, and our RVE will be *a small part of a single crystal.* The constitutive equations and time-integration scheme presented in the previous chapter have been implemented in the finite-element program ABAQUS/Explicit [1995]. We shall show that the predictions for the texture and stress-strain response from the model are in reasonably good agreement with experiments in plane strain compression for a differently oriented crystal. In this chapter we report on finite element modeling to predict the operative twinning dominated deformations and crystallographic texture evolution during plane strain compression of f.c.c. *single crystals* which have been experimentally studied by Chin *et al.* [1969]. We show that our model, which is described in the previous chapter, is able to reasonably reproduce both the experimentally-measured pole figures, and approximate the measured stress levels during plane strain compression of two specially oriented crystals, one in which two twin systems are operative, and another in which only one twin system is operative.

Let $f$ denote the volume fraction of the twin system with the maximum value of $f^i$ at a given time $t$, and let $\xi = 0.3$ denote a representative maximum value of $f$ in a RVE. The lattice reorientation condition suggested by Van Houtte [1978], and adopted here, is that if $f > \xi$, then the orientation of the RVE be replaced by the twin related orientation[1]. That is, if $\{\mathbf{e}_i^c | i = 1, 2, 3\}$ denotes a local orthonormal basis associated with the crystal lattice in the old relaxed configuration, then once this

[1]Van Houtte actually suggested use of a probablistic criterion with $\xi \in [0, 1]$ denoting a random number. In single crystal simulations, all RVEs have initially the same lattice orientation, and a big fraction of elements reaches the critical condition at the same time. We use the trigger effect of the first "twinned" element by wetting the threshold $\xi$ to a fixed number.

criterion is met the crystal basis in the new relaxed configuration of the crystal be taken as $\mathbf{e}_i^{c\,*} = \mathbf{R}^{tw}\mathbf{e}_i^c$.

Further, if the lattice reorientation condition is met, then $f^i$ is reinitialized to zero, and subsequent twinning in the RVE is suppressed by setting the twin system deformation resistances to a large value. However, subsequent slip in this RVE is allowed, and the values of all slip system resistances are set equal to the value of the resistance for the slip system(s) parallel to the twin system with the maximum $f^i$ prior to the reorientation.

## 3.2 Plane-Strain Deformation of F.C.C. Co-8% Fe Single Crystals

The elastic constants for Co-8% Fe single crystals are taken to be the same as that for Co (Simmons and Wang, 1971):

$$C_{11} = 260\ \text{GPa},\ C_{12} = 150\ \text{GPa}, C_{44} = 78\ \text{GPa}.$$

Slip in f.c.c. crystals occurs on twelve $\{111\} < 110 >$ slip systems. Note that on a given slip system, slip can occur in either the positive or negative $< 110 >$ slip direction in a $\{111\}$ plane. Twinning in f.c.c. crystals occurs on twelve $\{111\} < 11\bar{2} >$ twin systems. Note that unlike the slip systems twinning, because the underlying atomic arrangement is polar in nature, can occur in only one $< 11\bar{2} >$ type direction on a $\{111\}$ plane, and the twin systems correspond to the easy direction of twinning[2].

Representation of the slip-twin hardening and hardening interactions is one of the major uncertainties, and much work needs to be done to improve our understanding of these hardening interactions and their mathematical representation. In this preliminary study, we shall concentrate more on lattice reorientation due to slip and twinning during plane strain compression of the crystals, and we will pay only marginal attention to the details of the stress-strain response. Accordingly, during the

[2]We do not consider the possibility of "de-twinning" in this dissertation.

"pseudo-slip" phase the slip and twin system deformation resistances will be taken as constant. Leffers and co-workers (e.g., 1991, 1993) have reported that during plane strain compression of brass, twins form thin lamellae which cluster to form bundles in grains, and that subsequent slip is restricted to planes which are parallel to these twin bundles. We have modeled this important kinematic restriction on the activity of the slip systems as follows. When the fraction $f = \max\{f^\alpha\}$, the maximum value of $f^\alpha$ taken over all twin systems, reaches a value $\lambda \approx 0.05$; slipping and twinning in systems whose slip/twin planes are not parallel to the plane of the twin system with maximum $f^\alpha$ are restricted by choosing appropriate values of slip and twin resistances. Let $\mathcal{T}_\lambda$ denote the single-element set denoting the twin system for which $f^\alpha$ reaches the value $\lambda$, with corresponding resistance $s_{tw,\lambda}$. Also, let $\mathcal{S}_\lambda$ denote the set of slip systems which are parallel to this twin system. Then $s_{tw,\lambda}$ is still taken to be equal to its initial value $s_{tw,\lambda} = s_{tw,0}$, however for the other twinning systems, setting

$$s^\alpha = 5 \cdot s_{tw,0}, \quad \text{for} \quad \alpha \notin \mathcal{T}_\lambda, \tag{3.1}$$

renders them inoperative. Similarly, for the slip systems we require

$$\begin{aligned} s^i(\tau) &= s_0^i \qquad \text{for} \quad i \in \mathcal{S}_\lambda, \\ s^i(\tau) &= 5 \cdot s_0^i \quad \text{for} \quad i \notin \mathcal{S}_\lambda. \end{aligned} \tag{3.2}$$

We shall simulate plane-strain compression of two specially oriented single crystals Co-8%Fe tested by Chin et al. [1969]. A schematic of plane-strain compression in a channel-die fixture is shown in Fig. 3-1.

In the metallurgical literature, the geometry of such experiments is typically described by a pair of Miller indices $(hkl)[uvw]$, where $(hkl)$ denotes the Miller indices of the crystallographic plane parallel to the compression plane with outward unit normal $\mathbf{e}_2$, as shown in Fig. 3-1, and $[uvw]$ denotes the Miller indices of the crystallographic direction parallel to the free direction, $\mathbf{e}_1$ in Fig. 3-1. The particular orientations of the crystals experimentally studied by Chin *et al.* (1969) that we have chosen to

simulate in this paper are (110)[$\bar{3}34$] and (335)[$\bar{5}\bar{5}6$]. These initial crystal orientations may alternatively be described in terms of the Euler angle notation $\{\theta, \phi, \omega\}$ of Kalidindi *et al.* (1992); these Euler angles are listed in Table 3.1.

Table 3.1: Single-crystal orientations specified by Euler angles

| Orientation | $\theta$ | $\phi$ | $\omega$ |
|---|---|---|---|
| (110)[$\bar{3}34$] | 43.31 | 45 | 270 |
| (335)[$\bar{5}\bar{5}6$] | 90 | 225 | 40.32 |

For the numerical simulation of plane strain compression, 900 two-dimensional ABAQUS-CPE4R elements (continuum, plane-strain, 4-noded, reduced integration) were assigned to the single crystal. Fig. 3-2 shows the initial mesh geometry. Each finite element represents a RVE. In order to simulate a single crystal deformation, the initial crystallographic lattice orientation of each RVE is taken the same.

It is important to note that our 2-D finite element simulations incorporate the full 3-D slip and twin system structure. With respect to Fig. 3-2, plane strain compression was modeled by constraining the top and bottom boundaries of the mesh to remain straight, with the bottom boundary subjected to zero displacement in the 2-direction, and top boundary subjected to a negative displacement in the 2-direction for a total compressive strain of 20%. For the vertical boundaries we imposed periodic boundary conditions, defined as follows. Let $\mathbf{u}_l$ and $\mathbf{u}_r$ respectively denote the displacements for a node on the left boundary and another on the right boundary which is at the same horizontal level in the initial mesh, and let $\mathbf{d} = \mathbf{u}_r - \mathbf{u}_l$ denote the relative displacement for this pair of corresponding nodes on the left and right boundaries. Then, partially periodic boundary conditions are specified by requiring that $\mathbf{u}_{right} - \mathbf{u}_{left} = \mathbf{d}$, where $\mathbf{u}_{left}$ and where $\mathbf{u}_{right}$ are the vectors of displacements of all the nodes for the left and right boundaries, respectively.

In the numerical simulations reported below, we have used the the following values for the slip and twin resistances:

$$s_0^i = 70\,\text{MPa}; \quad s_0^\alpha = 40\,\text{MPa}.$$

We first simulated plane strain compression experiments on a $(110)[\bar{3}34]$ oriented crystal. A micrograph of the deformed specimen taken from Chin et al. [1969] is shown in Fig. 3-3. This picture shows that a mixture of slip and twinning has occurred on the (111) and $(11\bar{1})$ planes. Our corresponding finite element simulation is shown in Fig.3-4. Our calculations also predict slip occurs on the $(111)[\bar{1}01]$ and $(11\bar{1})[0\bar{1}\bar{1}]$ systems, and twinning occurs on the $(111)[1\bar{2}1]$ and $(\bar{1}\bar{1}1)[\bar{1}21]$ systems. The elements twinned by the $(111)[1\bar{2}1]$ system are colored red, and those twinned by the $(\bar{1}11)[\bar{1}21]$ system are colored blue. The calculated twin bands intersect at an angle close to that observed in the experiments (Fig. 3-3).

Texture evolution is one of the most important characteristics of slip/twin systems activity. Fig.3-5(a) presents the $\{111\}$ pole figure[3] of the crystal in its initial orientation. The pole figure predicted by the finite element calculations is shown in Fig.3-5(b), together with the experimentally measured (Chin et al., 1969) pole figure in Fig. 3-5(c). The agreement between numerically predicted and experimentally measured texture is very good.

The stress-strain data of Chin *et al.* (1969) is shown in Fig.3-6. Note that they do not report data for strains less than $\approx 10\%$. It was this stress-strain data which was chosen to estimate the slip and twin resistances used in our numerical simulations. The computed stress-strain curve is also shown in Fig. 3-6. Overall, the computed stress levels are in the range of that observed in the experiments. The first part of the curve up to strains of less than $\approx 2.5\%$ corresponds to the general plastic deformation by combined slip and twinning with twinning treated as pseudo-slip. The sudden jump in the stress at a strain of approximately 2.5% corresponds to the attainment of the first threshold when slip in certain elements is constrained to be operative on slip systems which are parallel to the dominant twin systems. The subsequent drops in stress on the calculated stress-strain curve correlate with the reorientation of the crystallographic lattices of elements due to twinning. Note that if we were to increase substantially the number of elements used in the finite element simulation, then the computed curve would be smoother.

[3]All pole figures shown in this section are in stereographic projection.

Next, we simulated plane strain compression of a (335)[$\bar{5}\bar{5}$6] oriented crystal. A micrograph of the deformed specimen taken from Chin *et al.* [1969] is shown in Fig. 3-7. Chin *et al.* report that during the early stages of deformation, slip on (111)[$\bar{1}\bar{1}$0] and (1$\bar{1}$1)[$\bar{1}\bar{1}$0] systems predominated. With increasing deformation, twinning on (111)[11$\bar{2}$] became predominant.

Our calculations, (in Fig.3-8) show the same twin system, (111)[11$\bar{2}$], to be dominant at a strain of 20%. The twinned elements in the deformed finite element mesh are colored red. Because of the activation of only one twin system, the macroscopic shear deformations became significant and the mesh was visibly sheared. The twinned regions of the (335)[$\bar{5}\bar{5}$6] single crystals have a new twin-related orientation, which deforms easely than parent crystal. One can see from Fig 3-8 that the major deformation occurs inside twinned regions. The {111} pole figure for the initial orientation is shown in Fig.3-9(a).

The calculated and experimentally measured (Chin et al., 1969) textures after plane strain compression to 20 % are shown in Figs. 3-9(b) and 3-9(c), respectively. As for the previous calculation, the calculated texture captures the main features of the experimental texture. The calculated stress-strain curve together with the experimental data by Chin *et al.* (1969) is shown in Fig.3-10. The calculated stress levels are in the right range.

## 3.3 Concluding Remarks

Our calculations clearly demonstrate the ability of our constitutive model and computational procedure to capture the major features of plastic deformation of a single crystal due to slip and twinning. However, as formulated, the constitutive model has a number of limitations: (*i*) The model at this stage is essentially non-hardening. (*ii*) The important role of twin-boundary energy is neglected in the model. (*iii*) There is no length scale in the model. Much work needs to be done to improve our understanding of the slip and twin hardening and hardening interactions, and their mathematical representation.

The limitations in the finite element calculations are mostly related to our use of a small number of elements. Because of the coarse mesh, the twin bands propagate at an angle that is determined not only by the underlying slip and twin systems, but also by the finite element mesh itself. A more refined mesh should mitigate this problem. However, the problem of the width of the twin bands is not solved by refining the mesh. For this, a suitable length scale associated with non-local effects of twinning needs to be introduced into the constitutive model.

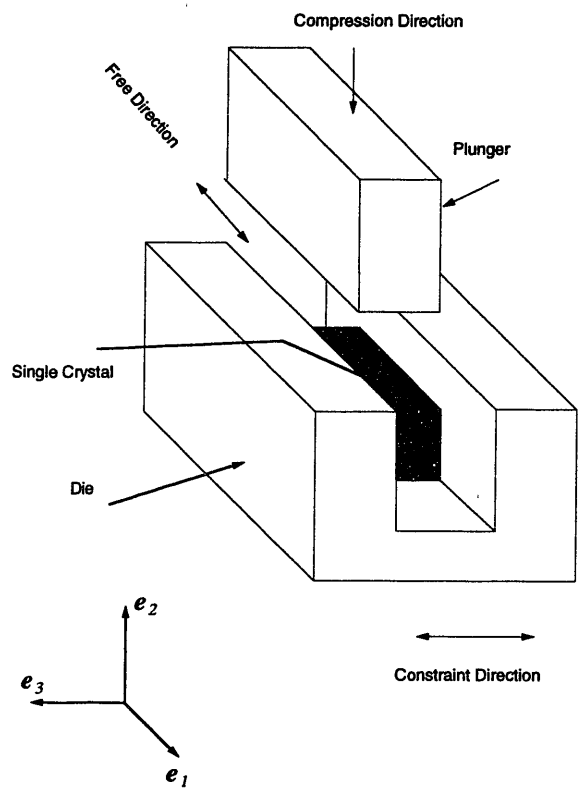


Case 1. [110] is parallel to $e_2$; $[\bar{3}34]$ is parallel to $e_1$

Case 2. [335] is parallel to $e_2$; $[\bar{5}\bar{5}6]$ is parallel to $e_1$

Figure 3-1: Schematic of plane-strain compression experiments.

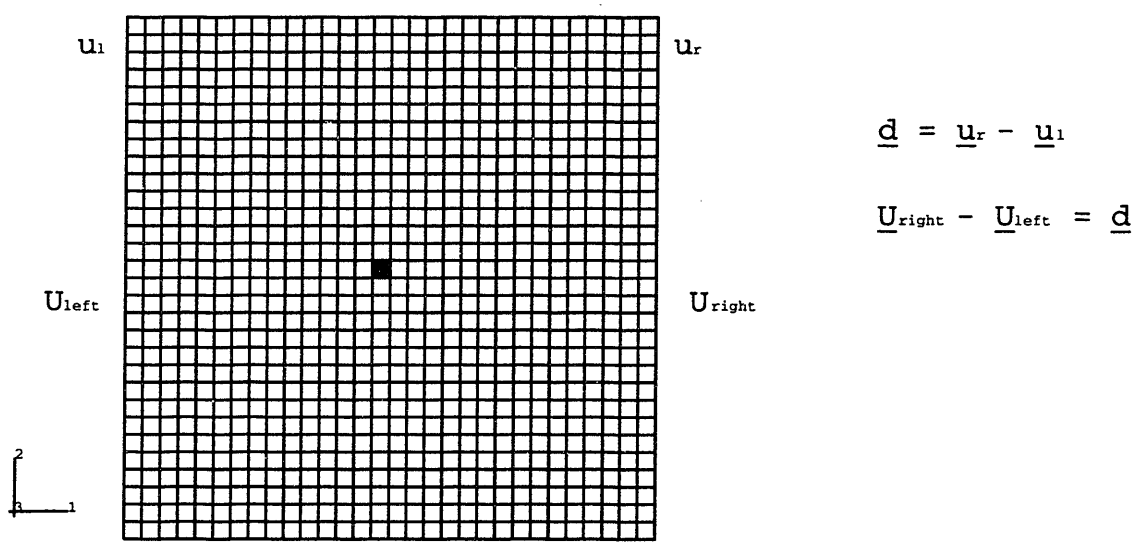


Figure 3-2: Initial finite element mesh. Each finite element represents a RVE.

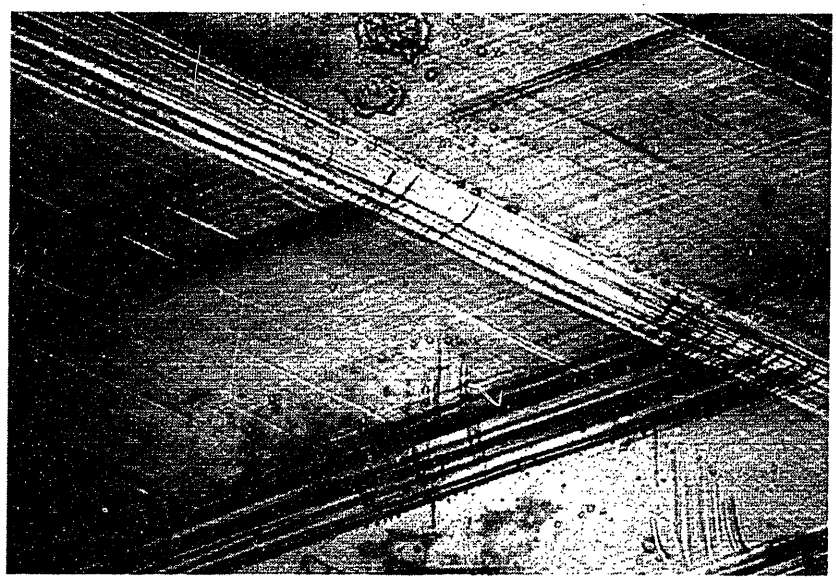

Figure 3-3: Micrograph of the (110)[$\bar{3}$34] oriented crystal showing twin bands (from Chin *et al.*, 1969).

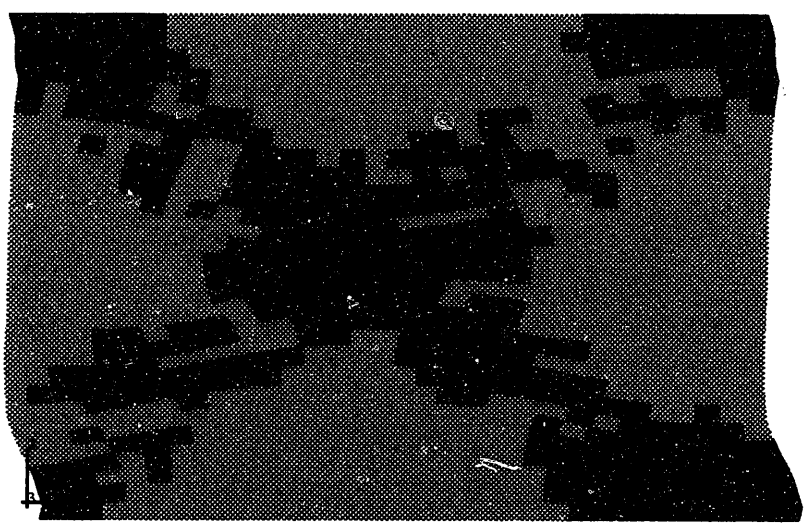

Figure 3-4: The deformed FEM mesh with calculated twin bands.

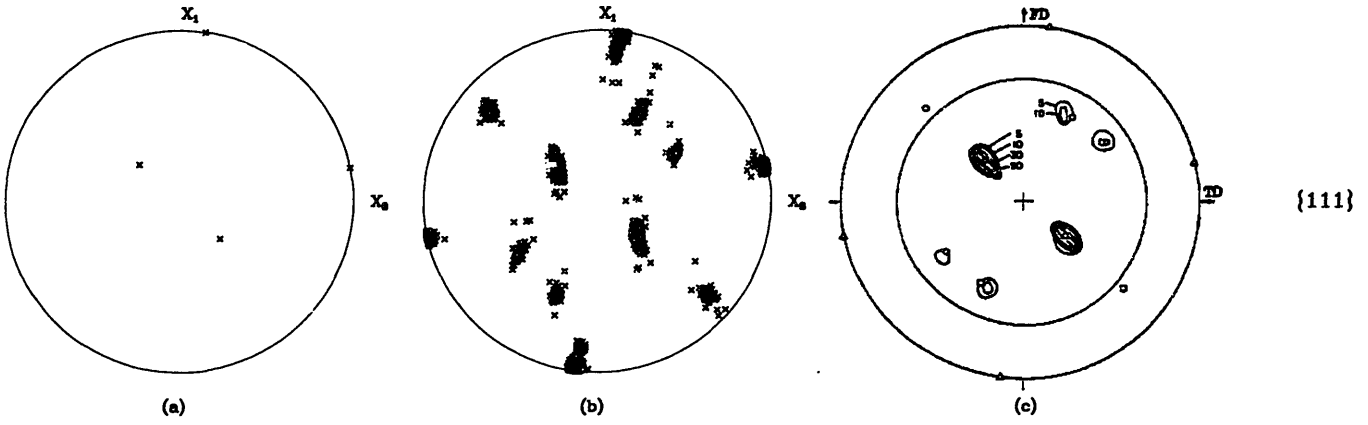


Figure 3-5: {111} pole figures for [$\bar{3}34$] oriented crystal. Initial (a), FEM calculated after plane strain compression to 20% (b), and experimentally measured (Chin et al., 1969) (c).

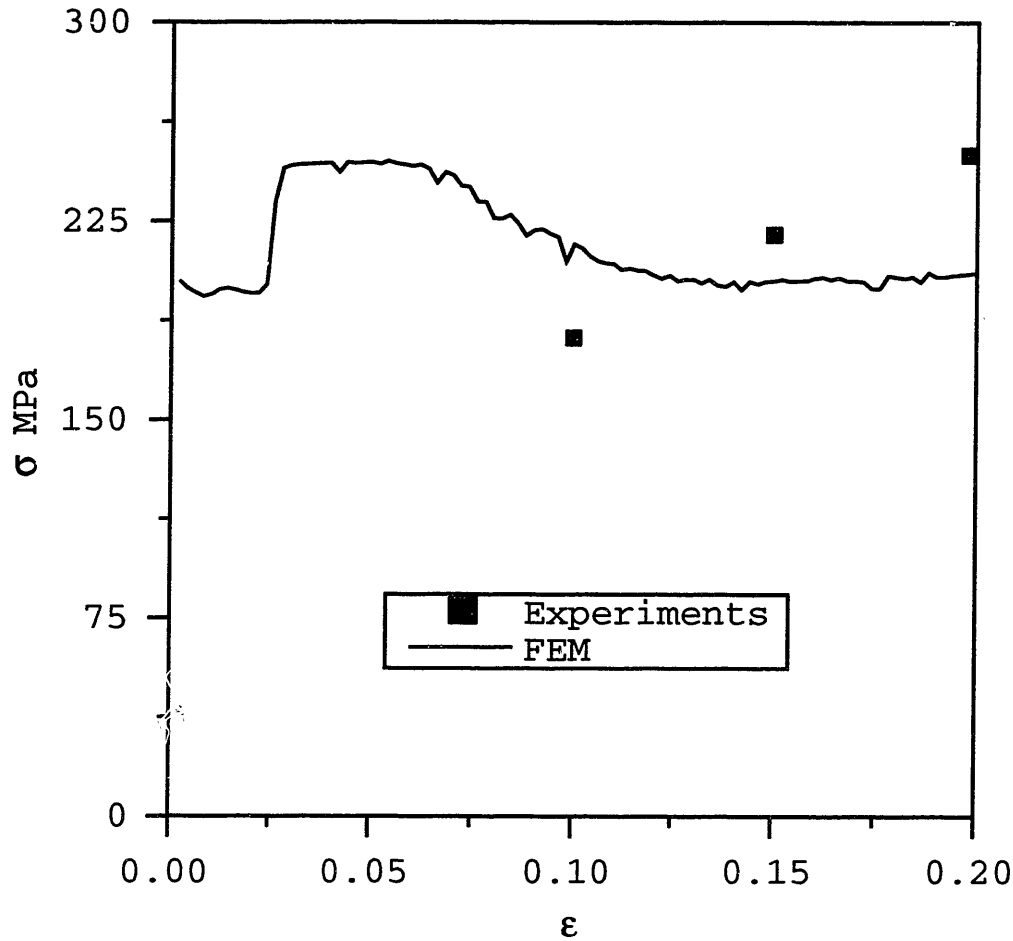


Figure 3-6: Stress-strain data for plane strain compression of (110)[$\bar{3}$34] oriented crystal.

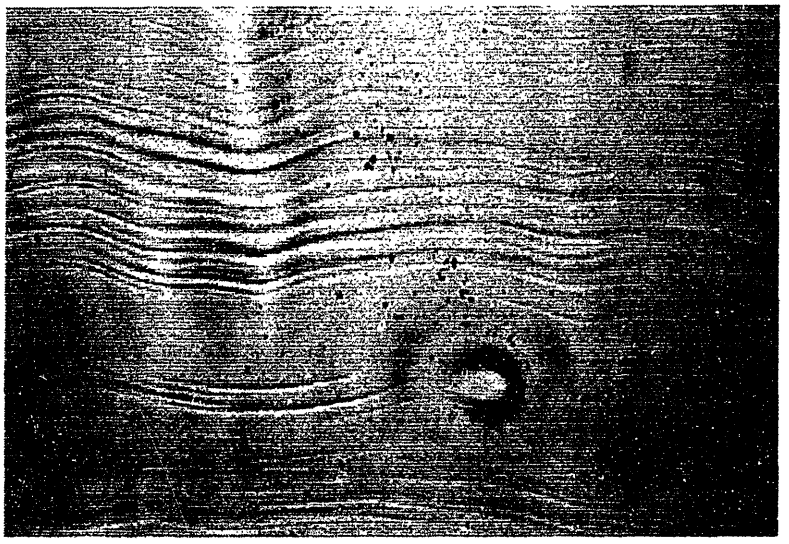

Figure 3-7: Micrograph of the (335)[$\bar{5}\bar{5}$6] oriented crystal showing twin bands (from Chin *et al.*, 1969).

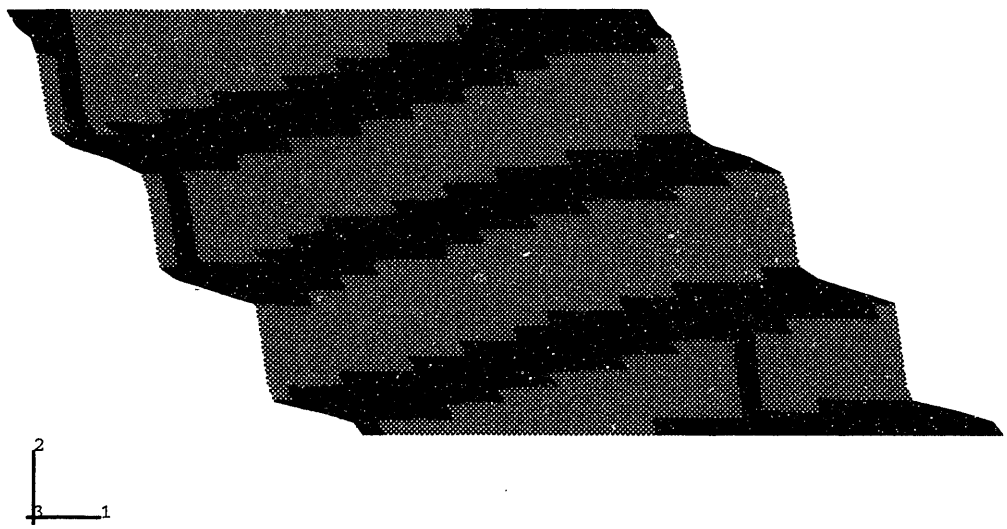


**Figure 3-8: The deformed FEM mesh with calculated twin bands.**

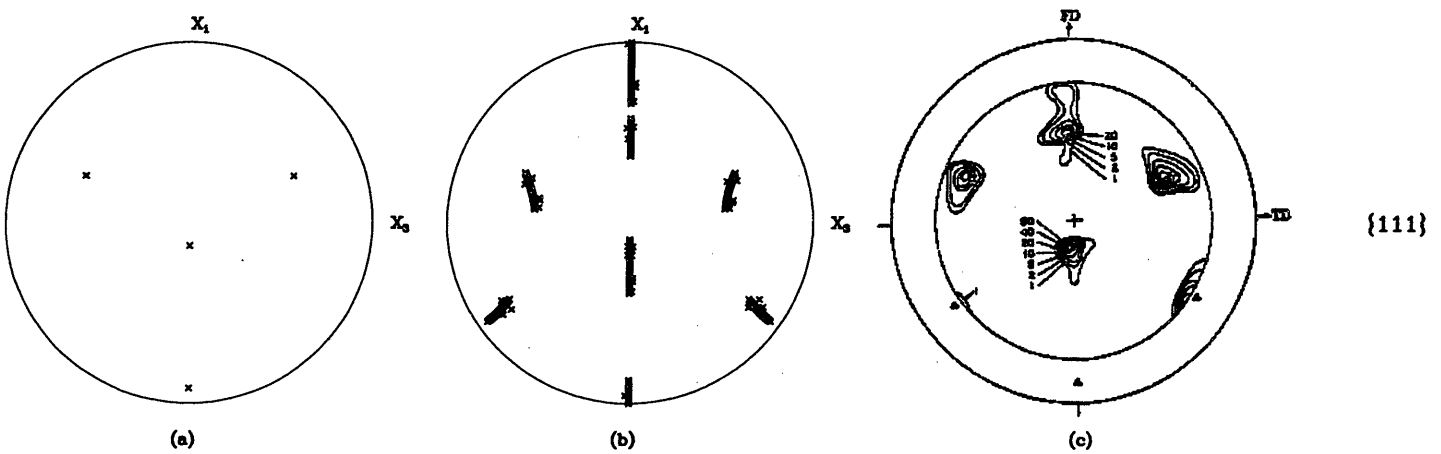


Figure 3-9: {111} pole figures for (335)[$\bar{5}\bar{5}$6] oriented crystal. Initial (a), FEM calculated after plane strain compression to 20% (b), and experimentally measured (Chin *et al.*, 1969) (c).

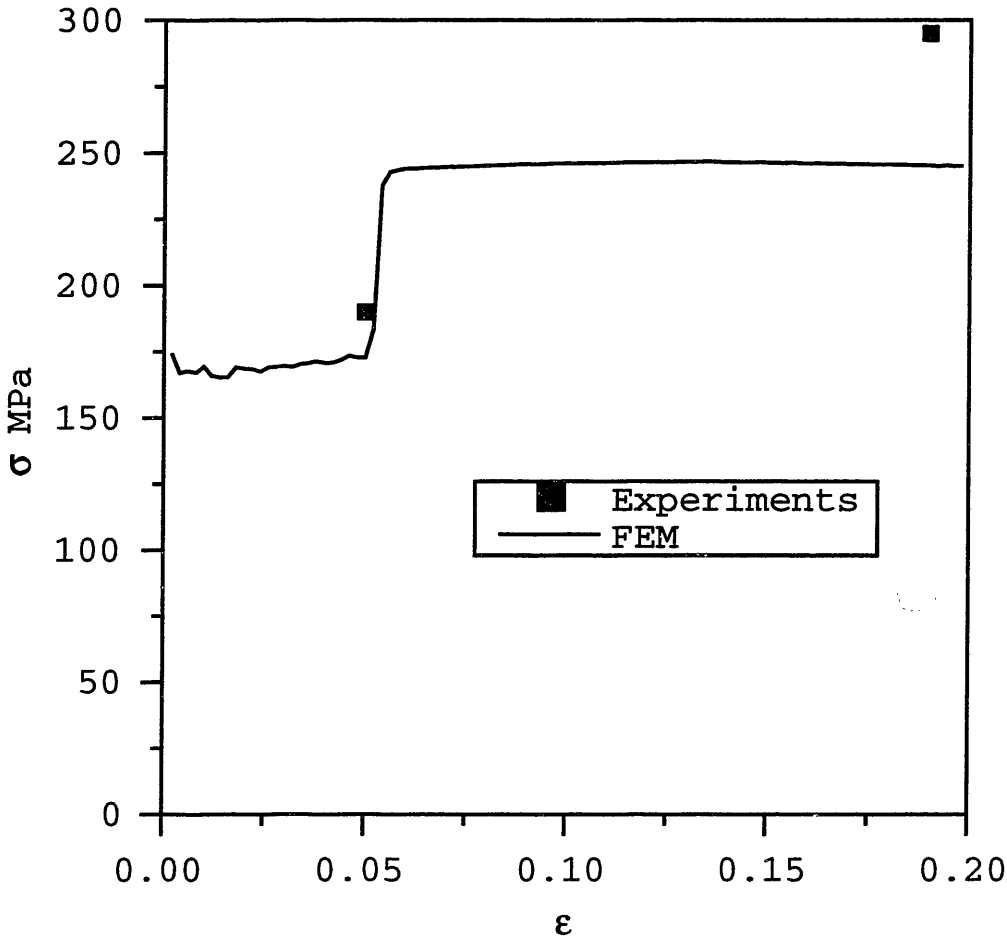


Figure 3-10: Stress-strain data for plane strain compression of (335)[$\bar{5}\bar{5}$6] oriented crystal.

# Chapter 4

# Evaluation of the Constitutive Model for FCC Polycrystalline Materials

## 4.1 Experimental Procedure and Results for $\alpha$-brass

The material we study in this chapter is polycrystalline alloy, consisting of Cu( 68.8 % ), Zn( 29.5 %), Pb( 1.3 %), and remained elements, mostly Fe. This CuZn alloy system is commonly known as $\alpha$-brass or brass 70-30. X-ray analysis indicated face centered cubic crystallographic structure with the lattice space $a = 3.6853\,\mathring{A}$. Structure of the as-received $\alpha$-brass is shown in a scanning electron micrograph in Fig. 4-1. The intrinsic stacking fault energy of such an alloy is $\gamma = 36\,mJ/m^2$ – almost half that of the value for the pure copper, $\gamma = 73\,mJ/m^2$ (Thornton and Mitchell [1962]). In pure copper twinning was observed only at low temperature. The commercial Cu 70%-Zn 30% alloy twins at room temperature and has only two mode of deformations: crystallographic slip and twinning.

As-received 70-30 brass was annealed at 600°C for one hour in an inert atmosphere. Plane strain experiments were conducted at room temperature and at a quasi-static

strain rate of 0.006 $s^{-1}$. The dimensions of the plane strain compression specimens were 12.7 mm in the compression direction, 10 mm in the constrained direction, and 11 mm in the free direction. For the simple compression experiments, cylindrical specimens with an initial ratio between height and diameter of 1.5 were used. The specimens were lubricated with $MoS_2$ lubricant and teflon film to reduce friction. Mechanical tests were conducted to large deformations up to $\epsilon = -1$.

Servo-hydraulic Instron machines were used for mechanical testing. Data acquisition and active test control was performed with LabTech Notebook software. This software allows one to conduct experiments with controlled strain rate.

For microstructural analysis the samples were electrolytically polished and chemically etched. Initial surface preparation for final electro-polishing starts from mechanical polishing, using diamond-impregnated clothes. The preferred abrasive should be diamond paste from 9 $\mu$m to 15 $\mu$m. A wheel speed of 300 rpm was generally used. Brass is very soft metal and, the abrasive leaves micro scratchs that are hard to distinguish from twins during microscopic analysis. Electrolytic polishing of brass alleviates many of the problems specific to mechanical polishing. For this purpose a solution of 2 parts of $H_3PO_4$ and 3 parts of $H_2O$ was used. The polishing regime has two voltage bounds: if the voltage is less than the lower bound etching takes place, and if the voltage is higher than the upper bound pitting is observed. For successful polishing we should determine the low voltage bound, increase working voltage on 2 - 3 V and to check if polishing process running. If the sample is being polished, we should hold the level of current. Current is a more important parameter than voltage during the electric polishing procedure. In our experiments we used "Struers Polectrol" in the following regime: the voltage $U = 18\,V$ and flow rate $f = 3$ within 20 seconds. For brass 70-30 microanalysis the most clear results were obtained with the usage of an etchant consisting of 5 parts $HNO_3$, 5 parts of acetic acid, and 1 part $H_3PO_4$ by immersing for 3-5 sec. Micrographes, typical for $\alpha$-brass after plane strain compression are shown in Fig. 4-2.

Experimental measurements of texture of the samples after deformation were carried out by X-ray irradiation, using a Rigaku RU200 diffractometer. Pole figures were

obtained by using the Shultz reflection method with copper-$K_\alpha$ radiation. For most of our pole figure measurements we used the following dimensions of the divergence slit as $1^0$, scatter slit as $5\,mm$. To process the experimental data, the Preferred Orientation Package (Kallend et al., [1991]) was employed. Each measured pole figure was corrected for background and defocusing, and also extrapolated for the outer 15°. The {111}, {100}, and {110} pole figures for plane strain compression after 100% compression are shown in Fig. 2-1; all pole figures are equal-area projections of the specified crystallographic planes.

For model verification and for the fitting model parameters we compared model results against experimental ones. We show this comparison in the section describing our numerical experiments.

## 4.2 Finite Element Simulations

Our literature search showed that all previous calculations of polycrystalline plasticity due to slip and twinning have been limited to the Taylor (Van Houtte, [1978]), Sachs (Leffers, [1993]), or self-consistent (Lebensohn and Tome, [1994]) averaging schemes. These averaging schemes add another level of assumptions which may mask some of the consequences of the underlying features in our constitutive model for the response of a single crystal. To circumvent this difficulty we have performed full three-dimensional finite-element calculations, in which each element represents a single crystal. In the finite-element model of a polycrystal, both compatibility and equilibrium conditions are satisfied; and there is no need for the Taylor, Sachs or any other hypotheses, which have been classically used to obtain the response of polycrystalline aggregates.

We use a set of 343 initially "randomly"-oriented crystals to simulate an initially isotropic polycrystal. Fig. 4-3a shows the initial finite-element mesh using 343 elements to model such a polycrystal. The planes corresponding to $x_1 = 0$, $x_2 = 0$, and $x_3 = 0$ are confined such that all the nodes on these faces have zero $u_1$, $u_2$, and $u_3$ displacements, respectively.

The planes corresponding to $x_1 = 0$, $x_2 = 0$, and $x_3 = 0$ are confined such that all the nodes on these faces have zero $u_1$, $u_2$, and $u_3$ displacements, respectively. For plane-strain compression simulations the displacement for the outer face of the specimen in the $x_1$ direction is set to $u_1 = 0$; the outer face in the $x_2$ direction has zero tractions, while a negative $u_3$ displacement is applied on the outside $x_3$-face of the specimen.

For simulations of simple compression tests the constraint condition $u_1 = 0$ for the outer face of the specimen in the $x_1$ direction was substituted by zero traction condition.

### 4.2.1 Combined Slip and Twinning – Non-hardening Model

The material was modeled as an elastic-plastic, non-hardening material with elastic moduli (Simmons and Wang, [1971]): $C_{11} = 134$ GPa, $C_{12} = 105$ GPa, $C_{44} = 70$ GPa, a constant value of slip system resistance $s_{sl} = 25$ MPa, and three different constant values of the twin system resistance $s_{tw}$, such that the ratio $R = s_{tw}/s_{sl}$ had three different values of $R = 4,\ 1.1,$ and 0.8. The deformed configuration after a nominal plane strain compression of 100% for a representative value of $R$ is shown in Fig. 4-3b.

The stress-strain curves corresponding to the three different values of $R$ are shown in Fig. 4-4. The stress-drops in Fig. 4-4 correspond to the beginning of the twin-induced lattice reorientation process. Numerically, one can control where the stress-drop occurs by changing the lower bound of the random number $\xi \in [\phi, 1]$ used in our algorithm to determine the onset of lattice reorientation due to twinning. For the representative calculations shown here, we chose $\phi = 0.1$.

The calculated pole figures after 100% plane strain compression for the three different values of the parameter $R$ are shown in Fig. 4-5. The copper-type texture obtained in this work for $R = 4$ is similar to the pole figures obtained for non-hardening materials earlier by Bronkhorst et al., [1992]. Incorporation of twinning changes the texture from copper-type to brass-type. The pole figures for $R = 1.1$ show a greater similarity to the experimentally observed textures of 70-30 brass after

100% plane strain compression, Fig. 2-1, than to the textures calculated for $R = 0.8$. This is a reflection of the fact that for brass, slip is a more dominant mode of inelastic deformation than twinning. Plastic deformation in brass begins by crystallographic slip, and only after some finite deformation, when the slip systems have hardened sufficiently that the critical deformation resistance for slip exceeds that for twinning, does twinning occur. A non-hardening model is not able to capture this physical phenomenon in sufficient detail. To analyze the effects of hardening on texture evolution and stress-strain response we have developed a simple hardening model described in the next section. However, we note that even an oversimplified non-hardening model is able to catch the main features of the transition from a copper-type texture to a brass-type texture, which is a direct manifestation of plasticity by combined slip and twinning, rather than by slip alone.

### 4.2.2 Combined Slip and Twinning – Hardening Model

In this section we revert to our original notation $s^i$ and $s^\alpha$, for the slip and twin resistance, respectively. Representation of the slip-twin hardening and hardening interactions is one of the major uncertainties, and much work needs to be done to improve our understanding of these hardening interactions and their mathematical representation. A simple phenomenological model for the evolution of $s^i$ and $s^\alpha$ is formulated below.

During the "pseudo-slip" phase the twin system deformation resistances may be taken as constant, and the slip system deformation resistances are taken to evolve in the form (e.g. Kalidindi et al., [1992]):

$$s^i(\tau) = s^i(t) + \sum_j h^{ij}(t)\Delta\gamma^j, \quad \text{where} \quad h^{ij} = q^{ij}h^j. \tag{4.1}$$

Here $h^{ij}$ are components of the hardening matrix,

$$q^{ij} = \left[q + (1-q)\delta^{ij}\right] \tag{4.2}$$

is the matrix describing the latent hardening, with $q = 1.0$ for co-planar systems and $q = 1.4$ for non-coplanar systems[1], and

$$h^j = h_0(1 - \frac{s^j}{\tilde{s}})^a \tag{4.3}$$

is the single slip hardening rate, with $\{h_0,\ \tilde{s}, a\}$ slip system hardening parameters, which are taken to be identical for all slip systems.

As mentioned previously, Leffers and co-workers (e.g.,[1990], [1991]) have reported that during plane strain compression of brass, twins form thin lamellae which cluster to form bundles in grains, and that subsequent slip is restricted to planes which are parallel to these twin bundles. We have modeled this kinematic restriction on the activity of the slip systems as follows. When the fraction $f = \max\{f^\alpha\}$, the maximum value of $f^\alpha$ taken over all twin systems, reaches a value $\lambda$ (between 3% to 5%), slipping and twinning in systems whose slip/twin planes are not parallel to the plane of the twin system with maximum $f^\alpha$ are restricted by choosing appropriate values of slip and twin resistances. Let $\mathcal{T}_\lambda$ be the single element set denoting the twin system for which $f^\alpha$ reaches the value $\lambda$, with corresponding resistance $s_{tw,\lambda}$. Also, let $\mathcal{S}_\lambda$ denote the set of slip systems which are parallel to this twin system. Then the evolution of $s_{tw,\lambda}$ may be taken in the saturation form

$$s_{tw,\lambda}(\tau) = s_{tw,\lambda}(t) \ + \ h_{tw}\Delta\gamma_{tw}, \quad \text{with} \quad h_{tw} = h_0^{tw}\left(1 - \frac{s_{tw,\lambda}(t)}{\tilde{s}_{tw}}\right)^{a_{tw}}, \tag{4.4}$$

where $\Delta\gamma_{tw}$ is the shear increment due to twinning in the major twin system, and $h_0^{tw}, \tilde{s}_{tw}$, and $a_{tw}$ are constants for particular material. Also, for the other twinning systems, setting

$$s^\alpha(\tau) = 5 \cdot s_{tw,0}, \quad \text{for} \quad \alpha \notin \mathcal{T}_\lambda, \tag{4.5}$$

renders them inoperative. Here $s_{tw,0}$ is the initial twinning resistance. For the slip

[1]We recognize that this is a greatly simplified description of latent hardening. However, our numerical experiments show that the macroscopic stress-strain curves and crystallographic texture evolution are not significantly altered when we change the values of $q$.

systems co-planar with the major twin system, requiring

$$s^i(\tau) = s^i(t) + \sum_j h^{ij}(t)\Delta\gamma^j \leq s_{tw,\lambda}(\tau), \quad \text{for} \quad i \in \mathcal{S}_\lambda,$$

keeps them operative. Also, since twin lamellae are serious obstacles to dislocation glide they cause additional hardening of the slip systems not in $\mathcal{S}_\lambda$. A simple phenomenological form for this hardening interaction is as follows:

$$s^i(\tau) = s^i(t) + \sum_j h^{ij}(t)\Delta\gamma^j + h^i_{tw-sl}\Delta\gamma^{tw}, \quad \text{for} \quad i \notin \mathcal{S}_\lambda, \tag{4.6}$$

where $\Delta\gamma_{tw}$ is the shear increment due to twinning in the major twin system, and the last term represents twin-slip hardening. A simple saturation-type form for the twin - slip hardening rate is

$$h^i_{tw-sl} = h_0^{tw-sl}\left(1 - \frac{s^i(t)}{\tilde{s}_{tw-sl}}\right)^{a_{tw-sl}}, \tag{4.7}$$

where $h_0^{tw-sl}$, $\tilde{s}_{tw-sl}$, and $a_{tw-sl}$ are additional material constants.

Thus, to account for slip-twin interactions and the reorientation due to twinning we chose two thresholds related to the "twin fraction" calculated by treating twinning as a "pseudo-slip." Slip is restricted to planes parallel to the dominant twin system when the first threshold is reached, and the crystal lattice in the relaxed configuration is rotated to the twinning-related orientation when the second threshold is reached. The flowchart for calculations to model these twinning effects is given in Fig. 4-6. To summarize, the hardening parameters in the model are $s_0^i, s_0^\alpha$, the initial values of the slip and twin resistances. The hardening parameters $\{h_0, \tilde{s}, a\}$ are associated with slip hardening during the pseudo-slip phase. The hardening parameters $\{h_0^{tw}, \tilde{s}_{tw}, a_{tw}\}$ are associated with the self-hardening of the major twin system. And the parameters $\left\{h_0^{tw-sl}, \tilde{s}_{tw-sl}, a_{tw-sl}\right\}$ are associated with the enhanced hardening due to the interaction of the dominant twin system with the slip systems not parallel to it. These parameters are obtained by judiciously adjusting their values so that the model reproduces the plane strain compression stress-strain curve obtained from experiments

on 70-30 brass. The stress-strain curve obtained from these experiments is shown in Fig.4-7. Finite-element calculations for plane strain compression of an aggregate of 343 initially randomly-oriented grains (with the same boundary conditions as in the non-hardening calculations) were carried out with various values of the material parameters. The process of curve-fitting the plane strain compression stress-strain data to obtain the value of the hardening parameters yielded

$$s_0^i = 25 \text{ MPa}, \; s_0^\alpha = 155 \text{ MPa},$$

$$h_0 = 135 \text{ MPa}, \; \tilde{s} = 400 \text{ MPa}, \; a = 2,$$

$$h_0^{tw} = 452 \text{ MPa}, \; \tilde{s}_{tw} = 245 \text{ MPa}, \; a_{tw} = 0.25, \text{ and}$$

$$h_0^{tw-sl} = 1.06 \text{ GPa}, \; \tilde{s}_{tw-sl} = 245 \text{ MPa}, \; a_{tw-sl} = 0.25.$$

The quality of the curve-fit is shown in Fig. 4-7. One can see that the calculated stress-strain response is very close to the experimentally observed one. The jumps on the numerically calculated curve at strains greater than $\approx 0.5$ are due to the crystal lattice rotations of the grains during twinning[2].

The $\{111\}$, $\{100\}$, and $\{110\}$ pole figures for plane strain compression after 100% compression are shown in Fig. 4-8; all pole figures are equal-area projections of the specified crystallographic planes. This figure also shows the numerically-predicted pole figures. The agreement between the numerical prediction and experimental measurements, especially for the $\{111\}$ and $\{100\}$ pole figures, is very good.

The numerical calculations show that because of the difference in values of $s_0^i = 25$ MPa and $s_0^\alpha = 155$ MPa, in the initial stages of deformation the grains deform by crystallographic slip only. The slip deformation resistances increase due to strain-hardening, and at a level of macroscopic strain of approximately 10%-15%, the first threshold, $\lambda = 0.04$, for the twin fraction $f = \max\{f^\alpha\}$ used to restrict slip, is

[2]Comparison of the predicted stress-strain curves using 100 elements rather than 343 elements shows that the curves are smoother when a larger number of elements are used in the polycrystal model simulation.

reached in some grains. At this stage the resistances for twinning on all systems other than the twin system with maximum value of $f^\alpha$ were set to values five times their initial values, and our choice of hardening parameters ensures that the slip resistances increase very fast for all systems other than those which are co-planar with the dominant twin system; dominant crystallographic shearing occurs along the chosen crystallographic plane in a given crystal. When the second threshold for the twin fraction $f = \max\left\{f^\beta\right\}$ is reached, $f > \xi, \quad \xi \in [0.2, 1]$, with $\xi$ a random number, the crystal lattice is replaced with a twin-related one, and all slip system deformation resistances and all twin system resistances are set to the values corresponding to those for the active twin system. With our choice of material parameters, the crystal lattice rotation due to twinning starts at about 45% macroscopic strain. Before this level of deformation, the calculated pole figures are very close to those typical for f.c.c. materials deforming by slip alone. In our model twinning affects the predicted texture of the material in two ways: (*i*) restriction of slip to slip planes parallel to the dominant twin system in a grain; and (*ii*) reorientation of the lattice of grains to the twin-related orientations. Our numerical experiments show that the first mechanism alone is insufficient to produce the distinguishing "brass-type" texture.

Numerical results show that the "brass-texture" is a result of both constrained slip, *and* the lattice reorientation due to twinning.

The set of material parameters fit to the plane strain compression data has also been used to predict the response in simple compression. The initial and deformed finite element mesh is shown in Fig. 4-9. The graphs in Fig. 4-10 show that numerically-predicted stress-strain response is close to the experimentally measured one. Fig. 4-11 shows the measured and predicted pole figures at strain of 100%. The agreement is very good.

### 4.2.3 Texture Evolution in Non-hardening and Hardening Models for Slips Only

In this section we turn out our attention to the influence of slip hardening on texture evolution. As already noted by Bronkhorst et al. [1992], Kalidindi [1992], and as we ourselves observed, the FEM calculations give a softer response when compared to the response from the Taylor-type model for the same values of the slip hardening parameters. The finite element calculations are a necessary step in evaluating of the model (in particular, Taylor-type model) accuracy. However, even for this kind of simulation the influence of hardening parameters on crystallographic texture is not fully understood.

Our finite element calculations for plane strain compression in the non-hardening case indicated that the resulting texture is much sharper than one obtained from strain-hardening calculations and very close to the Taylor-type model texture. We analyzed the influence of the boundary conditions and number of mesh elements on texture evolution. We obtained very similar results when we performed the calculations with 343 3D elements that represent 343 grain orientations (cube 7 X 7 X 7), 675 3D elements that represent 675 grain orientations (parallelepiped 15 X 15 X 3), and 400 2D elements that represent 400 initial grain orientations (square 20 X 20). The comparison between non-hardening finite element calculations and strain hardening finite element calculations for copper to plane strain compression $\epsilon = -1$ is given in Fig. 4-14. The similarity between non-hardening finite element texture prediction and Taylor-type model calculation, can be explained, from our point of view, by the local homogeneity of strain field presented in the both models.

## 4.3 Taylor-Model Simulations

A very large body of literature exists on application of the Taylor model for texture prediction. The main assumption of this model for a polycrystal is that the deformation gradient in each grain is homogeneous and equal to the macroscopic one at

a material point. The compatibility condition is automatically satisfied in this approximation; however, equilibrium holds only inside a grain, but is violated between grains. If, in addition, we assume that all grains have equal volume, then the average Cauchy stress at each macroscopic continuum point is simply the number-averaged stress (Taylor, [1938]; Asaro and Needleman, [1985]):

$$\mathbf{T} = \frac{1}{N} \sum_{k=1}^{k=N} \mathbf{T}^k \tag{4.8}$$

where $\mathbf{T}^k$ is the Cauchy stress in the $k$-th crystal, and $N$ is the total number of crystals comprising the material point.

By comparing the Taylor model predicted stress-strain responses and crystallographic textures against results from FEM simulations, Bronkhorst et al., [1992] showed that a Taylor-type model of a polycrystal provides an acceptable description of the behavior of single-phase f.c.c. polycrystals deforming by slip alone. We have employed the same method to check on the applicability of a Taylor model for combined slip and twinning. With the material parameters calibrated for a full finite-element model of a polycrystal, our Taylor model simulations slightly overpredict the stress-strain responses in both plane strain compression and simple compression, Fig. 4-7 and Fig.4-10, respectively. Fig.4-12 and Fig. 4-13 show the predictions for the crystallographic texture, using both the finite-element model and the Taylor model for plane strain compression and simple compression, respectively. The texture predictions from the two modeling schemes are very similar. Thus, as for f.c.c. materials which deform by slip alone, the Taylor model may also be used for obtaining computationally inexpensive and reasonably accurate predictions of both the stress-strain curve and the crystallographic texture of f.c.c. materials deforming by combined slip and twinning.

## 4.4 Concluding Remarks

To summarize, a rate-independent, elastic-plastic, constitutive model for plastic deformation of f.c.c. polycrystalline materials deforming by both slip and twinning has been developed. The model was implemented in the finite-element program ABAQUS/Explicit [1995].

Full finite-element models of a polycrystal (in which both compatibility and equilibrium are satisfied) were used to carry out plane strain compression simulations. By using comparisons between model predictions and macroscopically-measured stress-strain curves on 70-30 brass, we deduced information about the values of the single-crystal parameters associated with slip and twin system deformation resistances and hardening due to slip and twinning. The predicted crystallographic texture from the finite-element calculations is in good accord with experiments. The model also successfully predicts the stress-strain response and crystallographic texture evolution in simple compression experiments.

We have also evaluated the applicability of a simple Taylor-type model for combined slip and twinning. Our experiments and calculations show that, for the high-symmetry f.c.c. brass, a Taylor model for a polycrystal deforming by combined slip and twinning is able to predict reasonably well the macroscopic stress-strain curves and crystallographic texture evolution in both plane strain and simple compression.

We wish to emphasize that there are several limitations in the present model which make it unsuitable for modeling the fine-scale features of deformation of *single crystals* by slip and twinning. The two major limitations are: (*i*) During the pseudo-slip phase, the amount of shear on twin systems never actually reaches the large value of $\gamma_0 = 1/\sqrt{2}$ on any twin system. (*ii*) The assumption that the lattice of the crystal is unchanged until a large volume fraction of the crystal is "twinned," and then, based on a probabilistic criterion, the lattice is given the orientation corresponding to the twin system with the largest accumulated pseudo-slip. This modeling assumption does not comprehend the experimentally-observed layered -composite microstructure of matrix and twin lamellae in single crystals. Nevertheless, as shown in this chapter,

for a *polycrystalline material*, the major features of the averaged macroscopic texture evolution and stress-strain curves, are adequately represented by the model for engineering simulations.

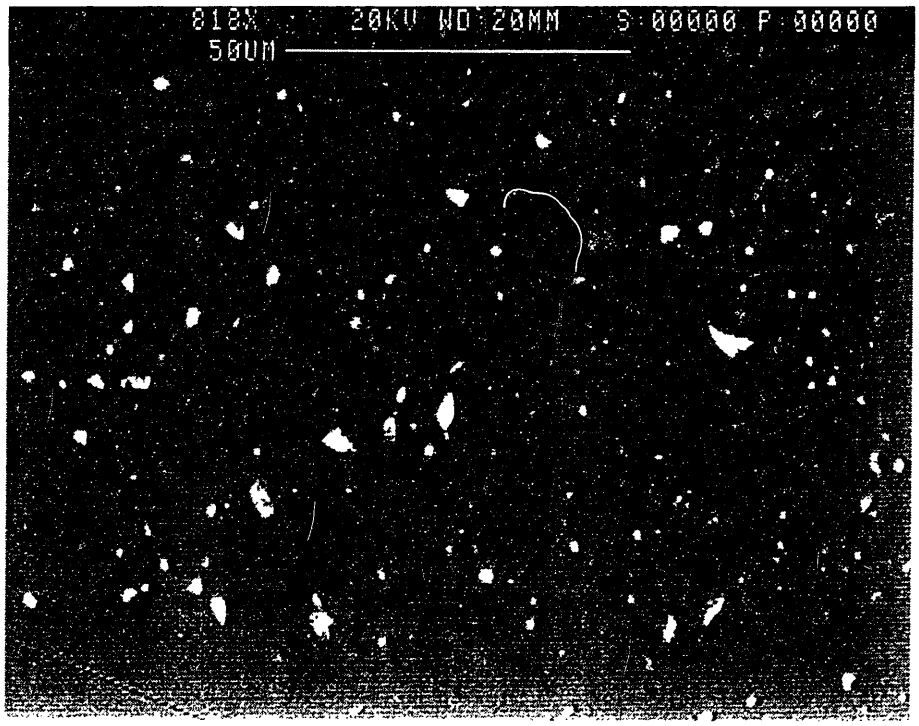


Figure 4-1: The SEM micrograph of as-received $\alpha$-brass.

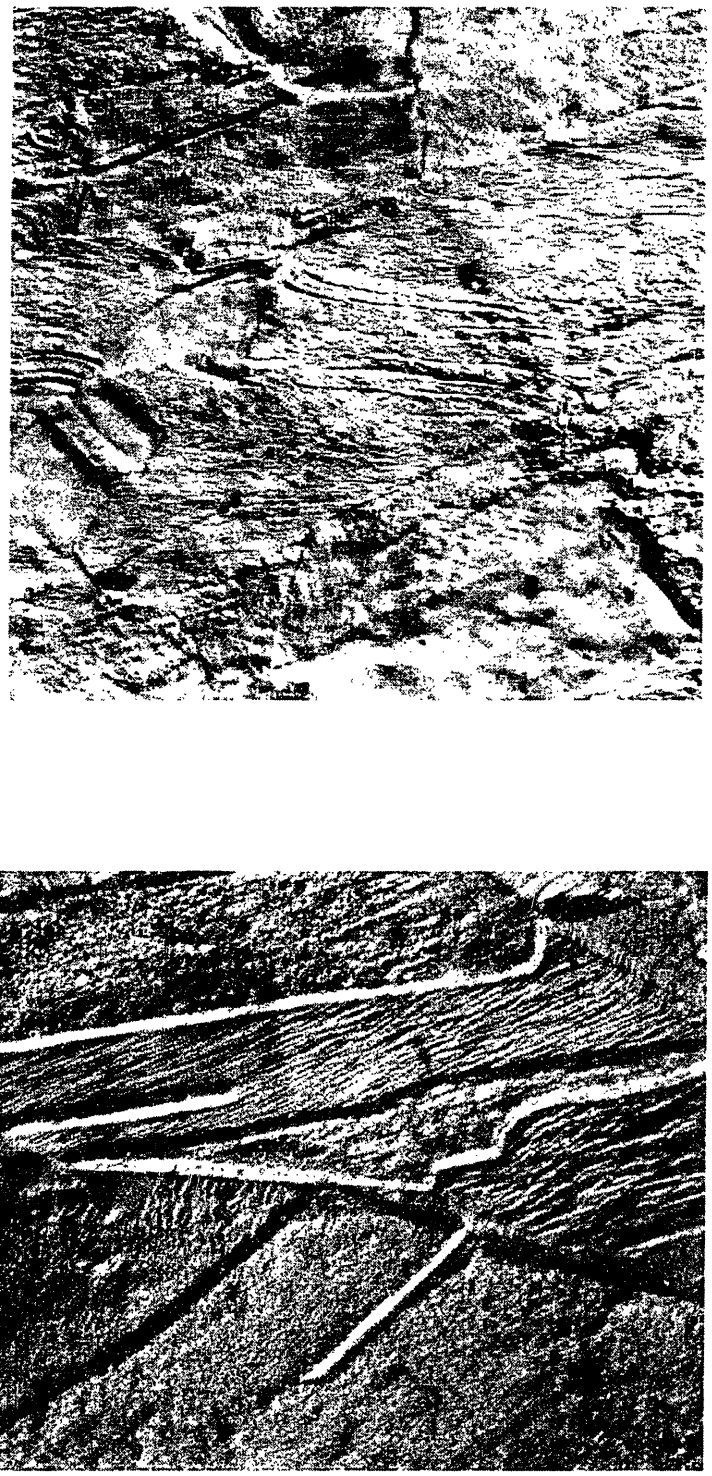

Figure 4-2: The optical micrographs of $\alpha$-brass after plane-strain compression to $\epsilon = -0.5$; magnifications (a) 400X and (b) 1000X

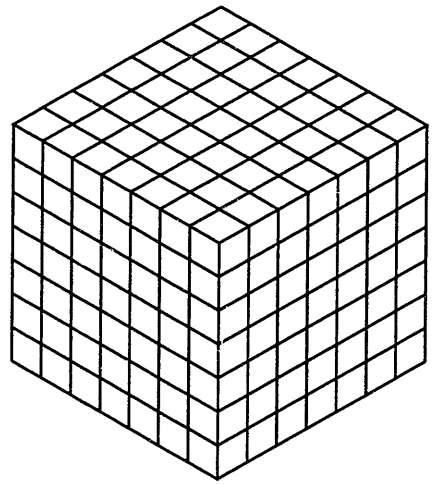

(a) Initial mesh

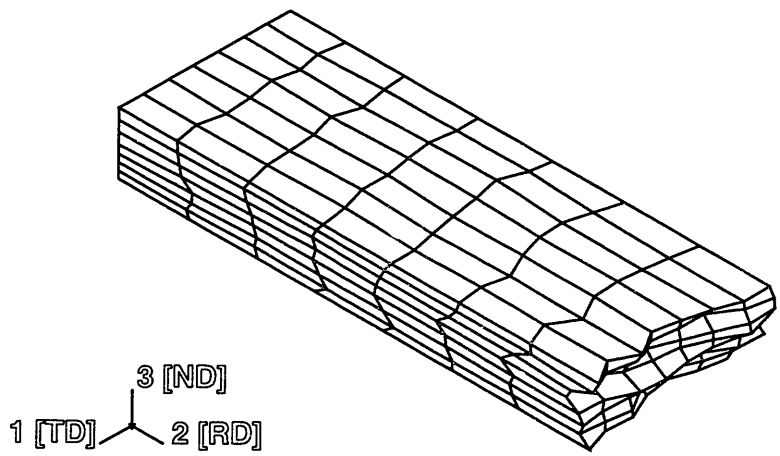


(b) Deformed mesh

Figure 4-3: Representative (a) initial, and (b) deformed 3-D finite-element meshes for plane strain compression.

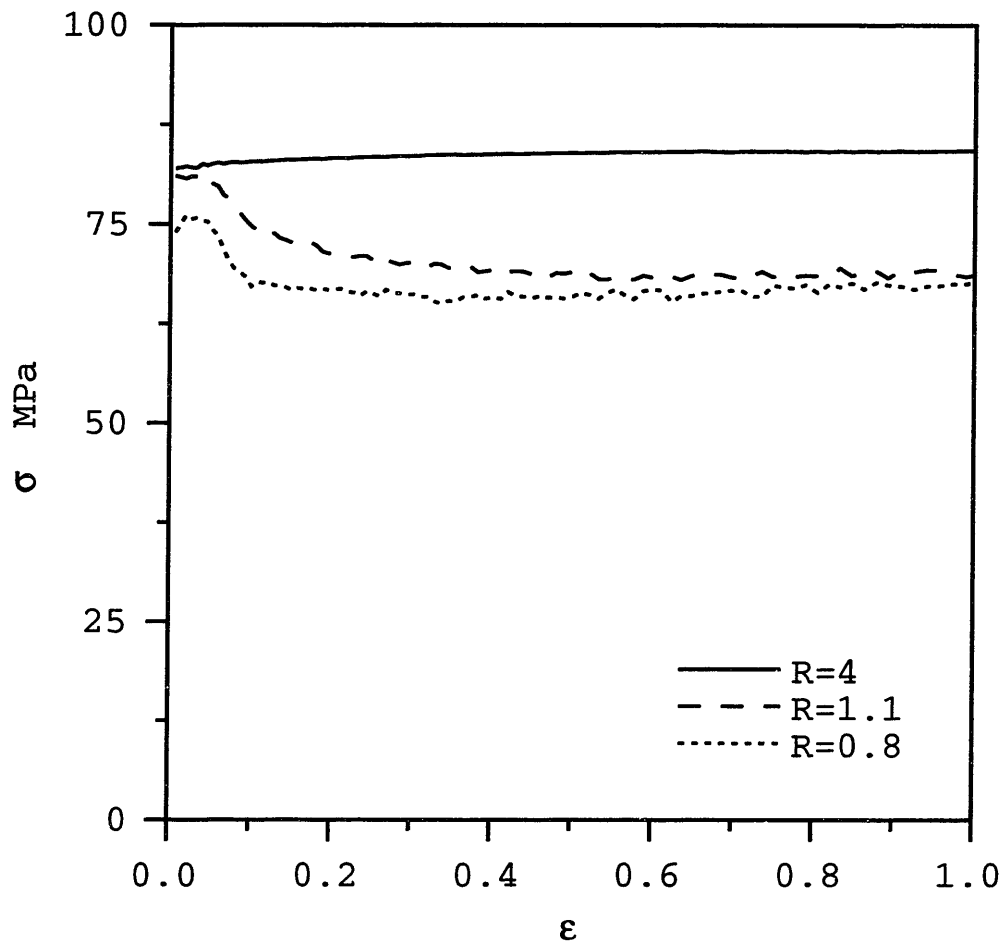


Figure 4-4: Stress-strain curves for non-hardening simulations of plane strain compression for three different values of the ratio $R = s_{tw}/s_{sl} = 4,\ 1.1,$ and 0.8.

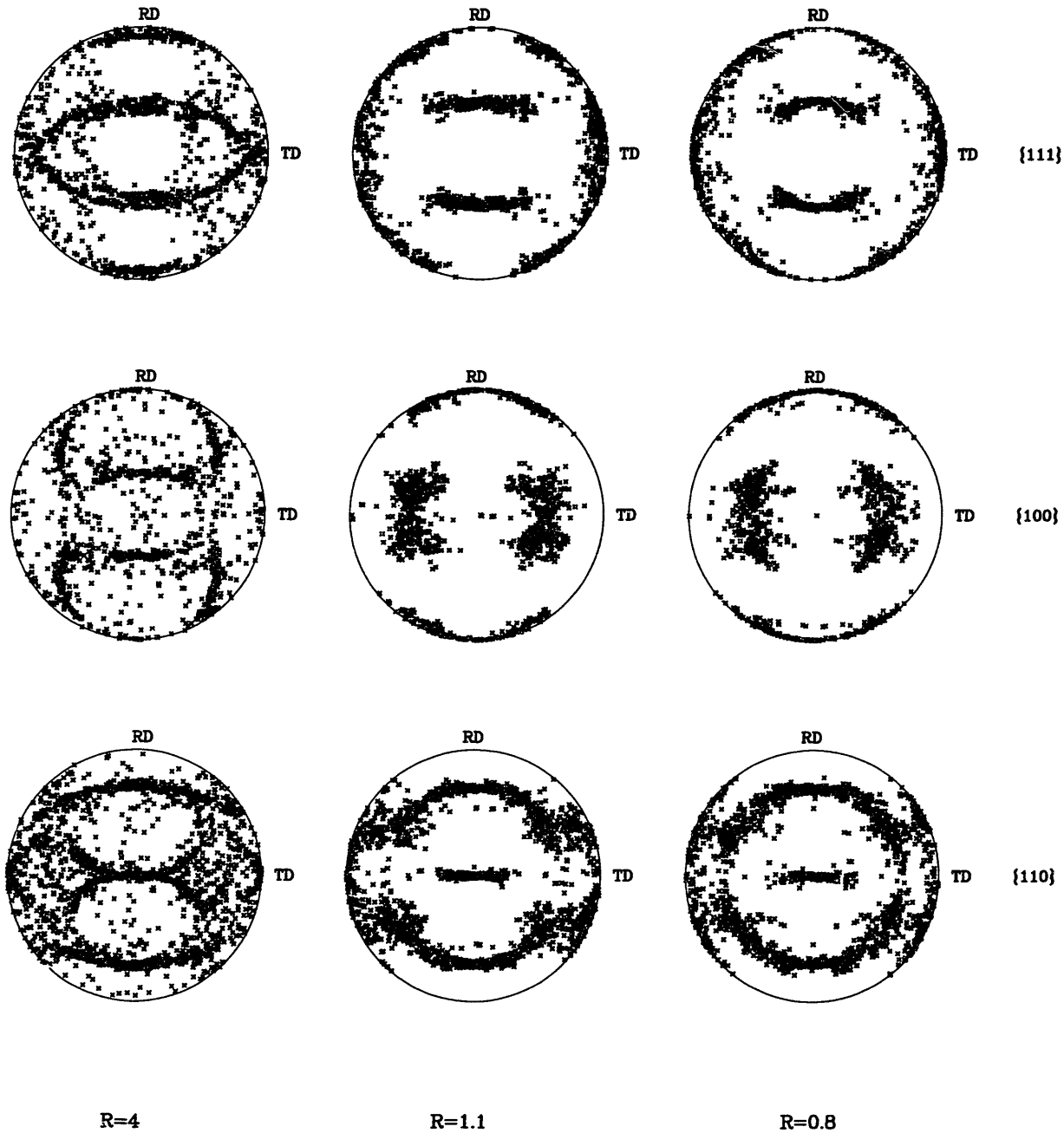


Figure 4-5: Crystallographic textures at 100% plane strain compression for non-hardening simulations for three different values of the ratio $R = s_{tw}/s_{sl} = 4$, 1.1, and 0.8.

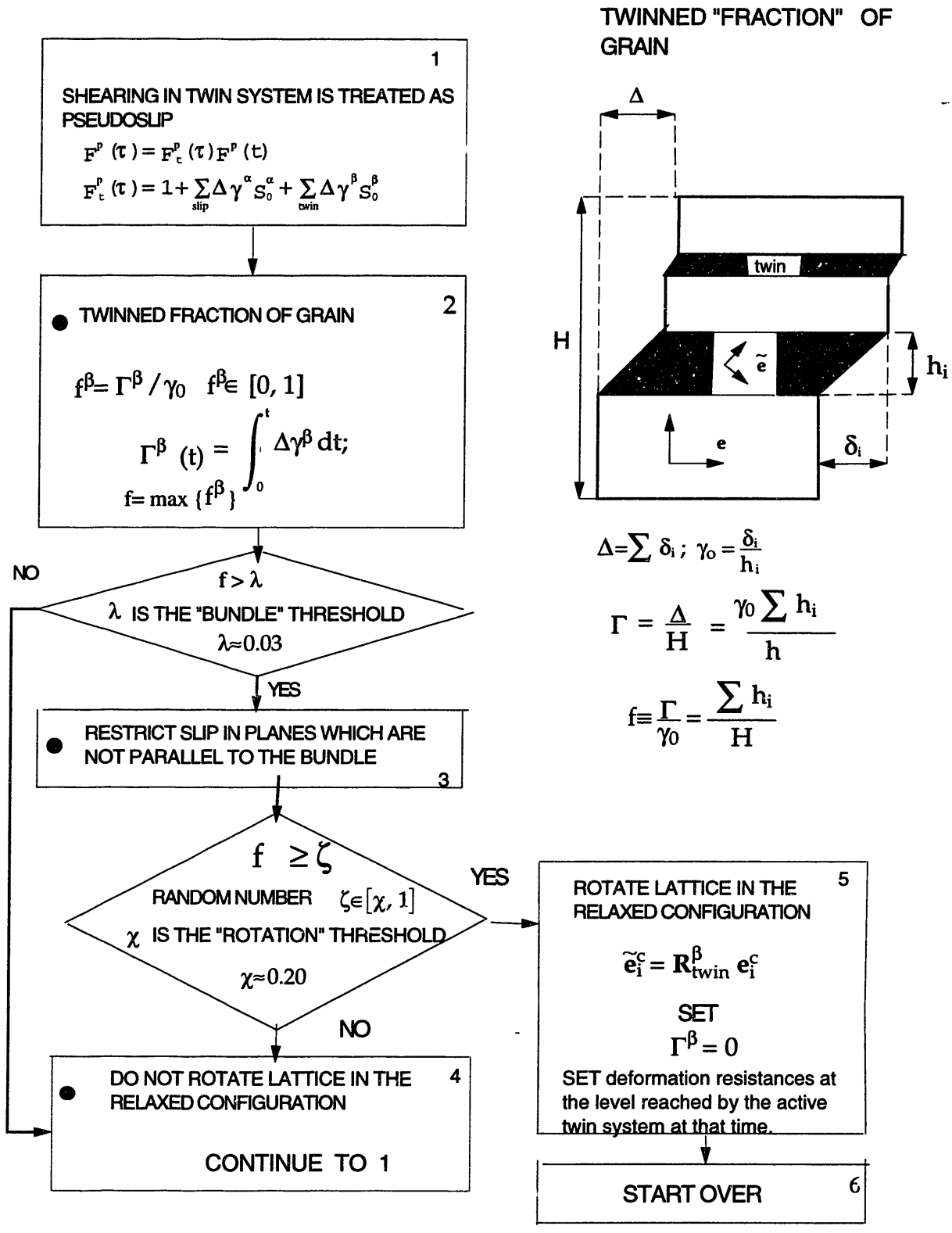


Figure 4-6: Algorithm of the computational procedure

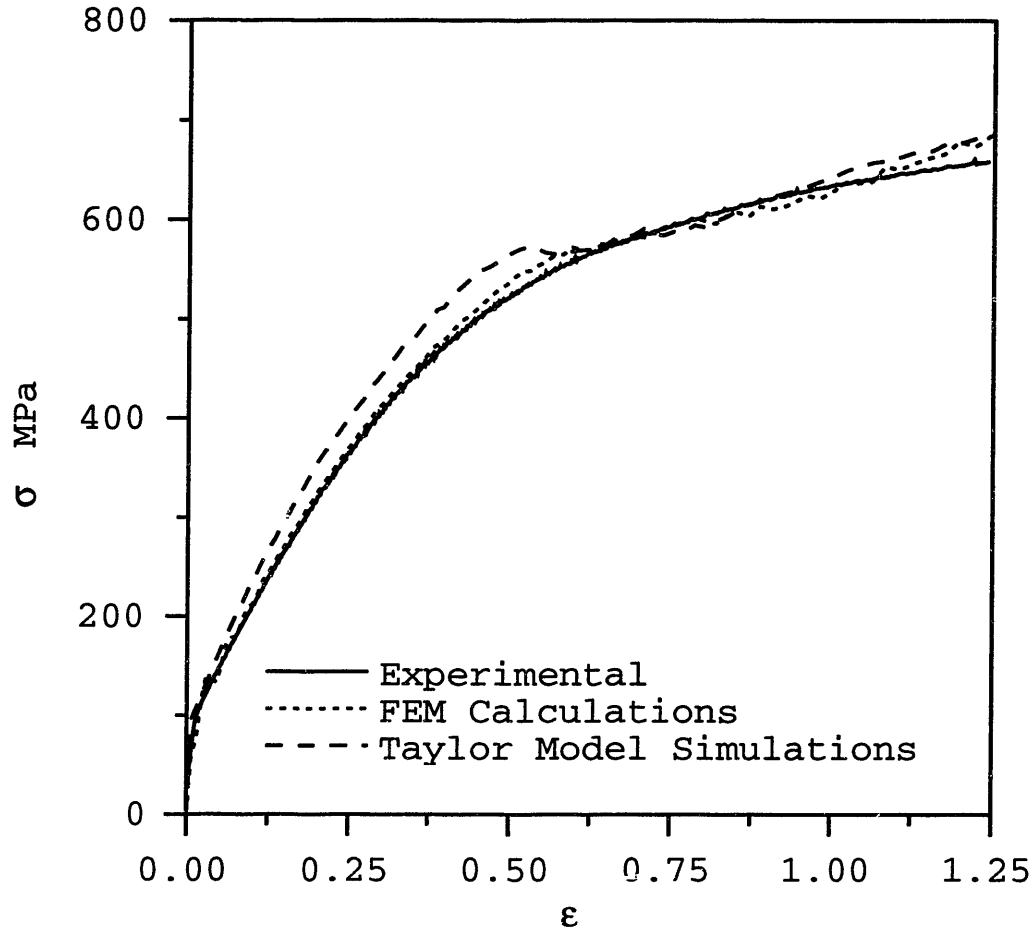


Figure 4-7: Comparison of the experimentally-measured stress-strain curves for plane strain compression of $\alpha$-brass against a finite-element model of a polycrystal, as well as against a Taylor model.

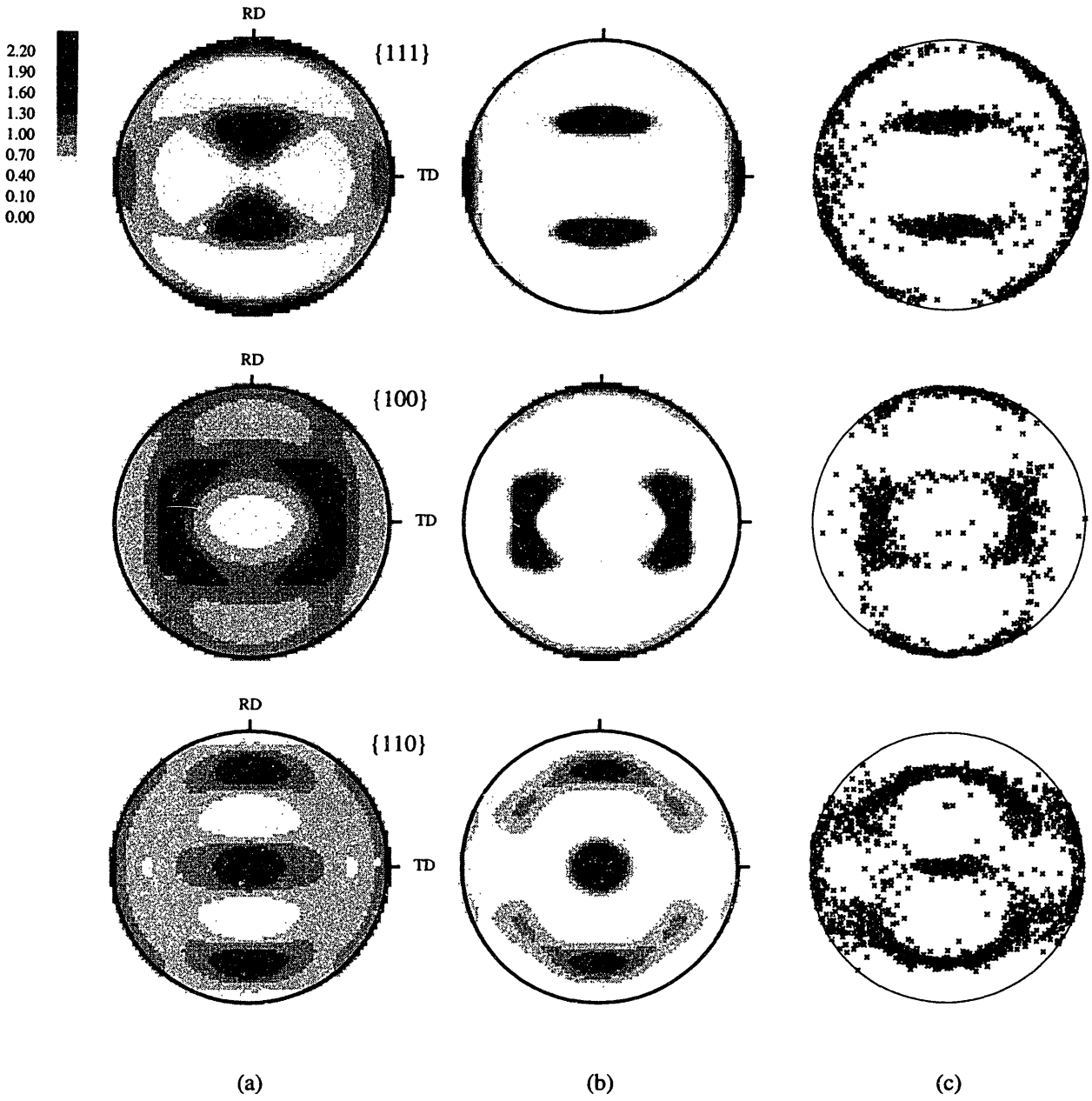


Figure 4-8: Comparison of experimentally-measured pole-figures after 100% plane strain compression of $\alpha$-brass against predictions from numerical simulations. (a) Experimental results. (b) The discrete predictions from finite-element calculations shown in (c), are smoothed to show grey-scale intensities using popLA.

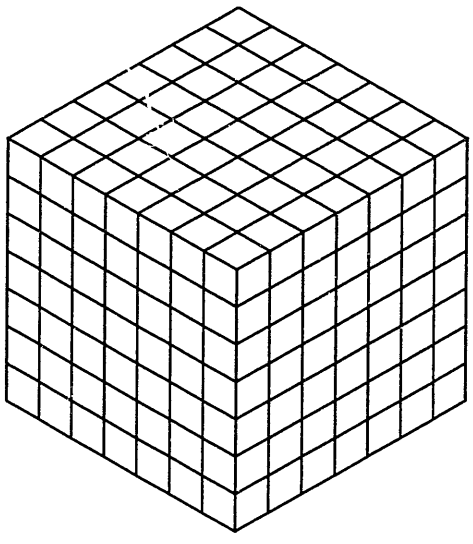

(a) Initial mesh

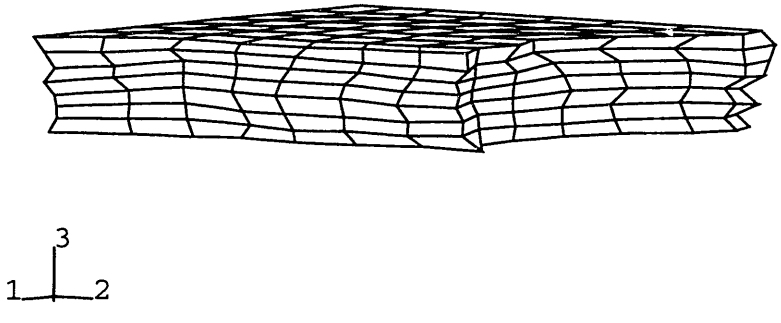


(b) Deformed mesh

Figure 4-9: Representative (a) initial, and (b) deformed 3-D finite element meshes for simple compression.

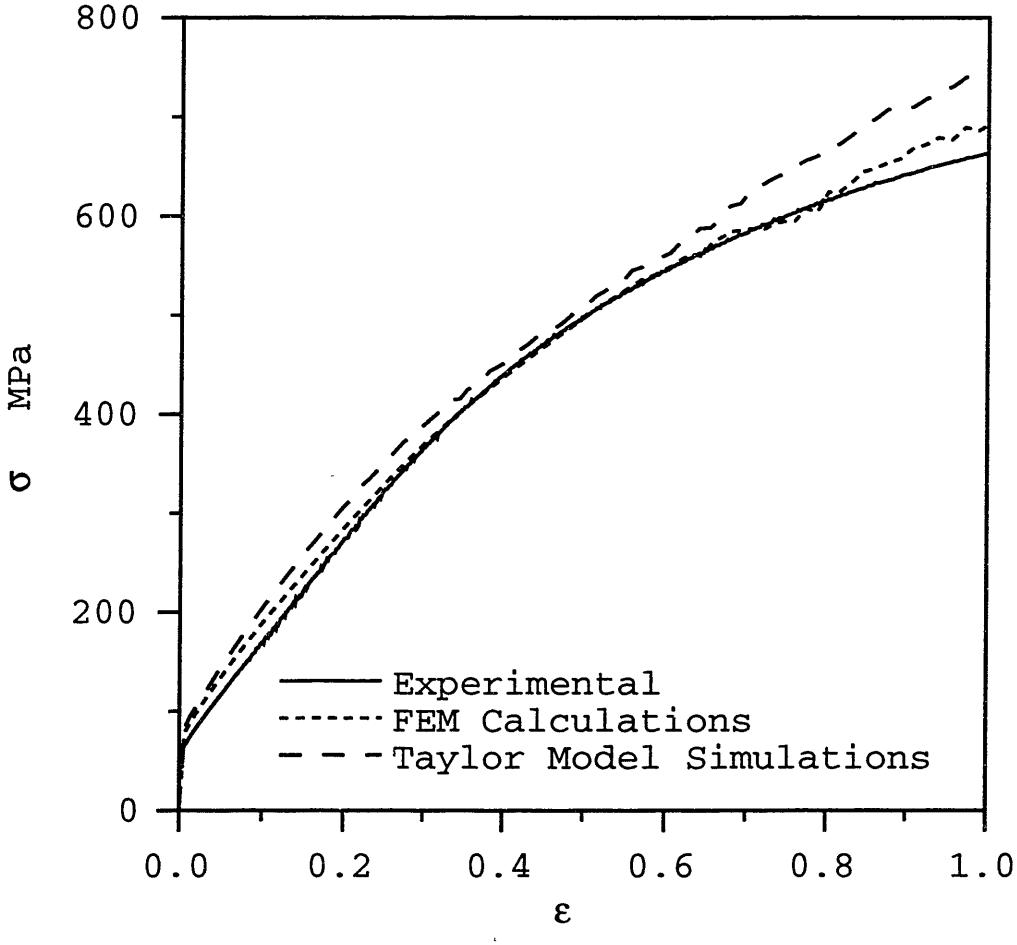


Figure 4-10: Comparison of the experimentally-measured stress-strain curves for simp le compression of $\alpha$-brass against a finite element model of a polycrystal, as well as against a Taylor model.

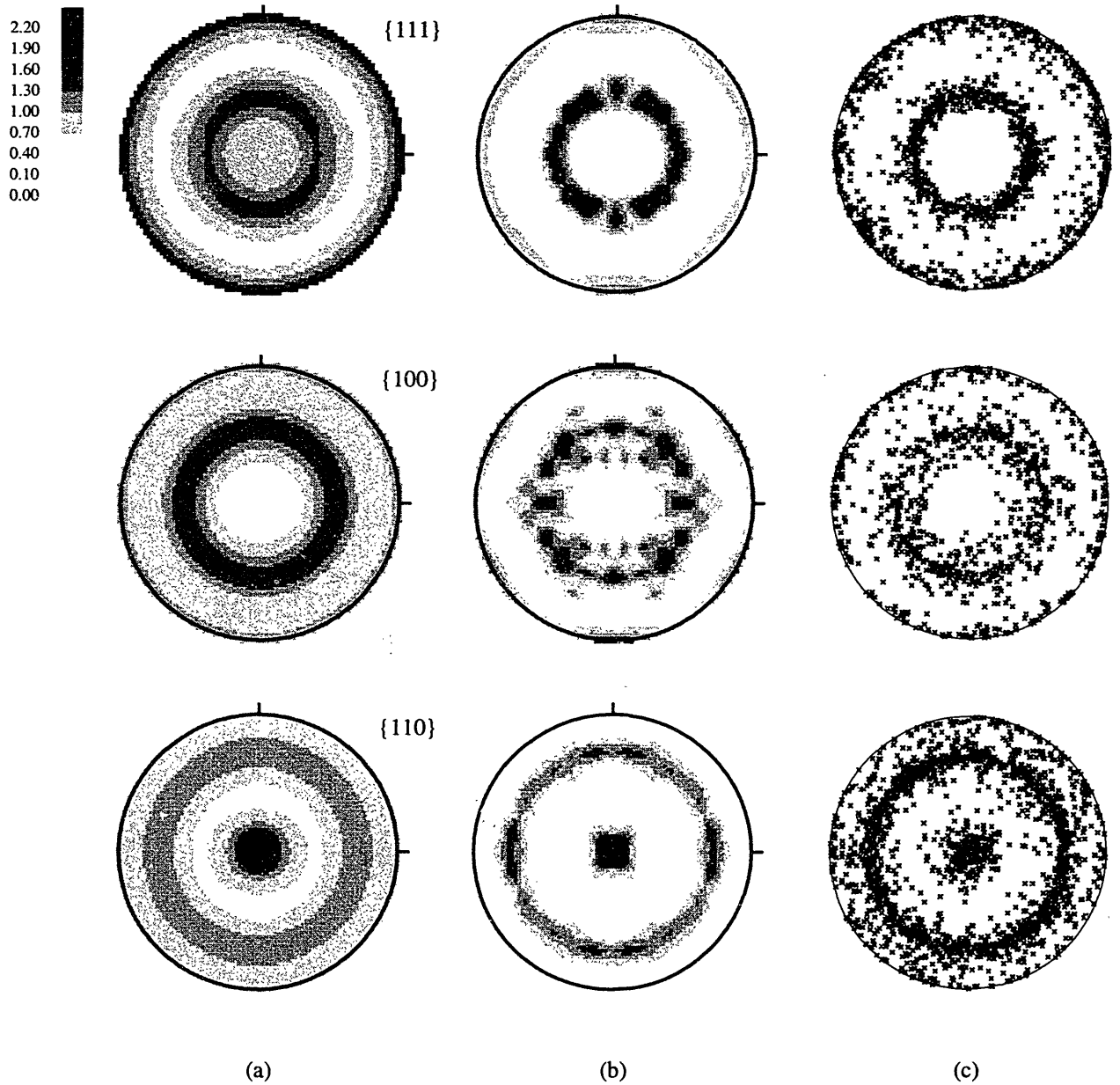


Figure 4-11: Comparison of experimentally-measured pole-figures after 100% simple compression of $\alpha$-brass against predictions from numerical simulations. (a) Experimental results. (b) The discrete predictions from finite-element calculations shown in (c), are smoothed to show grey-scale intensities using popLA.

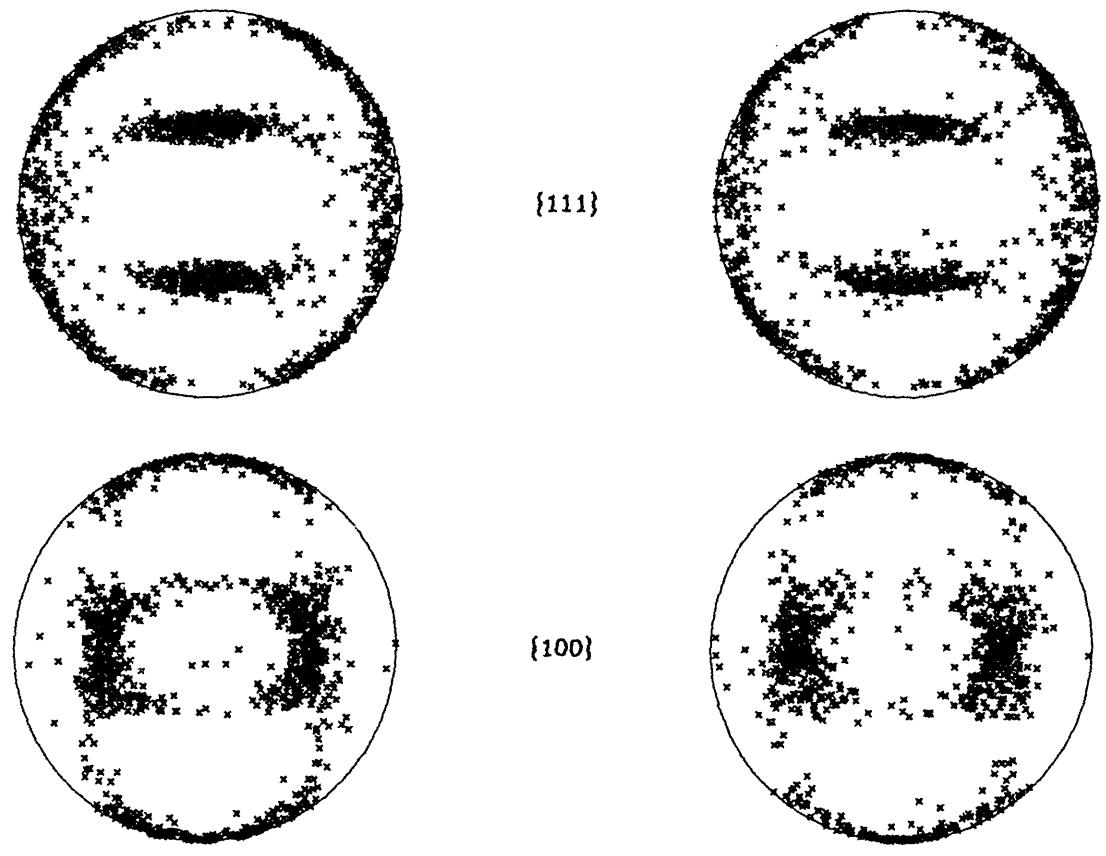


Figure 4-12: Comparison of the pole-figures after 100% plane strain compression predicted from a finite-element model of a polycrystal against those predicted by a Taylor model.

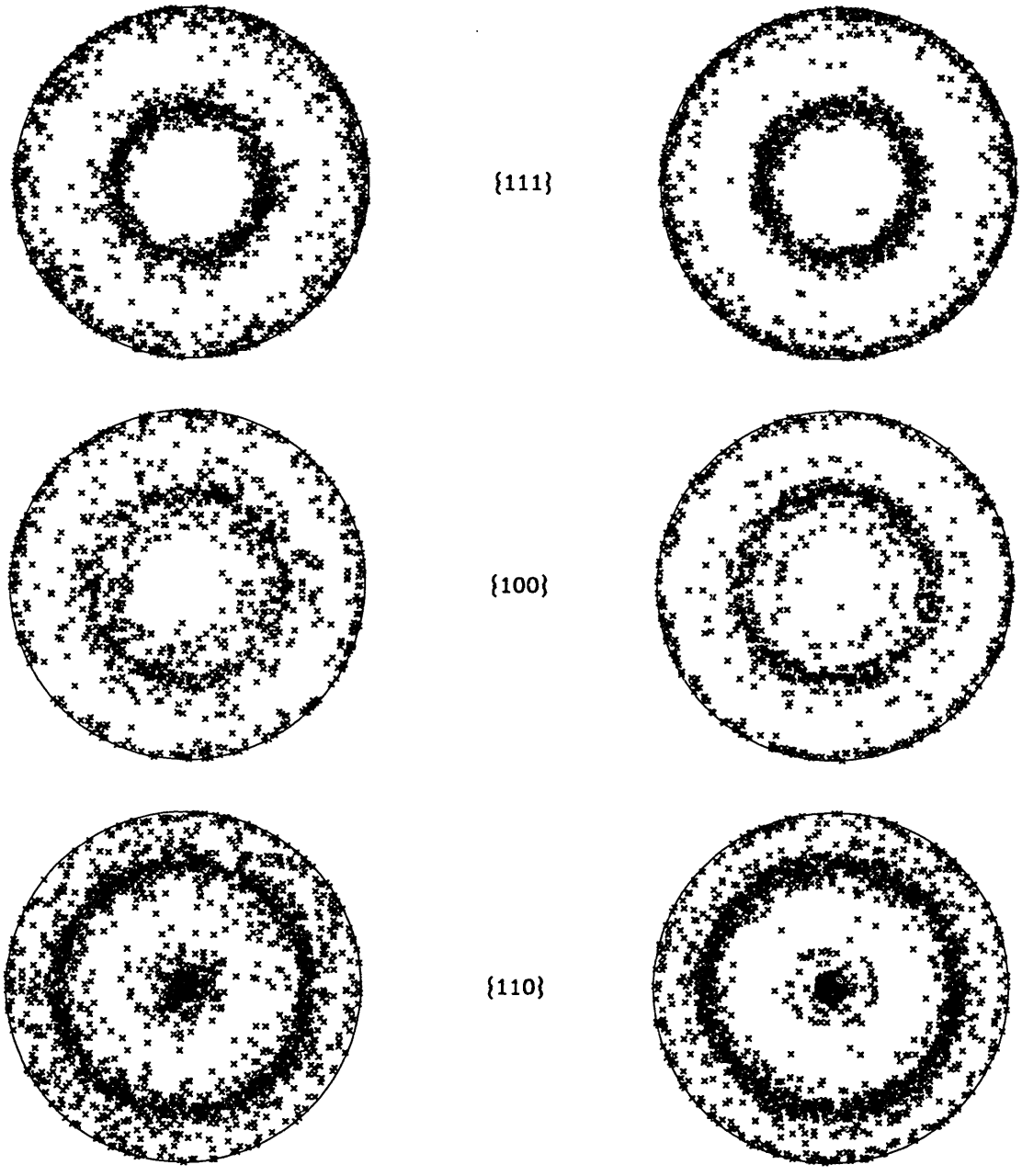


Figure 4-13: Comparison of the pole-figures after 100% simple compression predicted from a finite-element model of a polycrystal against those predicted by a Taylor model.

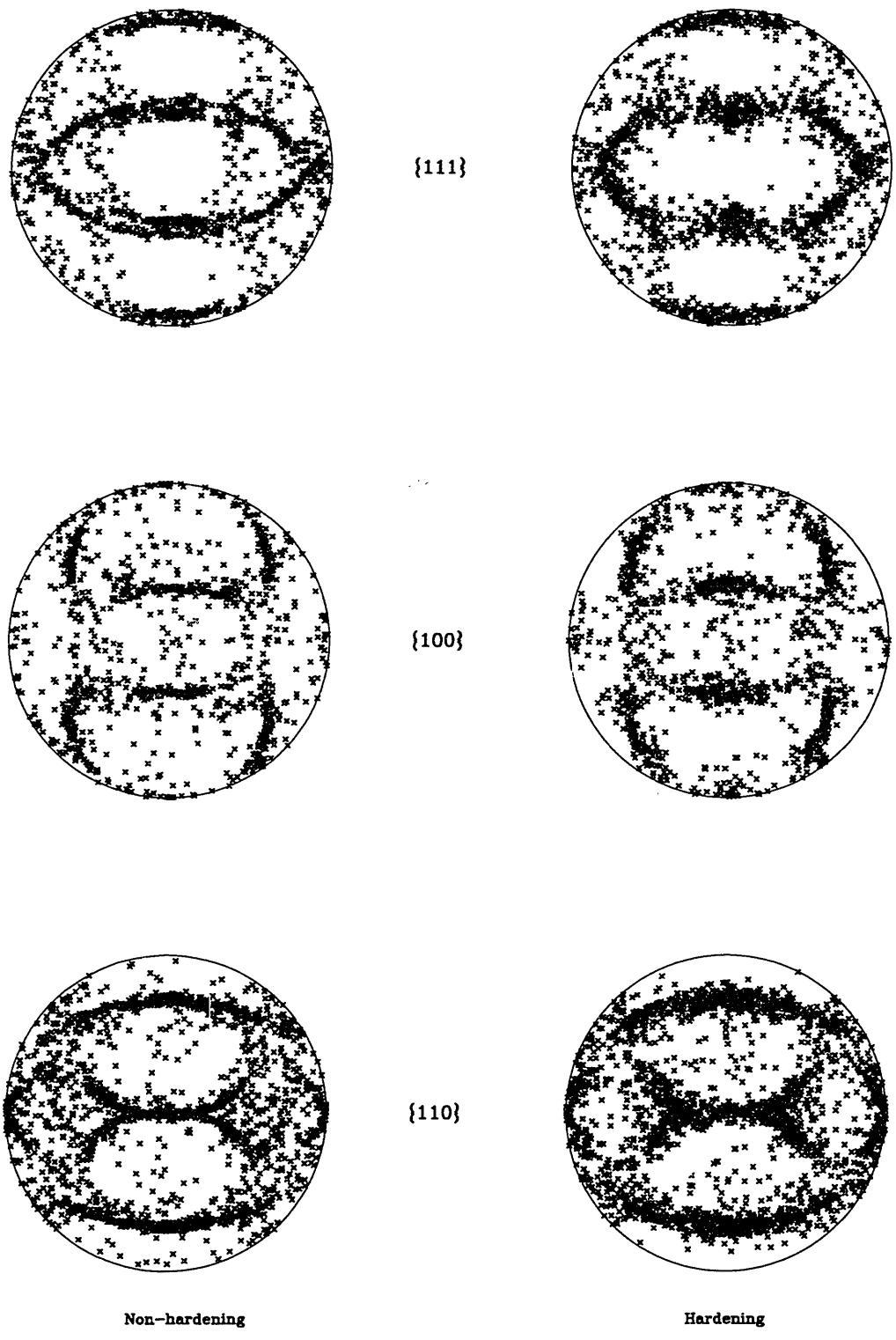


Figure 4-14: Comparison between the calculated pole figures (a) in non-hardening and (b) in strain hardening models for copper plane strain compression to $\epsilon = -1$.

# Chapter 5

# Plastic Deformation of HCP Materials at Room Temperature. Applications to Magnesium alloy AZ31B.

In this chapter we present a constitutive model for h.c.p. metals at room temperature, and calibrate the model parameters for the magnesium alloy AZ31B.

By using comparisons between model predictions and macroscopically-measured stress-strain curves and texture evolution we have deduced information about the values of the single-crystal parameters associated with slip and twin system deformation resistances. We show that a non-hardening model is able to reproduce both the experimentally measured pole figures and the stress-strain curves in different modes of deformation. Our calculations show that two main crystallographic mechanisms, slip on basal $(0001) < 11\bar{2}0 >$ systems and twinning on pyramidal $\{10\bar{1}2\} < \bar{1}011 >$ systems play the dominant role in the deformation of magnesium at room temperature.

## 5.1 Mechanisms of plastic deformation in magnesium

In hexagonal structures crystallographic Miller-Bravais indices based on the three axes $\mathbf{a_1}$, $\mathbf{a_2}$, and $\mathbf{a_3}$ belonging to the basal plane and axis $\mathbf{c}$ orthogonal to them are used. Fig. 5-1 shows indices of the directions in the hexagonal system. The basal plane (0001) is the closest packed among all crystallographic planes in h.c.p. materials. The crystal geometry, particularly, the ratio $c/a$, where $a$ is interatomic distance on the basal plane in any of the three $< 11\bar{2}0 >$ directions and $c$ is the distance between the first and the third layers, governs the deformation behavior of h.c.p. materials. The ideal $c/a$ ratio, calculated on the basis of a hard sphere model is 1.633. However, in real materials it varies from 1.567 for beryllium to 1.886 for cadmium. The increase in $c/a$ ratio means that the distance between the adjacent basal planes increases, so they appear relatively more close-packed than alternative planes, for example, prism or pyramidal. These planes are shown in Fig. 5-2. The smaller the ratio $c/a$, the easier non-basal slip systems operate. The axial ratio for magnesium is close to the ideal value and at room temperature equal to 1.624.

### 5.1.1 Crystallographic mechanisms of plastic deformation in magnesium

Basal slip dominates in plastic deformation of magnesium, but pyramidal $< a >$ and prismatic $< a >$ slip systems have also been observed even at room temperature (Burke and Hibbard [1952]). The movement of dislocations produces slip on particular planes, in a direction parallel to one of the close-packed rows of atoms, such as $[11\bar{2}0]$ illustrated in Fig. 5-2. The following table states the main slip and twin systems frequently quoted for magnesium. One can see from Table 5.1 that the first three most important slip systems have the same slip directions. Therefore, all h.c.p. materials, and magnesium in particular, do not have enough independent slip systems

Table 5.1: The main slip and twin systems in magnesium

| Type of the systems | System | Ease of operation | Reference |
|---|---|---|---|
| basal $< a >$ slip | $\{0001\} < 11\bar{2}0 >$ | | Burke and |
| pyramidal $< a >$ slip | $\{1\bar{1}01\} < 11\bar{2}0 >$ | mainly at high $T$ | Hibbard [1952] |
| prismatic $< a >$ slip | $\{1\bar{1}00\} < 11\bar{2}0 >$ | mainly at high $T$ | |
| pyramidal $< c+a >$ slip | $\{11\bar{2}2\} < \bar{1}\bar{1}23 >$ | anomalous mode | Morozumi et al. [1975] |
| twinning | $\{10\bar{1}2\} < \bar{1}011 >$ | $\gamma_0 = 0.129$ | Hall [1954] |
| twinning | $\{10\bar{1}1\} < \bar{1}012 >$ | $\gamma_0 = 1.066$ rare | |

to accumulate arbitrary deformation[1]. Because of the limited nature of common slip modes, twinning is one mechanism which allows plasticity in the $< c >$ direction. The most common twinning mode in h.c.p. metals is $\{10\bar{1}2\} < \bar{1}011 >$. The direction of shear associated with twinning depends on the $c/a$ ratio (Yoo [1981], Hosford [1993]). For all metals with $c/a < \sqrt{3}$ the direction of shear is $[\bar{1}011]$, and twinning occurs under tension parallel to the **c** axis. For those metals, where $c/a > \sqrt{3}$ the direction of shear is $[10\bar{1}\bar{1}]$, and twinning occurs under compression parallel to the **c** axis as schematically shown in Fig. 5-3. There are several twinning systems in magnesium that are reported in literature but the dominant one is $(10\bar{1}2)[\bar{1}011]$ (Fig. 5-4a). The correspondence schematic plan view of several hexagonal cells is given in Fig. 5-4b. In addition to twinning on the $\{10\bar{1}2\}$ plane, in rare cases twins on $\{10\bar{1}1\}$ were observed. Since this, $\{10\bar{1}1\}$ twinning mode is relatively unimportant, it will not be further considered. Thus, the twinning elements for h.c.p. magnesium are

$$K_1 = (10\bar{1}2), \quad \eta_1 = [\bar{1}011], \quad K_2 = (10\bar{1}\bar{2}), \quad \eta_2 = [10\bar{1}1]. \tag{5.1}$$

[1]In any material, five independent systems must be active for an arbitrary shape change. Our numerical experiments with f.c.c. materials demonstrated that crystals with different orientations operate different number of slip systems, but *the average* number of active slip system per grain is exactly equal to five. As was mentioned in previous chapters, f.c.c. crystals have twelve possible slip systems and several sets of five independent systems can be chosen for any prescribed deformation. In contrast, in h.c.p. metals there is a lack of independent slip systems.

The twinning shear corresponding to these elements may be written as

$$\mathbf{S} = \mathbf{1} + \gamma_0 \, \mathbf{m} \otimes \mathbf{n}, \quad \mathbf{m} \cdot \mathbf{n} = 0, \quad \gamma_0 = 0.129, \tag{5.2}$$

where $\mathbf{m}$ is a unit vector in the $\eta_1 = [\bar{1}011]$ direction, and $\mathbf{n}$ the unit normal to the $K_1 = (10\bar{1}2)$ plane. The most important role of twinning is reorientation of the crystallographic lattice to the new position, where basal slip can be easily operated. Fig. 5-4c schematically shows the local description of a twinned crystal, where we have two regions $R_1$ and $R_2$ which are separated by a plane $P$ with unit normal $\mathbf{n}$. For the case where the crystalline structure in $R_2$ can be obtained from the one in $R_1$ by means of a rotation of $\pi$ about an axis parallel to $\mathbf{n}$,

$$\mathbf{R}^{tw} = 2\mathbf{n} \otimes \mathbf{n} - \mathbf{1},$$

Figure 5-4d shows the atom movement during the twinning. New atoms do not exactly fit the atom sites of the original (parent) lattice. A minor movement, which must be added to the twinning shear, is called a "shuffle."

At room temperature, existence of pyramidal $< c + a >$ slip in magnesium is not established but these systems are important at elevated temperatures when twinning is suppressed.

In the end of this section we list directional cosines for all important slip/twin systems in Magnesium and Magnesium alloys. The Bravias lattice notation is not convenient for numerical modelling because of the absence of orthogonality. We transfer the four indices' notations into Miller indices by definition of the following orthogonal Cartesian system (see Fig. 5-1a) with unit vectors: $\mathbf{e_1^c}-$axis is $[\bar{1}2\bar{1}0]$; $\mathbf{e_2^c}-$ axis is $[\bar{1}010]$, and $\mathbf{e_3^c}-$axis is $[0001]$. In this Cartesian axis $\mathbf{n}$ is normal to a crystallographic plane (written through Miller indices), $\mathbf{m}$ is a direction in this plane. The main slip systems have the directional cosines shown in Tables 5.2 – 5.5 below.

The main $\{10\bar{1}2\} < \bar{1}011 >$ twin systems have the following directional cosines in the Cartesian system which shown in Table 5.6.

Table 5.2: Basal Slip Systems $(0001) < 11\bar{2}0 >$

| $\alpha$ | $[\mathbf{n}_o^\alpha]_c$ | $[\mathbf{m}_o^\alpha]_c$ | Bravias indices |
|---|---|---|---|
| 1 | 0 0 1 | $\frac{1}{2}$ -$\frac{\sqrt{3}}{2}$ 0 | $(0001)[11\bar{2}0]$ |
| 2 | 0 0 1 | $\frac{1}{2}$ $\frac{\sqrt{3}}{2}$ 0 | $(0001)[\bar{2}110]$ |
| 3 | 0 0 1 | -1 0 0 | $(0001)[1\bar{2}10]$ |

Table 5.3: Prismatic Slip Systems $\{10\bar{1}0\} < 11\bar{2}0 >$

| $\alpha$ | $[\mathbf{n}_o^\alpha]_c$ | $[\mathbf{m}_o^\alpha]_c$ | Bravias indices |
|---|---|---|---|
| 1 | 0 1 0 | 1 0 0 | $(10\bar{1}0)[1\bar{2}10]$ |
| 2 | $-\frac{\sqrt{3}}{2}$ $\frac{1}{2}$ 0 | $\frac{1}{2}$ $\frac{\sqrt{3}}{2}$ 0 | $(01\bar{1}0)[2\bar{1}\bar{1}0]$ |
| 3 | $-\frac{\sqrt{3}}{2}$ $-\frac{1}{2}$ 0 | $-\frac{1}{2}$ $\frac{\sqrt{3}}{2}$ 0 | $(\bar{1}100)[11\bar{2}0]$ |

Table 5.4: Pyramidal $< \mathbf{a} >$ Slip Systems $\{10\bar{1}1\} < 11\bar{2}0 >$

| $\alpha$ | $[\mathbf{n}_o^\alpha]_c$ | $[\mathbf{m}_o^\alpha]_c$ | Bravias indices |
|---|---|---|---|
| 1 | $0\ -\frac{2c}{\sqrt{4c^2+3a^2}}\ \frac{\sqrt{3}a}{\sqrt{4c^2+3a^2}}$ | 1 0 0 | $(10\bar{1}1)[1\bar{2}10]$ |
| 2 | $\frac{\sqrt{3}c}{\sqrt{4c^2+3a^2}}\ -\frac{c}{\sqrt{4c^2+3a^2}}\ \frac{\sqrt{3}a}{\sqrt{4c^2+3a^2}}$ | $\frac{1}{2}\ \frac{\sqrt{3}}{2}\ 0$ | $(01\bar{1}1)[\bar{2}110]$ |
| 3 | $\frac{\sqrt{3}c}{\sqrt{4c^2+3a^2}}\ \frac{c}{\sqrt{4c^2+3a^2}}\ \frac{\sqrt{3}a}{\sqrt{4c^2+3a^2}}$ | $-\frac{1}{2}\ \frac{\sqrt{3}}{2}\ 0$ | $(\bar{1}101)[\bar{1}\bar{1}20]$ |
| 4 | $0\ \frac{2c}{\sqrt{4c^2+3a^2}}\ \frac{\sqrt{3}a}{\sqrt{4c^2+3a^2}}$ | -1 0 0 | $(\bar{1}011)[\bar{1}2\bar{1}0]$ |
| 5 | $-\frac{\sqrt{3}c}{\sqrt{4c^2+3a^2}}\ \frac{c}{\sqrt{4c^2+3a^2}}\ \frac{\sqrt{3}a}{\sqrt{4c^2+3a^2}}$ | $-\frac{1}{2}\ -\frac{\sqrt{3}}{2}\ 0$ | $(0\bar{1}11)[2\bar{1}\bar{1}0]$ |
| 6 | $-\frac{\sqrt{3}c}{\sqrt{4c^2+3a^2}}\ -\frac{c}{\sqrt{4c^2+3a^2}}\ \frac{\sqrt{3}a}{\sqrt{4c^2+3a^2}}$ | $\frac{1}{2}\ -\frac{\sqrt{3}}{2}\ 0$ | $(1\bar{1}01)[11\bar{2}0]$ |

Table 5.5: Pyramidal $< \mathbf{c}+\mathbf{a} >$ Slip Systems $\{11\bar{2}2\} < 11\bar{2}3 >$

| $\alpha$ | $[\mathbf{n}_o^\alpha]_c$ | $[\mathbf{m}_o^\alpha]_c$ | Bravias indices |
|---|---|---|---|
| 1 | $\frac{c}{2(\sqrt{c^2+a^2})}\ -\frac{\sqrt{3}c}{2(\sqrt{c^2+a^2})}\ \frac{a}{(\sqrt{c^2+a^2})}$ | $-\frac{a}{2(\sqrt{c^2+a^2})}\ \frac{\sqrt{3}a}{2(\sqrt{c^2+a^2})}\ \frac{c}{(\sqrt{c^2+a^2})}$ | $(11\bar{2}2)[\bar{1}\bar{1}23]$ |
| 2 | $\frac{c}{(\sqrt{c^2+a^2})}\ 0\ \frac{a}{(\sqrt{c^2+a^2})}$ | $-\frac{a}{(\sqrt{c^2+a^2})}\ 0\ \frac{c}{(\sqrt{c^2+a^2})}$ | $(\bar{1}2\bar{1}2)[1\bar{2}13]$ |
| 3 | $\frac{c}{2(\sqrt{c^2+a^2})}\ \frac{\sqrt{3}c}{2(\sqrt{c^2+a^2})}\ \frac{a}{(\sqrt{c^2+a^2})}$ | $-\frac{a}{2(\sqrt{c^2+a^2})}\ -\frac{\sqrt{3}a}{2(\sqrt{c^2+a^2})}\ \frac{c}{(\sqrt{c^2+a^2})}$ | $(\bar{2}112)[2\bar{1}\bar{1}3]$ |
| 4 | $-\frac{c}{2(\sqrt{c^2+a^2})}\ \frac{\sqrt{3}c}{2(\sqrt{c^2+a^2})}\ \frac{a}{(\sqrt{c^2+a^2})}$ | $\frac{a}{2(\sqrt{c^2+a^2})}\ -\frac{\sqrt{3}a}{2(\sqrt{c^2+a^2})}\ \frac{c}{(\sqrt{c^2+a^2})}$ | $(\bar{1}\bar{1}22)[11\bar{2}3]$ |
| 5 | $-\frac{c}{(\sqrt{c^2+a^2})}\ 0\ \frac{a}{(\sqrt{c^2+a^2})}$ | $\frac{a}{(\sqrt{c^2+a^2})}\ 0\ \frac{c}{(\sqrt{c^2+a^2})}$ | $(1\bar{2}12)[\bar{1}2\bar{1}3]$ |
| 6 | $-\frac{c}{2(\sqrt{c^2+a^2})}\ -\frac{\sqrt{3}c}{2(\sqrt{c^2+a^2})}\ \frac{a}{(\sqrt{c^2+a^2})}$ | $\frac{a}{2(\sqrt{c^2+a^2})}\ \frac{\sqrt{3}a}{2(\sqrt{c^2+a^2})}\ \frac{c}{(\sqrt{c^2+a^2})}$ | $(2\bar{1}\bar{1}2)[\bar{2}113]$ |

Table 5.6: Pyramidal $< \mathbf{c}+\mathbf{a} >$ Twin Systems $\{10\bar{1}2\} < \bar{1}011 >$

| $i$ | $[\mathbf{n}_o^i]_c$ | $[\mathbf{m}_o^i]_c$ | Bravias indices |
|---|---|---|---|
| 1 | $0\ -\frac{c}{\sqrt{c^2+3a^2}}\ \frac{\sqrt{3}a}{\sqrt{c^2+3a^2}}$ | $0\ \frac{\sqrt{3}a}{\sqrt{c^2+3a^2}}\ \frac{c}{\sqrt{c^2+3a^2}}$ | $(10\bar{1}2)[\bar{1}011]$ |
| 2 | $0\ \frac{c}{\sqrt{c^2+3a^2}}\ \frac{\sqrt{3}a}{\sqrt{c^2+3a^2}}$ | $0\ -\frac{\sqrt{3}a}{\sqrt{c^2+3a^2)}}\ \frac{c}{\sqrt{c^2+3a^2}}$ | $(\bar{1}012)[10\bar{1}1]$ |
| 3 | $-\frac{\sqrt{3}c}{2(\sqrt{c^2+3a^2})}\ -\frac{c}{2(\sqrt{c^2+3a^2})}\ \frac{\sqrt{3}a}{(\sqrt{c^2+3a^2})}$ | $\frac{3a}{2(\sqrt{c^2+3a^2})}\ \frac{\sqrt{3}a}{2(\sqrt{c^2+3a^2})}\ \frac{c}{2(\sqrt{c^2+3a^2})}$ | $(1\bar{1}02)[\bar{1}101]$ |
| 4 | $\frac{\sqrt{3}c}{2(\sqrt{c^2+3a^2})}\ \frac{c}{2(\sqrt{c^2+3a^2})}\ \frac{\sqrt{3}a}{(\sqrt{c^2+3a^2})}$ | $-\frac{3a}{2(\sqrt{c^2+3a^2})}\ -\frac{\sqrt{3}a}{2(\sqrt{c^2+3a^2})}\ \frac{c}{2(\sqrt{c^2+3a^2})}$ | $(\bar{1}102)[1\bar{1}01]$ |
| 5 | $\frac{\sqrt{3}c}{2(\sqrt{c^2+3a^2})}\ -\frac{c}{2(\sqrt{c^2+3a^2})}\ \frac{\sqrt{3}a}{(\sqrt{c^2+3a^2})}$ | $-\frac{3a}{2(\sqrt{c^2+3a^2})}\ \frac{\sqrt{3}a}{2(\sqrt{c^2+3a^2})}\ \frac{c}{2(\sqrt{c^2+3a^2})}$ | $(01\bar{1}2)[0\bar{1}11]$ |
| 6 | $-\frac{\sqrt{3}c}{2(\sqrt{c^2+3a^2})}\ \frac{c}{2(\sqrt{c^2+3a^2})}\ \frac{\sqrt{3}a}{(\sqrt{c^2+3a^2})}$ | $\frac{3a}{2(\sqrt{c^2+3a^2})}\ -\frac{\sqrt{3}a}{2(\sqrt{c^2+3a^2})}\ \frac{c}{2(\sqrt{c^2+3a^2})}$ | $(0\bar{1}12)[01\bar{1}1]$ |

### 5.1.2 Non-crystallographic effects of plastic deformation in magnesium.

Deformation mechanisms in polycrystalline magnesium are much more complex than for single crystals. As Raynor [1959] pointed out, in addition to basal slip and pyramidal twinning, there exist more prolific twinning and non-basal slipping caused by inhomogeneous stressing and grain boundary constraints.

The most important non-crystallographic mechanism of inelastic deformations is grain boundary sliding (Jillson [1950], Hauser et al. [1955], and Raynor [1959]) as shown on micrograph in Fig. 5-5. Shear displacements across grain boundaries are observable at relatively low strains. One can see from Fig. 5-5 that grain boundary gives rise to multiple slip and twinning in the adjacent grain boundary area. This additional plastic yielding results in stress relief.

Thus, in magnesium in addition to slip and twinning several noncrystallographic features take part in maintaining generalized plastic flow. To account for them in

numerical simulations two different approaches can be chosen. *First*, to subdivide each grain into small RVE's (as it was done for analysis of deformation of f.c.c. single crystals) and allow multiple slip/twinning in the elements adjacent to grain boundaries as well as sliding and separation between elements. This requires very expensive numerical calculations in addition to special constitutive modeling of "grain boundary and interface elements." *A second* approach is not to focus on details of local inhomogeneity inside each grain, but assume that all non-crystallographic and grain boundaries effects can be described by a composite model where the grain boundary region is modeled as "isotropic" while the interior of the grain is modeled by crystal plasticity model. This method does not require additional information about multiple slip/twin interaction near grain boundaries and is also computationally inexpensive. Because the actual physical picture of the deformation process is still far from clear, successful simulations of plastic deformation of h.c.p. structures are rare. We aim to obtain a simple constitutive model and time-integration procedure to simulate inelastic deformation of h.c.p. metals at room temperature. It is for these reasons we concentrate on the second approach in our attempt to simulate the deformation process of magnesium at room temperature. We suggest a constitutive model based on crystal plasticity by slip and twinning in the bulk of a grain, and an "isotropic" plasticity component to model a thin grain boundary region. For purposes of geometrical interpretation of the model, and because most non-crystallographic effects are localized around grain boundaries, we imagine a "grain boundary layer" which deforms in accordance with isotropic plasticity. The volume fraction of this part of a crystal is a small and denoted by the $\xi$. The rest of the crystal with volume fraction $(1-\xi)$ deforms according to crystal plasticity theory. The schematic picture of this combined model is given in Fig[2] 5-6. Texture evolution is described by the crystal plasticity terms. The isotropic plasticity does not affect the crystallographic texture, but serves the important function of bounding the stress levels.

[2]In this work we use volume-averaged models and that is why the model in Fig. 5-6 is only one of possible geometrical interpretation. Actually, the features of isotropic plasticity and crystal plasticity are averaged over the grain volume with different weights.

### 5.1.3 Elastic properties of h.c.p. materials

There are twenty one elastic constants, that determines general elastic behavior of an anisotropic body. This number can be greatly reduced, if the symmetry of crystals is taken into account. For the hexagonal single crystals, there are five independent elastic moduli, $C_{11}$, $C_{12}$, $C_{13}$, $C_{33}$, and $C_{55}$, with $C_{22} = C_{11}$, $C_{23} = C_{13}$, $C_{44} = C_{55}$, and $C_{66} = \frac{1}{2}(C_{11} - C_{12})$. All other elements of the symmetric anisotropic elasticity tensor $\mathcal{C}$ are zero. These five constants are defined as follows,

$$
\begin{aligned}
C_{11} &= (\mathbf{e}_1^{\mathbf{c}} \otimes \mathbf{e}_1^{\mathbf{c}}) \cdot \mathcal{C}[\mathbf{e}_1^{\mathbf{c}} \otimes \mathbf{e}_1^{\mathbf{c}}], \\
C_{12} &= (\mathbf{e}_1^{\mathbf{c}} \otimes \mathbf{e}_1^{\mathbf{c}}) \cdot \mathcal{C}[\mathbf{e}_2^{\mathbf{c}} \otimes \mathbf{e}_2^{\mathbf{c}}], \\
C_{13} &= (\mathbf{e}_1^{\mathbf{c}} \otimes \mathbf{e}_1^{\mathbf{c}}) \cdot \mathcal{C}[\mathbf{e}_3^{\mathbf{c}} \otimes \mathbf{e}_3^{\mathbf{c}}], \\
C_{33} &= (\mathbf{e}_3^{\mathbf{c}} \otimes \mathbf{e}_3^{\mathbf{c}}) \cdot \mathcal{C}[\mathbf{e}_3^{\mathbf{c}} \otimes \mathbf{e}_3^{\mathbf{c}}], \\
C_{55} &= (\mathbf{e}_1^{\mathbf{c}} \otimes \mathbf{e}_3^{\mathbf{c}}) \cdot \mathcal{C}[2\,\mathrm{sym}\{\mathbf{e}_1^{\mathbf{c}} \otimes \mathbf{e}_3^{\mathbf{c}}\}],
\end{aligned}
$$

where $\mathbf{e}_i^{\mathbf{c}}$, $i = 1, 2, 3$ is an orthonormal basis aligned with the $[\bar{1}2\bar{1}0]$, $[\bar{1}010]$, and $[0001]$ crystallographic directions of the h.c.p. lattice. The values of these elastic parameters for a variety of materials are tabulated in standard books (e.g. Simmons and Wang [1971]). Careful determination of the elastic constants for magnesium have been carried out by Long and Smith [1957] using an ultrasonic pulse echo technique.

## 5.2 Experimental procedure and results.

In this section we describe the experimental program, which has been conducted to study the magnesium alloy AZ31B. The mechanical tests include simple tension, simple compression, and plane strain compression in different directions. All experiments presented were performed at quasi-static rates of deformation. These experiments are simulated with a finite element model of a polycrystal using "single crystal" constitutive equations.

### 5.2.1 Material characterization

The material, alloy AZ31B, has the following composition: Mg – 96.486 %; Al – 2.798%; and Zn – 0.715% as spectrum analysis showed. Figure 5-7a shows the SEM micrograph of the materials. The composition of inclusions seen in Fig. 5.5 is Mn, Al, and Fe. The volume fraction of inclusions does not exceed 0.7%.

We used two types of materials for sample preparation: first, hot-extruded rod for the uniaxial tension and compression tests, and second, hot-rolled plate for plane strain compression tests. The average grain size for both rod and plate varies from $12\mu m$ to $25\mu m$. An optical micrograph of initial state of the rod form of alloy AZ31B is shown in Fig. 5-7b.

For the microstructure analysis samples were polished and etched. Magnesium is a very soft material, and mechanical finish polishing is always a laborious procedure. Finish polishing is carried out with moderate pressure using 0.05 $\mu$m alumina or diamond paste. However, even this procedure does not guarantee the absence of fine scratches. For critical examination, electrolytic polishing procedure is recommended[3]. The etchant, which gives the clearest results, has a composition of 2 parts acetic acid, 2 parts distilled water, 5 parts ethanol (95%), and a small but necessary addition of picric acid (1/3 part). The specimen was immersed face up with gentle agitation for 15 seconds. After that, it was washed in alcohol and dried. A heavy brown film was developed and permitted observation of grain (twin) boundaries.

The plate has a strong fiber texture type orientation with relatively similar properties along the rolling and transverse directions. The results of hardness tests (Rockwell scale K: ball 1/8" at 150 kg) are presented in Fig. 5-8 together with the notation for plate faces and plate and rod directions which we will use in this work.

Crystallographic texture was measured by X-ray irradiation using a Rigaku RU200 diffractometer with pole figure goniometer. Partial pole figures were generated by using the Schulz slit (Schulz [1949]) on $\{0001\}$, $\{10\bar{1}0\}$, $\{10\bar{1}1\}$, and $\{11\bar{2}0\}$ crystallographic planes. Copper $K_\alpha$ radiation was used in the measurements. The typical

[3]We describe this procedure in the next chapter, devoted to experiments with magnesium at elevated temperatures.

dimensions of the slits for pole figure measurements are the following: divergence slit $DG = 1/2^o$; scatter slit $SS = 3^0$; receiving slit with height limit $RS = 4\,mm$. The values of the $2\theta$ positions of the goniometer, at which each crystallographic plane satisfies the Bragg law (Cullity [1978]), are close to each other for materials mentioned above.

Crystallographic pole figures of the initial texture for both rod and plate samples are given in Figures 5-9 and 5-10 respectively. The normal direction is parallel to the cylindrical axis for the rod, and is parallel to the normal to the rolling plane for plate samples.

### 5.2.2 Simple tension

The specimens were machined from 0.50" diameter rod. The gage section of the specimen had a length of 1.75" and a diameter of 0.25". Simple tension tests were performed to final true strain 0.16, at which stage the specimens failed. Axial displacement was measured using both an extensometer and displacement control from the Instron data acquisition system. The difference between these variants of strain measurement was observed only at the late stage of loading when necking occurred. Experiments were performed at constant true strain rates of $2 \times 10^{-5}\,sec^{-1}$ and $2 \times 10^{-4}\,sec^{-1}$. Stress-strain curves of both experiments are indistinguishable as one can see from the graphs in Fig. 5-11. The $\{0001\}$, $\{10\bar{1}0\}$, $\{10\bar{1}1\}$, and $\{11\bar{2}0\}$ pole figures for simple tension after 15% are shown in Fig. 5-12. The intensity of the $\{10\bar{1}0\}$ pole corresponding to the prism planes increased drastically. Such a rapid crystal reorientation cannot be explained by slip alone; it is caused by active twinning. Optical micrograph presented in Fig. 5-13 shows twinning lamellae in deformed sample after simple tension.

### 5.2.3 Simple compression

The specimens were machined from the same rod and the length to diameter ratio[4] was 1.1. Teflon film of 0.001" thickness was used as end lubrication. Displacement control has been accomplished by the use of an extensometer. Simple compression experiments were performed to final true strain about 0.18, at which stage the samples fractured.

Figure 5-14 illustrates the stress-strain responses at different strain rates. The higher strain rate the lower stress level is. This "inverse" strain rate dependence is specific for materials with twinning as a dominant deformation mode.

In simple compression crystals reorient from $\{10\bar{1}0\}$ initial fiber texture (Fig. 5-9 to the strong $\{0001\}$ fiber texture. The pole figures after compression to $\epsilon = -0.18$ are shown in Fig. 5-15. The basal planes of the grains tend to be strongly aligned parallel to the axis of loading. Deformation twinning is the dominant mechanism which can provide fast lattice reorientation of the grains. Optical micrographs presented in Fig. 5-16 clearly demonstrate twinning lamellae in deformed specimens after simple compression.

After comparing Figs. 5-11 and 5-14 it is very interesting to note that yielding occurs in tension at stresses which are almost three times larger than in compression.

### 5.2.4 Plane strain compression

The second set of experiments was performed for plane strain compression tests. Plane strain compression specimens were machined from the plate specimens. Initially specimens were made almost cubical with the constrained dimension direction 0.377± 0.003". The specimens were lubricated on all four contact surfaces inside the fixture with both a teflon film of 0.001" thickness and $MoS_2$ grease. For reliability of the results each test was repeated at least twice. The typical deformation prior to fracture did not exceed 20%. The initial plate already has strong texture. This is why the

[4]Such small ratio was chosen after a number of unsuccessful trials to conduct the test using specimens with the higher value of the ratio. In the unsuccessful trials the specimens sheared.

anisotropy of the polycrystalline samples resembles single crystal anisotropy (Kelley and Hosford [1968]).

In all investigated samples twin lamellae were observed after deformation (see Figs. 5-17(a) and (b)). In these figures the constraint direction is out of the page. Figure 5-18 shows the experimental stress-strain curves and Figure 5-19 shows four $\{0001\}$, $\{10\bar{1}0\}$, $\{10\bar{1}1\}$, and $\{11\bar{2}0\}$ measured equal area projection pole figures after an axial compressive strain of -0.15 parallel to the (direction $\mathbf{e_3}$ in our nomenclature, see Fig. 5-8). The basal planes of the magnesium crystals tend to be aligned along the rolling direction of the plate. One can see very strong basal fiber texture.

Next two sets of experiments are:

*(i)* compression direction is the direction ($\mathbf{e_2}$) (see Fig. 5-8) with free direction ($\mathbf{e_1}$) (i.e., compression in the plate rolling direction and free direction is plate transverse direction). The stress-strain curves for polycrystalline specimens increased steadily as shown in Fig. 5-20. The texture evolves to the basal plane, but more diffused than we observed after compression in plate normal direction. The basal pole alignment is accompanied with some spread of basal poles about the transverse direction. Four equal area pole figures are presented in Fig. 5-21.

*(ii)* compression direction is the direction ($\mathbf{e_2}$) (see Fig. 5-8) with free direction ($\mathbf{e_3}$) (i.e., compression in the plate rolling direction and free direction is the normal to the rolling plane of the plate). It is interesting to note that with changing the free direction to ($\mathbf{e_3}$) the qualitative character of the stress-strain relation changes as shown in Fig. 5-22. The stress-strain curves rise more sleeply than in previous test, and the curve is concave[5]. The significant feature of the texture is the strong basal pole alignment in the thickness direction and greater rotational spread of basal poles about rolling direction than about transverse direction. Please note that measured pole figures in Fig. 5-23 resemble the pole figures after plane strain compression with direction ($\mathbf{e_1}$) as a free direction but rotated on $90^o$ about normal direction.

Texture evolution has a strong tendency to align the $< c >$ crystallographic axis

[5]Experiments, not reported here, show that concave stress-strain curves correspond to tests in which direction ($\mathbf{e_3}$) is free direction.

along the compressive stress direction or normal to the rolling plane. Significant reorientation of the crystal lattice in all experiments were already observed after axial strain to 15% – 20%.

### 5.2.5 Analysis of samples fractures

All specimens deformed at room temperature cracked. The analysis of the fracture surfaces and modes of fracture gives additional information about the deformation mechanisms. Cracked specimens after simple compression, simple tension, and plane strain compression tests are shown in Fig. 5-24. The angle between the compressive axis and the normal to the crack plane is close to 35°. The tension specimens exhibit relatively little necking before fracture and fractured by the apparent shear. Figure 5-25a shows the SEM micrographs of fracture surfaces of tension samples at room temperature. Figure 5-25b shows the SEM micrographs of fracture surfaces of compression samples at room temperature. These micrographs support the suggestion that the fractures were relatively brittle.

## 5.3 Combined crystal plasticity and isotropic plasticity model

The constitutive model proposed in chapter 2 for f.c.c. materials when applied for the analysis of deformation of magnesium gave spurious results. Even with twinning allowed, the stress level was very high and the twin systems were very active. As a result, the number of crystal lattice rotation was incredibly large. This led to saw-like type of stress-strain curves, which (even qualitatively) did not resemble experimental data. The incorrect stress levels caused errors in the texture prediction. To avoid these difficulties we modified the constitutive model by incorporating an "isotropic plasticity term," which bounds the stress level and does not effect the lattice rotation. The incremental plastic strain from the "isotropic" boundary layer is taken as $\xi \mathbf{M}$

with

$$\mathbf{M} = \begin{cases} 0 & \text{if } \bar{\sigma} \leq s_{th} \\ \Delta\epsilon \left\{ \frac{\bar{\sigma}(t) - s_{th}}{s(t)} \right\}^{\frac{1}{m}} \frac{\mathbf{T}^{*\prime}(t)}{\bar{\sigma}(t)} & \text{if } \bar{\sigma} > s_{th} \end{cases} \tag{5.3}$$

Here $\mathbf{T}^{*\prime}$ is the deviator of Piola-Kirchhoff stress, $s$ is the internal variable, $s_{th}$ is the threshold, and $\bar{\sigma} = \sqrt{(3/2)\mathbf{T}^{*\prime} \cdot \mathbf{T}^{*\prime}}$ is an equivalent stress. Please note that the "isotropic term" is activated only if the stress $\bar{\sigma}$ exceeds a threshold value: $\bar{\sigma} > s_{th}$.

The governing variables in the constitutive model are taken as: $(i)$ The Cauchy stress, $\mathbf{T}$. $(ii)$ The deformation gradient, $\mathbf{F}$. $(iii)$ Crystal slip and twin systems labeled by integers $i$. Each system is specified by a unit normal $\mathbf{n}_0^i$ to the slip/twin plane, and a unit vector $\mathbf{m}_0^i$ denoting the slip/twin direction. The slip and twin systems $(\mathbf{m}_0^i, \mathbf{n}_0^i)$ are assumed to be known in the reference configuration. The amount of shear, $\gamma_0$, and the lattice rotation accompanying twinning, $\mathbf{R}^{tw}$, are also assumed to be known. $(iv)$ A plastic deformation gradient, $\mathbf{F}^p$, with $\det\mathbf{F}^p = 1$. This represents the cumulative effect of dislocation motion and shear due to twinning on the active slip and twin systems in the crystal. $(v)$ The slip and twin system deformation resistances $s^i > 0$; $s$ isotropic deformation resistance, with units of stress. $(vi)$ The twin fractions $f^i \geq 0$.

The elastic deformation gradient is defined by $\mathbf{F}^e \equiv \mathbf{F}\,\mathbf{F}^{p-1}$ with $\det\mathbf{F}^e > 0$, and it describes the elastic distortion of the lattice; it is this distortion that gives rise to the stress $\mathbf{T}$. For metallic materials the constitutive equation for stress is taken as a linear relation

$$\mathbf{T}^*(\tau) = \boldsymbol{\mathcal{C}}\left[\mathbf{E}^e(\tau)\right], \tag{5.4}$$

where $\boldsymbol{\mathcal{C}}$ is a fourth order anisotropic elasticity tensor. With

$$\mathbf{E}^e \equiv (1/2)\left\{\mathbf{F}^{eT}\mathbf{F}^e - \mathbf{1}\right\} \quad \text{and} \quad \mathbf{T}^* \equiv (\det\mathbf{F}^e)\,\mathbf{F}^{e-1}\mathbf{T}\mathbf{F}^{e-T} \tag{5.5}$$

The scalar $\tau(\tau) = \{\mathbf{C}^e(\tau)\,\mathbf{T}^*(\tau)\}\cdot\mathbf{S}_0(t)$ is the Schmid stress on a slip or twin system at time $\tau$. Tensor $\mathbf{S}_0^i = \mathbf{m}_0^i \otimes \mathbf{n}_0^i$ denotes the Schmid tensor for the $i-$th slip/twin system. Then, the conditions for slip and twinning in the bulk of the crystal are taken

as

$$\phi^i = \left|\tau^i\right| - s^i \leq 0. \tag{5.6}$$

For the combined model the incremental flow rule is expressed as:

$$\mathbf{F}^p{}_t(\tau) = \mathbf{1} + (1-\xi)\sum_i \Delta\gamma^i \mathbf{S}_0^i + \xi\mathbf{M}, \quad \mathbf{M} = \begin{cases} 0 & \text{if } \bar{\sigma} \leq s_{th} \\ \Delta\epsilon \left\{\frac{\bar{\sigma}(t)-s_{th}}{s(t)}\right\}^{\frac{1}{m}} \frac{\mathbf{T}^{*\prime}(t)}{\bar{\sigma}(t)} & \text{if } \bar{\sigma} > s_{th} \end{cases} \tag{5.7}$$

where $\mathbf{F}_t^p(\tau)$ is the volume averaged incremental plastic deformation gradient for a single crystal[6], $\mathbf{M}$ is incremental isotropic plastic strain tensor, parameters $\xi$, $\Delta\epsilon$, and $m$ are constants, $\mathbf{T}^{*\prime}$ is the deviator of Piola-Kirchhoff stress, $s$ is an internal variable with dimensions of stress, $s_{th}$ is the threshold, $\bar{\sigma} = \sqrt{(3/2)\mathbf{T}^{*\prime}\cdot\mathbf{T}^{*\prime}}$ is equivalent stress, and $\Delta\gamma^i > 0$ is shear increment of the $i-$th slip/twin system.

All mathematical transformations are done in linear approximation, i.e., the inverse matrix $\mathbf{F}_t^{p\,-1}(\tau)$ can be written in the form:

$$\mathbf{F}^p{}_t^{-1}(\tau) = \mathbf{1} - (1-\xi)\sum_i \Delta\gamma^i \mathbf{S}_0^i - \xi\mathbf{M} + O(\xi^2 + \Delta\gamma^2) \tag{5.8}$$

Also, the slip and twin systems resistances are denoted simply by $s^i$; the evolution equation for these resistances is taken in a generic form as

$$s^i(\tau) = s^i(t) + \sum_{j\in\mathcal{PA}} h^{ij}(t)\,\Delta\gamma^j, \quad i = 1,\cdots,N, \tag{5.9}$$

where $h^{ij}$ are the hardening moduli, and $N$ is the total number of slip and twin systems. In the following section we will examine texture evolution and stress-strain response in a non-hardening model, i.e., set $h^{ij} = 0$.

Next, we substitute equality (5.8) into the expression for elastic strain measure and define a trial elastic strain and stress at time $\tau$ in the same sense as it was done

[6]refer to chapter 2 for all notations

in previous chapters:

$$\begin{aligned}
\mathbf{F}^e(\tau)^{\mathrm{tr}} &= \mathbf{F}(\tau)\,\mathbf{F}^p(t)^{-1}, \\
\mathbf{C}^e(\tau)^{\mathrm{tr}} &= (\mathbf{F}^e(\tau)^{\mathrm{tr}})^T\mathbf{F}^e(\tau)^{\mathrm{tr}}, \\
\mathbf{E}^e(\tau)^{\mathrm{tr}} &= (1/2)\{\mathbf{C}^e(\tau)^{\mathrm{tr}} - \mathbf{1}\}. \\
\mathbf{T}^*(\tau)^{\mathrm{tr}} &= \boldsymbol{\mathcal{C}}[\mathbf{E}^e(\tau)^{\mathrm{tr}}] \\
\tau^i(\tau)^{\mathrm{tr}} &= \mathbf{T}^*(\tau)^{\mathrm{tr}} \cdot \mathbf{S}_0^i(t).
\end{aligned}$$

As a result we obtain:

$$\begin{aligned}
\mathbf{E}^e(\tau) &= (1/2)\,\{\mathbf{C}^e(\tau) - \mathbf{1}\} = \mathbf{E}^e(\tau)^{\mathrm{tr}} - \\
&\sum_{j\in\mathcal{PA}} \Delta\gamma^j \mathrm{sign}\left(\tau^j(\tau)^{\mathrm{tr}}\right) \mathrm{sym}\left(\mathbf{C}^{e\mathrm{tr}}\mathbf{S}_0^j\right) - \xi\,\mathrm{sym}\left(\mathbf{C}^{e\mathrm{tr}}\mathbf{M}\right). \quad (5.10)
\end{aligned}$$

In this expression $\mathcal{PA}$ is the set of all potentially active slip and twin systems. The relation (5.10) can be rewritten in a more instructive form, namely:

$$\mathbf{E}^e(\tau) = \mathbf{E}^e(\tau)^{\mathrm{crystal}} - \xi\,\mathrm{sym}\left(\mathbf{C}^{e\mathrm{tr}}\mathbf{M}\right) \quad (5.11)$$

where we separated the crystal plasticity term $\mathbf{E}^e(\tau)^{\mathrm{crystal}}$ and additional term caused by isotropic plasticity. Use of linear relation between Piola-Kirchhoff stress and Green elastic strain measure (5.4) together with (5.11) gives

$$\mathbf{T}^*(\tau) = \mathbf{T}^*(\tau)^{\mathrm{crystal}} - \xi\,\boldsymbol{\mathcal{C}}\left[\mathrm{sym}\left(\mathbf{C}^{e\mathrm{tr}}\,\mathbf{M}\right)\right] \quad (5.12)$$

From here we immediately obtain that

$$\left|\tau^i(\tau)\right| = \left|\tau^i(\tau)^{\mathrm{crystal}}\right| - \xi\,\boldsymbol{\mathcal{C}}\left[\mathrm{sym}\left(\mathbf{C}^{e\mathrm{tr}}\,\mathbf{M}\right)\right]\cdot\mathbf{S}_0^i, \quad (5.13)$$

or in expanded form:

$$\left|\tau^i(\tau)\right| = \left|\tau^i(\tau)^{\mathrm{tr}}\right| -$$

$$\sum_{j\in\mathcal{PA}} \left\{ \operatorname{sign}\left(\tau^i(\tau)^{\mathrm{tr}}\right) \operatorname{sign}\left(\tau^j(\tau)^{\mathrm{tr}}\right) \right.$$
$$\left. \mathbf{S}_0^i(t) \cdot \boldsymbol{\mathcal{C}}\left[\operatorname{sym}\left(\mathbf{C}^e(\tau)^{\mathrm{tr}}\mathbf{S}_0^j(t)\right)\right]\right\} \Delta\gamma^j -$$
$$\xi\, \mathbf{S}_0^i(t) \cdot \boldsymbol{\mathcal{C}}\left[\operatorname{sym}\left(\mathbf{C}^e(\tau)^{\mathrm{tr}}\mathbf{M}(t)\right)\right] \tag{5.14}$$

Use of (5.14) in the consistency condition

$$\left|\tau^i(\tau)\right| = s^i(\tau)$$

gives the linear system

$$\sum_{j\in\mathcal{PA}} A^{ij}\, x^j = b^j\,, \qquad i \in \mathcal{PA},$$

with

$$A^{ij} = h^{ij} + \operatorname{sign}\left(\tau^i(\tau)^{\mathrm{tr}}\right) \operatorname{sign}\left(\tau^j(\tau)^{\mathrm{tr}}\right) \mathbf{S}_0^i(t) \cdot \boldsymbol{\mathcal{C}}\left[\operatorname{sym}\left(\mathbf{C}^e(\tau)^{\mathrm{tr}}\mathbf{S}_0^j(t)\right)\right], \tag{5.15}$$

$$b^i = \left|\tau^i(\tau)^{\mathrm{tr}}\right| - s^i(t) - \xi\, \mathbf{S}_0^i(t) \cdot \boldsymbol{\mathcal{C}}\left[\operatorname{sym}\left(\mathbf{C}^e(\tau)^{\mathrm{tr}}\mathbf{M}(t)\right)\right] > 0, \tag{5.16}$$

$$x^j \equiv \Delta\gamma^j \geq 0. \tag{5.17}$$

Thus, one can see that the only difference in the linear system arising from incorporating of the isotropic term $\mathbf{M}$ is change of the right side of the system. All numerical approaches that have been developed for the analysis of f.c.c materials are applicable here.

The isotropic term does not affect the texture evolution. The "crystallographic part" of this model is responsible for lattice rotations. We keep the logic of the model unchanged with respect to the constitutive model for f.c.c. materials (see chapter 2), i.e., first, treat twinning as a pseudo-slip, and then rotate the lattice to new "twin-related" orientation if a sufficiently large fraction of the grain has twinned. Let $f$ denote the volume fraction of the twin system with the maximum value of $f^i$ at a

given time $t$, and let a random number $\xi \in [0.3, 1]$ denote a representative maximum value of $f$ in a RVE. The lattice reorientation condition suggested by Van Houtte [1978], and adopted here, is that if $f > \xi$, then the orientation of the RVE be replaced by the twin related orientation. The single-crystal constitutive equations developed in this section have been implemented in the finite element program ABAQUS/Explicit [1995] by writing a user subroutine "VUMAT." The polycrystal calculations shown below have been carried out by modeling each grain in polycrystalline magnesium as a single finite element.

## 5.4 Verification of the constitutive model

In this section, we now evaluate the accuracy of the constitutive model in predicting the stress response and texture evolution in h.c.p. magnesium alloy AZ31B at room temperature. We compare the numerical predictions against experimental results, described in section 5.2. We performed full three-dimensional finite element calculations in which each element represents a single crystal. Because the simulated material had strong texture before experiments, we analyzed the deformation of initially anisotropic polycrystalline material. The popLA package was used to numerically represent initial material texture. Experimentally measured initial textures of the magnesium alloy AZ31B rod and plate and their numerical representations using 343 grain orientations are shown in Fig. 5-26 and Fig. 5-27 respectively. For the modeling we used a set of 343 (cube 7 X 7 X 7) finite elements ABAQUS-C3D8R. Magnesium was modeled as an elastic-plastic, non-hardening material. Elastic constants were taken as (Simmons and Wang, [1971]):

$$C_{11} = 58\,GPa;\ C_{12} = 25\,GPa;\ C_{13} = 20.8\,GPa;$$
$$C_{33} = 61.2\,GPa;\ \text{and}\ C_{55} = 16.6\,GPa.$$

Also, we take[7] $\xi = 0.05$, $\Delta\epsilon = 0.00003$, and $m = 0.07$. for the "isotropic term" in the model.

[7]the reason for such choice is as follows: the stable time increment in ABAQUS/Explicit calculation is approximately 0.03 and $\dot{\epsilon_0} \sim 0.001$. Therefore, $\Delta\epsilon = \dot{\epsilon_0}\Delta t \sim 0.00003$.

The model parameters for rod specimens were estimated by a curve-fitting procedure for simple tension experimental data. The model parameters for plate samples were estimated from plane strain compression test where the compression direction was normal to the plate rolling plane. Such a calibrated model has been used to predict material behavior in other regimes of deformation. In order to simulate deformation at room temperature we use basal $< a >$ slip systems, pyramidal $< a >$ slip systems, and pyramidal $\{10\bar{1}2\} < \bar{1}011 > < c+a >$ twinning mode.

We shall show that the major part of the macroscopic strain hardening of the material may be explained by crystal lattice reorientation only.

### 5.4.1 Simple tension

Finite element calculations for simple tension of the aggregate of 343 grains were carried out with various values of material parameters. The process of curve-fitting stress-strain data to obtain the value of *non-hardening* model parameters yielded

$$s_{basal} = 0.55 \text{ MPa}, \; s_{pyramidal<a>} = 105 \text{ MPa}, \; s_{twin} = 18 \text{ MPa},$$

$$s_{th} = 170 \text{ MPa}, \; s = 220 \text{ MPa}.$$

It is interesting to note that despite slip resistance for pyramidal $< a >$ systems is much higher than resistance of basal plane slip systems, but the variation of $s_{pyramidal<a>}$ influences the resulting stress-strain curve as shown in Fig. 5-28.

The quality of curve-fit is demonstrated in Fig. 5-29. Both the slip and twinning systems were active in these model simulations. The $\{0001\}$, $\{10\bar{1}0\}$, $\{10\bar{1}1\}$, and $\{11\bar{2}0\}$ pole figures for simple tension after 15 % are shown in Fig. 5-30 together with numerically-predicted pole figures. Qualitatively the character of the texture is the same as was before deformation, but the sharpness of $\{10\bar{1}0\}$ pole increased more than twice. To give a complete information about preferred orientations, the measured and numerically-predicted inverse pole figures are given in Fig. 5-31. The tensile axis in most crystals is aligned with the $\{10\bar{1}0\}$ poles. The agreement between

the numerical results and experimental measurements is very good.

We see from the simulations that non-hardening model is capable to predict both the stress-strain response and texture evolution in simple tension. Having estimated all necessary parameters in the model, we simulated a simple compression experiment.

### 5.4.2 Simple compression

In simple compression crystals reoriented from $\{10\bar{1}0\}$ initial fiber texture to the strong $\{0001\}$ fiber texture. The yield stress here depends on the value of $s_{twin}$. Changes in values of pyramidal $< a >$ slip resistances influence the stress-strain level in the same fashion as we observed for simple tension. In this case the pyramidal $< a >$ slip systems were active when grains aligned their $< c >$ axis along compression direction and the resolved shear stress on the basal plane again was negligible.

Initial orientation is favorable for active basal slipping in simple compression. Basal $< a >$ slip activity prior the twinning may be the reason for the concave shape of stress-strain curves. Experimentally measured and numerically predicted stress-strain curves are shown in Fig. 5-32. A set of four equal area pole figures for both the experiments and FEM calculations is presented in Fig. 5-33. Comparison of numerically-predicted inverse pole figure against experimental results is given in Fig. 5-34. Correlation between prediction and experiment is again very high. We emphasize that simulations have been done using *a non-hardening* model. Changes in stress levels, i.e. polycrystalline hardening, are related only with texture evolution.

### 5.4.3 Plane strain compression

The second set of calculations was performed for the simulation of plane strain compression tests. For these simulation we also used a full three dimensional finite element mesh as was done earlier for f.c.c. metals. The initial state of the plate was different from that of the rod samples. It led to different initial values of the state variables in

the isotropic part of our model.

$$s_{th} = 210 \text{ MPa}, \; s = 295 \text{ MPa}.$$

These parameters were obtained by a curve-fitting procedure for the case when compression axis was parallel to the normal to the plate rolling plane and the free direction was parallel to the plate rolling direction. It is important to note, that other parameters of this *non-hardening* model were the same as that for rod specimens. We simulated plane-strain compression experiments of this textured material and compared our predictions for different directions of loading against measurements.

Figure 5-35 shows the experimental and calculated stress-strain curves and Figure 5-36 shows a comparison of the experimental and numerically-predicted equal area projection pole figures after an axial compressive strain of -0.15 parallel to the previously compression direction (direction $\mathbf{e_3}$, see Fig. 5-8). Figure 5-37 shows measured and calculated inverse pole figures. The preferred orientation is qualitatively the same as before loading, but basal pole is much more intense The stress-strain curve and texture prediction are in very good agreement with experimental observations.

This model was used to predict material behavior for plane strain compression of the sample in the direction ($\mathbf{e_2}$) (see Fig. 5-8 for notation) with free direction ($\mathbf{e_3}$) (i.e., compression in the plate rolling direction and free direction is plate normal to the rolling directions). Results of computations are presented in Figs. 5-38, 5-39, and 5-40. One can see that calculated results capture the main features of the experimental data. Calculated stress-strain curves resemble experimental relations, but stress level increases too fast in comparison against experimental data.

We show in Figures 5-41 and 5-42 the measured and predicted direct and inverse pole figures for plane strain compression in the direction $\mathbf{e_2}$ (see Fig. 5-8) with free direction $\mathbf{e_1}$ (i.e., compression in the plate rolling direction and free direction is plate transfer direction). Both direct pole figures and inverse pole figures demonstrate the ability of the model to predict the texture evolution.

We now consider the possibility of adding isotropic hardening of the boundary

layer:

$$s(\tau) = s(t) + h \cdot \Delta\epsilon \left( \frac{\bar{\sigma}(t) - s_{th}(t)}{s(t)} \right)^{1/m} \tag{5.18}$$

with the evolution equation for $h$:

$$h = h_0 \cdot \left( 1 - \frac{s(t)}{s^*} \right)^{\nu} \tag{5.19}$$

Here $s^*$ is saturation resistance, $h_0$ and $\nu$ are material constants. For plane strain compression experiments, the better fit was obtained by the isotropic strain hardening model with hardening parameters as follows:

$$s_0 = s_{th} = 90\,\text{MPa}; \quad s^* = 320\,\text{MPa}; \quad h_0 = 60\,\text{MPa}; \quad \nu = 2$$

where $h_0$ and $s_0$ are initial values of the state variables $h$ and $\bar{s}$ respectively. Comparison of predicted and measured stress-strain curves are presented in Figs. 5-43 and 5-44. One can see that numerical prediction is very close to actually observed data. Anyhow, computational results demonstrate that the texture evolution is the main mechanism of the magnesium strain hardening. Texture evolution has a strong tendency to align the $< c >$ crystallographic axis along the compressive stress direction or normal to the rolling plane. Our numerical experiments demonstrated that twinning $\{10\bar{1}2\} < \bar{1}011 >$ is the most important mechanism of texture evolution. If we suppressed twinning activities by adding the pyramidal $< c + a >$ slip system $\{11\bar{2}2\} < \bar{1}\bar{1}23 >$ (Morozumi et al. [1975]) in the model instead the "isotropic" term, the tendency of grains to align is very weak and full reorientation of crystals from fiber texture $\{10\bar{1}0\}$ to fiber texture $\{0001\}$ during 15% of simple compression (as observed in experiments) is impossible[8] However, these $< c + a >$ slip systems may

[8]We did numerical experiments in which isotropic plasticity term was substituted with additional pyramidal $\{11\bar{2}2\} < \bar{1}\bar{1}23 >$ slip systems with slip resistence $s_{<c+a>} = 50MPa$. The twinning was suppressed in this case. Incorporation of these pyramidal slip systems with $s_{<c+a>} = 250MPa$ gives reasonably good prediction of texture evolution and stress-strain curves. However, in this case, accumulated slip shears for these slip systems are significant and the traces of $< c + a >$ pyramidal slips should have been observed in experiments. Results of such kind observations at room temperature are not mentioned in known publications.

play an important role in bounding stress levels. Most probably they are active at elevated temperatures, which case we consider in the next chapter.

## 5.5 Concluding remarks

An elastic-plastic, non-hardening model for plastic deformation of h.c.p. metals deforming by slip and twinning has been developed and implemented in the finite-element program ABAQUS/Explicit (1995).

We performed a series of experiments to measure the stress-strain response and texture evolution of polycrystalline magnesium (magnesium alloy AZ31B) during different modes of deformation to large strain.

The predicted crystallographic textures and stress-strain curves are in good agreement with experimentally observed curves. We emphasize that the main mechanisms of plastic deformation of magnesium at room temperature are basal slip and $\{10\bar{1}2\} < \bar{1}011 >$ twinning. Polycrystalline hardening can be explained mostly by grain reorientation during the deformation process. Our simulations demonstrated that the most important mechanism of fast crystal lattice rotation is mechanical twinning. Finally, we note that the combined theoretical-numerical-experimental study of polycrystalline magnesium presented here is the first of its kind and shows substantial promise for further refinement.

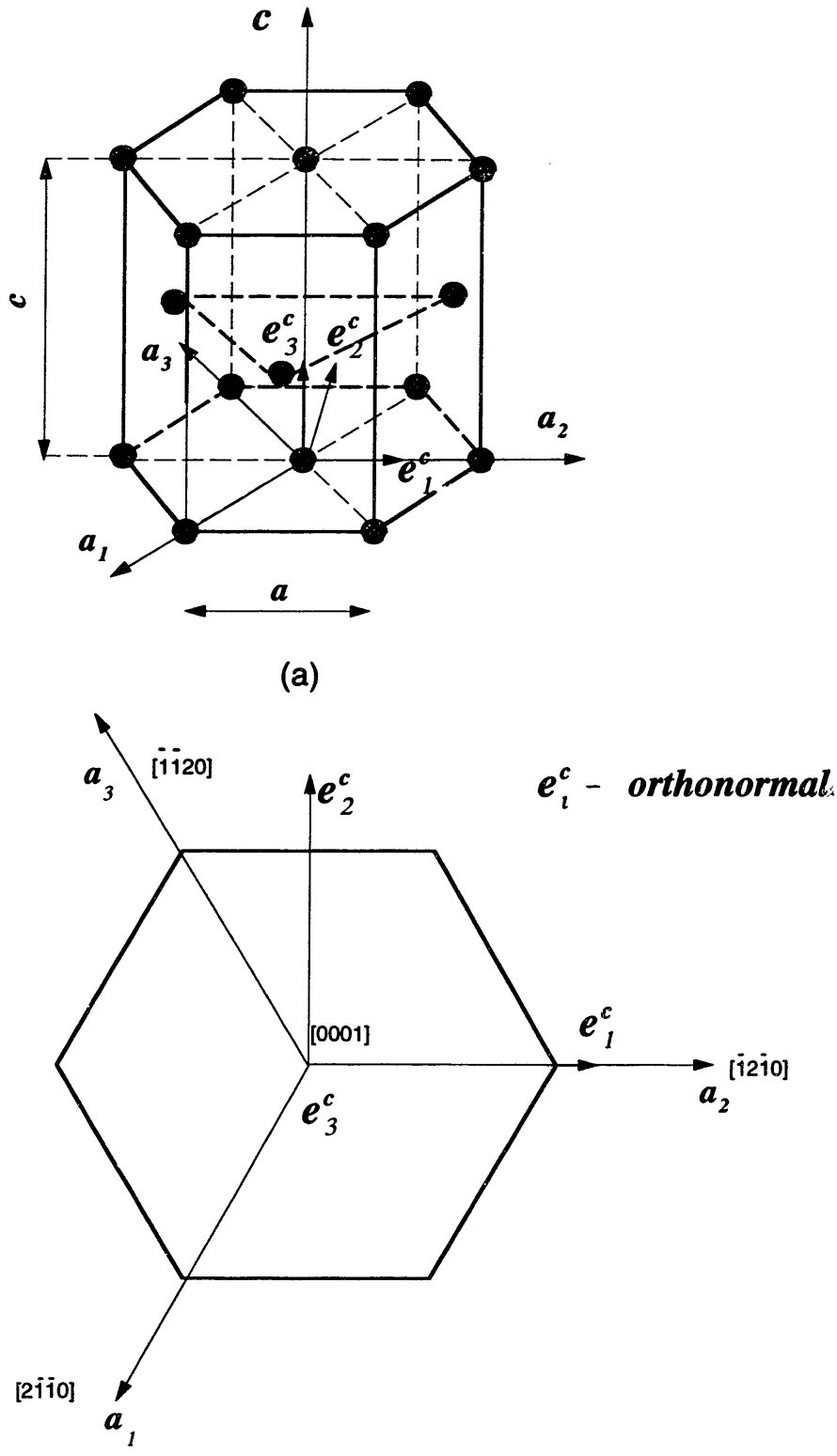


Figure 5-1: Structure of a h.c.p. crystal

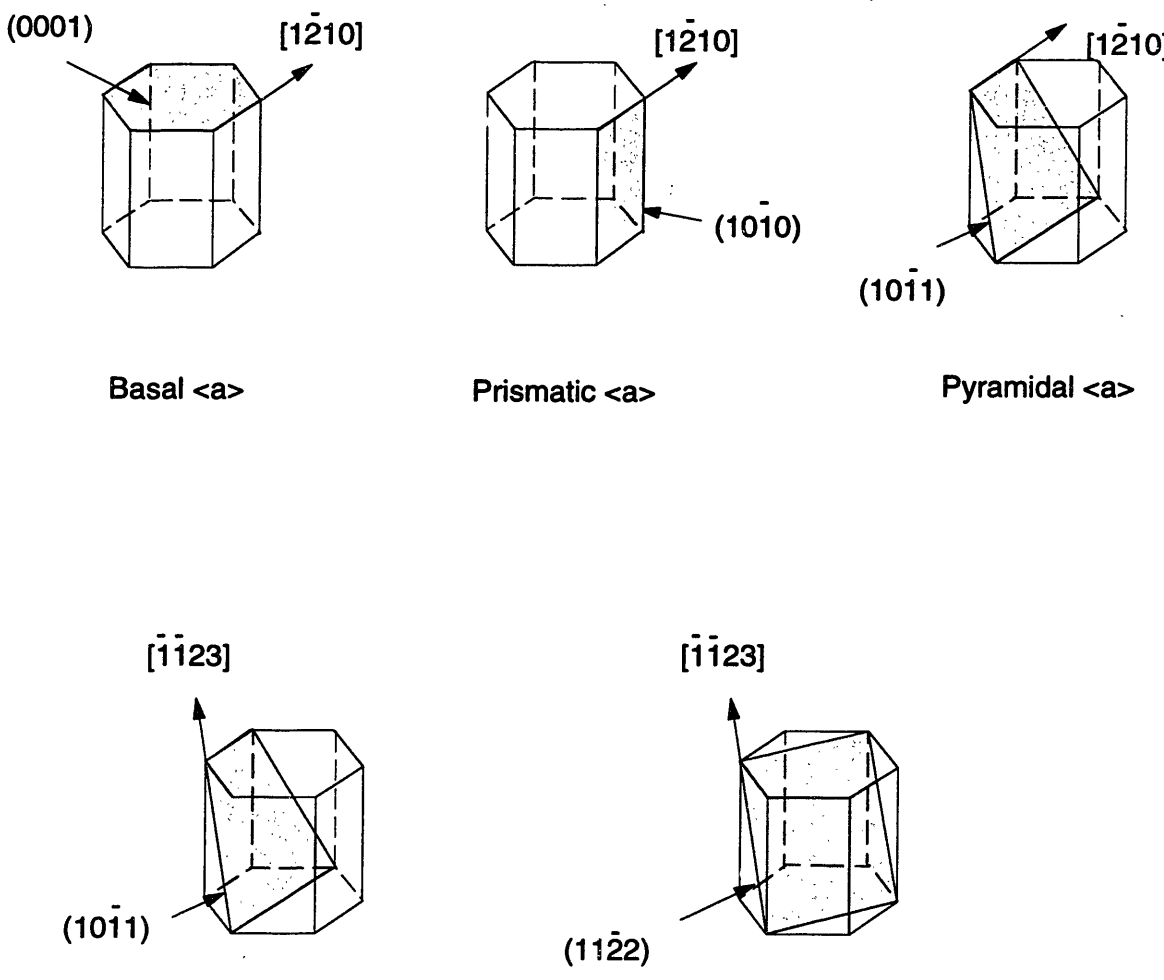


Figure 5-2: Typical slip systems in h.c.p. structures

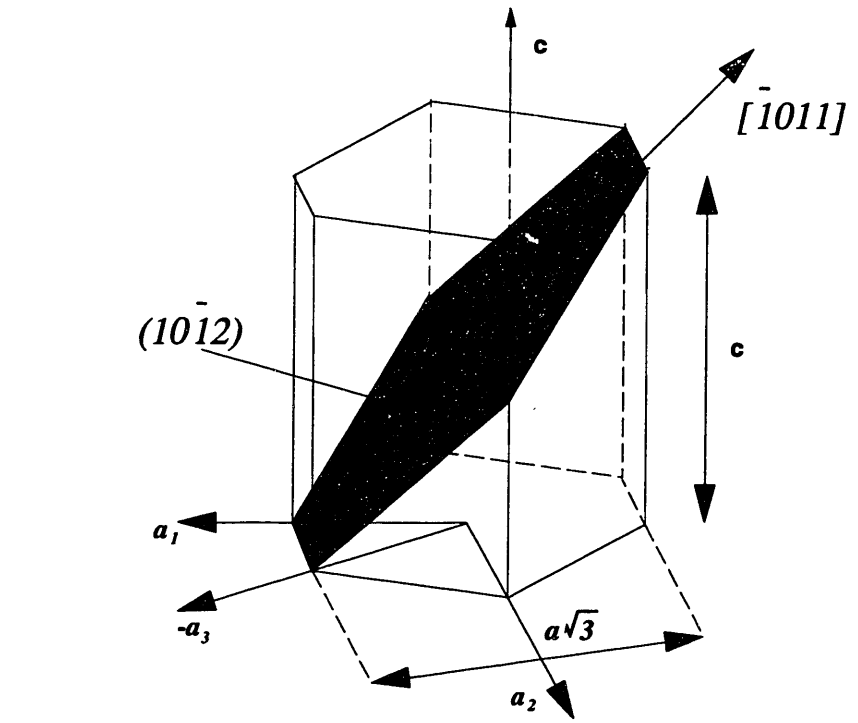


(a)

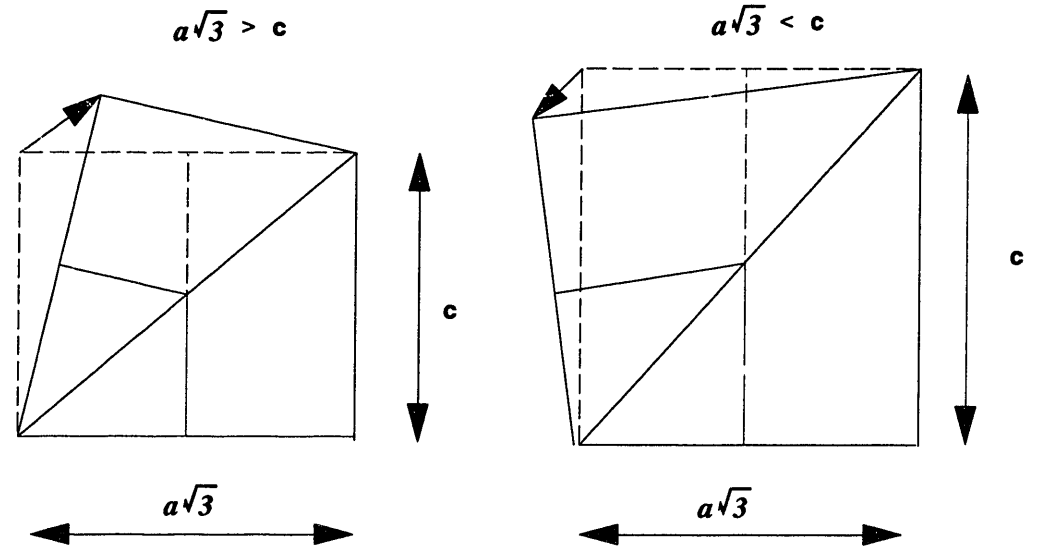


(b) (c)

Figure 5-3: (a) Twinning plane and twinning direction in the h.c.p. structure, (b) the direction of shear is $[\bar{1}011]$ for metals with $c/a < \sqrt{3}$, and twinning occurs under tension parallel to the **c** axis; (c) for $c/a > \sqrt{3}$ the direction of shear is $[10\bar{1}\bar{1}]$, and twinning occurs under compression parallel to the **c** axis (After Hosford [1993]).

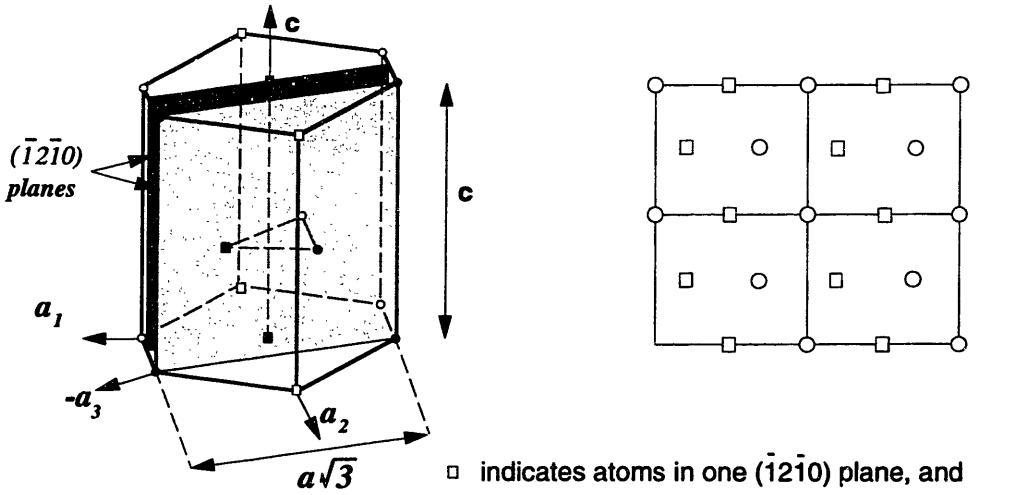


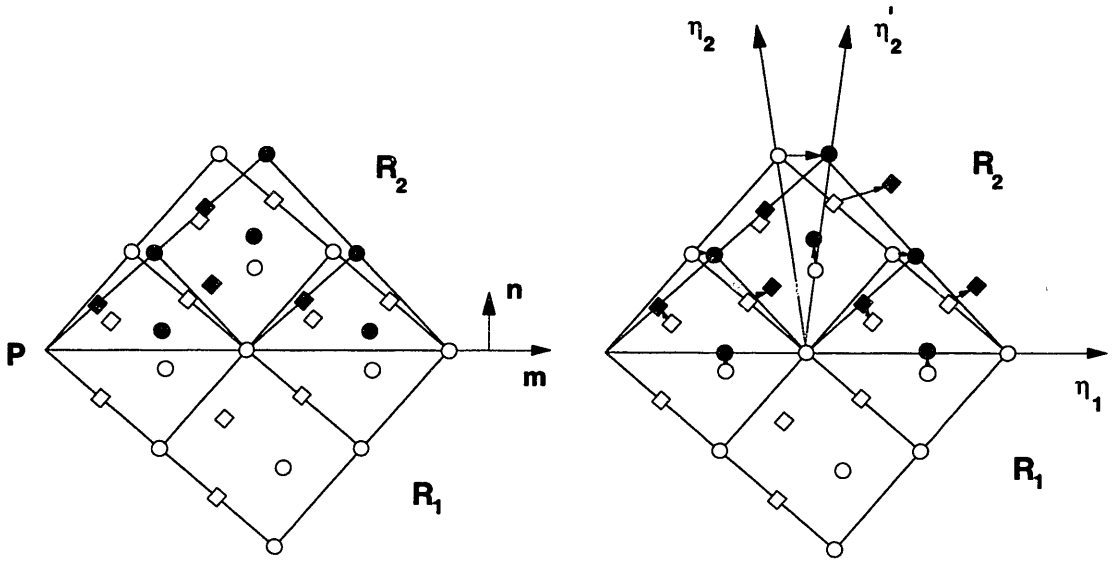


$K_1 = (10\bar{1}2)$ $\eta_1 = [\bar{1}011]$ $\eta_2 = [10\bar{1}1]$

(c) (d)

Figure 5-4: Depiction of twinning in a local region of a h.c.p. crystal. (a) Hexagonal cell showing atom position in adjacent $(\bar{1}2\bar{1}0)$ planes. (b) Plan view of several hexagonal cells in $\{\bar{1}2\bar{1}0\}$ planes. Squares indicate one $(\bar{1}2\bar{1}0)$ plane, and circles show the adjacent $(\bar{1}2\bar{1}0)$ planes. Atoms belonging to the marked planes are shadowed black, others are shadowed white. (c) The atom positions of "parent" and twinned lattices. (d) The necessary movements of the atoms and twinning elements $\{K_1, \eta_1$, and $\eta_2\}$ in h.c.p. magnesium (After Hosford [1993]).

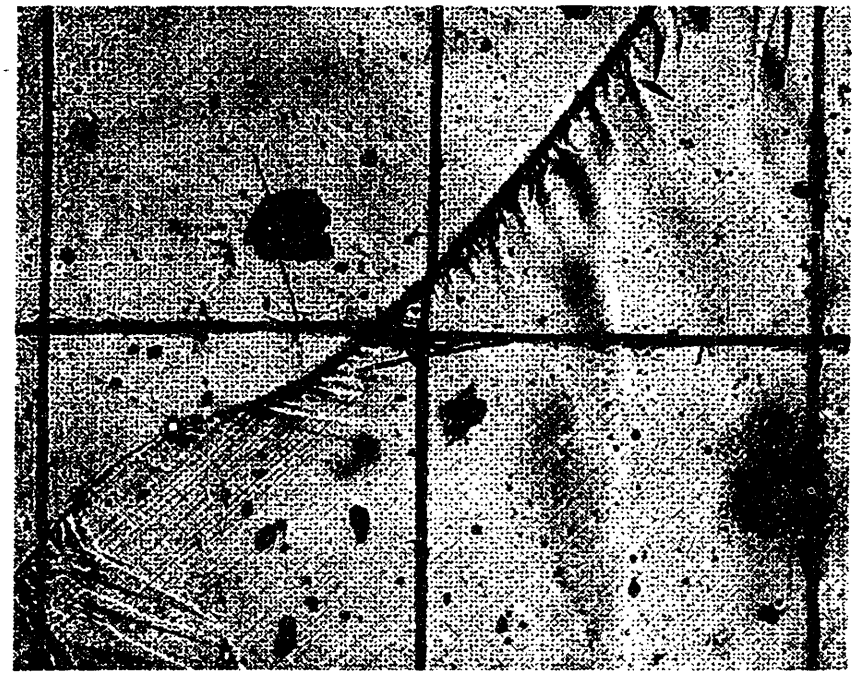

Figure 5-5: Optical micrograph reveals grain boundary shear in magnesium (After Hauser et al. [1954])

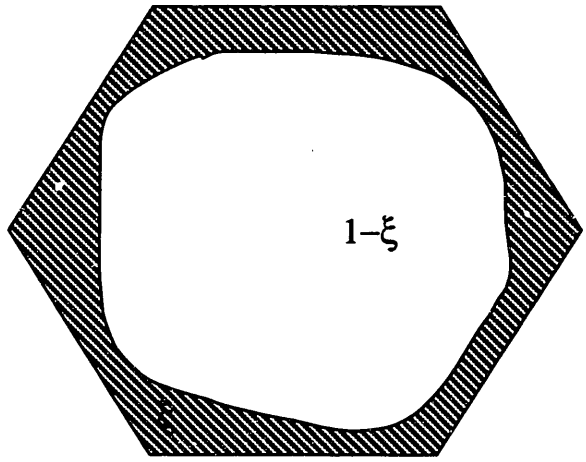


Slip and Twinning

Isotropic part

$$F_t^p(\tau) = 1 + (1-\xi)\Delta\gamma^{\alpha} m^{\alpha} \otimes n^{\alpha} + \xi M$$

$$M = \dot{\varepsilon}_0 \Delta t \left( \frac{\bar{\sigma} - s_{th}}{s} \right)^{\frac{1}{m}} \frac{T^{*'}}{\bar{\sigma}} ; \quad \bar{\sigma} = \sqrt{\frac{3}{2} T^{*'} \cdot T^{*'}}$$

Figure 5-6: Combined crystal plasticity and isotropic plasticity model.

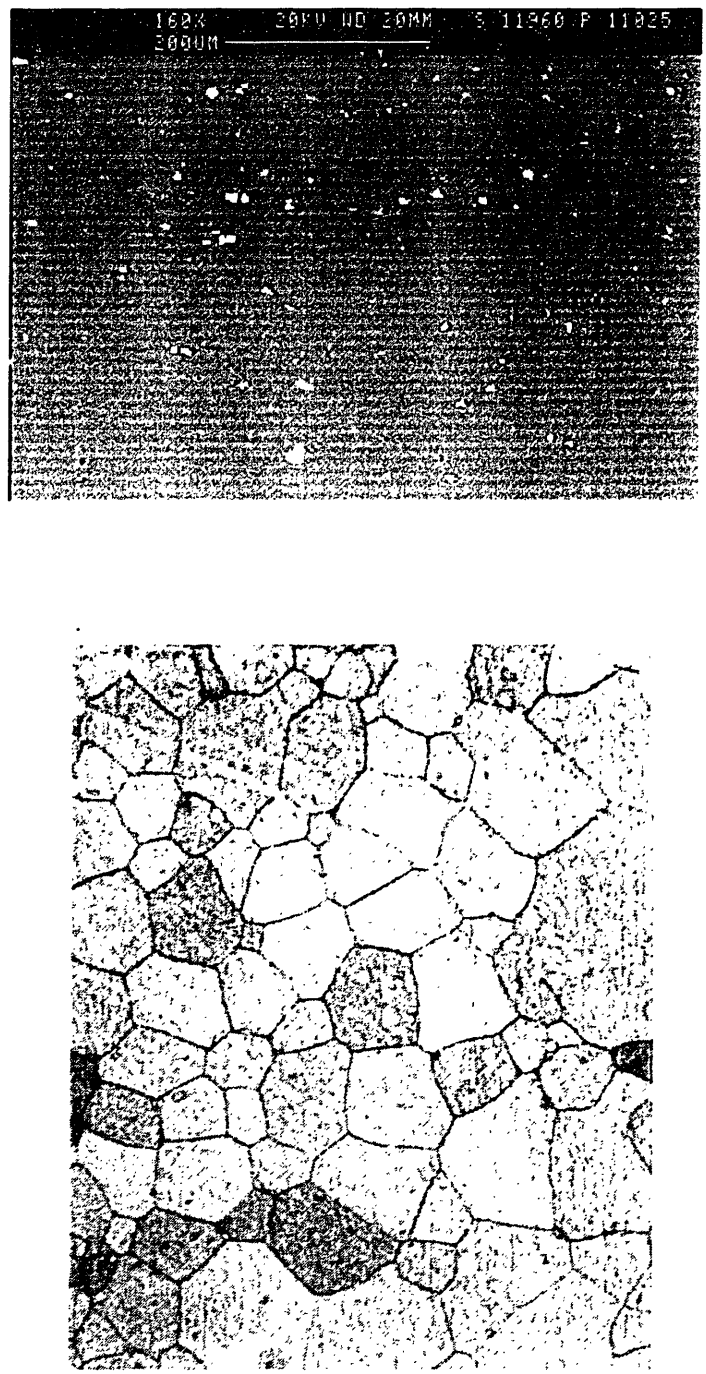


Figure 5-7: Initial state of the magnesium alloy AZ31B. (a) SEM micrograph and (b) optical micrograph with magnification 1000X.

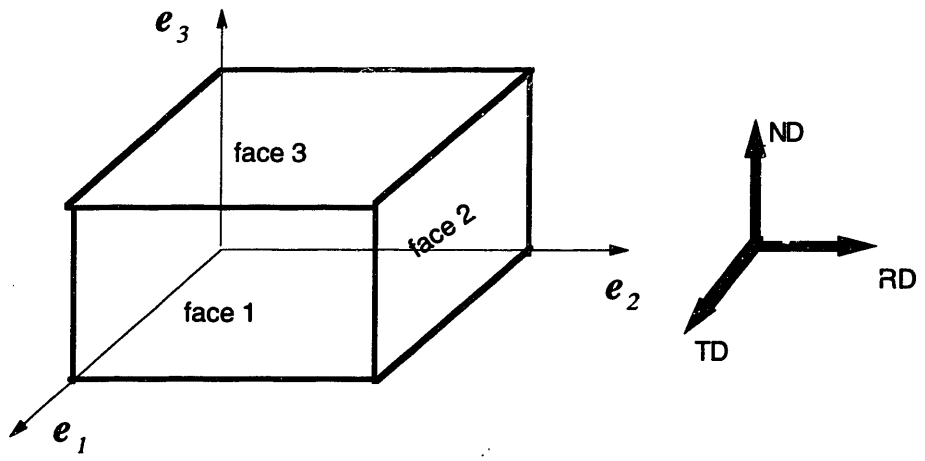


HARDNESS OF EACH FACE (BALL 1/8", 150 kg)

| face | hardness | average |
|---|---|---|
| face 1 | 12 -16 | 14 |
| face 2 | 16 - 20 | 18 |
| face 3 | 28 -33 | 30.5 |

(a)

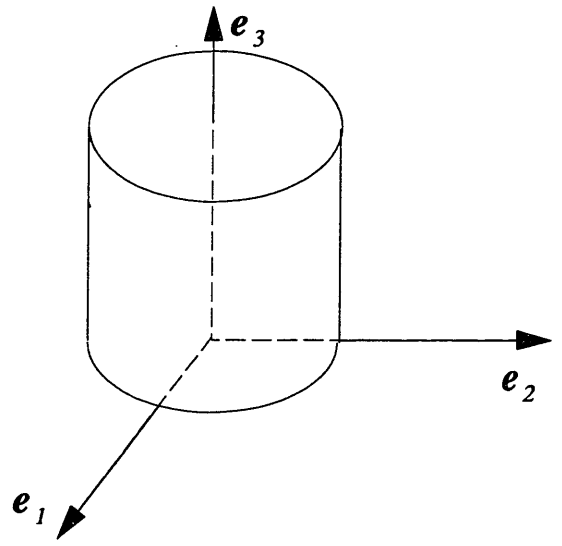


(b)

Figure 5-8: Samples notation for (a) plane strain compression and (b) for simple compression tests.

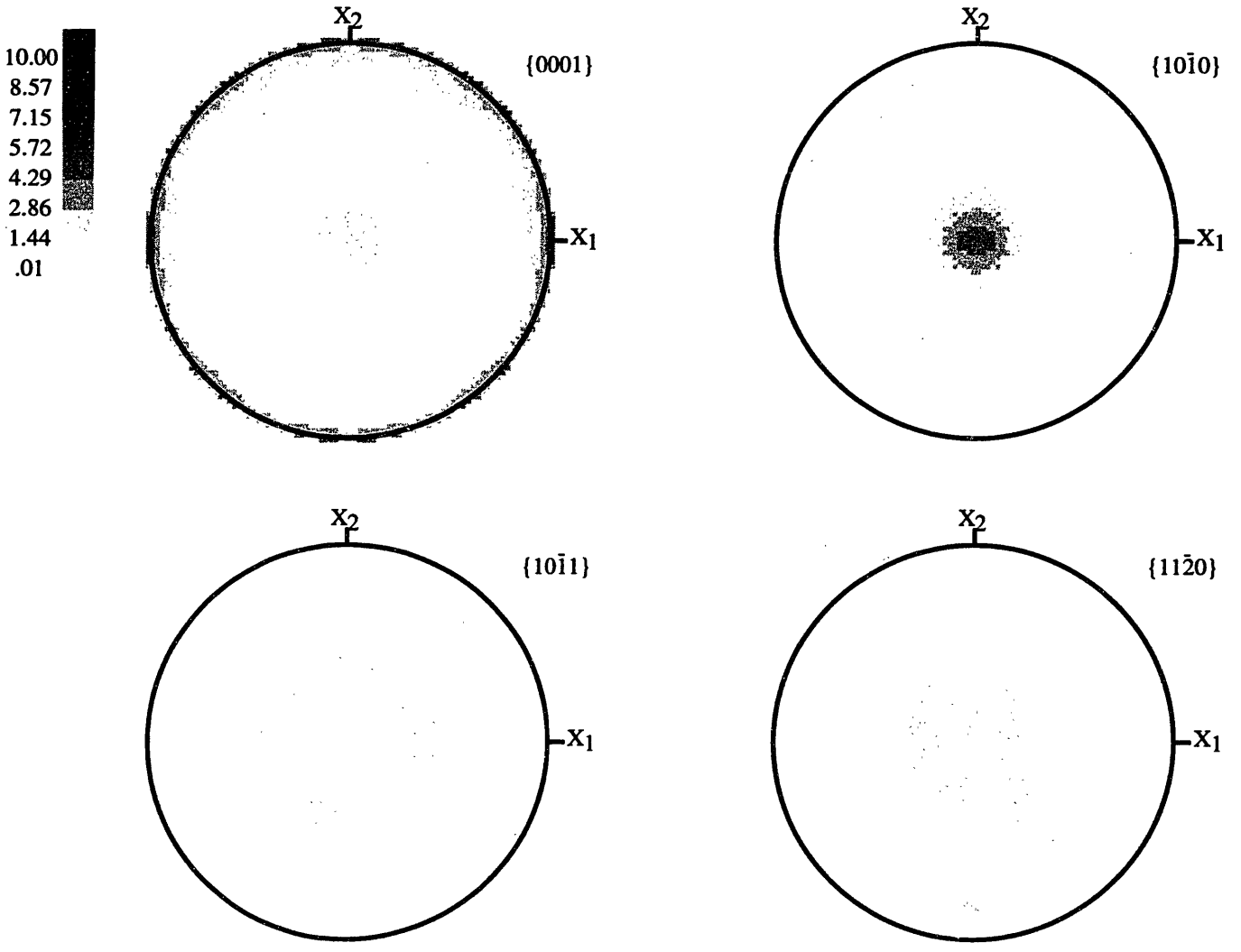


Figure 5-9: Equal area projection pole figures for initial state of rod samples.

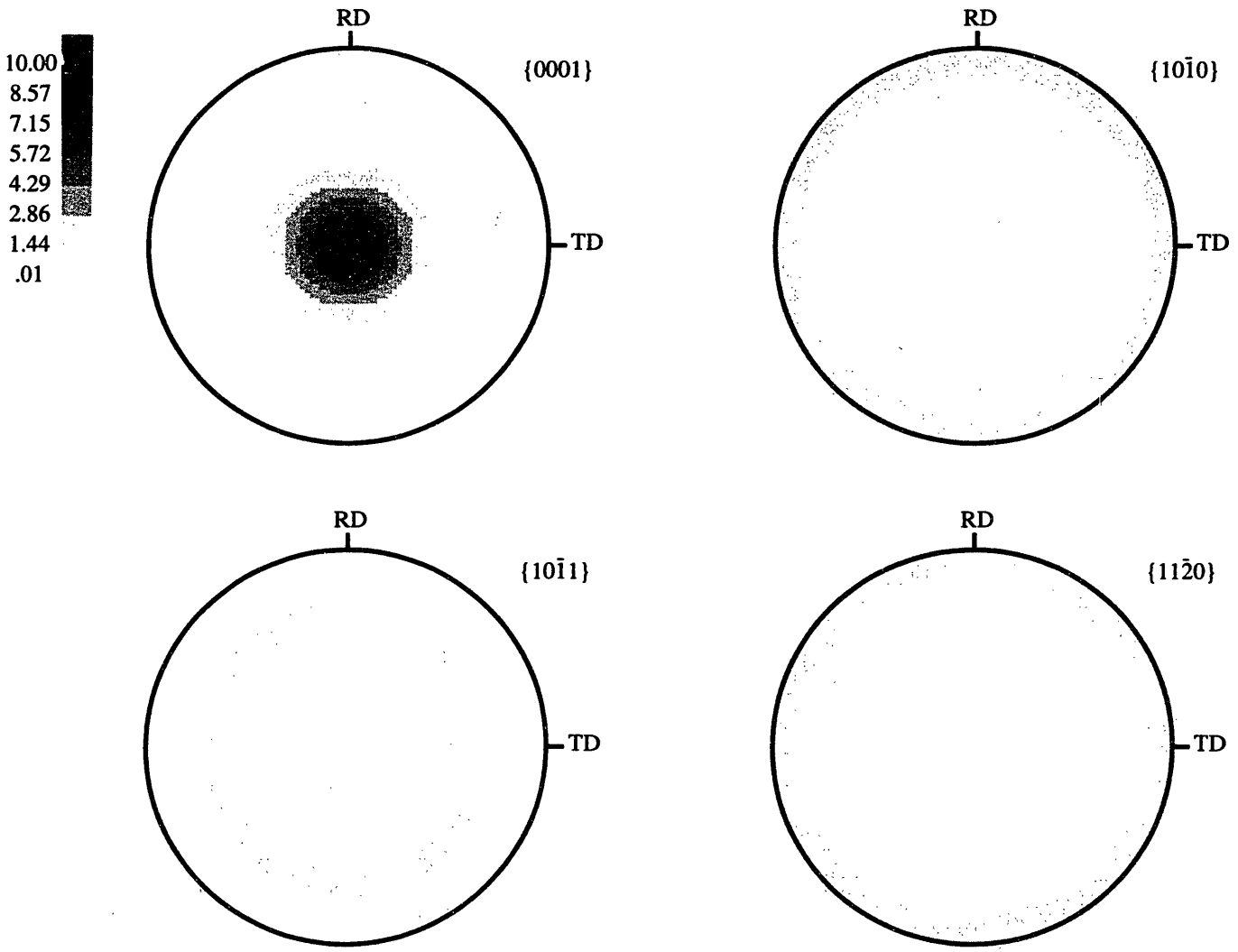


Figure 5-10: Equal area projection pole figures for initial state of plate samples.

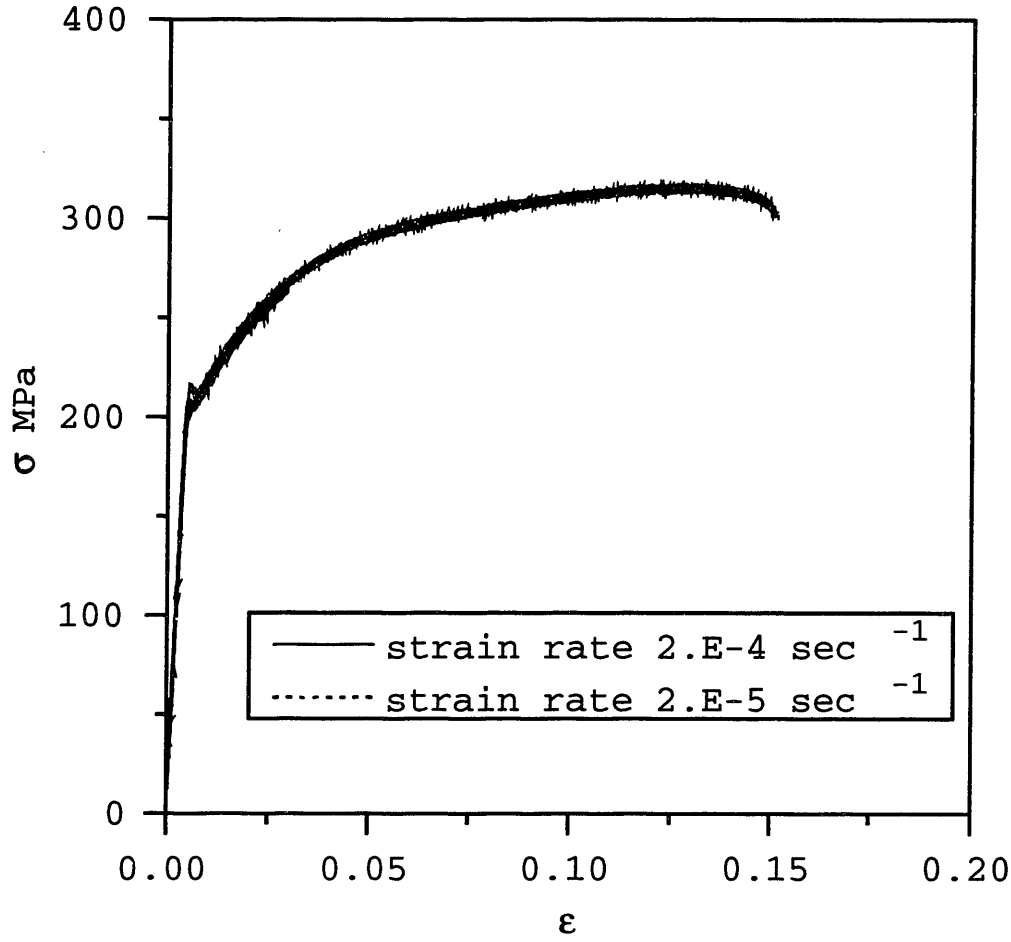


Figure 5-11: Axial true stress $\sigma$ versus axial true strain $\epsilon$ response in simple tension of the magnesium alloy AZ31B at room temperature.

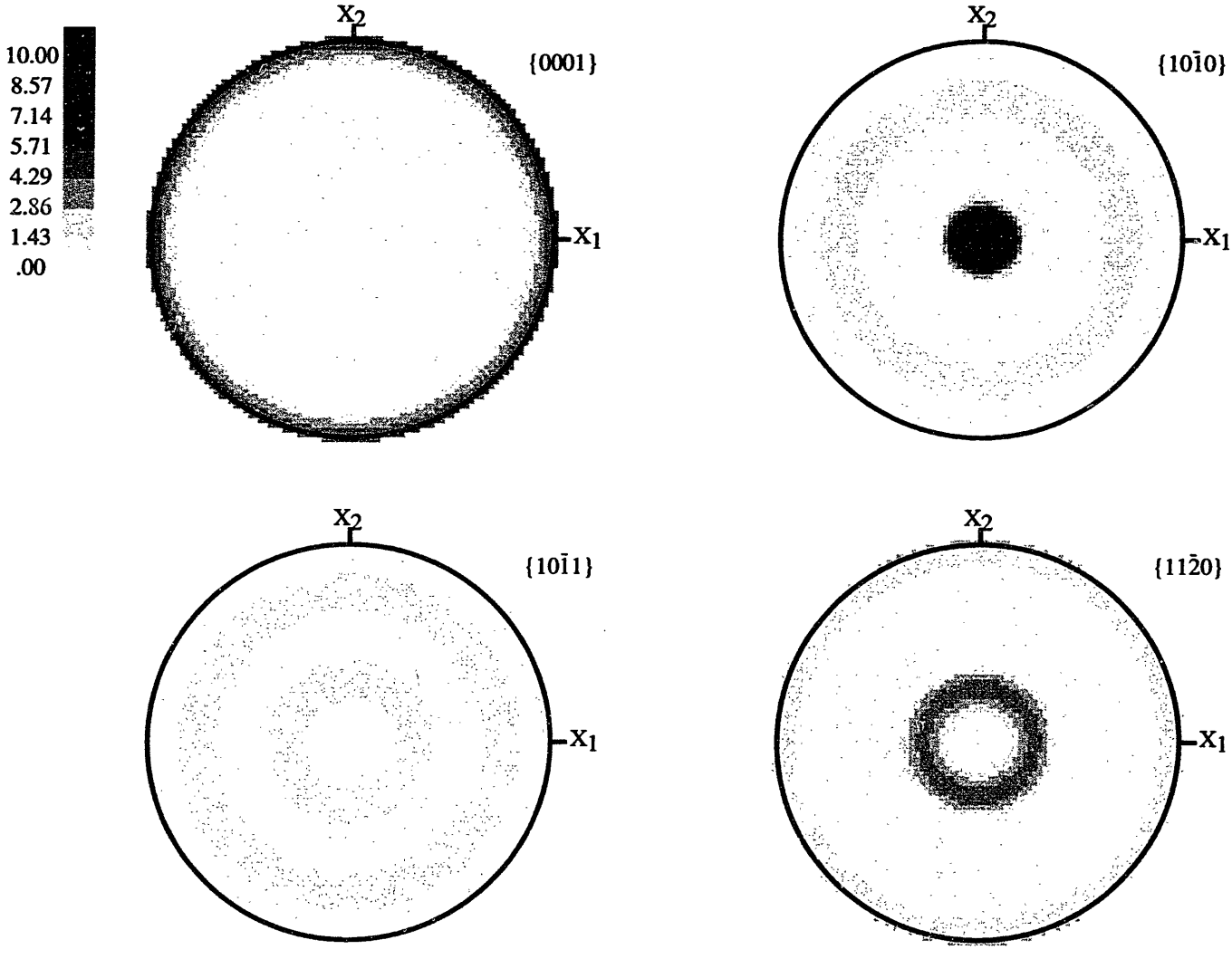


Figure 5-12: Experimental equal area projection pole figures of the magnesium alloy AZ31B deformed in simple tension to $\epsilon = 0.15$.

Figure 5-13: Optical micrograph of the specimen subjected to simple tension to $\epsilon = 0.15$.

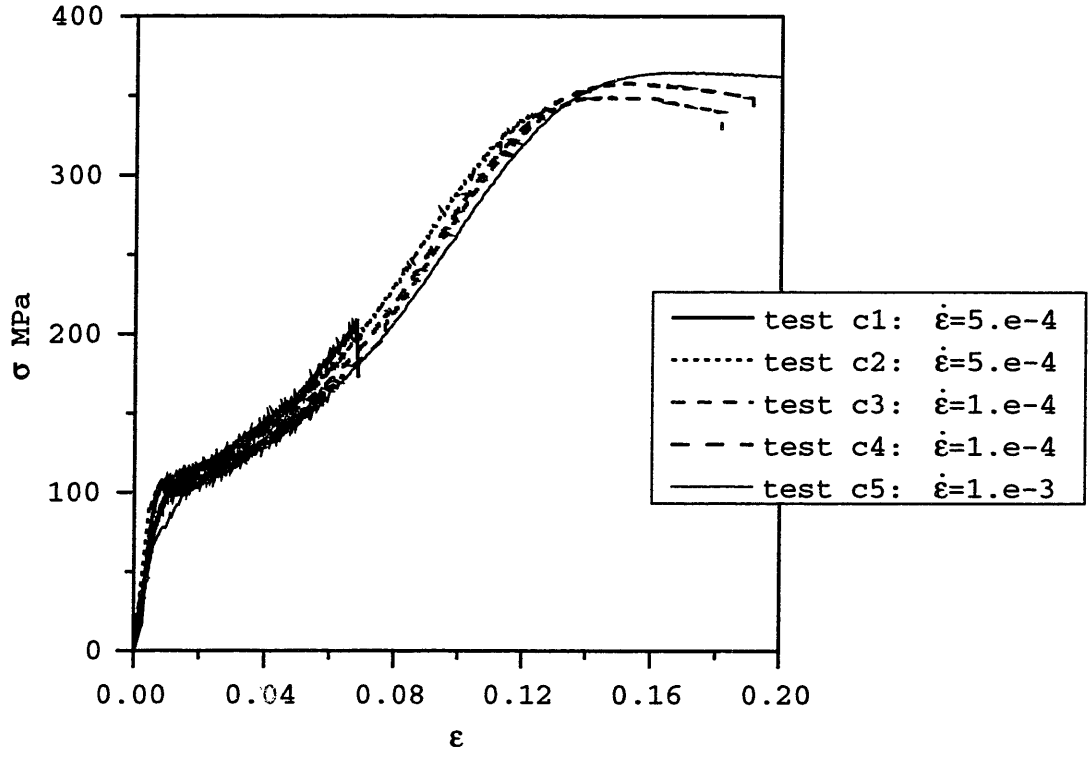


Figure 5-14: Axial true stress $|\sigma|$ versus axial true strain $|\epsilon|$ response in simple compression of the magnesium alloy AZ31B at room temperature.

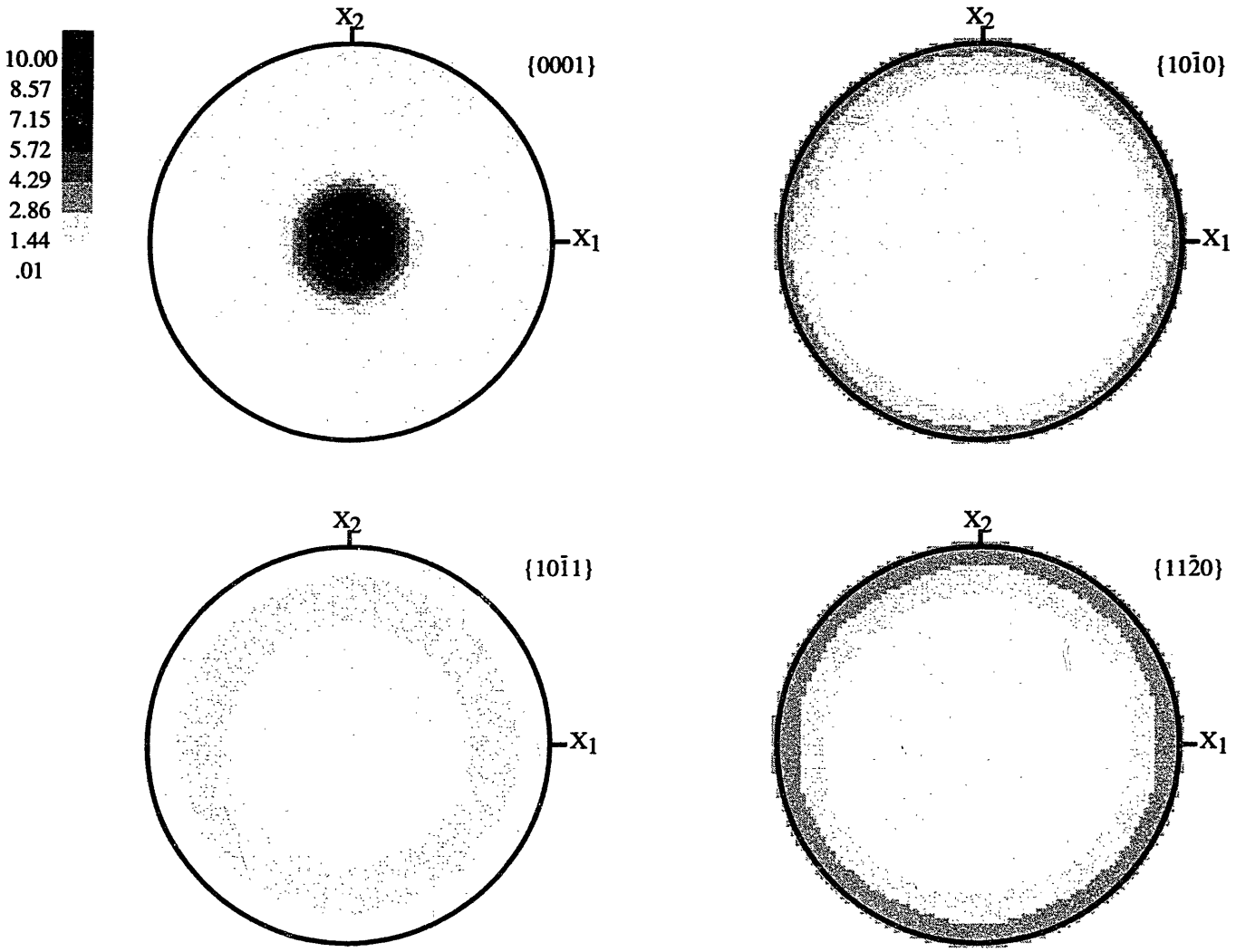


Figure 5-15: Experimental equal area projection pole figures of the magnesium alloy AZ31B deformed in simple compression to $\epsilon = 0.18$.

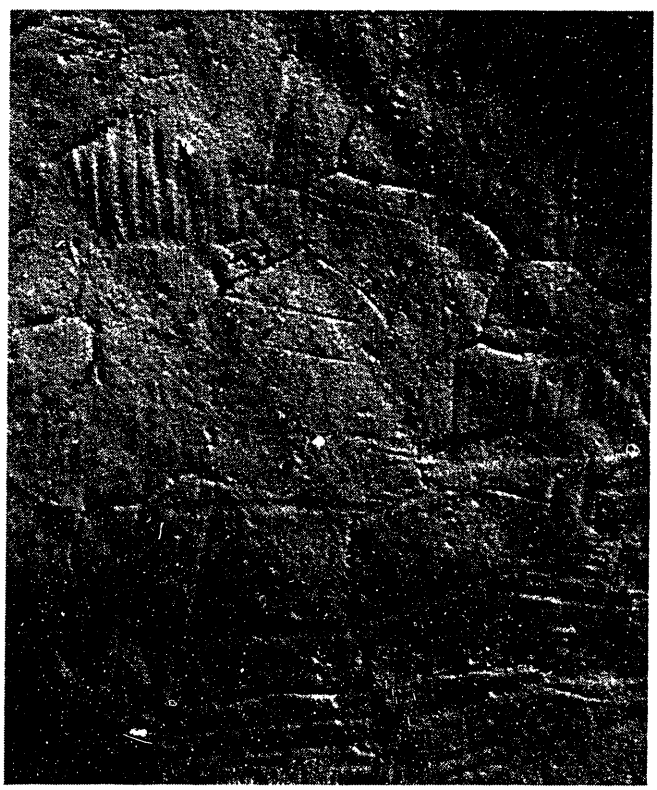

Figure 5-16: Optical micrograph of the specimen subjected to simple compression to $\epsilon = -0.18$.

(a)

(b)

Figure 5-17: Micrographs of the specimens subjected to plane strain compression (a) parallel to the plate normal direction and (b) parallel to plate free direction.

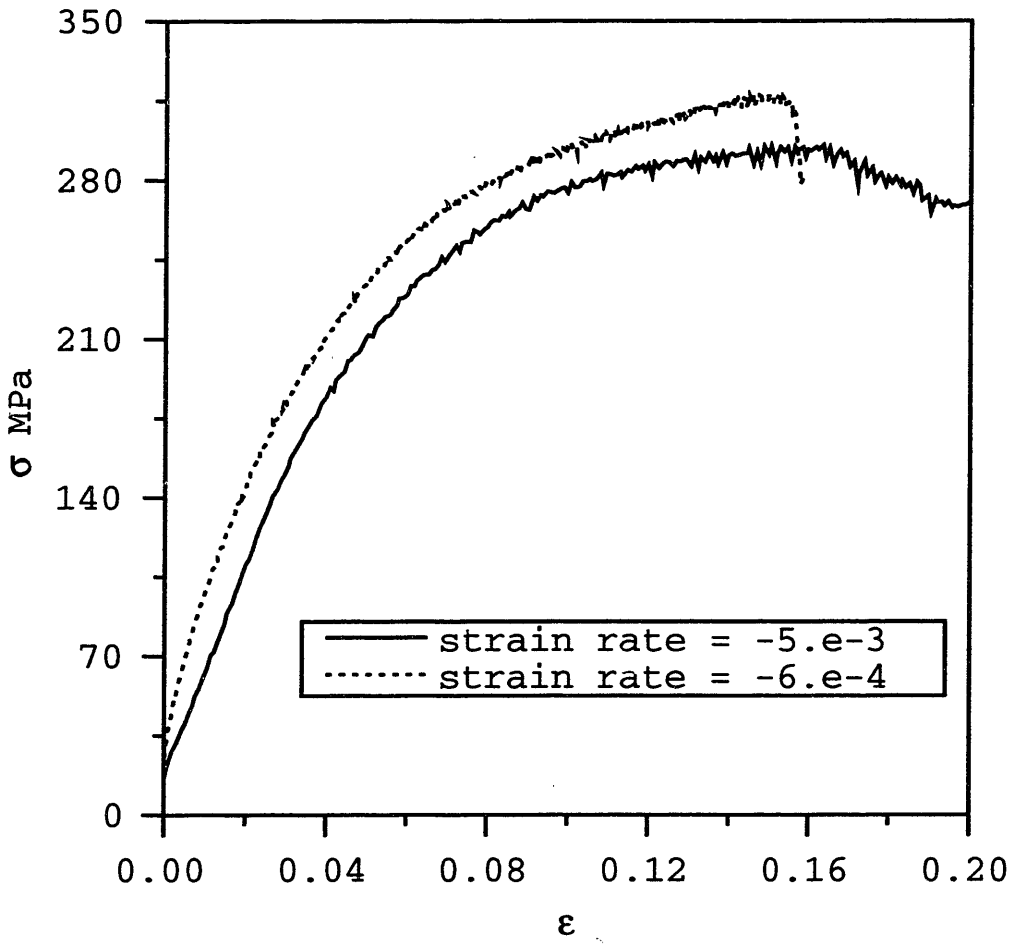


Figure 5-18: True stress $\sigma$ versus true strain $\epsilon$ response in plane strain compression parallel to the normal direction of the plate of the magnesium alloy AZ31B at room temperature.

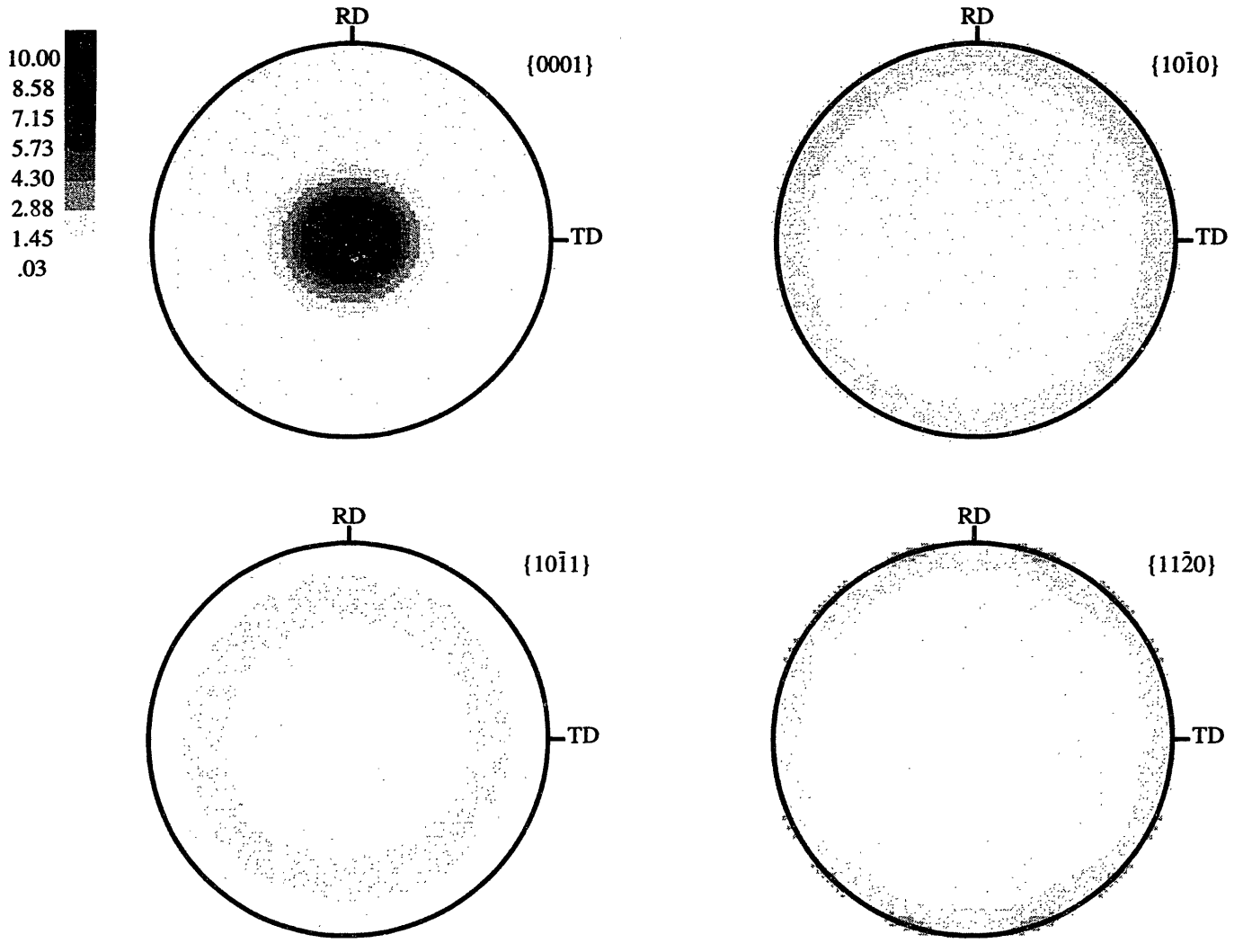


Figure 5-19: Experimental equal area projection pole figures of the magnesium alloy AZ31B deformed in plane strain compression to $\epsilon = -0.18$ parallel to the plate normal direction.

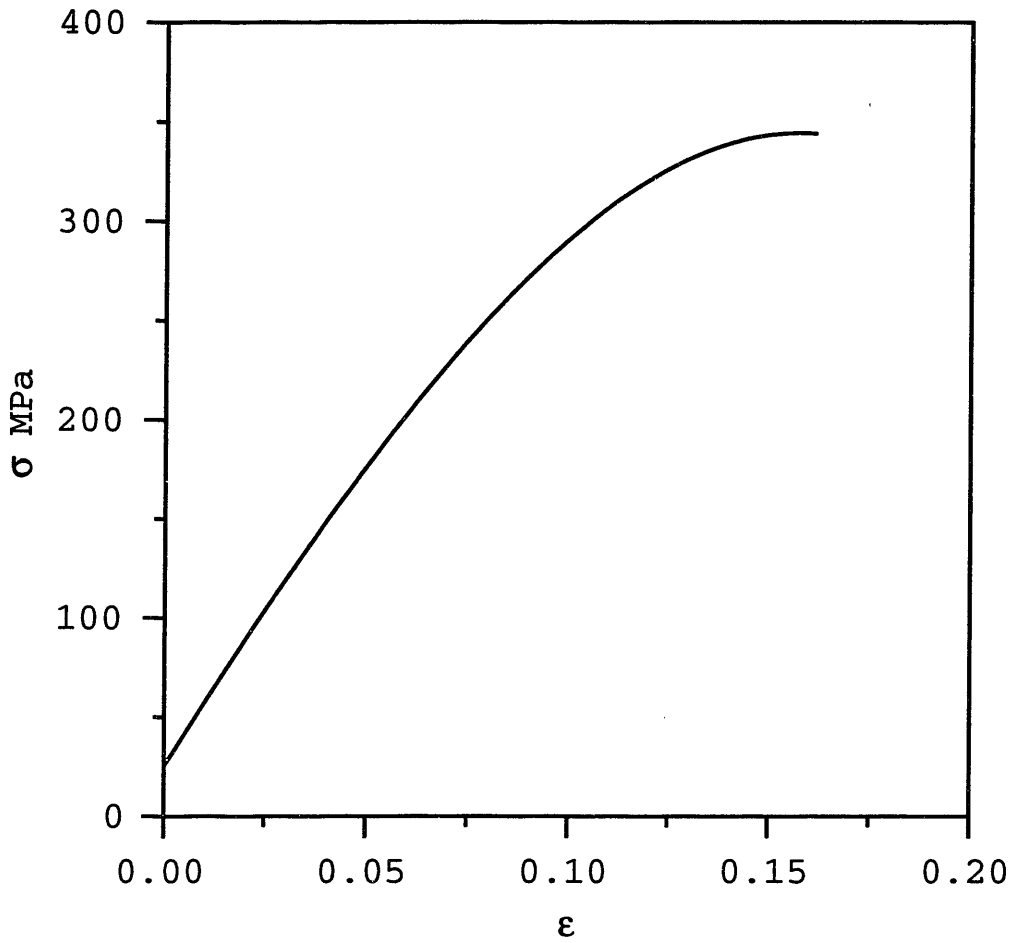


Figure 5-20: True stress $\sigma$ versus true strain $\epsilon$ response in plane strain compression parallel to the rolling plane of the plate and with free direction parallel to the plate transverese direction of the magnesium alloy AZ31B at room temperature.

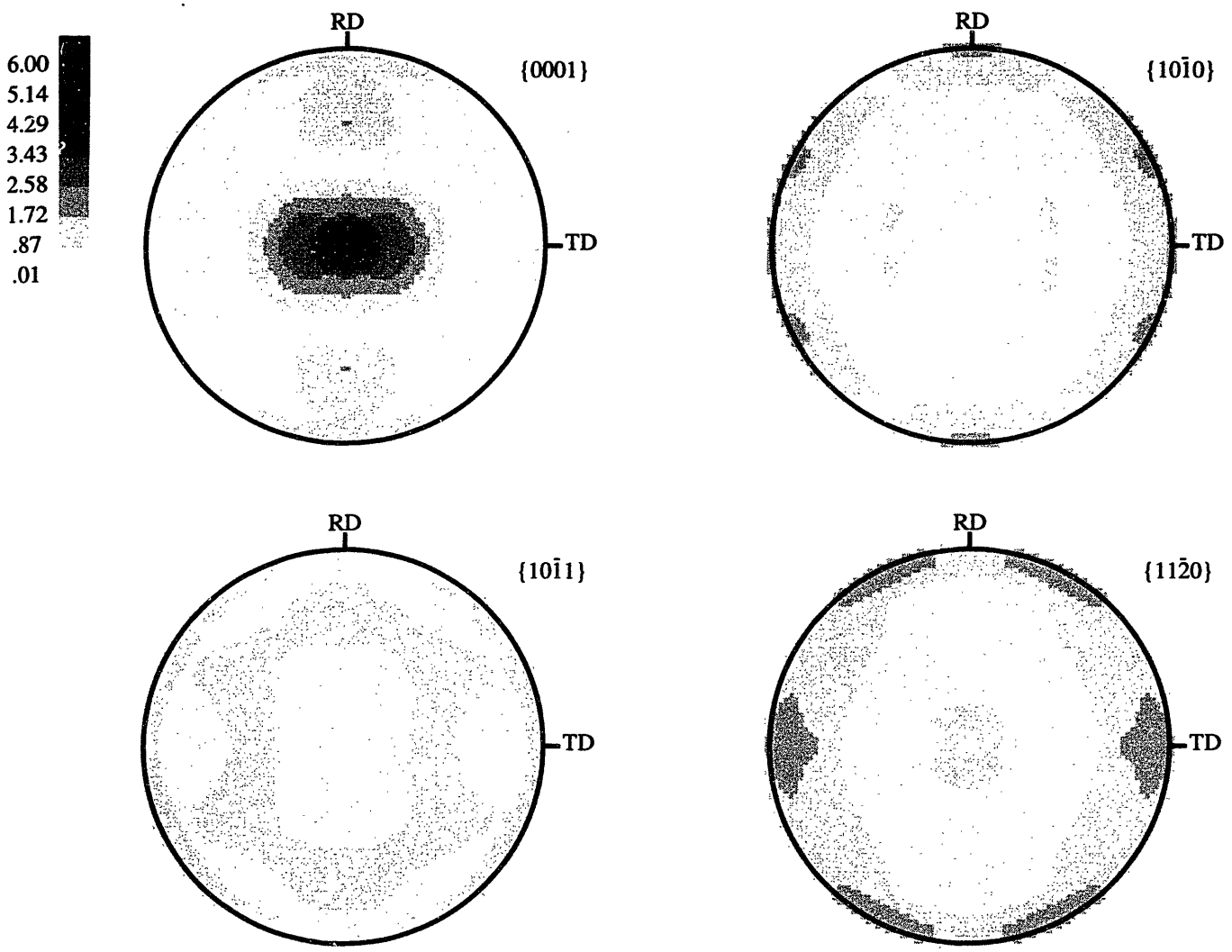


Figure 5-21: Experimental equal area projection pole figures of the magnesium alloy AZ31B deformed in plane strain compression to $\epsilon = -0.2$ parallel to the plate rolling direction with free direction is parallel to the plate transverse direction.

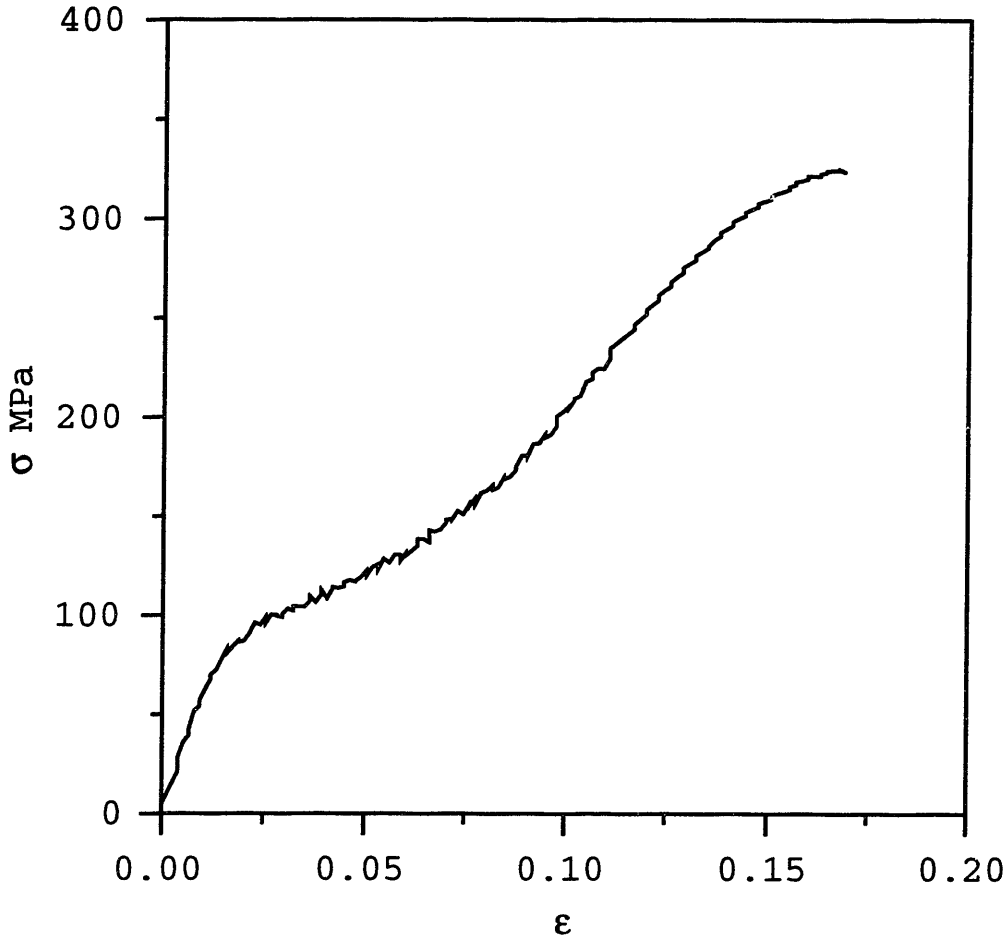


Figure 5-22: True stress $\sigma$ versus true strain $\epsilon$ response in plane strain compression parallel to the plate rolling direction with free direction parallel to the plate normal direction of the magnesium alloy AZ31B at room temperature.

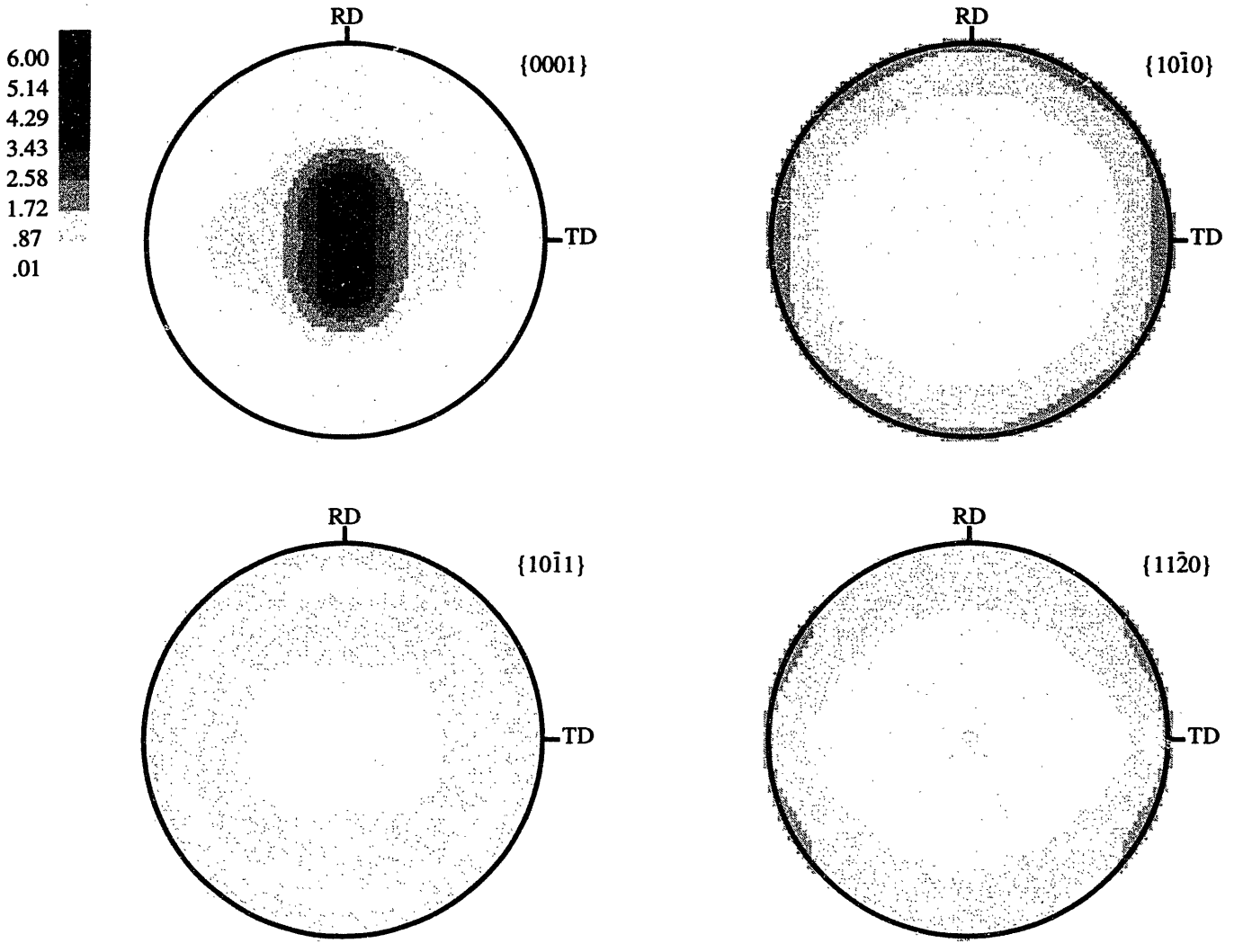


Figure 5-23: Experimental equal area projection pole figures of the magnesium alloy AZ31B deformed in plane strain compression to $\epsilon = -0.2$ parallel to the plate rolling direction with free direction parallel to the plate normal direction.

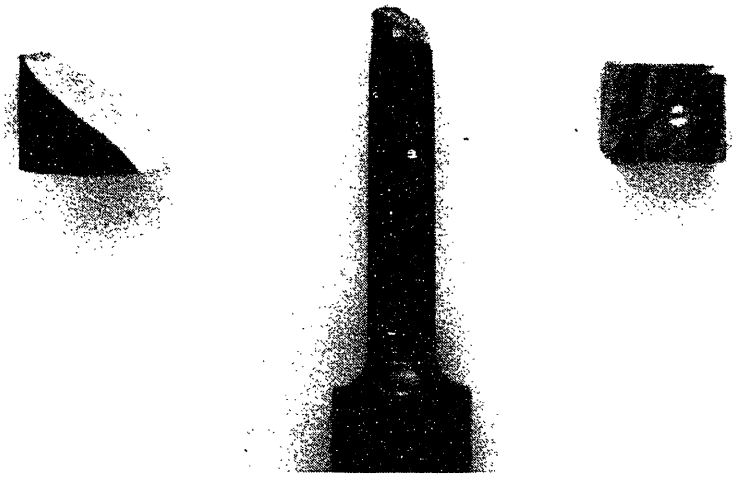

Figure 5-24: Fractured specimens after simple compression, simple tension, and plane strain compression tests (from left to right) at room temperature.

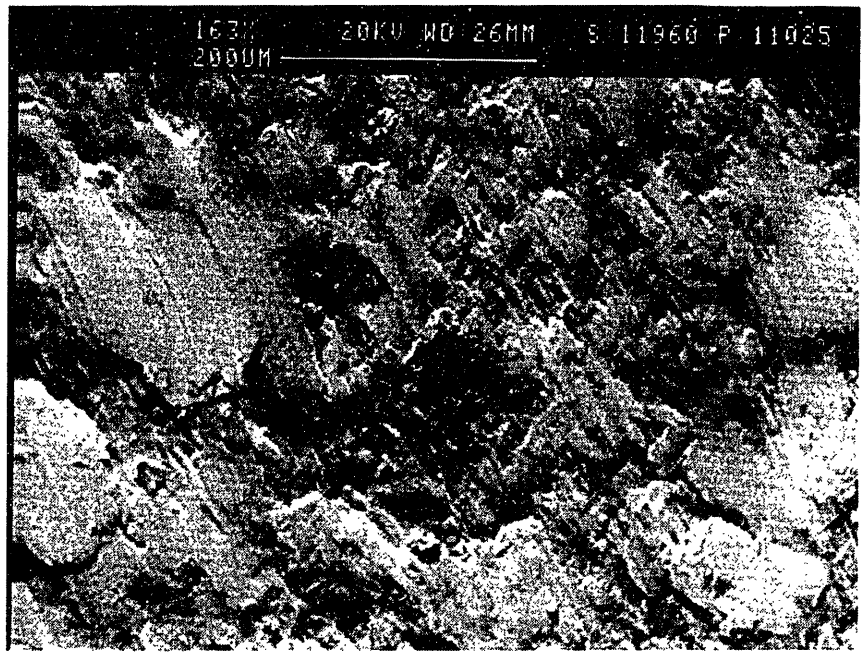


(a)

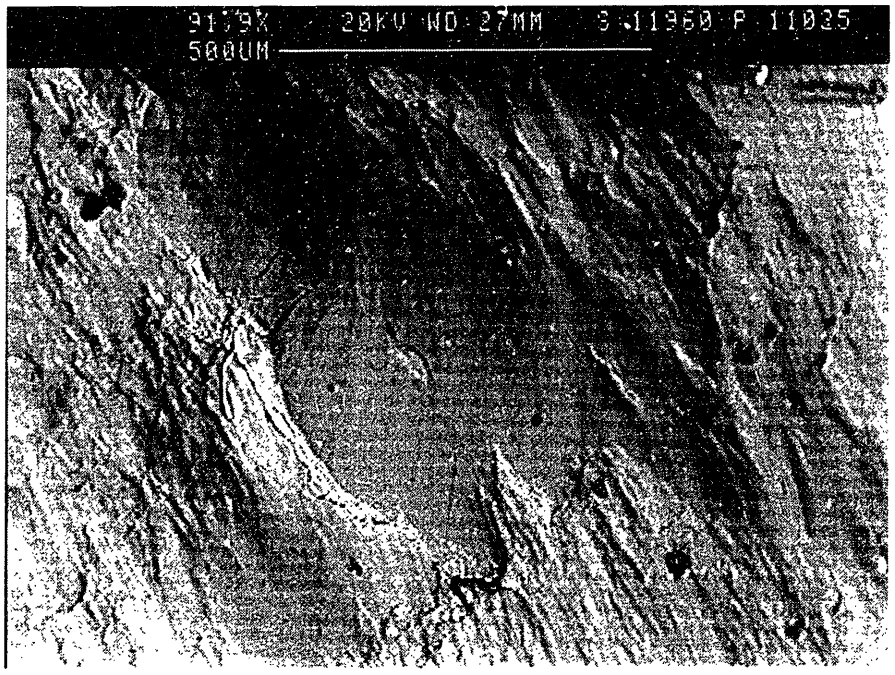


(b)

Figure 5-25: Fractographes of the magnesium alloy AZ31B after (a) simple tension and (b) simple compression at room temperature.

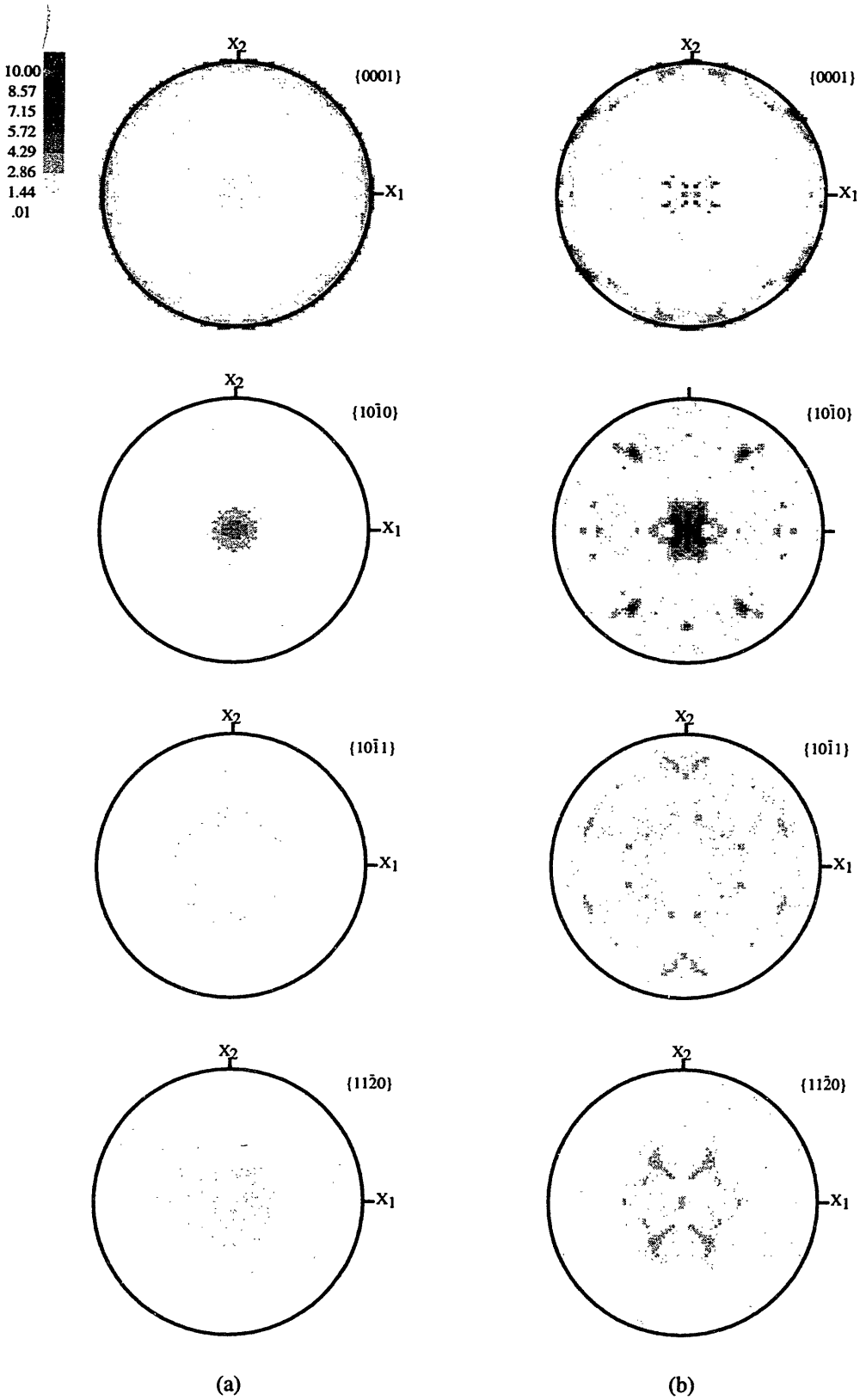


Figure 5-26: Initial texture of magnesium rod. (a) Experimentally measured and (b) numerically represented using 343 grain orientations.

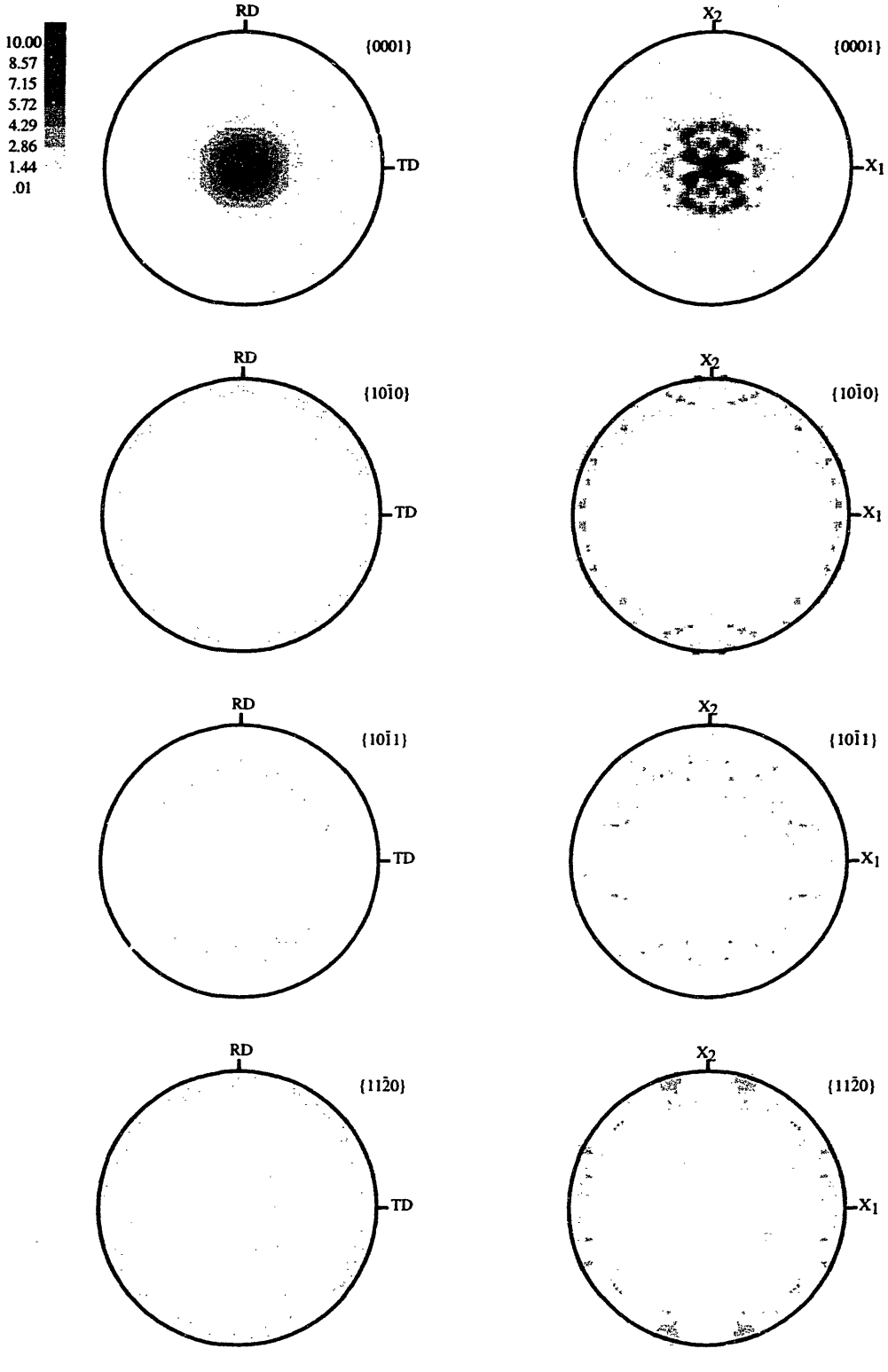


Figure 5-27: Initial texture of magnesium plate. (a) Experimentally measured and (b) numerically represented using 343 grain orientations.

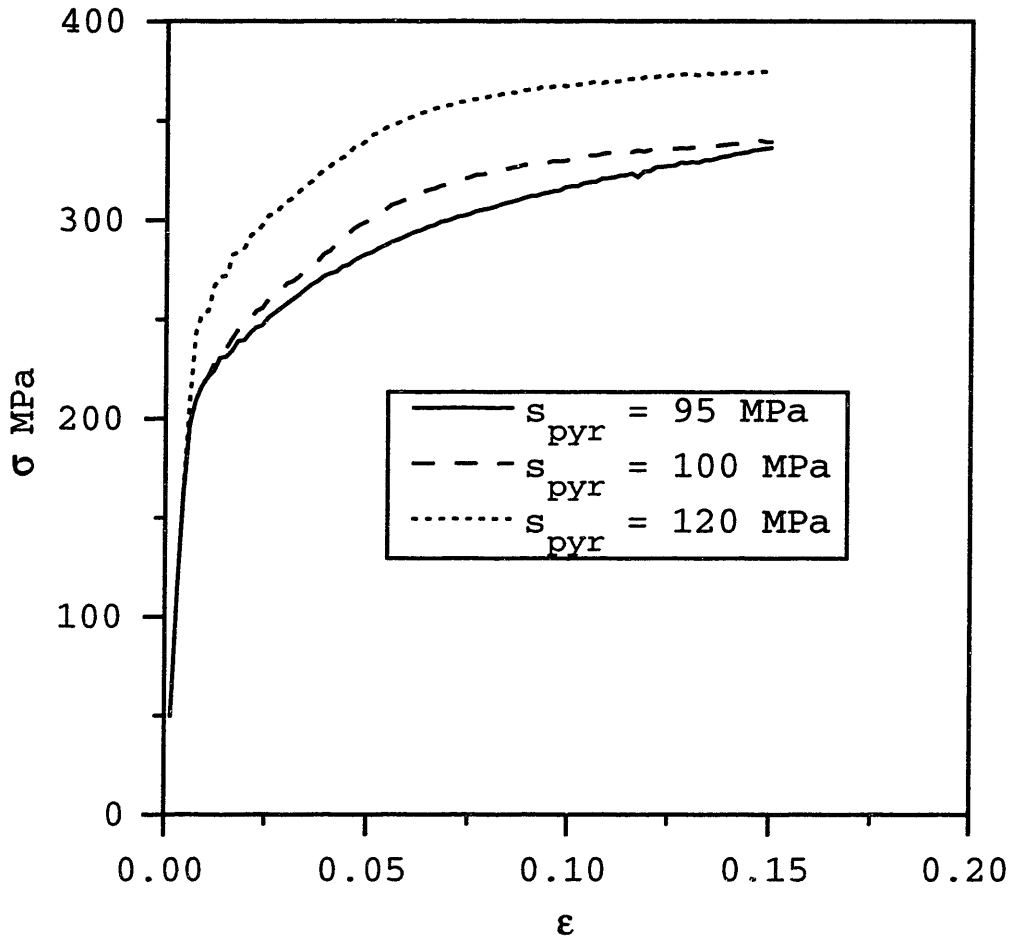


Figure 5-28: Stress-strain curves in simple tension calculated for different values of $s_{pyramidal\ <a>}$.

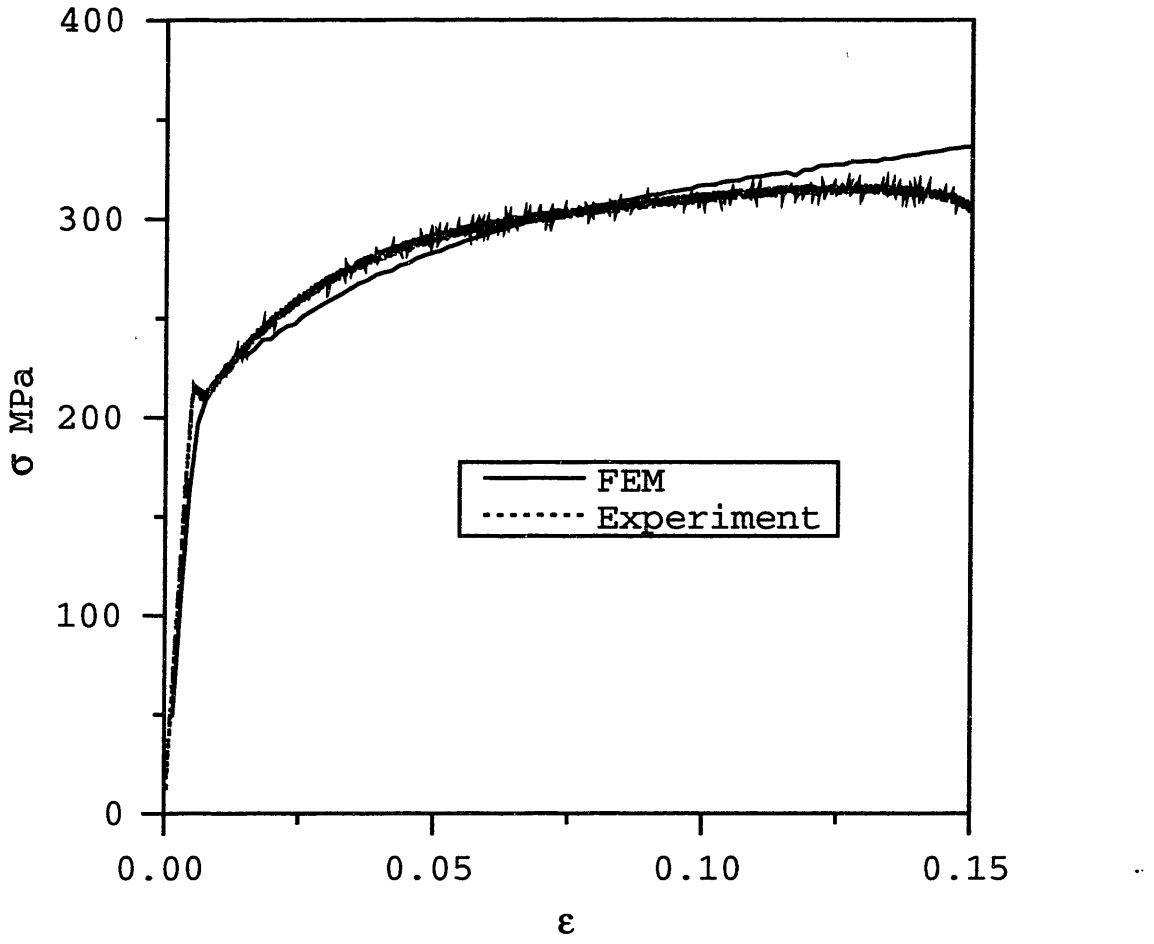


Figure 5-29: Experimentally measured and FEM predicted axial true stress $\sigma$ versus axial true strain $\epsilon$ response in simple tension of the magnesium alloy AZ31B at room temperature.

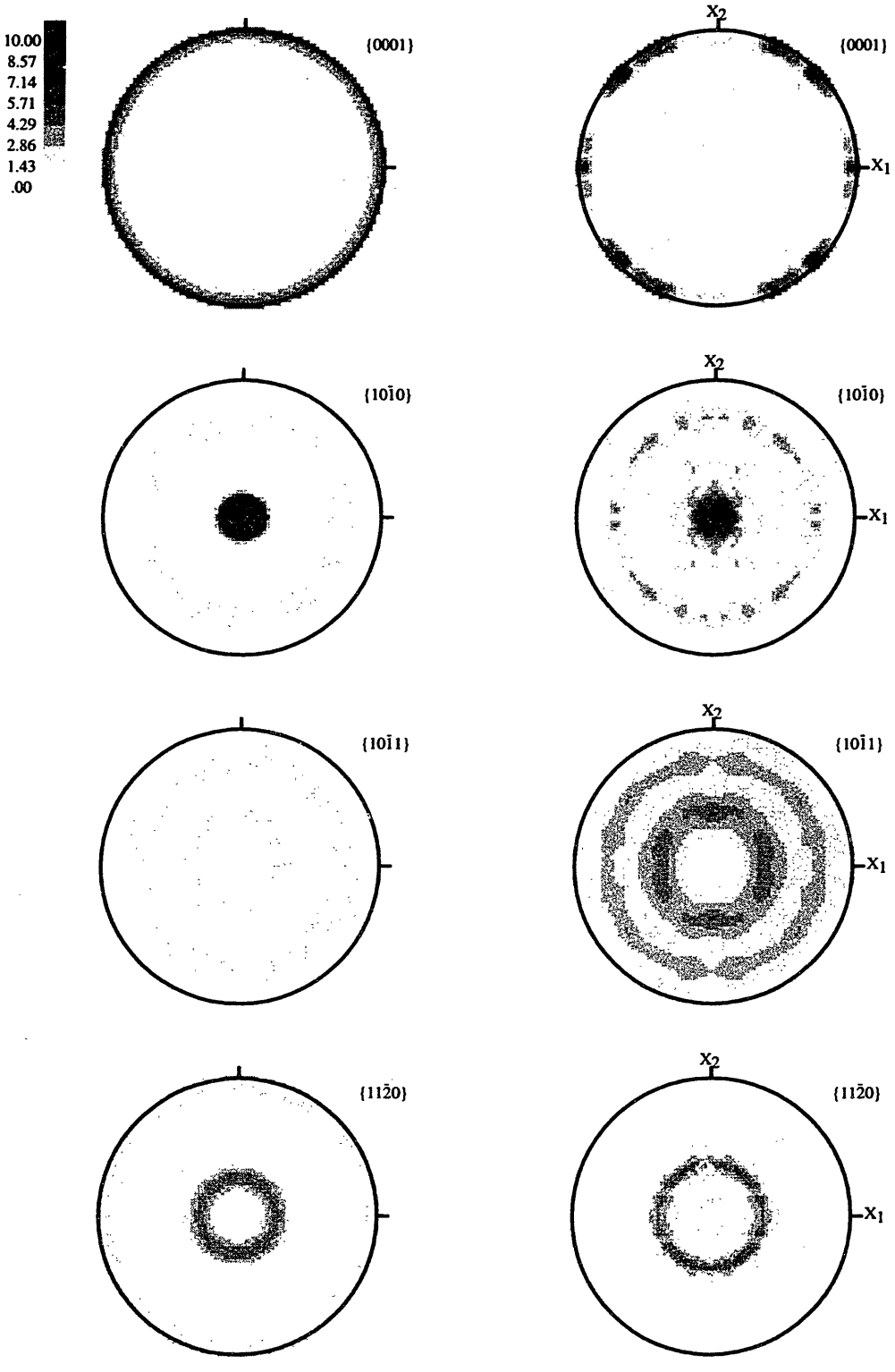


Figure 5-30: Experimentally measured (a) and FEM calculated (b) pole figures after simple tension of the magnesium alloy AZ31B to 15%.

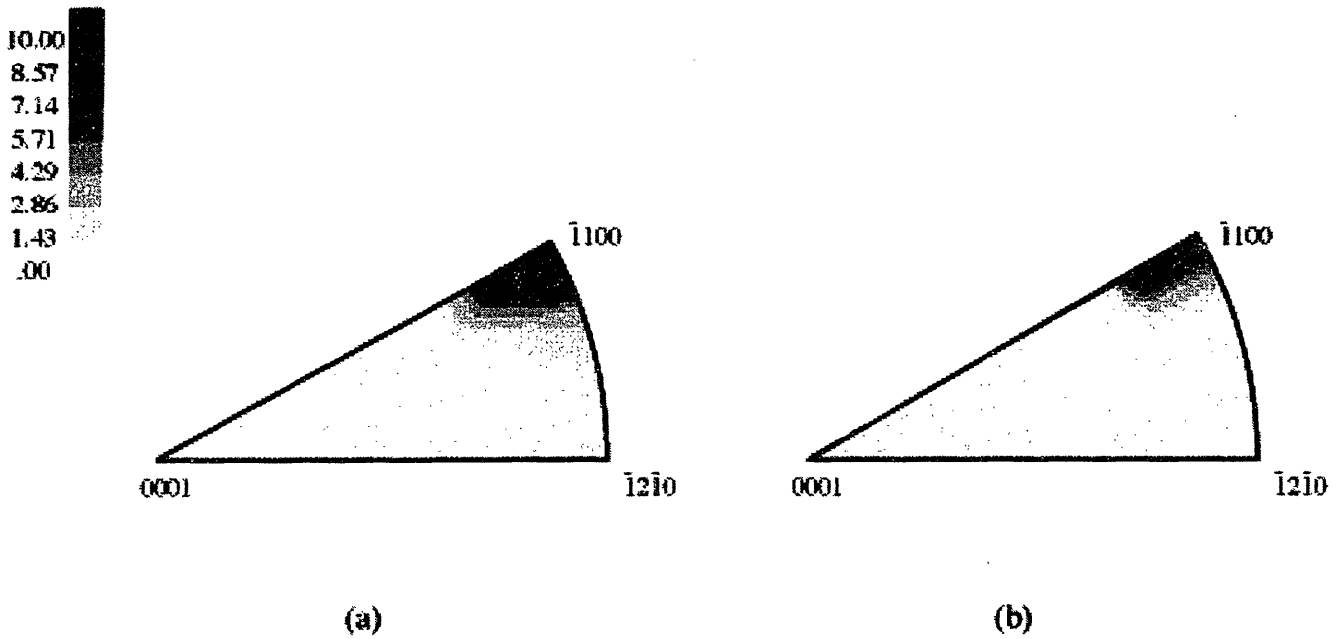


Figure 5-31: Experimentally measured (a) and FEM calculated (b) inverse pole figures after simple tension of the magnesium alloy AZ31B to 15%.

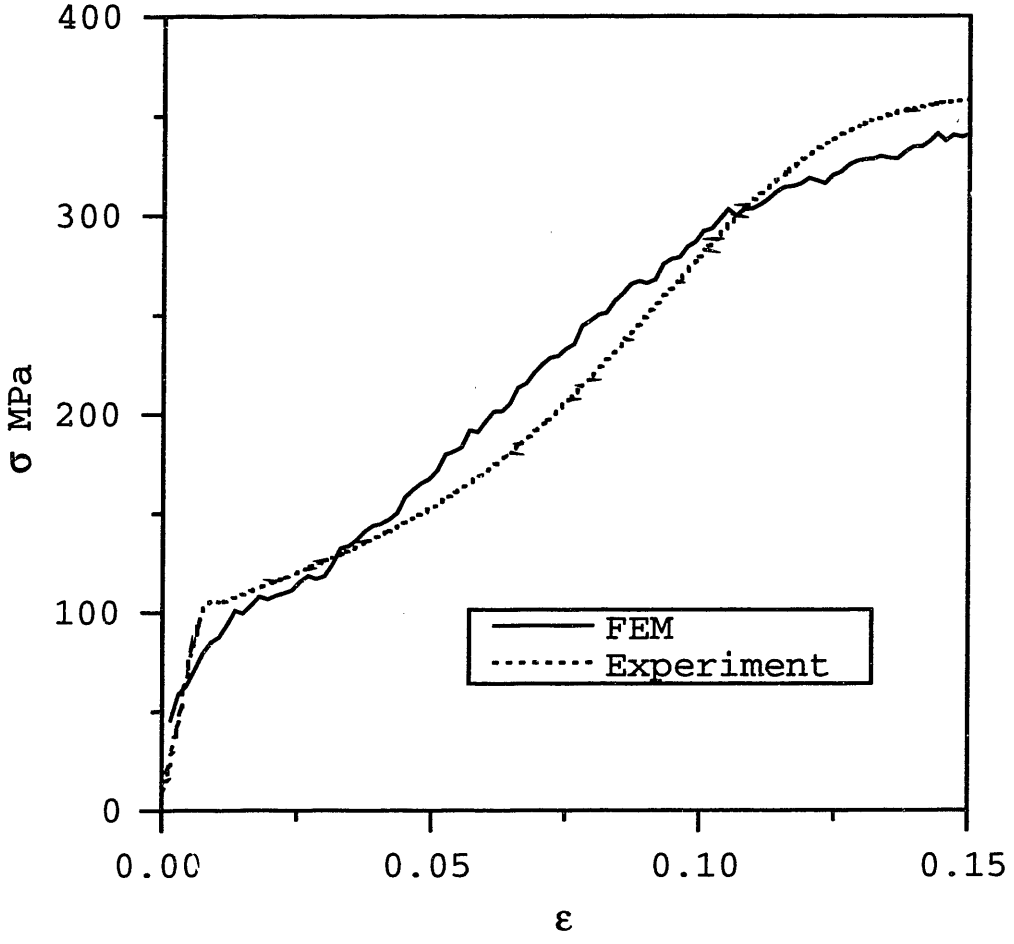


Figure 5-32: Experimentally measured and FEM predicted axial true stress $\sigma$ versus axial true strain $\epsilon$ response in simple compression of the magnesium alloy AZ31B at room temperature.

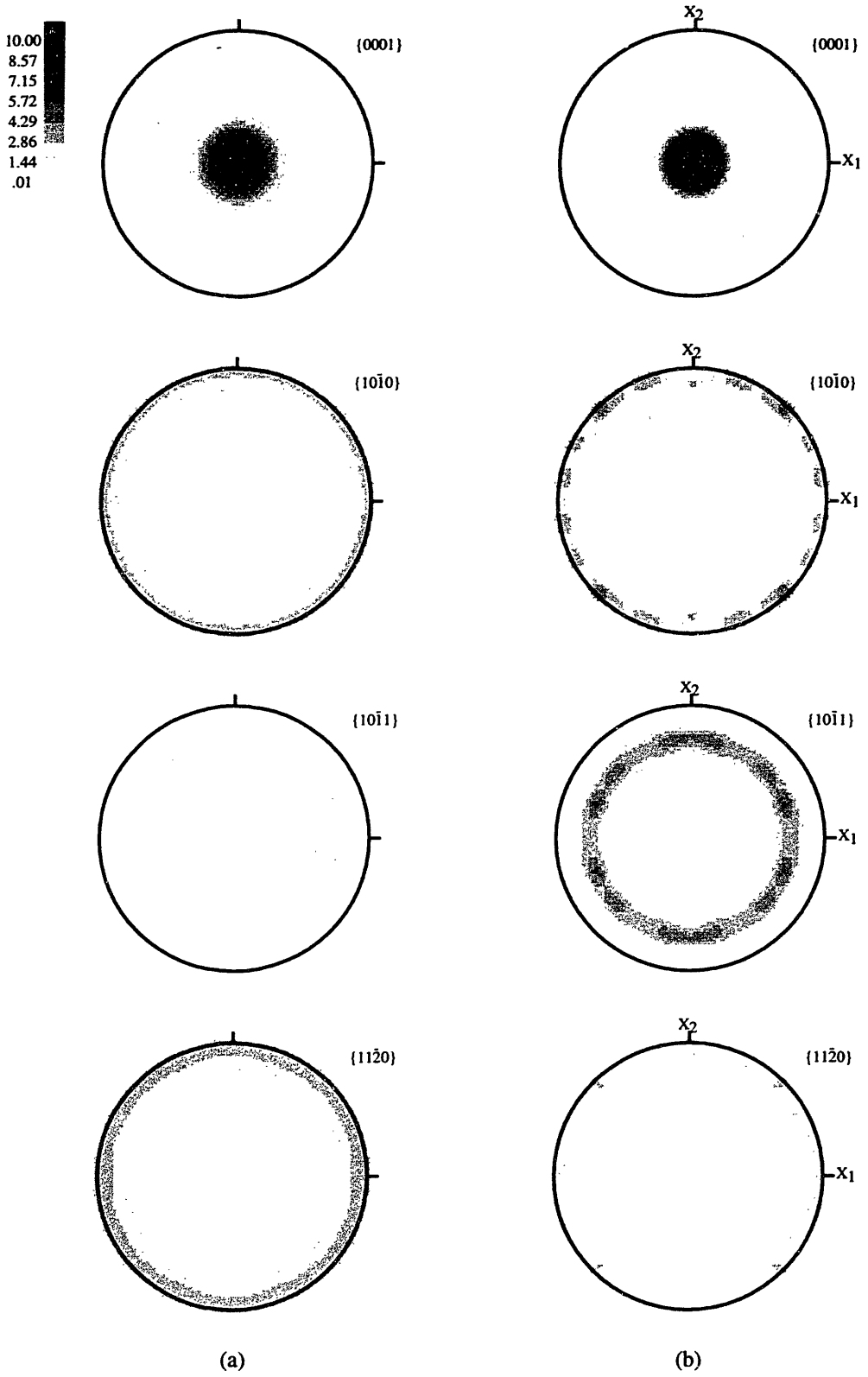


Figure 5-33: Experimentally measured (a) and FEM calculated (b) pole figures after simple compression of the magnesium alloy AZ31B to 18%.

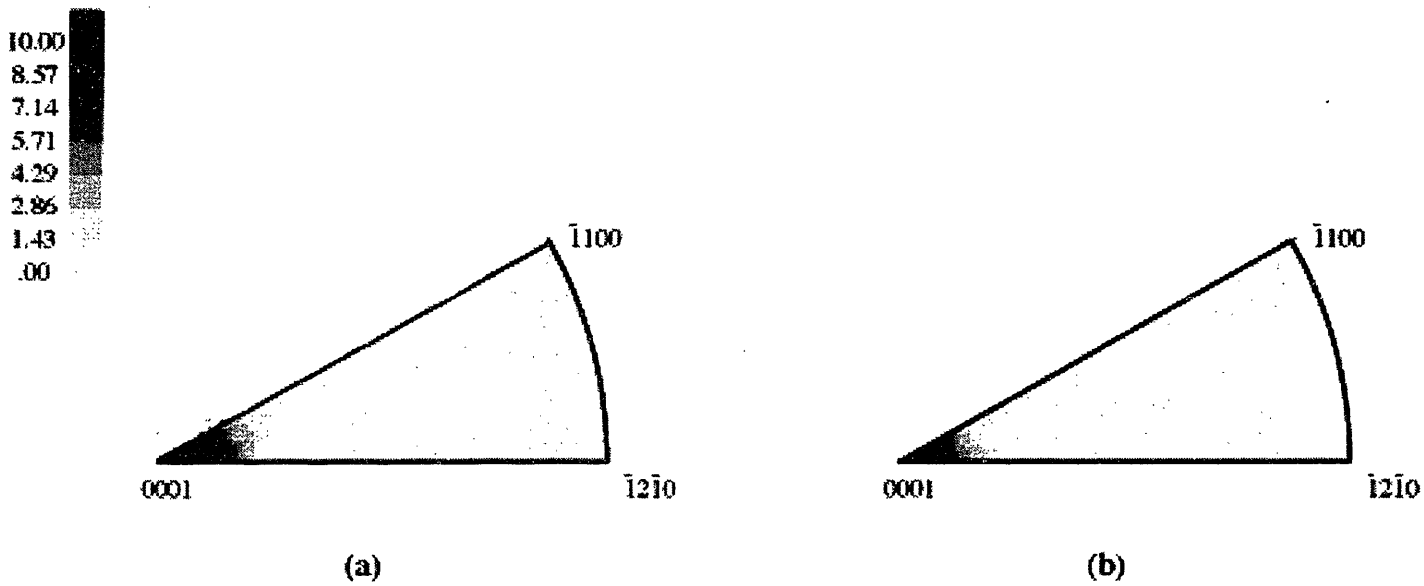


Figure 5-34: Experimentally measured (a) and FEM calculated (b) inverse pole figures after simple compression of the magnesium alloy AZ31B to 18%.

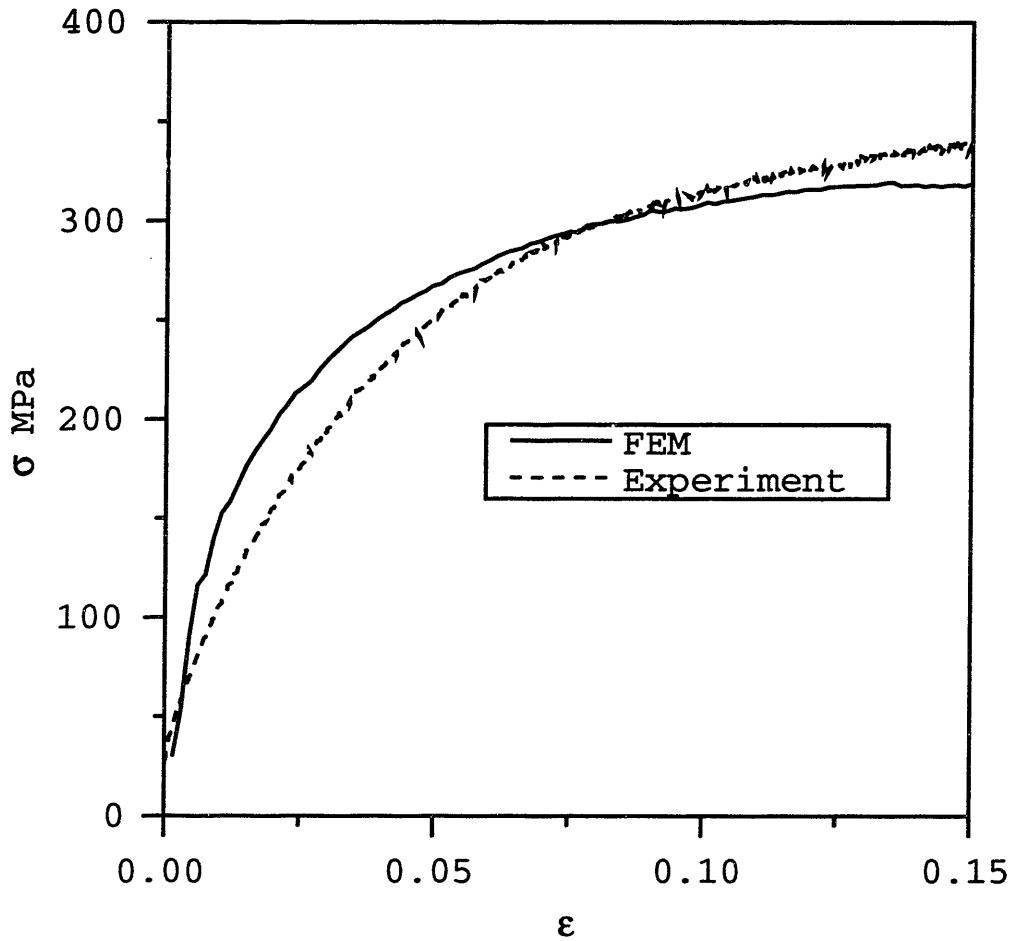


Figure 5-35: Experimentally measured and FEM predicted true stress $\sigma$ versus true strain $\epsilon$ response in plane strain compression in the plate normal direction of the magnesium alloy AZ31B at room temperature.

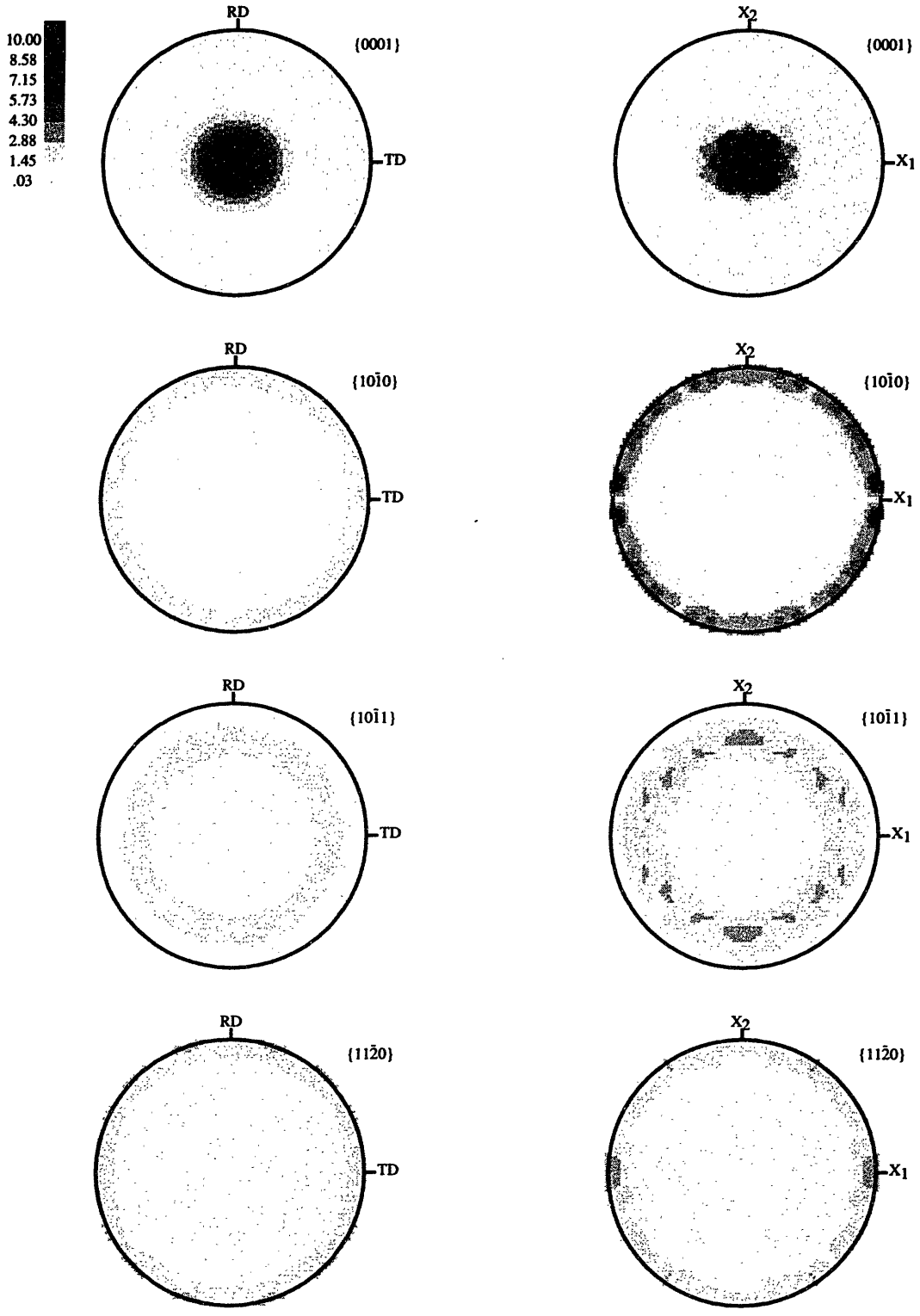


Figure 5-36: Experimentally measured (a) and FEM calculated (b) pole figures after plane strain compression in the plate normal direction of the magnesium alloy AZ31B to 20%.

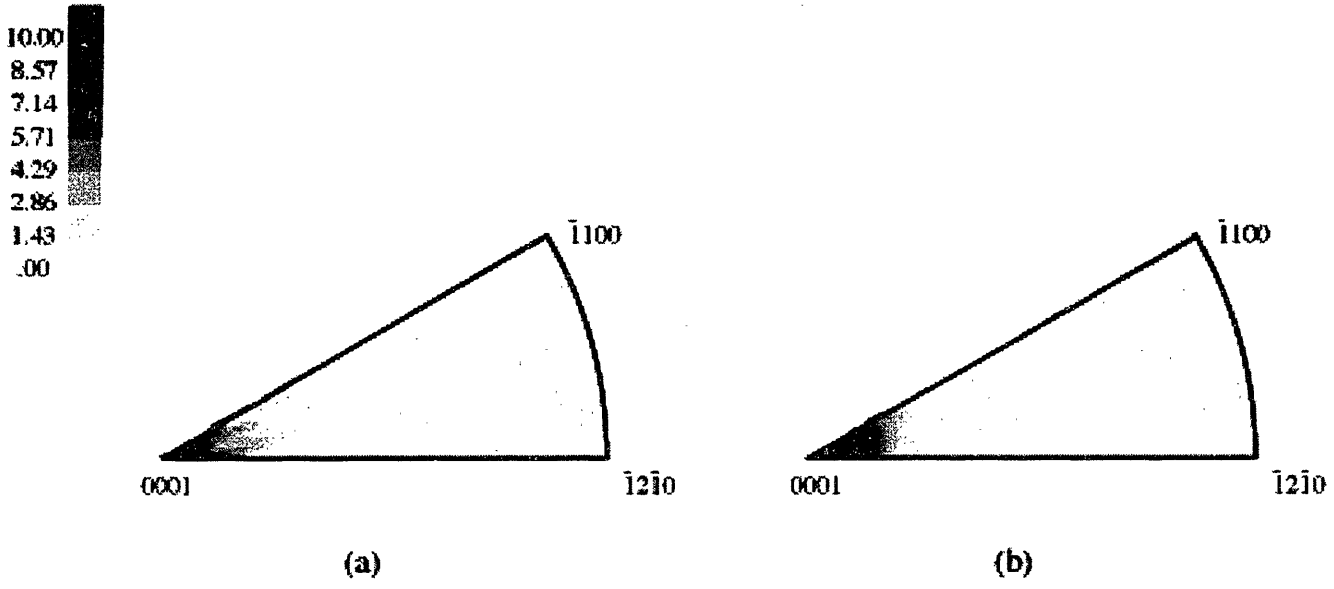


Figure 5-37: Experimentally measured (a) and FEM calculated (b) inverse pole figures after plane strain compression in the plate normal direction of the magnesium alloy AZ31B to 20%.

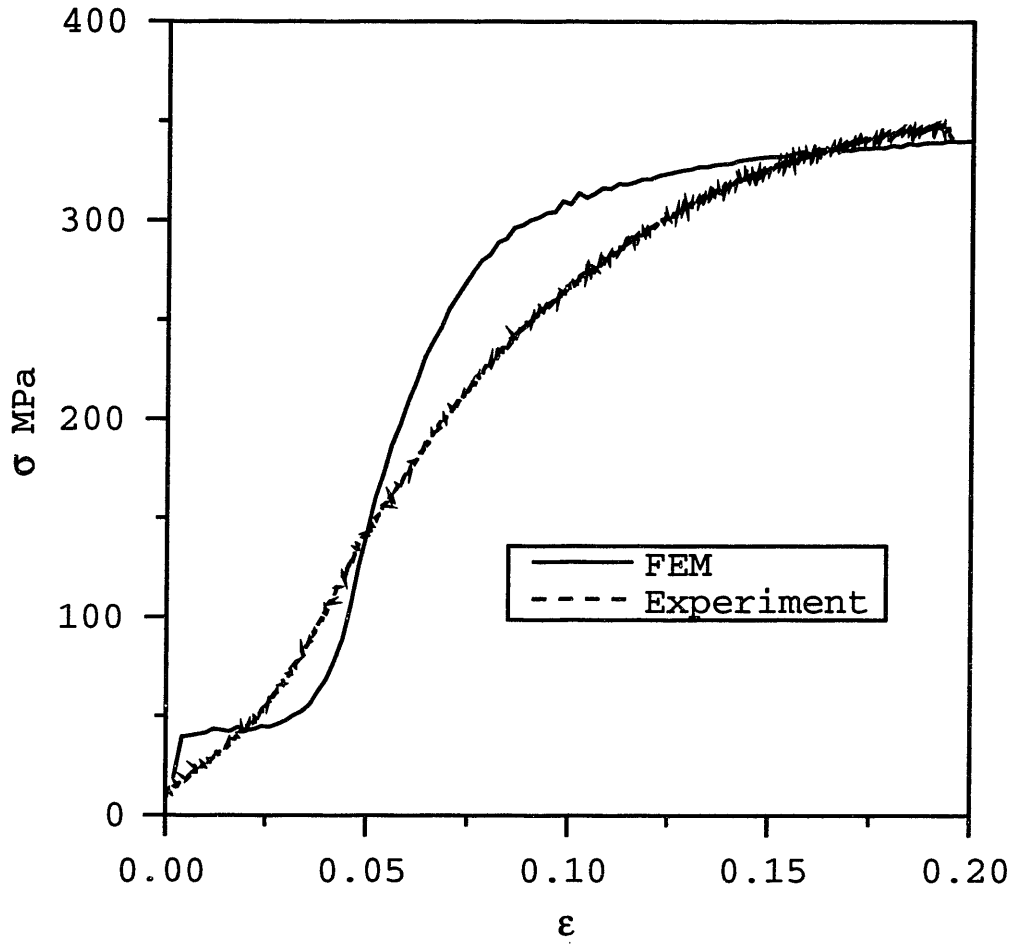


Figure 5-38: Experimentally measured and FEM predicted true stress $\sigma$ versus true strain $\epsilon$ response in plane strain compression in the the plate rolling direction and free direction is plate normal to the rolling direction.

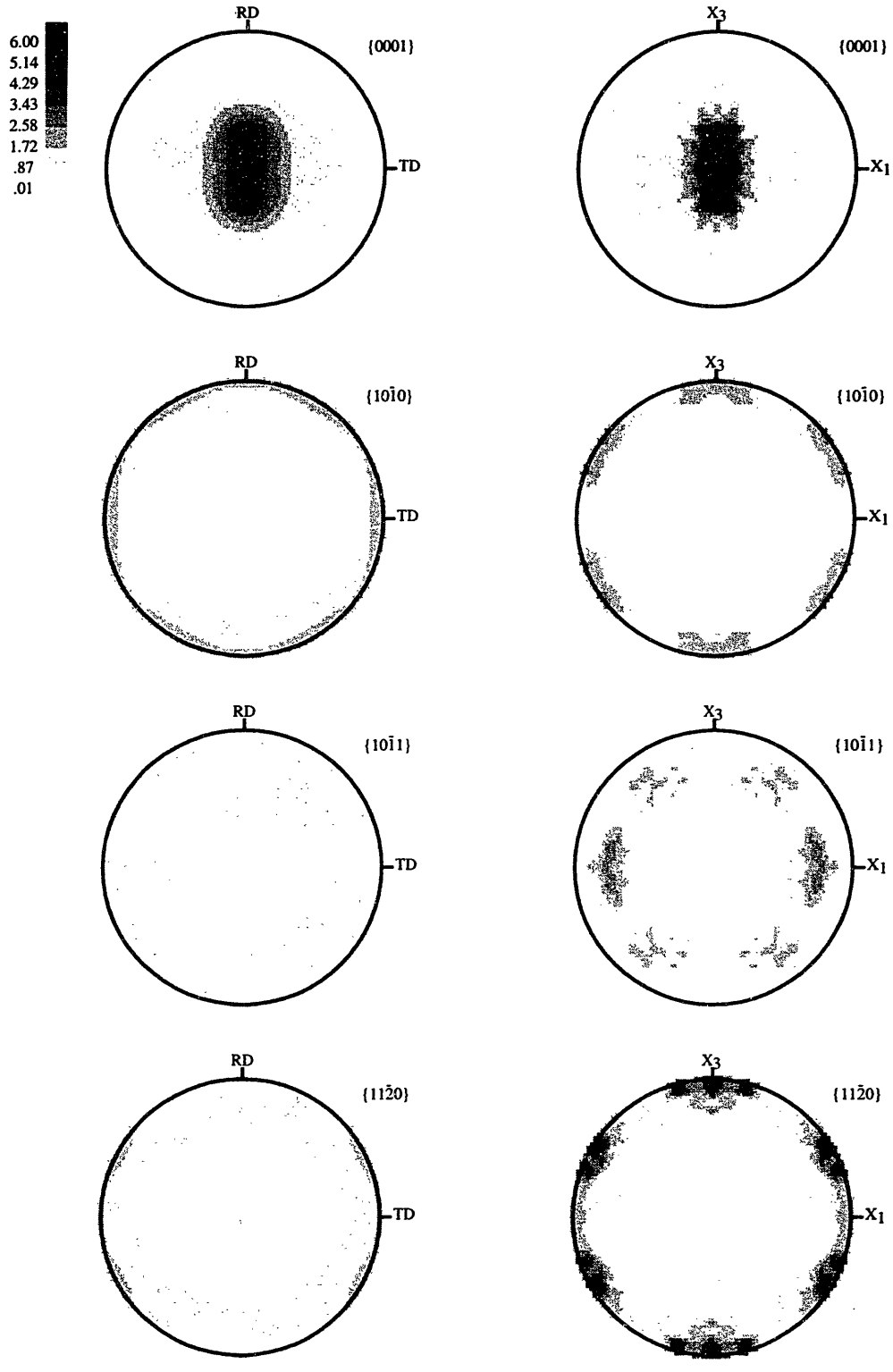


Figure 5-39: Experimentally measured (a) and FEM calculated (b) pole figures after plane strain compression in the plate rolling direction and free direction is plate normal to the rolling direction to 20%.

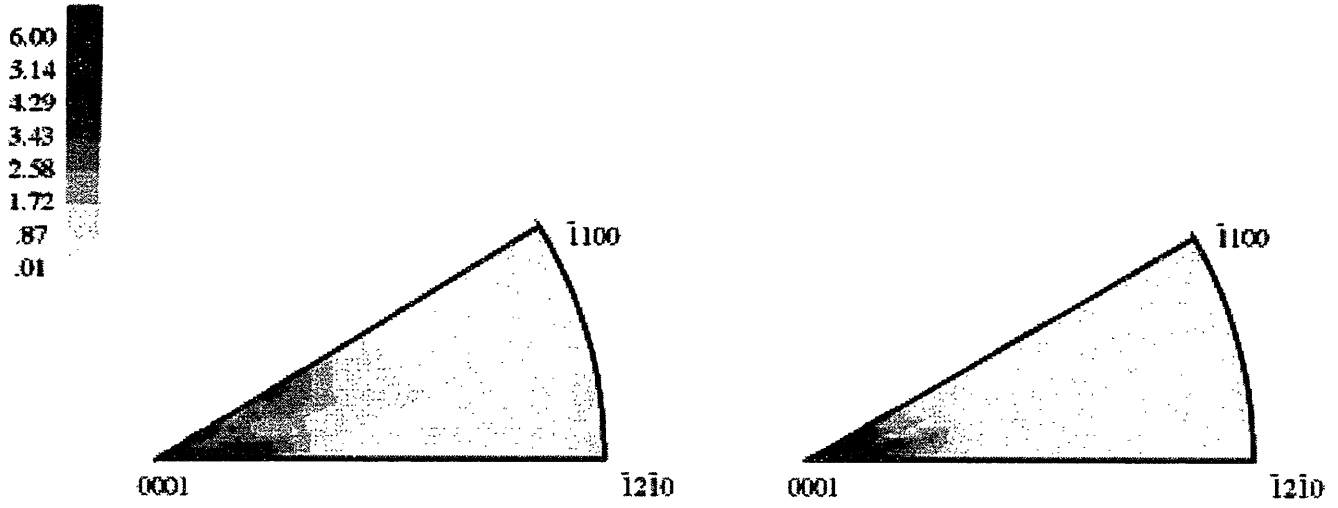


Figure 5-40: Experimentally measured (a) and FEM calculated (b) inverse pole figures after plane strain compression in the plate rolling direction and free direction is plate normal to the rolling direction to 20%.

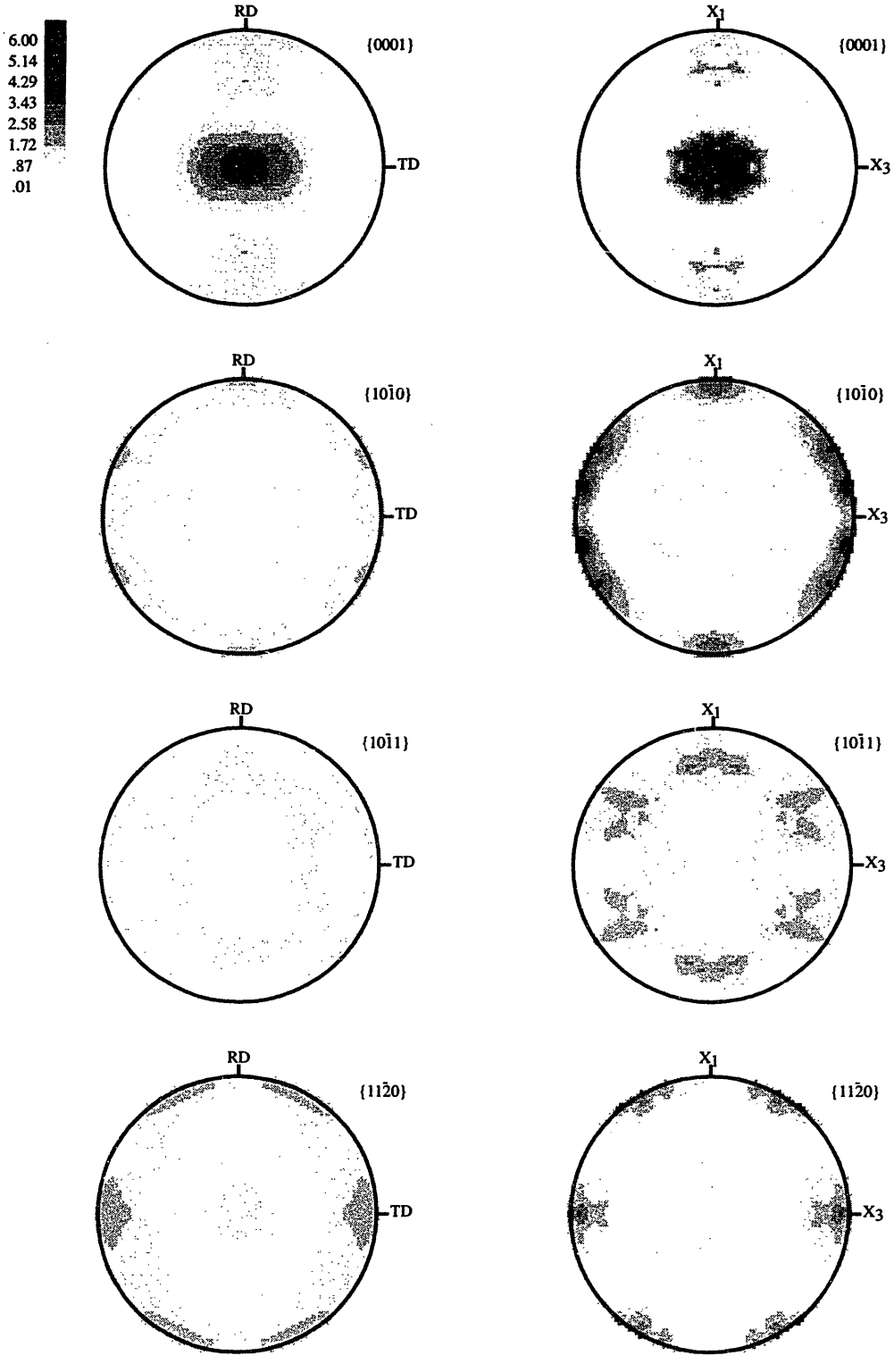


(a) (b)

Figure 5-41: Experimentally measured (a) and FEM calculated (b) pole figures after plane strain compression in the plate rolling direction and free direction is plate transverse direction to 20%.

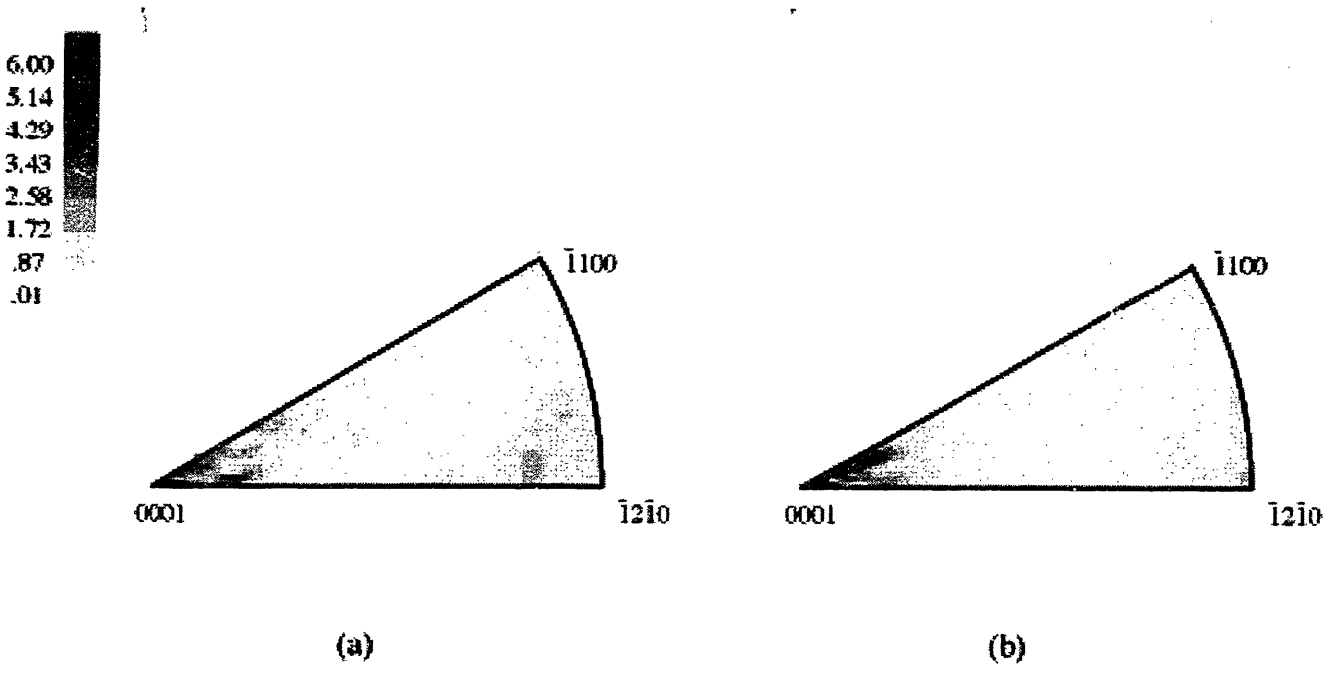


(a) (b)

Figure 5-42: Experimentally measured (a) and FEM calculated (b) inverse pole figures after plane strain compression in the plate rolling direction and free direction is plate transverese direction to 20%.

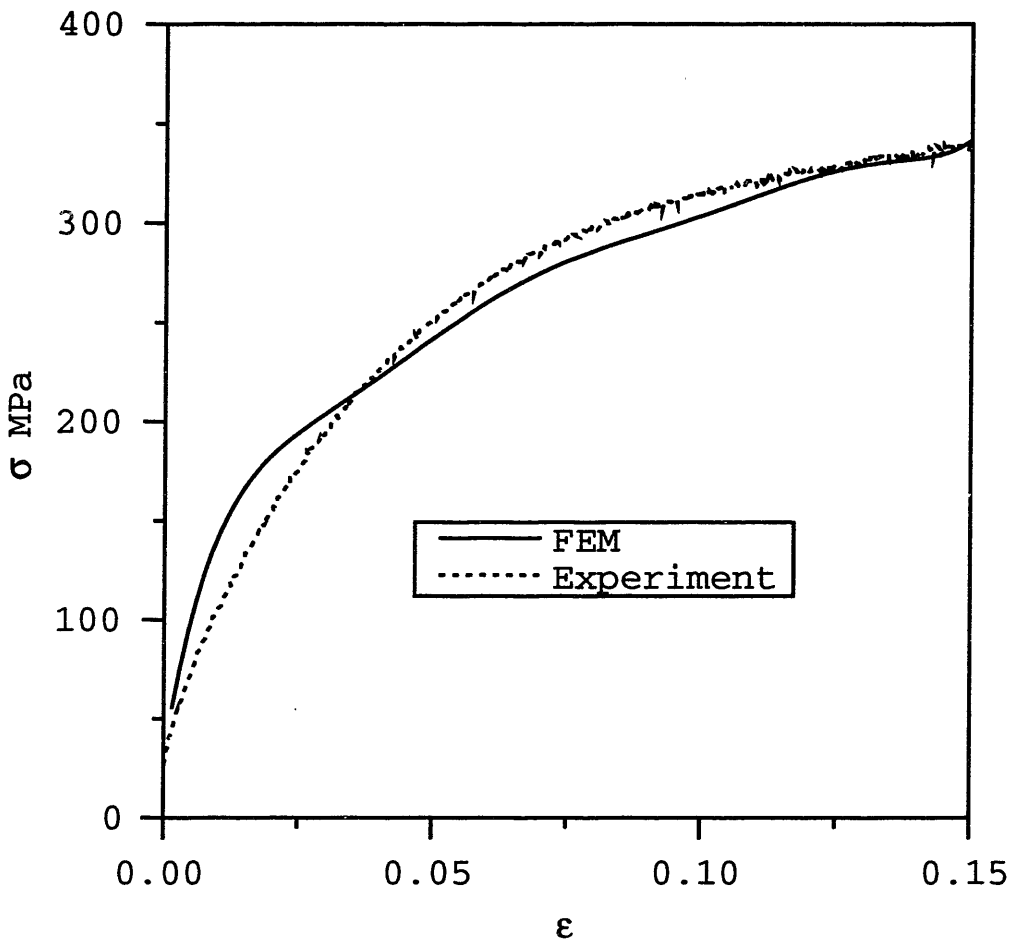


Figure 5-43: Experimentally measured and FEM predicted by isotropic hardening model true stress $\sigma$ versus true strain $\epsilon$ response in plane strain compression in the the plate normal direction.

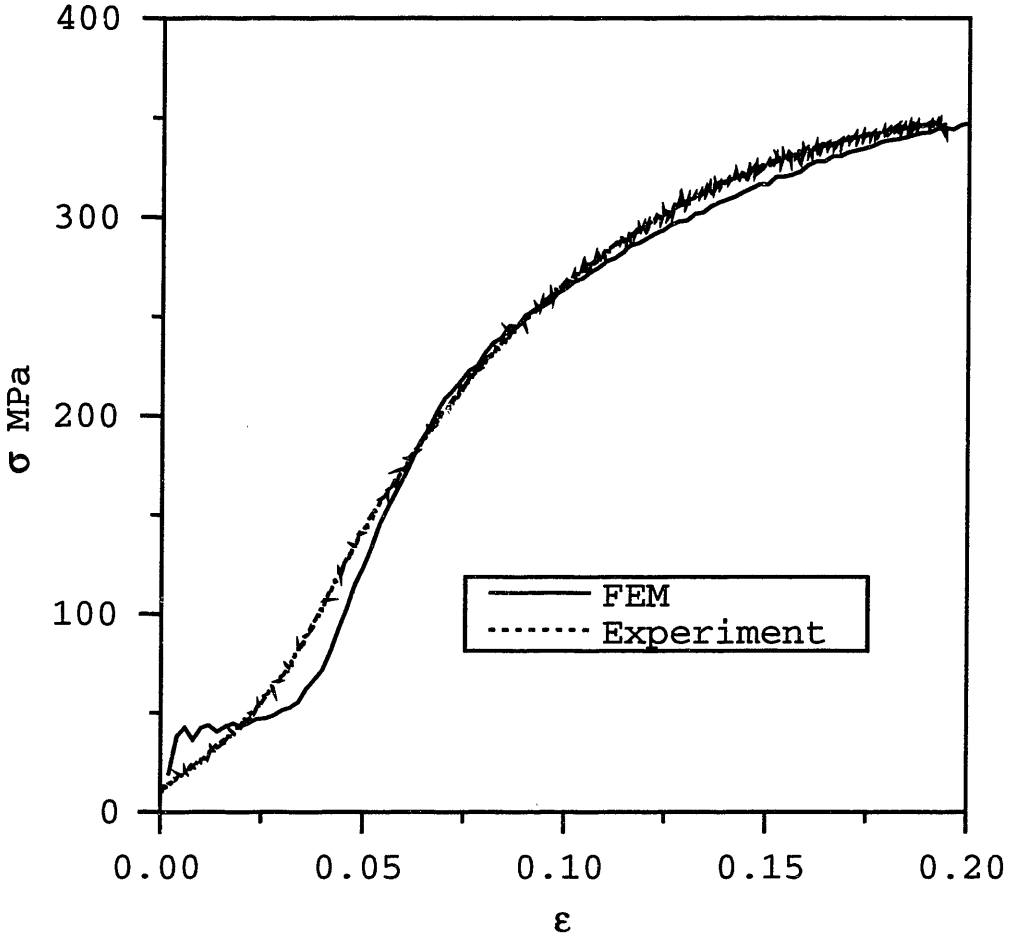


Figure 5-44: Experimentally measured and FEM predicted by isotropic hardening model true stress $\sigma$ versus true strain $\epsilon$ response in plane strain compression in the the plate rolling direction and free direction is plate normal to the rolling direction.

# Chapter 6

# Plastic Deformation of Magnesium at Elevated Temperatures. Experimental Study.

We showed in the previous chapter that experimentally observed polycrystalline strengthening of magnesium alloy AZ31B could be mainly explained on the basis of grain reorientation mechanism, without any additional assumptions for strain hardening. In this part of the thesis we turn our attention to material behavior at moderately high temperatures. We show that the insignificance of polycrystalline hardening at elevated temperatures is explained by the fact, that twinning is suppressed, and therefore, texture evolves slowly in comparison with room temperature experiments.

We estimate the texture evolution and anisotropic stress-strain responses of h.c.p. magnesium alloy AZ31B at temperatures[1] $350^o C$ and $400^o C$. At these temperatures we still assume that diffusion processes are second-order effects in magnesium plastic flow. Raynor [1959] presented data for self-diffusion coefficients in magnesium. He also derived the formula for the heat activation of self-diffusion, i.e. $D = \exp(-32,000/RT)\, cm^2/sec$. For the testing temperature of $400^o C$ this coefficient does not exceed the value of $3.3 \cdot 10^{-11}\, cm^2/sec$, which is at least two orders of

[1] the melting point reported for pure magnesium is $650^o C$.

magnitude less than the minimum threshold value we should take into account. On the other hand this range of temperatures is high enough to suppress twinning and to activate non-basal slip systems. In single crystals in addition to basal, prismatic $< a >$, and pyramidal $< a >$ systems, slip may occur on the six second order pyramidal $< \mathbf{c} + \mathbf{a} >$ systems $\{11\bar{2}2\} < \bar{1}\bar{1}23 >$, and the degree of plasticity increases markedly, becoming comparable to that of cubic metals. At $300^o C$ the possible elongation before failure is approximately nine times that at room temperature, as noted by Raynor [1959]. Very good example of this may be seen from the analysis of fracture surfaces after tension tests. At high temperature the specimen was fractured leading to an ideal (and very sharp) cup and cone appearance of Fig. 6-1a. For comparison in Fig. 6-1b is shown the specimen tested at room temperature with typical shear fracture. Figure 6-2 shows the SEM micrographs of the fracture surface after tension at $350^o C$. For the purposes of comparison, the SEM micrograph of the fracture surface of the sample deformed at room temperature is also presented in the figure 6-2. These micrographs illustrate the postulate (Yoo [19[illegible]]) that at room temperature magnesium is cracked by twin-induced cleavage fracture. With suppression of twinning and activation of $< \mathbf{c} + \mathbf{a} >$ slip systems the intrinsic resistance to cleavage increases as well as the ductility.

A specimen deformed by plane strain compression to $\epsilon = -0.5$ at $400^o C$ was electro-polished and etched. Optical micrographs shown in Fig. 6-3 clearly reveals the absence of twins in the grains. The average grain size is much less than we observed in the specimens deformed at room temperature. The tensile specimen fractured after extensive necking. Our objective here is to estimate experimentally the role of non-basal slip systems and twinning systems on deformability and anisotropic properties of magnesium.

The greater part of the literature on the plastic deformation of magnesium at elevated temperatures dates back to the 1950's and is devoted to the investigation of single crystal behavior (see, for example, Bakarian and Mathewson [1943], Reed-Hill and Robertson [1957]). We attempted to fill this gap and analyzed the deformation behavior of textured polycrystalline of magnesium alloy. The deformation of textured

magnesium must be controlled by the same mechanisms observed in single crystals, and the degree of anisotropy should depend on the intensity of the texture.

## 6.1 Experimental apparatus and sample preparation

For elevated temperature tests, a radiant furnace was used to bring the sample to the desired temperature. The furnace, a Quad Elliptical Heating Chamber (Research Inc.,), contains four quartz lamps with tungsten emitters (power 5 KW each; the temperature of the emitters is approximately $2000^o C$). A water cooling system is used to maintain working regime. The time required for the environment of the furnace to reach $400^o C$ is about 20 min. The furnace working area is 14 cm high and 6 cm in diameter. This size is sufficient for simple and plane strain compression tests. For conducting simple tension tests, special grips were developed. The sketch of a simple tension test specimen and of a grip is shown in Fig. 6-4. The specimen temperature was monitored by type-K thermocouples and a digital thermometer. A Tigtech Inc., welder 116 SRL with inert argon atmosphere was used for welding thermocouple to the specimen. The appropriate temperature was maintained by a manual thermocontroller. To protect the hydraulic system against overheating, the ceramic rod-platens were used during the experiments. The mechanical tests were performed in the strain rate control mode[2] on an Instron 1350 servohydraulic machine with real time data acquisition. As before, the simple compression specimens were cylindrical and had a diameter of 12.7 mm (1/2") with the ratio between length and diameter of the sample close to 1.1. These dimensions of the specimens were chosen to prevent specimen shearing during the test. Specimens for plane strain compression tests were approximately cubes with dimension in the constraint direction of 8.9 mm (0.35"). At high temperatures we can no longer use the same lubricants we used for the room temperature tests. The lubricant used for the tests at $350^o C$ was oil-based

[2]because of high temperature we could not use the standard extensometer.

graphite lubricant DAG41. For experiments conducted at $400^o C$, a methanol-based lubricant containing 1 part boronitride and 8 parts glass powder 8463 was used. A table of lubricants recommended for different temperature regimes is given in Brown et. al. [1989].

Electrolytic polishing was used to obtain a stretch-free surface. The electrolyte consisted of three parts 85% phosphoric acid ($H_3PO_4$) and five parts 95% ethanol; both were cooled to approximately $0^o C$ before mixing using liquid nitrogen. Specimens were polished through 15$\mu$m diamond paste before electric polishing. Voltage about 30 V was applied for 4 min. After polishing the specimen was rinsed in running tap water.

## 6.2 Experimental procedure and test results

At elevated temperatures we conducted essentially the same tests as we did at room temperature. The principal difference from the room temperature tests was in the value of the final degree of deformation. Compression tests were conducted to true strains $-0.5$ and $-1.0$; tension tests were conducted up to failure. The tests were performed at constant true strain rates of 0.001 $s^{-1}$. Material behavior at both temperatures $350^o C$ and $400^o C$ is qualitatively the same. Because the pole figures for the two temperatures regimes are essentially the same they are shown only for one temperature.

Several tension tests were performed at different temperatures. After about 10% deformation, extensive necking was observed. This process of nonuniform deformation makes the true stress - true strain relations hard to determine. Accordingly, figure 6-5 gives the engineering stress-engineering strain relations for different elevated temperatures. The yield point drops very fast with increasing temperature. This means that the experiments were done in regimes where slip resistances are very sensitive to temperature changes. Pole figures at four crystallographic planes after simple tension are shown in Figure 6-6. It is very important to note, according to our data, the intensity of the fiber $\{10\bar{1}0\}$ texture does not increase. This means

that some mechanisms, most probably pyramidal slip and dynamic recrystalization[3] together, make the texture more diffused. The absence of strong texture transition leads to the non-hardening of polycrystalline in tension.

Figure 6-7 shows the stress-strain relations obtained from simple compression tests.

As the temperature increases, the stress level drops significantly. The yield point is about 35 MPa at $350^o\,C$ and about 27 MPa at $400^o\,C$. The slip resistances decrease with the temperature rise. Equal area projection pole figures for simple compression after deformation of 100% are shown in Fig. 6-8. The intensity of the fiber structure increases with deformation. One can see from graphs in Fig. 6-7 that the material does not show strong strain hardening behavior. Initial softening (approximately to $\epsilon = -0.4$) may be explained by texture evolution. The small polycrystalline strengthening may be explained by both mechanisms: the texture evolution and strain hardening of non-basal slip systems. The more crystals have re-oriented, aligning their basal planes normal to the applied compressive load, the stronger the material is under the same loading conditions.

Figure 6-9 shows the stress-strain relationship for plane strain compression perpendicular to the rolling plane of the initial plate. In this mode of deformation the texture does not change qualitatively and only the intensity of the $\{0001\}$ pole increases with degree of deformation. This is one of explanations why the stress level grows with deformation. The pole figures after $\epsilon = -1$ are presented in Fig. 6-10. As expected, the predominanting orientation after all simple compression and plane compression tests was such that the basal planes were perpendicular to the direction of the applied load. The rate of texture evolution is very slow at temperature $400C^o$. A good example of this may be the plane strain compression test with compression in the direction parallel to the plate rolling plane. The free direction in this test was chosen to be parallel to the transverse direction of the as-received plate. The texture even after deformation $\epsilon = -1$ is close to the initial one (Fig. 6-11). For comparison,

[3]Decreasing of the average grain size may be considered as an evidence that dynamic recrystalization takes place in these conditions.

the correspondent texture after compression to 20% at room temperature has a strong basal pole (see Fig. 5-20). The stress-strain curve is given in Fig. 6-12.

## 6.3 Concluding remarks

Magnesium shows a considerable variation in strength and ductility depending on temperature regime. The increase in ductility should be caused by activation of $< \mathbf{c}+\mathbf{a} >$ slip system $\{11\bar{2}2\} < \bar{1}\bar{1}23 >$ at elevated temperatures as was observed by Stohr and Poirier [1972]. These slip systems together with basal slip systems and pyramidal $< a >$ systems form the full system, which is able to accommodate any prescribed deformation. Being active on $< \mathbf{c}+\mathbf{a} >$ pyramidal crystallographic planes slip system suppresses twinning activities. Our observations do not show any traces of twin lamellae at elevated temperatures. The observed stress-strain relationships support the hypothesis that strain hardening effects in magnesium are negligible. The strengthing of the material during deformation is caused mostly by crystal lattice reorientation and strain hardening of non-basal slip systems.

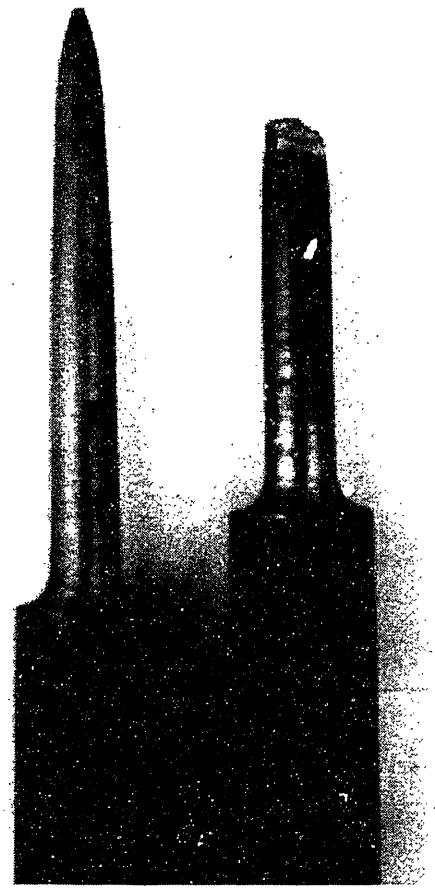

Figure 6-1: Samples after simple tension tests: at elevated (left) and at room (right) temperatures.

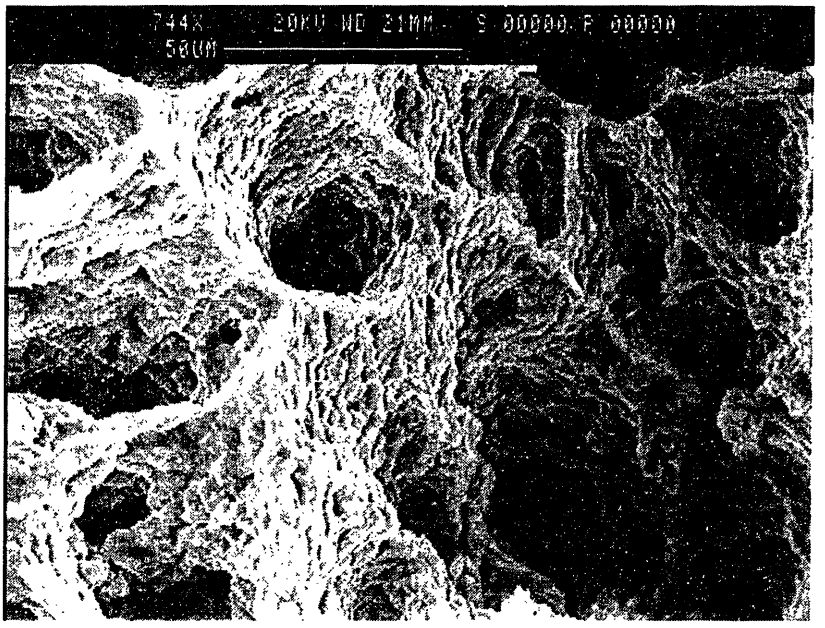


(a)

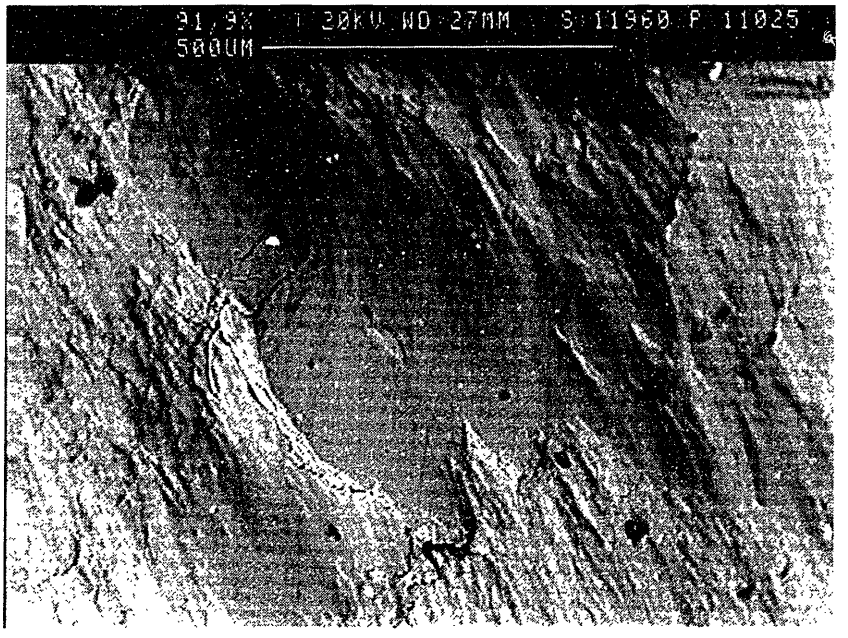


(b)

Figure 6-2: SEM micrographs of fracture surfaces after simple tension of magnesium alloy AZ31B (a) at $350°C$, (b) at room temperature.

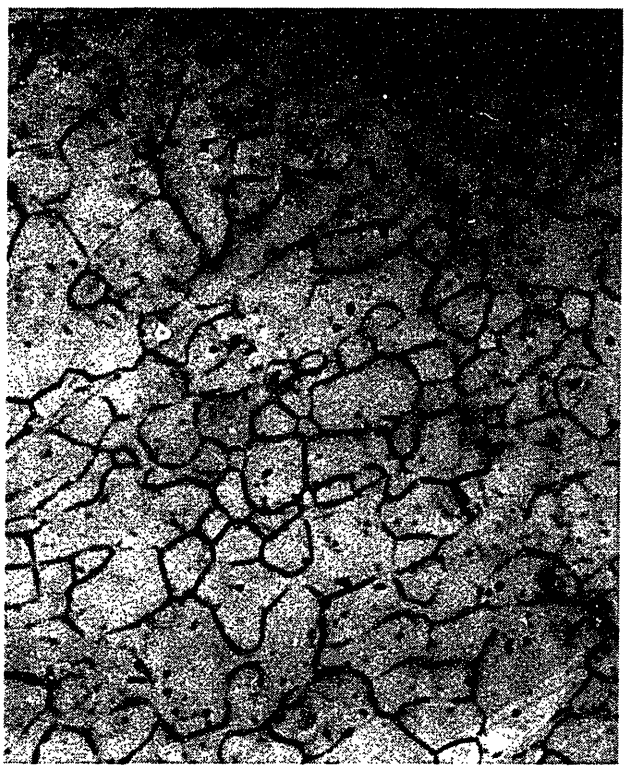

Figure 6-3: Micrograph of Magnesium alloy AZ31B deformed at 350°C by plane strain compression to $\epsilon = -0.5$. Magnification is 1000X.

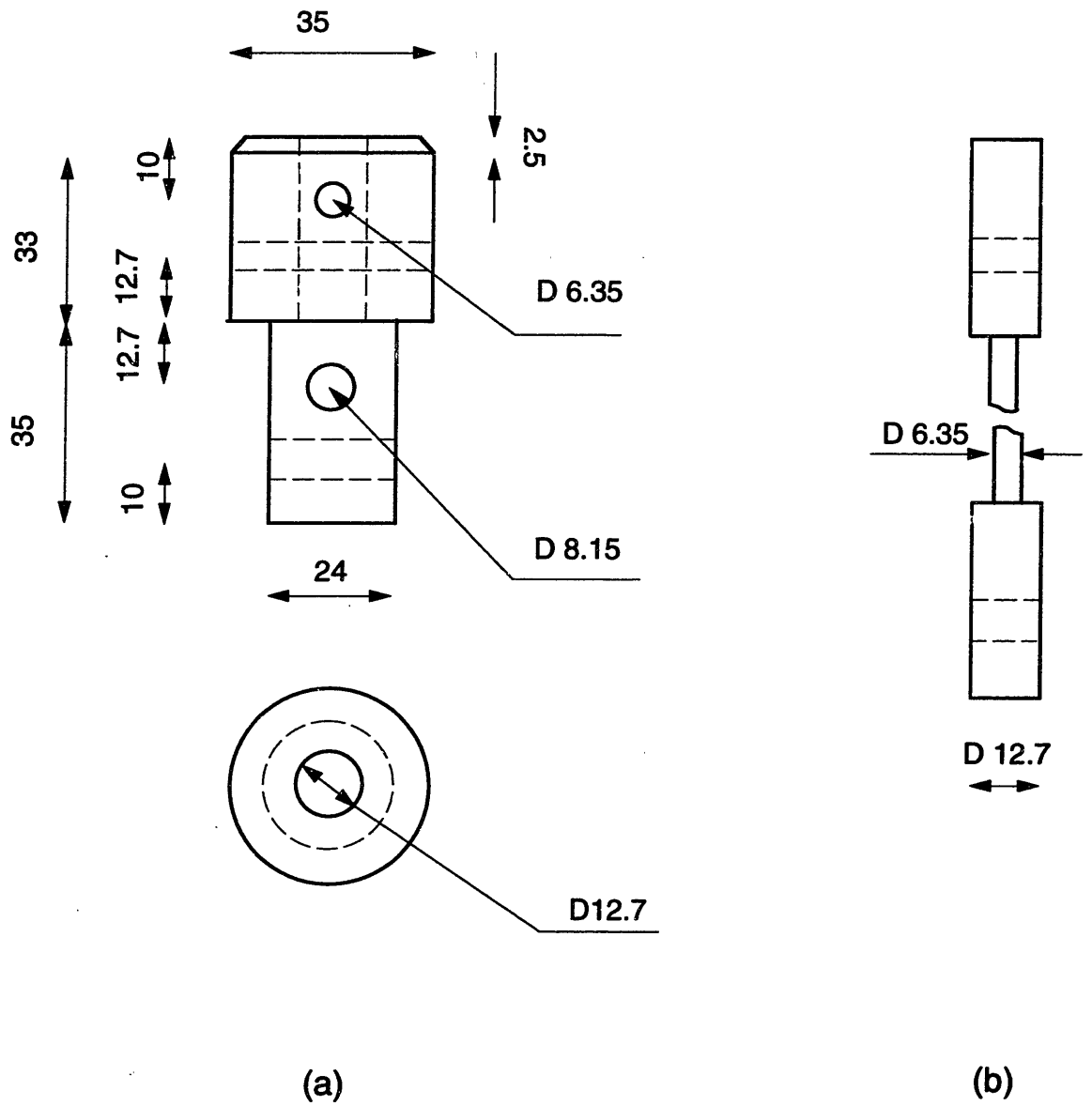


Figure 6-4: Scetches of a grip (a) and (b) a specimen for tension tests in the quartz furnace. All dimensions are given in *mm*.

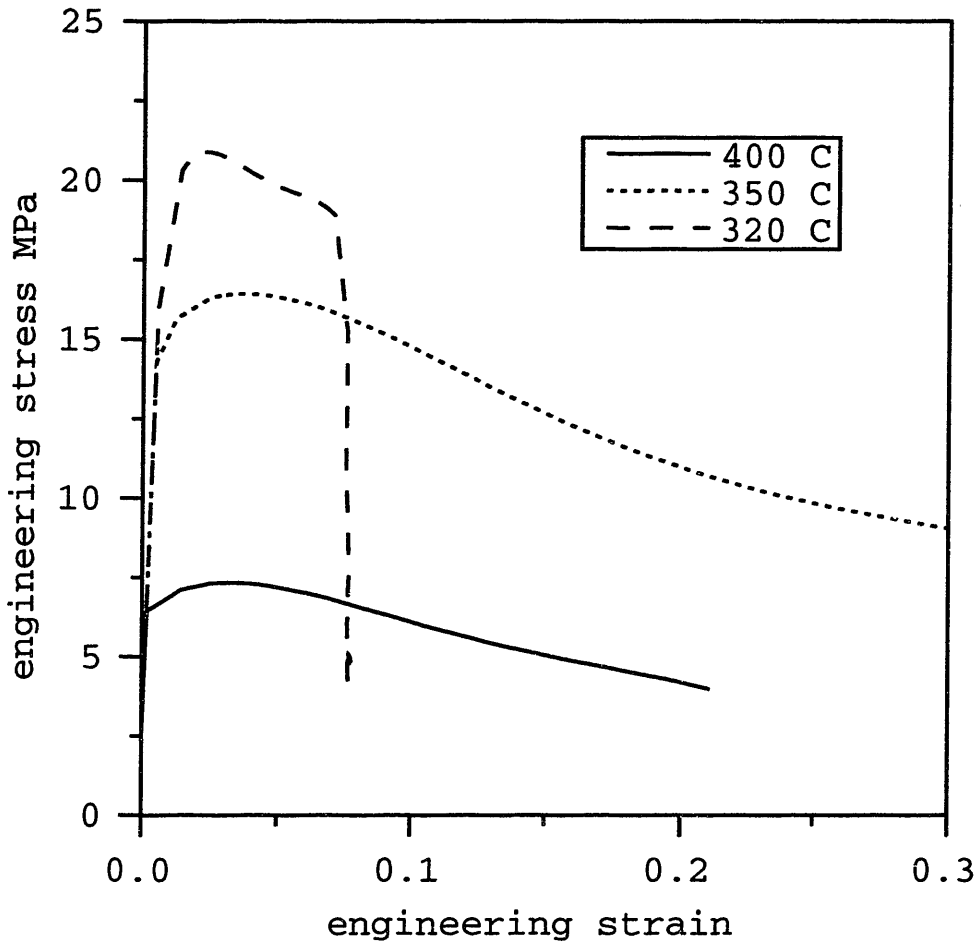


Figure 6-5: Engineering stress - engineering strain relations for simple tension of AZ31B at different elevated temperatures.

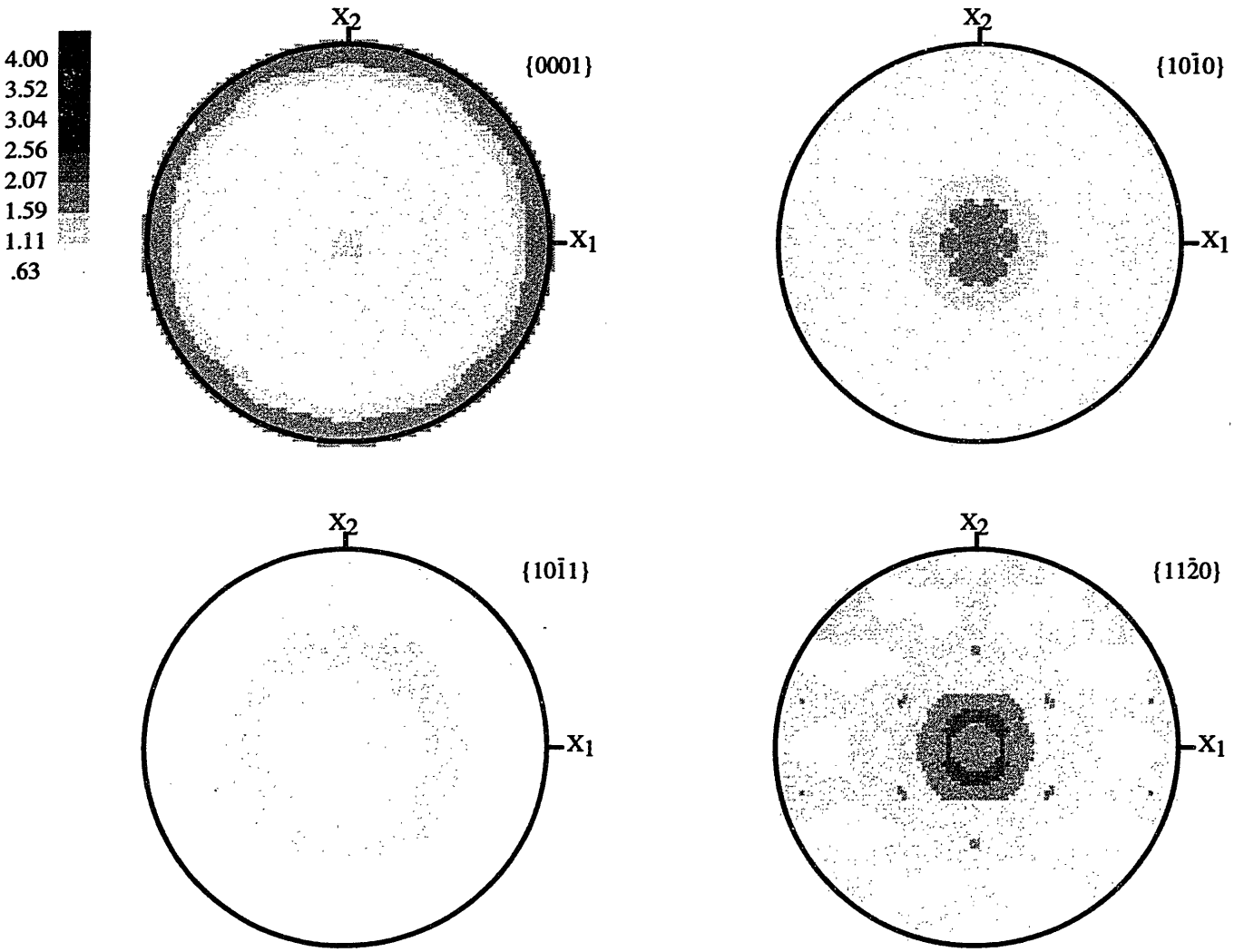


Figure 6-6: Experimentally measured texture in simple tension experiment on magnesium alloy AZ31B at elevated temperature

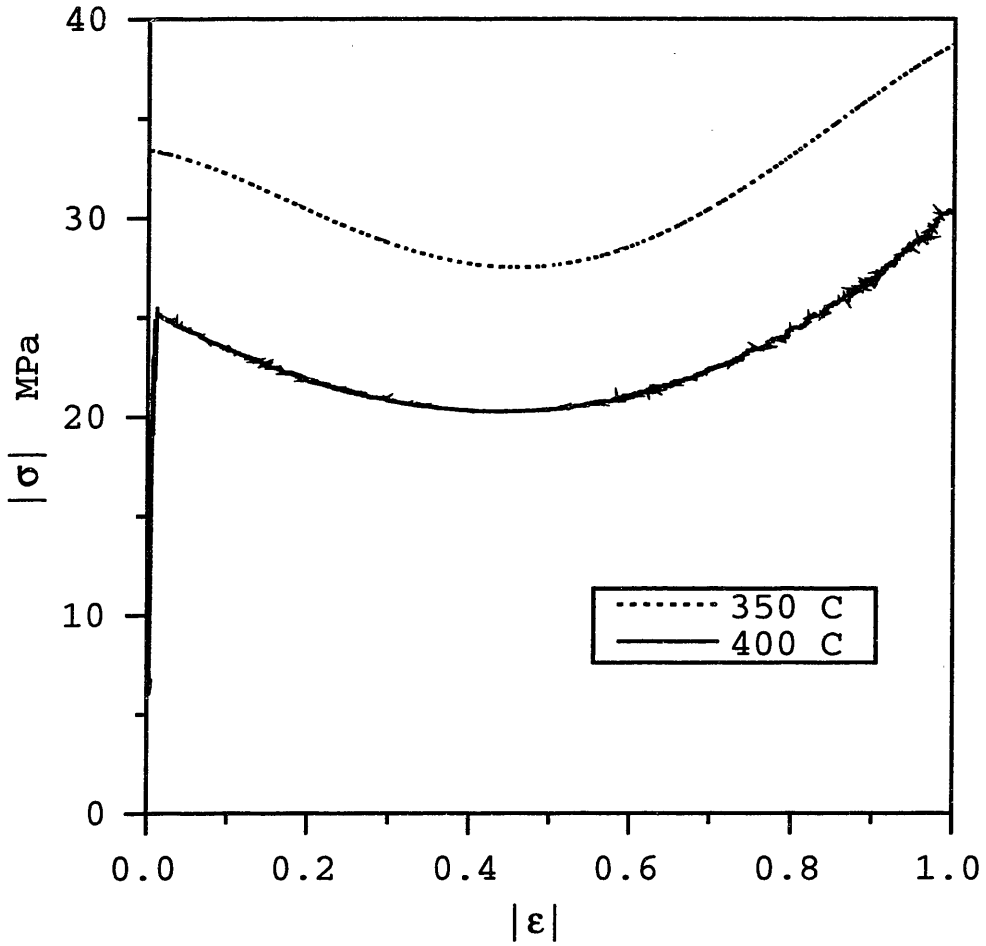


Figure 6-7: Stress - strain relations for simple compression of AZ31B at different elevated temperatures.

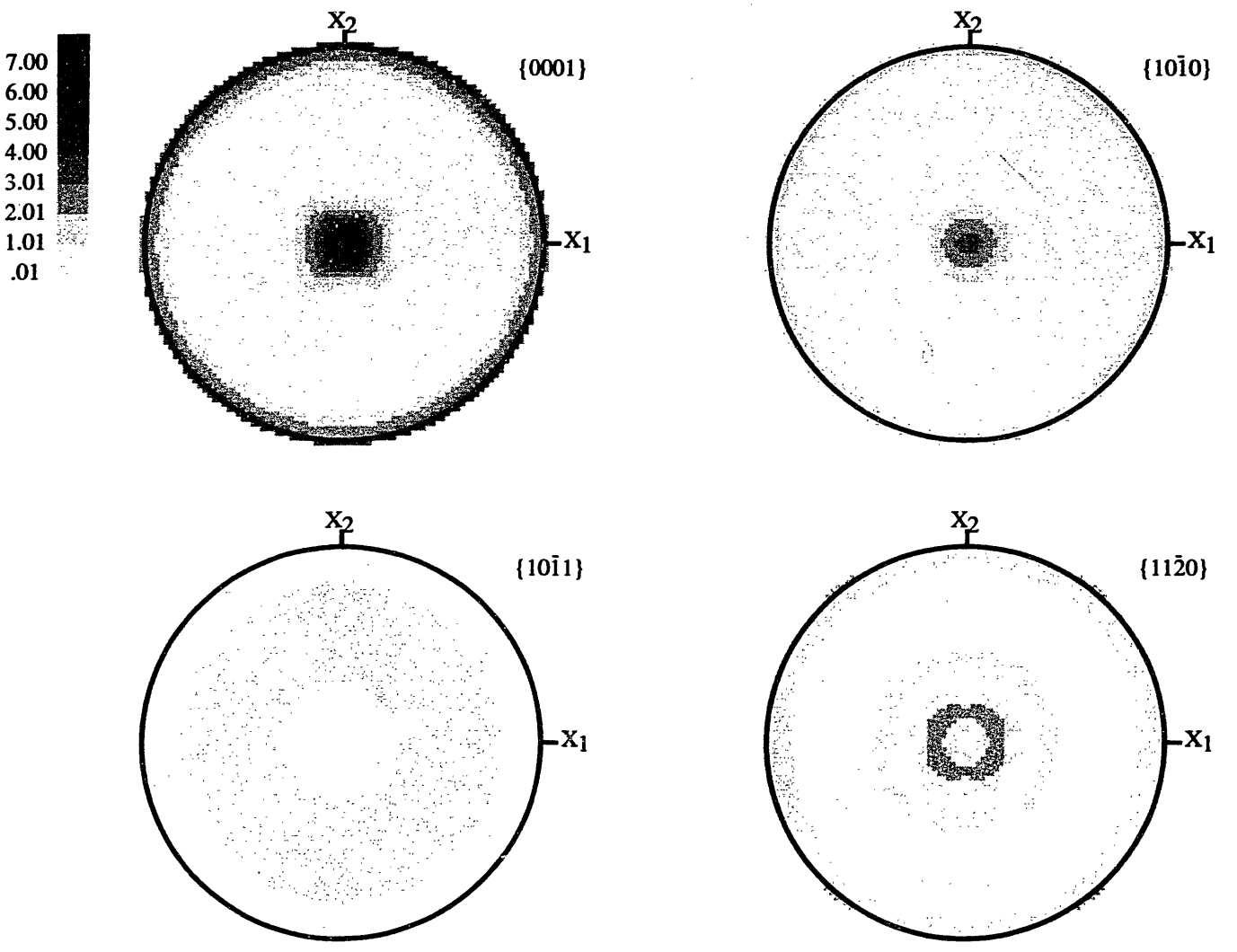


Figure 6-8: Experimentally measured texture in simple compression experiment to 100% on magnesium alloy AZ31B at elevated temperature

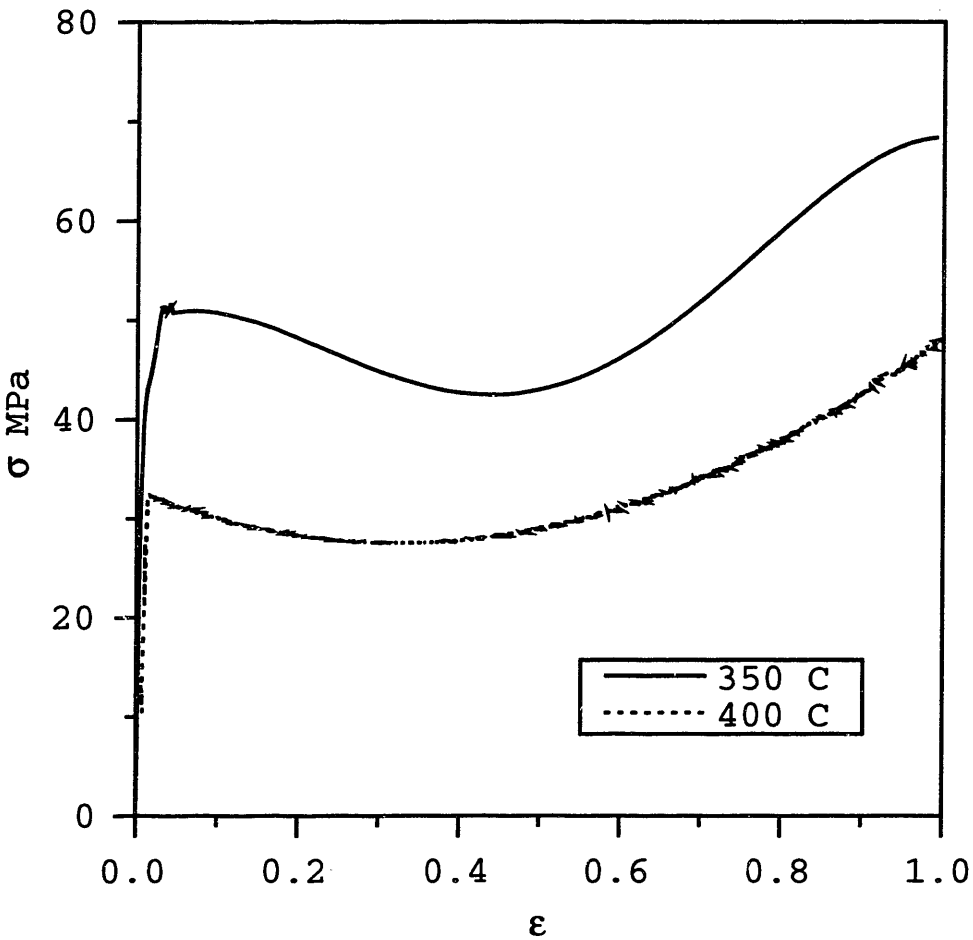


Figure 6-9: Stress - strain relations for plane strain compression of magnesium alloy AZ31B at two different elevated temperatures. Compression direction is parallel to the rolling plane normal of the received sample.

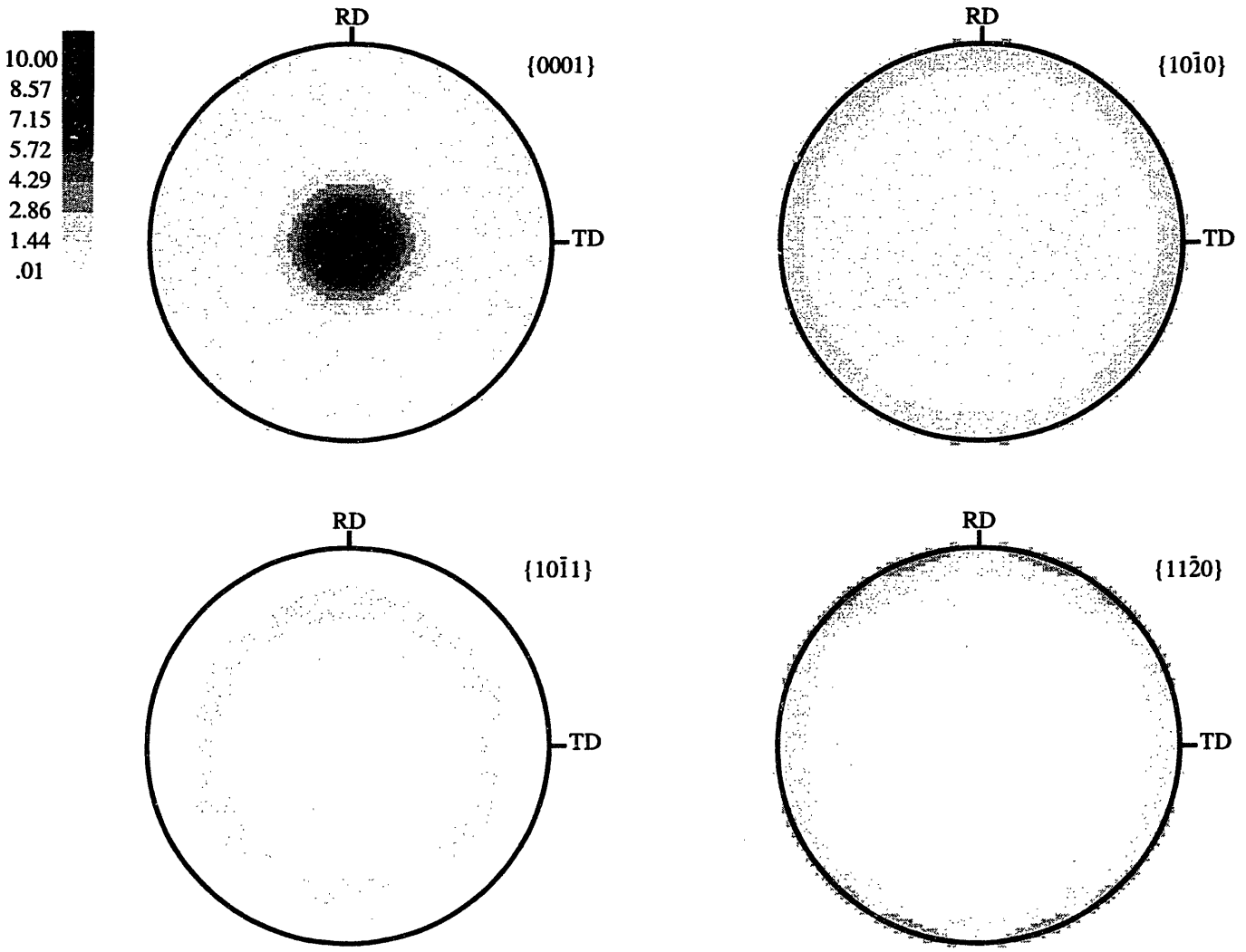


Figure 6-10: Experimentally measured texture in plane strain compression experiment to 100% on magnesium alloy AZ31B at elevated temperature. Compression direction is parallel to the normal of the rolling plane of the received specimen.

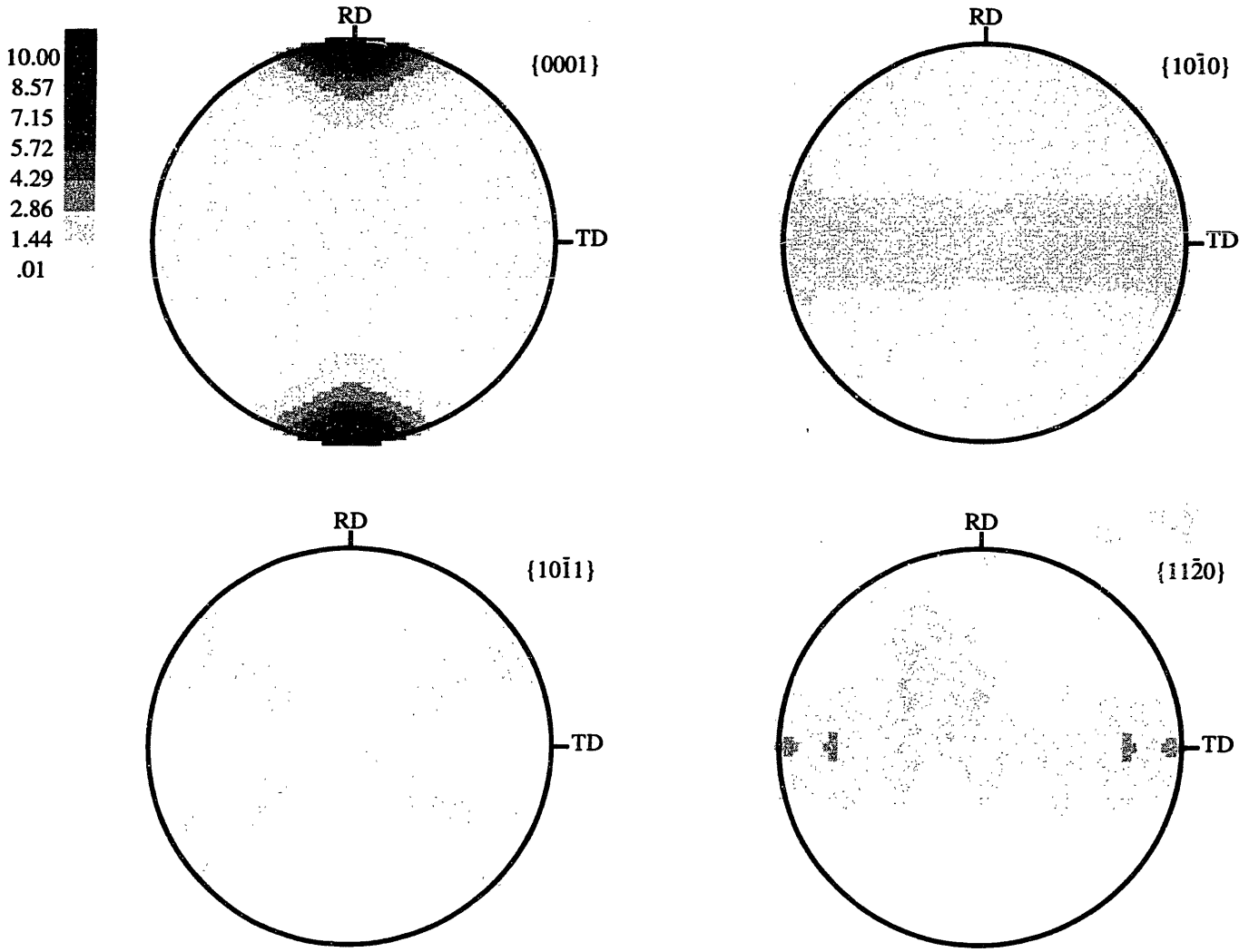


Figure 6-11: Experimentally measured texture in plane strain compression experiment to 100% on magnesium alloy AZ31B at elevated temperature. Compression direction is parallel to the free direction of the received specimen.

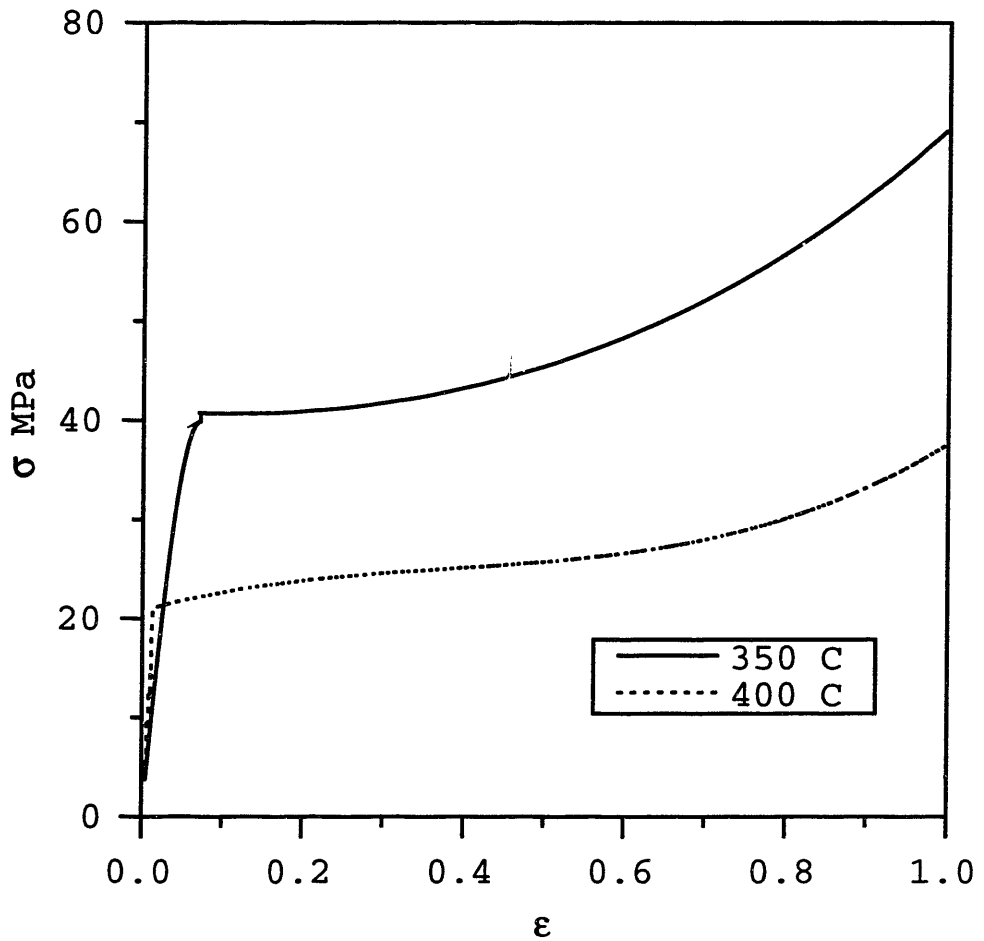


Figure 6-12: Stress - strain relations for plane strain compression of magnesium alloy AZ31B at two different elevated temperatures. Compression direction is parallel to the rolling direction of the received sample, free direction is parallel to the transverse direction of the received sample.

# Chapter 7

# Directions for future work

In this chapter we present some directions for future research envisioned by the author.

We have presented an incremental constitutive model which accounts for both slip and twinning, and where the ability to predict polycrystalline macro behavior through the single crystal model was clearly demonstrated.

However, single crystal *inhomogeneous deformation* is still one of the major uncertainties in the understanding of single crystal constitutive laws. Much work needs to be done to improve our understanding of slip-twin, twin-twin, slip-grain boundaries, and twin-grain boundaries hardening interactions and their formal description. The role of twin/grain boundary energy in the deformation process is still not well understood. Another group of unanswered questions, which is waiting for the proper analysis, is the influence of stress and temperature distribution on slip and twin nucleation and propagation.

One of the possible approaches to handle this group of problems is suggested by V. Bulatov and A. Argon [1993]. Their model based on the idea of stochastic inelastic transformations. The idea of this model may be applied for the analysis of large deformation using the fact that characteristic time-scale is different for slip and twinning. Slipping may be described by the constitutive model of Kalidindi and Anand [1994], and twinning by Monte-Carlo simulations.

To extend the scope of the physically-based modeling of deformation processing of different material classes, in addition to mentioned above, some further problems

may be considered:

- The crystal plasticity models considered in this work should be extended to other classes of crystal structures such as b.c.c. ($\alpha-Fe$), tetragonal ($In, \beta-Sn$), rhombohedral ($As, Sb$), orthorhombic ($\alpha - U$), etc. where deformation twinning plays an important role in maintaining the generalized plastic flow. It is important to estimate applicability of Taylor-type and other types of averaging schemes for these crystallographic structures.

- With the increase of the degree of deformation, such effects as grain boundary sliding and localized shear bands should be incorporated in the constitutive model.

- In the chapter 4 we presented a model for inhomogeneous deformation of single crystal by slip and twinning. The effective numerical scheme, which allows to build a model of polycrystalline behavior from inhomogeneously deformed single crystals, should be developed. This model would be able to analyze, in particular, intergranular interactions.

- The last but not the least, the model proposed in this work was applied for analysis of steady and quasi-static modes of deformation. The model should be extended for dynamic simulations.

# Chapter 8

# Closure

We have conducted a combined analytical-experimental - computational research program in order to develop physically based constitutive models and computational procedures for large anisotropic inelastic deformations of materials by two main mechanisms: crystallographic slip and mechanical twinning. We validated our results of numerical simulations by comparison against measurements from physical experiments.

The main developments of this dissertation are the follows:

- A new incremental rate-independent crystal plasticity constitutive model which accounts for both slip and twinning has been proposed along with a new scheme to determine the active systems and the shear increments on the active slip and twin systems.

- Constitutive equations have been implemented in the finite element program ABAQUS/Explicit (1995) to simulate the deformations of plane-strain compression and simple compression of a f.c.c. polycrystalline aggregate, using a multitude of single crystals. The predicted crystallographic textures and stress-strain responses from the finite element calculations are in good accord with experiments.

- We have evaluated the applicability of a simple Taylor-type model for combined slip and twinning. Our experiments and calculations show that, for the high-

symmetry f.c.c. brass, a Taylor model for a polycrystal deforming by combined slip and twinning is able to predict reasonably well the macroscopic stress-strain curves and crystallographic textures.

- We also have simulated the twinning-induced heterogeneity of plastic deformation in individual f.c.c. grains by subdividing the grains into small finite elements. It has been shown that the developed constitutive model allows to capture the micromechanical behavior of a single crystal as well as macro-behavior of polycrystalline aggregate.

- The constitutive model was modified and applied for prediction of the deformation behavior of a h.c.p. magnesium alloy. The predicted crystallographic textures and stress-strain curves are in good agreement with experimentally observed curves. It is shown that basal $< a >$ slip and pyramidal $\{10\bar{1}2\} < \bar{1}011 >$ twinning are the main mechanisms of plastic deformation of magnesium at room temperature. Experimentally observed polycrystalline hardening at room temperature is caused by grain reorientation during the deformation process.

- Series of experiments on Mg alloy for simple tension and compression, and plane strain compression to large strains at elevated temperatures have been conducted. We find that magnesium shows a considerable variation in strength and ductility depending on temperature regime. The significant (order of magnitude) increase in ductility in comparison with room temperature experiments has been observed at moderately high temperatures. This should be caused by activation of $< \mathbf{c}+\mathbf{a} >$ pyramidal slip system, which together with basal slip systems and pyramidal $< a >$ systems form the full system. Our numerical experiments support the idea that $\{11\bar{2}2\} < \bar{1}\bar{1}23 >$ slip systems play a crucial role in maintaining generalized plastic flow in deformation of magnesium and magnesium alloys at elevated temperatures. The experimental stress-strain relationships support the hypothesis that strain hardening effects in magnesium are not significant at high temperature.

# Bibliography

[1928] G. Sachs. Condition of flow for the polycrystal derived from the shear stress law. *Z. Veriens Deutsch Ingr.*, **72**:734.

[1938] G. I. Taylor. Plastic strain in metals. *Journal of the Institute of Metals*, **62**:307–324.

[1943] P. A. Bakarian and C. H. Mathewson. Slip and twinning of magnesium single crystals at elevated temperatures. *Transactions of the AIME*, **152**:226 – 247.

[1948] I. Lifshits. Macroscopic description of twinning phenomena in crystals. *Journal of Theoretical and Experimental Physics (JETP)*, **18(12)**:1134–1143.

[1949] L. G. Schulz. A direct method of determining prefered orientation of a flat reflection sample using a geiger counter x-ray spectrometer. *Journal of Applied Physics*, **20**:1030 – 1033.

[1950] D. C. Jillson. An experimental survey of deformation and annealing process in zinc. *Transactions of the AIME*, **188**:1009 – 1022.

[1952] E. C. Burke and Jr. W. R. Hibbard. Plastic deformation of magnesium single crystals. *Transactions of AIME*, **194**:295–303.

[1954] E. O. Hall. *Twinning and Diffusionless Transformations in Metals.* Butterworths Scientific Publications, London.

[1955] F. E. Hauser, C. D. Starr, L. Tietz, and J. E. Dorn. Deformation mechanisms in polycrystalline aggregates of magnesium. *Transactions of the ASM*, **47**:102 – 134.

[1957] R. E. Reed-Hill and W. D. Robertson. Additional modes of deformation twinning in magnesium. *Acta Metallurgica*, **5**:717 – 727.

[1957] J. D. Eshelby. The determination of the elastic field of an ellipsoidal inclusion, and related problems. *Proceedings of the Royal Society, A*, **241**:376 – 396.

[1957] T. Long and C. S. Smith. Single-crystal elastic constants of magnesium and magnesium alloys. *Acta Metallurgica*, **5**:200–207.

[1959] G. V. Raynor. *The Physical Metallurgy of Magnesium and Its Alloys.* Pergamon Press.

[1962] P. R. Thornton and R. E. Mitchell. Deformation twinning in alloys at low temperatures. *Philosophical Magazine*, **7**:361–375.

[1963] G. Wassermann. Der einflußmechanischer zwillingsbildung auf die entstehung der walztexturen kubisch flächenzentrierter metalle. *Zeitschrift für Metallkunde*, **54**:61 –65.

[1963] R. Fletcher and M. J. Powell. A rapidly convergent descent method for minimization. *Computer Journal*, **6**:163 – 168.

[1964] R. E. Smallman and D. Green. The dependence of rolling texture on stacking fault energy. *Acta Metallurgica*, **12**:145 – 154.

[1964] R. Fletcher and C. M Reeves. Function minimization by conjugate gradients. *Computer Journal*, **7**:149 – 154.

[1964] J. A. Venables. The nucleation and propagation of deformation twins. *Journal of The Physics and Chemistry of Solids*, **25**:693 – 700.

[1964] I. L. Dillamore and W. T. Roberts. Rolling textures in f.c.c. and b.c.c. metals. *Acta Metallurgica*, **12**:281 – 293.

[1968] E. W. Kelley and W. F. Hosford. The deformation characteristics of textured magnesium. *Transactions of the Metallurgical Society of AIME*, **242**:654 – 660.

[1968] S. R. Goodman and H. Hu. Texture development in copper and 70-30 brass. *Transactions of The Metallurgical Society of AIME*, **242**:88 – 93.

[1969] G. Y. Chin, W. F. Hosford, and D. R. Mendorf. Accommodation of constrained deformation in f.c.c. metals by slip and twinning. *Proceedings of The Royal Society A*, **309**:433–456.

[1969] G. Y. Chin and W. L. Mammel. Generalization and equivalence of the minimum work (Taylor) and maximum work (Bishop-Hill) principles of crystal plasticity. *Transactions of AIME*, **245**:1211 – 1214.

[1970] A. Kelly and G. W. Groves. *Crystallography and Crystal Defects.* Longman, London.

[1971] G. Simmons and H. Wang. *Single Crystal Elastic Properties and Calculated Aggregate Properties: A HANDBOOK.* The MIT Press, Cambridge, USA.

[1972] J. F. Stohr and J. P. Poirier. *Philosophical Magazine*, **63**:1313 – 1329.

[1974] N. Narita and J. Takamura. Deformation twinning in silver- and copper-alloy crystals. *Philosophical Magazine*, **29**:1001 – 1028.

[1975] S. Morozumi, H. Yoshiga, and T. Obara. $\{11\bar{2}2\} < \bar{1}\bar{1}23 >$ slip system in magnesium. *Metallurgical Abstracts on Light Metals and Alloys*, **9**:29 –31.

[1975] G. Y. Chin. Development of deformation textures. In A. S. Argon, editor, *Constitutive Equations in Plasticity*, pages 431–477, 1975.

[1978] B. D. Cullity. *Elements of X-Ray Diffraction.* Addison-Wesley.

[1978] P. Van Houtte. Simulation of the rolling and shear texture of brass by the taylor theory adapted for mechanical twinning. *Acta Metallurgica*, **26**:591 – 604.

[1979] Ya. D. Vishniakov, A. A. Babarako, S. A. Vladimirov, and I. V. Egis. *Theory of Texture Formation in Metals and Alloys.* Nauka, Moscow.

[1981] J. Gil Selivano, P. Van Houtte, and E. Aernoudt. Large strain work hardening and textures. *Progress in Materials Science*, **25**:69–412.

[1981] M. H. Yoo. Slip, twinning and fracture in hexagonal close-packed metals. *Metallurgical Transactions A*, **12A**:409 – 418.

[1981] K. S. Sree-Harsha. Stress concentration of terminating twins. *Metallurgical Transactions A*, **12**:365 – 370.

[1983] A. Khachaturyan. *Theory of Structural Transformation in Solids.* J. Wiley & Sons.

[1985] M. Pitteri. On the kinematics of mechanical twinning in crystals. *Archiv. Rat. Mech. Anal*, **84**:1 – 57.

[1985] R. J. Asaro and A. Needleman. Texture development and strain hardening in rate dependent polycrystals. *Acta Metallurgica*, **33**:923 – 953.

[1986] M. Pitteri. On type-2 twins in crystals. *International Journal of Plasticity*, **2**:99 – 106.

[1987] J. M. Ball and R. D. James. Fine phase mixtures as minimizers of the energy. *Archive of Rational Mechanics Anal.*, **100**:13–52.

[1988] J. Hirsch and K. Luke. Mechanism of deformation and development of rolling textures in polycrystalline f.c.c. metals. (Parts I and II). *Acta Metallurgica*, **36**:2863 – 2904.

[1988a] J. Hirsch, K. Luke, and M. Hatherly. Mechanism of deformation and development of rolling textures in polycrystalline f.c.c. metals. (Part III). *Acta Metallurgica*, **36**:2905 – 2927.

[1989] S. B. Brown, K. H. Kim, and L. Anand. An internal variable constitutive model for hot-working of metals. *International Journal of Plasticity*, **5**:95 – 130 .

[1989] K. K. Mathur and P. R. Dawson. On modeling and development of crystallographic texture in bulk forming processes. *International Journal of Plasticity*, **5**:67 – 94.

[1990] T. Leffers and J. B. Bilde-Sorensen. Intra- and intergranular heterogeneities in plastic deformation of brass during rolling. *Acta Metallurgica et Materialia*, **38**:1917–1926.

[1990] D. M. Parks and S. Ahzi. Polycrystalline plastic deformation and texture evolution for crystals lacking five independent slip systems. *Journal of the Mechanics and Physics of Solids*, **38**:701 – 724 .

[1990] K. K. Mathur and P. R. Dawson. Texture development during wire drawing. *ASME Journal of Engineering Materials and Technology*, **112**:292 – 297.

[1991] T. Leffers and D. J. Jensen. In *Textures and Microstructures*, 14-18, pages 933 – 952, 1991.

[1991] C. M. Tome, R. A. Lebensohn, and U.F. Kocks. A model for texture development dominated by deformation twinning: Application to zirconium alloys. *Acta Metallurgica et Materialia*, **39**:2667 – 2680.

[1991] J. S. Kallend, U. F. Kocks, A. D. Rollett, and H. R. Wenk. popLA: The preferred orientation package from Los Alamos. Technical report, Los Alamos National Laboratory., 1991.

[1991] R. Kohn. The relaxation of a double-well energy. *Continuum Mechanics and Thermodynamics*, **3**:193–236.

[1992] P. Rosakis. Compact zones of shear transformation in an anisotropic solid. *Journal of the Mechanics and Physics of Solids.*, **40**:1163–1195.

[1992] S. R. Kalidindi, C. A. Bronkhorst, and L. Anand. Crystallographic texture evolution during bulk deformation processing of fcc metals. *Journal of The Mechanics and Physics of Solids*, **40**:537 – 569.

[1992] C. A. Bronkhorst, S. R. Kalidindi, and L. Anand. Polycrystal plasticity and evolution of crystallographic texture in face-centered cubic metals. *Phil. Trans. R. Soc.*, **A341**:744–477.

[1993] W. F. Hosford. *The Mechanics of Crystals and Textured Polycrystals.* Oxford University Press.

[1993] T. Leffers. Microstuctures, textures, and deformation patterns at large strains. In Teodosiu, Raphanel, and Sidoroff, editors, *MECAMAT'91*, pages 73 – 86., Rotterdam, 1993. Balkema.

[1994] A. J. Beaudoin, P. R. Dawson, K. K. Mathur, U. F. Kocks, and D. A. Korzekwa. Application of polycrystalline plasticity to sheet forming. *Computer Methods in Applied Mechanics and Engineering*, **117**:49 – 70.

[1994] L. Anand and S. R. Kalidindi. The process of shear band formation in plane strain compression of fcc metals: Effects of crystallographic texture. *Mechanics of Materials*, **17**:223 – 243.

[1994] R. A. Lebensohn and C. M. Tome. A self-consistent viscoplastic model: Prediction of rolling textures of anisotropic polycrystals. *Materials Science and Engineering*, **A175**:71 – 82.

[1995] S. E. Schoenfeld, S. Ahzi, and R. J. Asaro. Elastic-plastic crystal mechanics for low symmetry crystals. *Journal of the Mechanics and Physics of Solids*, **43**:415 – 446 .

[1995] ABAQUS. *Reference Manuals.* Hibbitt, Karlsson & Sorensen Inc.

[1996] L. Anand and M. Kothari. A computational procedure for rate-independent plasticity. *Journal of The Mechanics and Physics of Solids*, **40**:525–558.

[1996] S. Balasubramanian and L. Anand. Single crystal and polycrystal elasto-viscoplasticity: Application to earing in cup drawing of f.c.c. materials. *Computational Mechanics*, **17**:209 – 225.

[1997] S. Asgari, S. R. Kalidindi, and R. D. Doherty. Strain hardening and microstructural evolution during large strain compression of low stacking fault energy fcc alloys that form deformation twins. *Submitted to Metallurgical Transactions.*

[1998] Srihari Balasubramanian. *Polycrystalline Plasticity: Application to Deformation Processing of Lightweight Metals.* PhD thesis, MIT, 1998.

# Appendix A

# Rate Form of the Governing Equations

A constitutive model for deformation of a single crystal by combined slip and twinning is developed by modifying the widely used framework for crystal plasticity by slip alone. The governing variables in the constitutive model are taken as: $(i)$ The Cauchy stress, $\mathbf{T}$. $(ii)$ The deformation gradient, $\mathbf{F}$. $(iii)$ Crystal slip and twin systems labeled by integers $i$. Each system is specified by a unit normal $\mathbf{n}_0^i$ to the slip/twin plane, and a unit vector $\mathbf{m}_0^i$ denoting the slip/twin direction. The slip and twin systems $(\mathbf{m}_0^i, \mathbf{n}_0^i)$ are assumed to be known in the reference configuration. The amount of shear, $\gamma_0$, and the lattice rotation accompanying twinning, $\mathbf{R}^{tw}$, are also assumed to be known. $(iv)$ A plastic deformation gradient, $\mathbf{F}^p$, with $\det\mathbf{F}^p = 1$. This represents the cumulative effect of dislocation motion and shear due to twinning on the active slip and twin systems in the crystal. $(v)$ The slip and twin system deformation resistances $s^i > 0$, with units of stress. $(vi)$ The twin fractions $f^i \geq 0$.

The elastic deformation gradient is defined by $\mathbf{F}^e \equiv \mathbf{F}\,\mathbf{F}^{p-1}$ with $\det\mathbf{F}^e > 0$, and it describes the elastic distortion of the lattice; it is this distortion that gives rise to the stress $\mathbf{T}$.

Let $\bar{\mathbf{S}}_0 = (\det\mathbf{F})\mathbf{T}\mathbf{F}^{-T}$ denote the first Piola-Kirchoff stress. Then, the stress power per unit reference volume is $\dot{\omega} = \bar{\mathbf{S}}_0 \cdot \dot{\mathbf{F}}$, which, since $\det\mathbf{F}^p = 1$, is also equal to the stress power per unit volume of the relaxed configuration determined by $\mathbf{F}^p$.

This stress power may be additively decomposed as $\dot{\omega} = \dot{\omega}^e + \dot{\omega}^p$, where $\dot{\omega}^e = \mathbf{T}^* \cdot \dot{\mathbf{E}}^e$ is the elastic stress power per unit volume of the relaxed configuration, with

$$\mathbf{E}^e \equiv (1/2)\left\{\mathbf{F}^{eT}\mathbf{F}^e - \mathbf{1}\right\} \quad \text{and} \quad \mathbf{T}^* \equiv (\det \mathbf{F}^e)\, \mathbf{F}^{e-1}\mathbf{T}\mathbf{F}^{e-T} \tag{A.1}$$

the Green elastic strain measure and the symmetric second Piola-Kirchoff stress tensor relative to the relaxed configuration, respectively, and

$$\dot{\omega}^p = (\mathbf{C}^e\, \mathbf{T}^*) \cdot \left(\dot{\mathbf{F}}^p\, \mathbf{F}^{p-1}\right), \qquad \mathbf{C}^e \equiv \mathbf{F}^{eT}\mathbf{F}^e, \tag{A.2}$$

is the plastic stress power per unit volume of the relaxed configuration.

Constitutive Equation For Stress:

Elastic stretches in metallic single crystals are generally small. Accordingly, the constitutive equation for the stress in a metallic single crystal is taken as the linear relation

$$\mathbf{T}^* = \boldsymbol{\mathcal{C}}\,[\mathbf{E}^e], \tag{A.3}$$

where $\boldsymbol{\mathcal{C}}$ is a fourth-order anisotropic elasticity tensor, where $\mathbf{E}^e$ and $\mathbf{T}^*$ are the strain and stress measures defined in equation (A.1).

Slip and Twinning Conditions:

Let

$$\mathbf{S}_0^i = \mathbf{m}_0^i \otimes \mathbf{n}_0^i \tag{A.4}$$

denote the Schmid tensors, and consistent with equation (A.2), and let

$$\tau^i = (\mathbf{C}^e\, \mathbf{T}^*) \cdot \mathbf{S}_0^i \tag{A.5}$$

denote the resolved shear stress on the $i$th slip/twin system. Then, the conditions for slip and twinning are taken as

$$\phi^i = \left|\tau^i\right| - s^i \leq 0. \tag{A.6}$$

Flow Rule:

The evolution of the plastic deformation gradient is

$$\dot{\mathbf{F}}^p = \mathbf{L}^p \mathbf{F}^p, \tag{A.7}$$

with $\mathbf{L}^p$ given by the sum of the shearing rates on all the slip and twin systems

$$\mathbf{L}^p = \sum_i \dot{\gamma}^i \operatorname{sign}(\tau^i)\, \mathbf{S}_0^i. \tag{A.8}$$

The shearing rates are restricted as follows:

$$\dot{\gamma}^i \geq 0, \quad \text{and} \quad \dot{\gamma}^i \phi^i = 0. \tag{A.9}$$

Evolution Equations For Slip and Twin Resistances:

These are generically taken as

$$\dot{s}^i = \sum_j h^{ij} \dot{\gamma}^j, \tag{A.10}$$

where $h^{ij}$ are the hardening moduli. More on this later.

Consistency Conditions:

During plastic flow the following consistency conditions must be satisfied:

$$\dot{\gamma}^i \dot{\phi}^i = 0 \quad \text{if} \quad \phi^i = 0. \tag{A.11}$$

The consistency conditions serve to determine the shearing rates $\dot{\gamma}^i \geq 0$ on the slip and twin systems.

Evolution Equations For Twin Volume Fractions:

For the twin systems,

$$\dot{f}^i = \dot{\gamma}^i / \gamma_0 \geq 0, \tag{A.12}$$

where $\gamma_0$ is the twinning shear.

Lattice Reorientation Condition:

Treating the twinned fractions as new orientations essentially involves introducing new crystals, and this quickly leads to a numerically-unmanageable number of crystals in a calculation of the response of a polycrystal. Van Houtte [1978] appears to have been the first to propose a simple tractable scheme for reorientation due to twinning; his scheme does not increase the number of crystals. In his approach, if a crystal twins, then the twin is first treated as a "pseudo-slip," and its lattice is given a twinning-related orientation only if a probabilistic criterion, based on the relative twin fractions of the twinned and non-twinned parts of a crystal, is met. Specifically, during the "pseudo-slip" phase, with $f^\alpha(\tau) \equiv \Gamma^\alpha(\tau)/\gamma_0$ denoting the "twin fraction" corresponding to a twin system, Van Houtte suggests that we compare the twin fraction $f(\tau) = \max\{f^\alpha(\tau)\}$ with a random number $\xi \in [0,1]$; if $f > \xi$, then the orientation of the *whole crystal* is replaced by the orientation of the twinned part of the grain corresponding to the system $\alpha$. That is, if $\bar{\mathbf{Q}}(t)$ denotes a rotation tensor which brings the orthonormal crystal basis $\left\{\mathbf{e}_i^{(c)}(t)\right\}$ to be in correspondence with the fixed orthonormal global basis $\left\{\mathbf{e}_i^{(g)}\right\}$, $\mathbf{e}_i^{(g)} = \bar{\mathbf{Q}}(t)\,\mathbf{e}_i^{(c)}(t)$, then for the reoriented crystal, for which the orientation of the crystal basis after twinning is $\mathbf{e}_i^{(c)}(\tau) = \mathbf{R}^{tw}(t)\mathbf{e}_i^{(c)}(t)$, the corresponding relationship between the global basis and the reoriented crystal basis is $\mathbf{e}_i^{(g)} = \left(\bar{\mathbf{Q}}(t)\,(\mathbf{R}^{tw}(t))^T\right)\,\mathbf{e}_i^{(c)}(\tau)$. Once a grain is given a new twin-related orientation, the accumulated strain $\Gamma^\alpha$ on all twin systems in that grain is set to zero, $\bar{\mathbf{Q}}(\tau)$ is set equal $\bar{\mathbf{Q}}(\tau) = \bar{\mathbf{Q}}(t)\,(\mathbf{R}^{tw}(t))^T$, and the algorithm continued.

# Appendix B

# Twinning-related lattice rotation

For convenience, in this Appendix we list the matrix relations used to keep track of the lattice reorientations due to twinning.

Let $\{\mathbf{e}_i^c | i = 1, 2, 3\}$ denote a local orthonormal basis associated with the crystal lattice, and let $\{\mathbf{e}_i^g | i = 1, 2, 3\}$ denote a fixed global orthonormal basis. Let $\bar{\mathbf{Q}}$ denote the rotation tensor which brings the orthonormal crystal basis to be in correspondence with the fixed orthonormal global basis, $\mathbf{e}_i^{(g)} = \bar{\mathbf{Q}}\,\mathbf{e}_i^{(c)}$. This last relation may be written as

$$\mathbf{e}_i^g = \sum_m \bar{Q}_{mi}\mathbf{e}_\mathbf{m}^\mathbf{c}, \quad \text{where} \quad \bar{Q}_{mi} = \mathbf{e}_m^c \cdot \mathbf{e}_i^g. \tag{B.1}$$

Alternatively, with

$$[Q] \equiv \left[\bar{Q}\right]^T, \tag{B.2}$$

we may write (B.1a) as

$$\mathbf{e}_i^g = \sum_m Q_{im}\mathbf{e}_m^c. \tag{B.3}$$

Following the notation of Kalidindi *et al.* [1992], the components of the matrix $[Q]$ may be calculated in terms of the resultant of three simple rotations, which are

specified using Euler angles $0 \leq \phi \leq 2\pi$, $0 \leq \theta \leq \pi$, and $0 \leq \omega \leq 2\pi$ :

$$[Q] = \begin{bmatrix} \cos\phi\cos\omega - \sin\phi\sin\omega\cos\theta & \sin\phi\cos\omega + \cos\phi\sin\omega\cos\theta & \sin\omega\sin\theta \\ -\cos\phi\sin\omega - \sin\phi\cos\omega\cos\theta & -\sin\phi\sin\omega + \cos\phi\cos\omega\cos\theta & \cos\omega\sin\theta \\ \sin\phi\sin\theta & -\cos\phi\sin\theta & \cos\theta \end{bmatrix}. \tag{B.4}$$

Next, let the crystal basis after twinning be related to that before twinning by

$$\mathbf{e}_i^{c\,*} = \mathbf{R}^{\mathbf{tw}}\mathbf{e}_i^c, \tag{B.5}$$

where $\mathbf{R}^{\mathbf{tw}}$ is the twinning rotation. Then, we may write

$$\mathbf{e}_i^g = \bar{\mathbf{Q}}^*\mathbf{e}_i^{c\,*}, \quad \bar{\mathbf{Q}}^* \equiv \bar{\mathbf{Q}}(\mathbf{R}^{\mathbf{tw}})^{\mathbf{T}}, \tag{B.6}$$

where $\bar{\mathbf{Q}}^*$ denotes the rotation tensor which brings the basis $\mathbf{e}_i^{c\,*}$ to be in correspondence with the fixed global basis.

Equation (B.6a) may be written as

$$\mathbf{e}_i^g = \sum_m \bar{Q}^*_{mi}\mathbf{e}_m^{c\,*}, \tag{B.7}$$

where

$$\begin{aligned} \bar{Q}^*_{mi} &= \mathbf{e}_m^{c\,*}\cdot\bar{\mathbf{Q}}^*\mathbf{e}_i^{c\,*} = \mathbf{e}_m^{c\,*}\cdot\left[\bar{\mathbf{Q}}(\mathbf{R}^{\mathbf{tw}})^{\mathbf{T}}\right]\mathbf{e}_i^{c\,*} = \left(\mathbf{R}^{\mathbf{tw}}\mathbf{e}_m^c\right)\cdot\left[\bar{\mathbf{Q}}(\mathbf{R}^{\mathbf{tw}})^{\mathbf{T}}\right]\left(\mathbf{R}^{\mathbf{tw}}\mathbf{e}_i^c\right) \\ &= \mathbf{e}_m^c\cdot\left[(\mathbf{R}^{\mathbf{tw}})^{\mathbf{T}}\bar{\mathbf{Q}}\right]\mathbf{e}_i^c = \mathbf{e}_m^c\cdot\left[(R^{tw}_{pq}\mathbf{e}_p^c\otimes\mathbf{e}_q^c)^{\mathbf{T}}\bar{\mathbf{Q}}\right]\mathbf{e}_i^c \\ &= \mathbf{e}_m^c\cdot\left[(R^{tw}_{pq}\mathbf{e}_q^c\otimes\mathbf{e}_p^c)\bar{\mathbf{Q}}\right]\mathbf{e}_i^c = R^{tw}_{pq}\delta_{mq}\bar{Q}_{pi} = R^{tw}_{pm}\bar{Q}_{pi}\,. \end{aligned} \tag{B.8}$$

In matrix notation,

$$\left[\bar{Q}^*\right] = \left[R^{tw}\right]^T\left[\bar{Q}\right], \tag{B.9}$$

where $[R^{tw}]$ is the matrix of components of the twin rotation in the crystal basis, and the components of the matrix $\left[\bar{Q}\right]$ have been defined previously in (B.1). Finally,

equation (B.7) may be rewritten as

$$\mathbf{e}_i^g = \sum_m Q_{im}^* \mathbf{e}_m^{c*}, \tag{B.10}$$

where

$$[Q^*] \equiv \left[\bar{Q}^*\right]^T = [Q]\left[R^{tw}\right], \tag{B.11}$$

to obtain the desired relationship between the crystal basis after twinning, $\{\mathbf{e}_m^{c*}\}$, and the fixed global basis, $\{\mathbf{e}_i^g\}$.

# Appendix C

# Model of inelastic deformation of f.c.c. single crystals with local twinning shears.

In this Appendix we estimate the role of twinning sudden large shear on deformation process. We use essentially the same model as described in chapter 2, but with minor modifications. Hence, here we describe only these modifications and estimate their importance. In our models each RVE contains enough twins to result in an acceptably smooth process at the continuum level. If we continue to refine a finite element mesh, we may reach the level when a RVE may contain only one twin. In this case the large shear accompanying twinning should be taken into account.

The main assumption of these simulations is the following: when the lattice reorientation criterion is met, the RVE crystal lattice is rotated to "twin-related" orientation and is also sheared. During "pseudo–slip" stage, the shear due to twinning and slip is gradually accumulated, but when the twin fraction corresponding to the dominant twin system $f = \max\{f^\alpha\}$ exceeds a value[1], $\xi \approx 0.75$ the incremental

[1]The value $\xi \approx 0.75$ was chosen to ensure the stability of the numerical scheme when the "twinned" element is subjected to large shear. The more mesh elements are in use, i.e., the finer the RVE the smaller $\xi$ may be.

plastic deformation is taken as due only to twinning on the dominant twin system,

$$\begin{aligned} \mathbf{F}_t^{\mathbf{p}}(\tau) &= \mathbf{1} + \Delta\gamma^{\alpha}\, \mathbf{m}_0^{\alpha} \otimes \mathbf{n}_0^{\alpha}, \quad \text{with} \\ \Delta\gamma^{\alpha} &= \mathbf{m}_0^{\alpha} \cdot \{(\mathbf{1} + \gamma_0^{\alpha}\, \mathbf{m}_0^{\alpha} \otimes \mathbf{n}_0)^{\alpha} \mathbf{F}^{\mathbf{p}-\mathbf{1}}(\mathbf{t}) - \mathbf{1}\} \mathbf{n}_0^{\alpha}, \end{aligned} \tag{C.1}$$

where $\gamma_0$ is the twinning shear.

After this, the crystal lattice of the RVE in the relaxed configuration is rotated to the new twinning-related orientation. That is, if $\bar{\mathbf{Q}}(t)$ denotes a rotation tensor which brings the orthonormal crystal basis $\left\{\mathbf{e}_i^{(c)}(t)\right\}$ to be in correspondence with the fixed orthonormal global basis $\left\{\mathbf{e}_i^{(g)}\right\}$, $\mathbf{e}_i^{(g)} = \bar{\mathbf{Q}}(t)\, \mathbf{e}_i^{(c)}(t)$, then for the reoriented region of the crystal for which the orientation of the crystal basis after twinning is $\mathbf{e}_i^{(c)}(\tau) = \mathbf{R}^{tw}(t)\mathbf{e}_i^{(c)}(t)$, the corresponding relationship between the global basis and the reoriented crystal basis is $\mathbf{e}_i^{(g)} = \left(\bar{\mathbf{Q}}(t)\, (\mathbf{R}^{tw}(t))^T\right)\, \mathbf{e}_i^{(c)}(\tau)$.

At the time a RVE is given a new twin-related orientation, that is when $\bar{\mathbf{Q}}(\tau)$ is set equal $\bar{\mathbf{Q}}(\tau) = \bar{\mathbf{Q}}(t)\, (\mathbf{R}^{tw}(t))^T$, then, (*i*) the accumulated strain $\Gamma^{\alpha}$ on all twin systems in that RVE is also set to zero, and (*ii*) since continued twinning of an already twinned RVE is seldom observed in experiments, the twinning resistances are set at a large number to suppress re-twinning, however slip in these regions is allowed, and the slip resistances for the slip systems in the RVE are set at the levels reached by the active slip system prior to reorientation.

To summarize, to account for slip-twin interactions and the reorientation due to twinning, we choose two thresholds related to the 'twin fraction' calculated by treating twinning as a 'pseudo-slip'. Slip is restricted to planes parallel to the dominant twin system when the first threshold is reached. The RVE is sheared to $\gamma_0$, and the crystal lattice of the RVE in the relaxed configuration is rotated to the twinning-related orientation when the second threshold is reached.

To trigger twinning, the initial twinning resistance of one element in the middle of the mesh was set to $0.75 \times s_0^{tw}$. The finite element mesh deforms gradually during "pseudo–slip." When the twin fraction corresponding to the dominant twin system exceeds a large value, $f = \max\{f^{\alpha}\} > \xi \approx 0.75$ in the trigger element, the element is

suddenly sheared by an additional large amount and the crystal lattice in this element is reoriented. Fig. C-1(a) shows an element in its initial state, and Fig. C-1(b) shows the same element after "twinning." The shear strain in the twinned element is close to 0.707.

We simulated the plane-strain compression experiments on a $(110)[\bar{3}34]$ oriented crystal. Finite element simulation is shown in Fig. C-2. Our calculations also predict twinning occurs on the $(111)[1\bar{2}1]$ and $(\bar{1}\bar{1}1)[\bar{1}21]$ systems. The elements twinned by the $(111)[1\bar{2}1]$ system are colored red, and those twinned by the $(\bar{1}\bar{1}1)[\bar{1}21]$ system are colored blue. The calculated twin bands intersect at an angle close to that observed in the experiments.

The highly non-uniform deformation that occurs in the crystal may be observed in the contour plots of the equivalent plastic strain[2], which is shown in Fig. C-3. The strain level in the twinned region is almost three times the average strain in the crystal. The stress-strain data is given in Fig. C-4. The saw-like shape of calculated stress-strain curve illustrates that twinning is strong stress relaxation mechanism. However, from numerical point of view, increase of the number of mesh elements makes the stress-strain curve smoother. The calculated textures in this case are very close to those shown in chapter 3 for calculations without local twinning-related large shear, and we do not show them here.

Next, we simulated plane strain compression of a $(335)[\bar{5}\bar{5}6]$ oriented crystal. Our calculations, (in Fig. C-5), show twin system, $(111)[11\bar{2}]$, to be dominant at a strain of 20%. The twinned elements in the deformed finite element mesh are colored red. The contours of equivalent plastic strain corresponding to this stage of deformation is shown in Fig. C-6. The strain level in twinned region in this case is more than twice the average strain in the rest of the crystal.

There are a lot of discussions about importance of elastic field of twin (see, for example, K. S. Sree Harsha [1981]) on further crystal plastic deformation. The approach described in this appendix is automatically takes into account the elastic field

[2]An "equivalent plastic strain rate" and "equivalent plastic strain" are defined as follows: $\dot{\bar{\epsilon}}^p = \frac{\sum \tau^i \dot{\gamma}^i}{\bar{\sigma}}$ and $\bar{\epsilon}^p = \int \dot{\bar{\epsilon}}^p dt$, where $\bar{\sigma} = \sqrt{\frac{3}{2}\mathbf{T}' \cdot \mathbf{T}'}$.

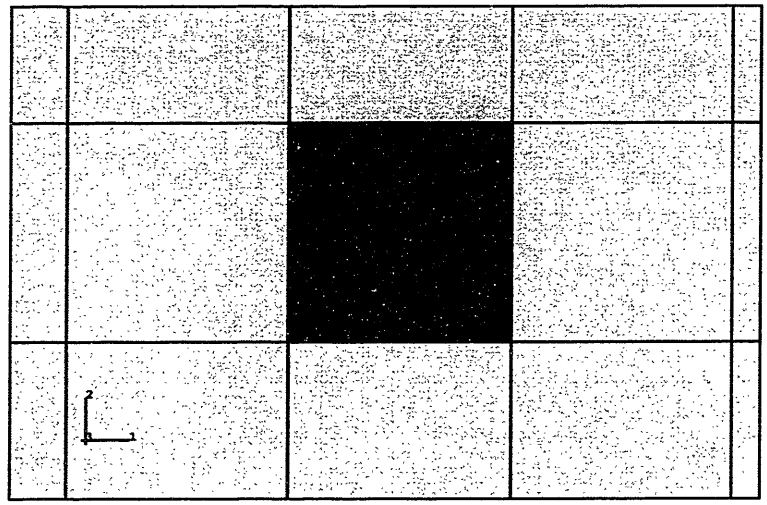

(a)

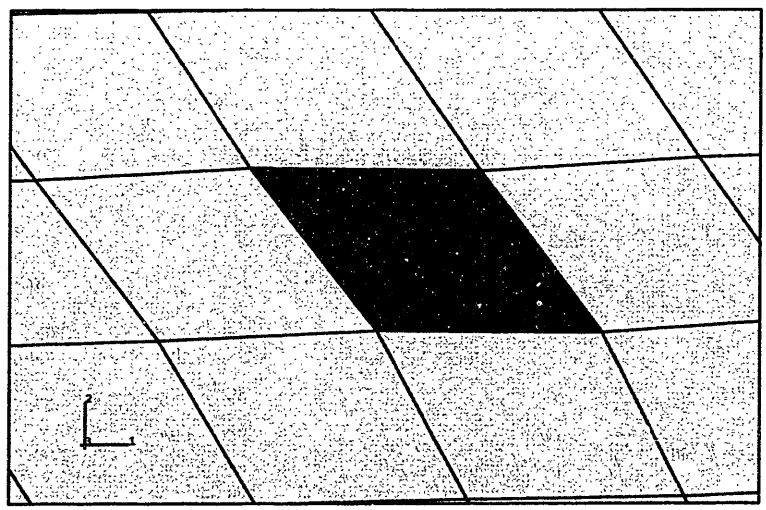

(b)

Figure C-1: Initial and twin-related sheared RVE.

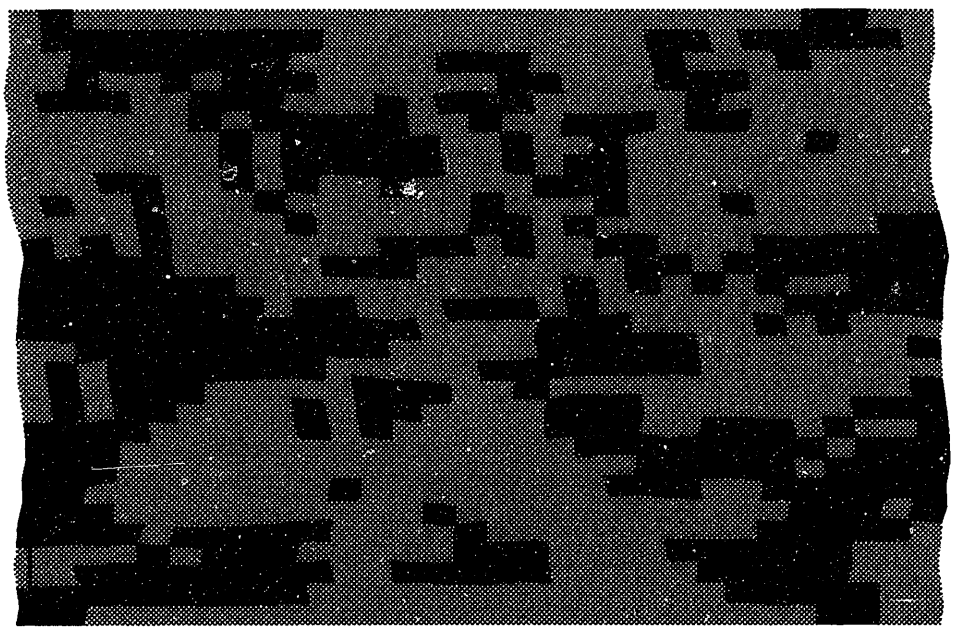

Figure C-2: The deformed FEM mesh with calculated twin bands of two systems.


Figure C-3: Contours of equivalent plastic strain after plane strain compression of single (110)[$\bar{3}$34] crystal to 20% .

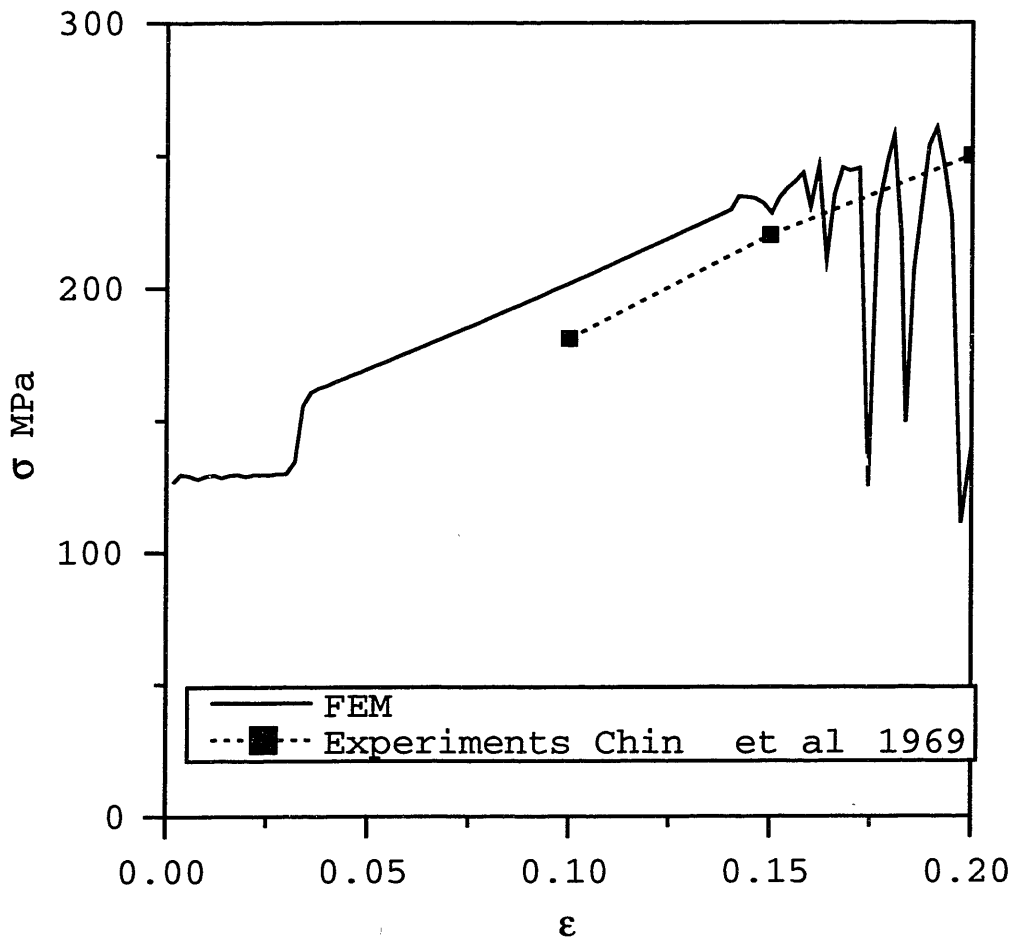


Figure C-4: The stress strain data for plane stress compression of single (110)[$\bar{3}$34] crystal to 20%.

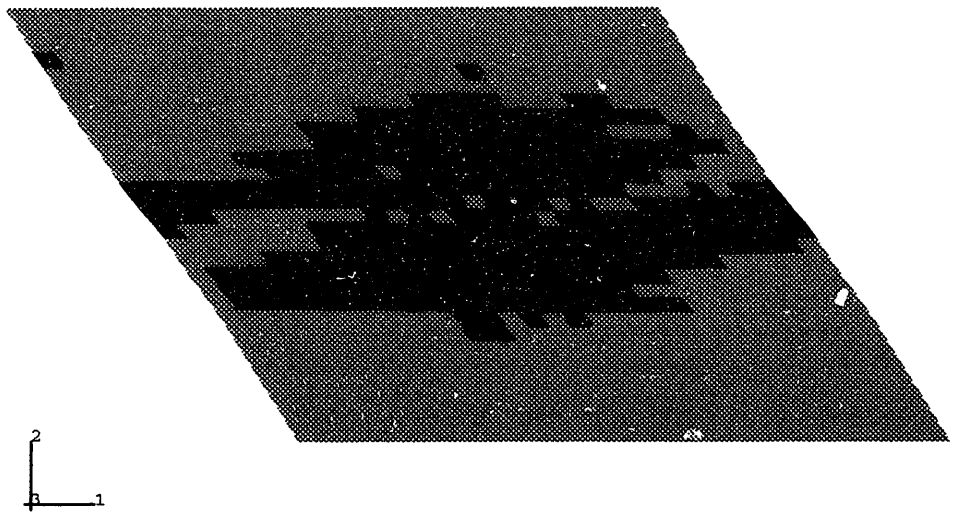


Figure C-5: The deformed FEM mesh with calculated twin bands of one system.

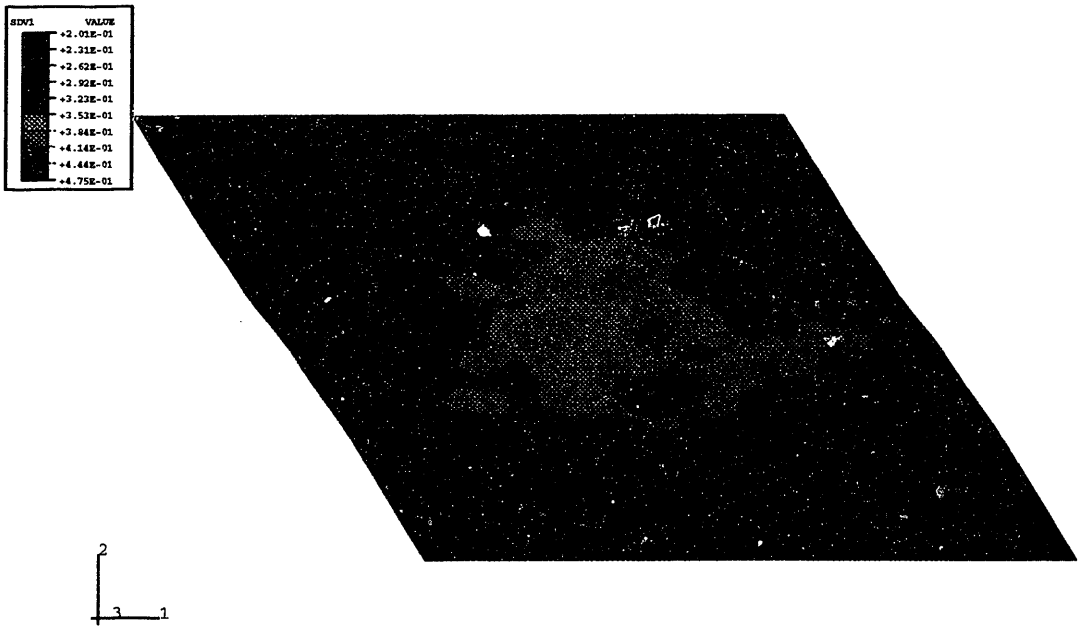


Figure C-6: Contours of equivalent plastic strain after plane strain compression of single (335)[$\bar{5}\bar{5}$6 crystal to 20% .

when a region within a solid suffers a spontaneous change of form, (so-called Eshelby inclusion problem (Eshelby [1957])). Our calculations showed that twinning shear is very strong trigger mechanism. However, the resulting twin bands and correspondent textures are similar to those calculated by modeling without accounting for large twinning shear. This means that twin-related lattice reorientation mechanism is more important than local stress concentrations in large inelastic deformations of crystals.

# Appendix D

# Numerical experiments to simulate deformation of Mg at elevated temperatures.

The mechanism of plastic deformation of magnesium at elevated temperatures is still not quite understood. Much work, both experimental and computational, needs to be done to clarify the physical picture. To do the first step in numerical simulation of high temperature deformation of magnesium we aimed to estimate the role of each slip system on texture formation. The single-crystal *rate-independent* constitutive equations[1] developed for h.c.p. materials deformed by slips only, have been implemented in the finite element program ABAQUS/Explicit [1995] by writing a user subroutine "VUMAT." We considered the contribution of basal, prismatic $< a >$, pyramidal $< a >$, and second order pyramidal $< c + a >$ slip systems to the plastic flow of magnesium at elevated temperatures. The polycrystal calculations shown below have been carried out by modeling each grain in polycrystalline magnesium as a single finite element. We use a set of 343 initially oriented crystals to simulate a textured polycrystal. Euler angles for the initial state were obtained by digitalizing

[1]We understand that plastic deformation at elevated temperature is rate-dependent. Our preliminary rate-independent simulations have been done in order to estimate the role of each slip system in maintaining plastic flow.

of the sample initial textures.

We calibrate model parameters by comparison of the results of numerical experiments with experimentally measured data for simple compression. It appears, that the texture shift to the basal fiber type is caused mainly by basal $< a >$ slips. Activization of prismatic $< a >$ and/or pyramidal $< a >$ slip systems leads to increase of $\{11\bar{2}0\}$ pole intensity. In order to obtain the simple compression texture close to experimentally measured, the basal slip deformation resistances should be significantly lower than deformation resistances of other slip systems. Because the nature of slip hardening is not clear, we used a non-hardening model as first approximation.

The set of parameters, which leads to reasonably good texture prediction is as follows:

$$s_{\text{basal}} = 0.55 \text{ MPa}, \; s_{\text{pyramidal}<c+a>} = 9 \text{ MPa},$$

$$s_{\text{pyramidal}<a>} = 30 \text{ MPa}, \; s_{\text{prismatic}<a>} = 30 \text{ MPa}.$$

Initial rod texture (see Fig. 5-9 has a pole on $\{10\bar{1}0\}$ crystallographic plane. During deformation, this pole first shifts to the intermediate $\{10\bar{1}1\}$ position, then appears on $\{0001\}$ pole figure, but does not reach the final basal pole position as shown in Fig. D-1. Numerical experiments of simple compression to $\epsilon = -1.5$ shows that basal pole density continuously increases, but still does not reach the pole. The calculated stress-strain relation has the same order as experimentally observed, but gradually decrease with deformation.

Thus, we see that numerically predicted behavior in simple compression resembles real material behavior, but predicted texture evolution is much slowly than observed. Some additional mechanisms of plastic deformation should be incorporated in the model to increase the rate of crystal reorientation.

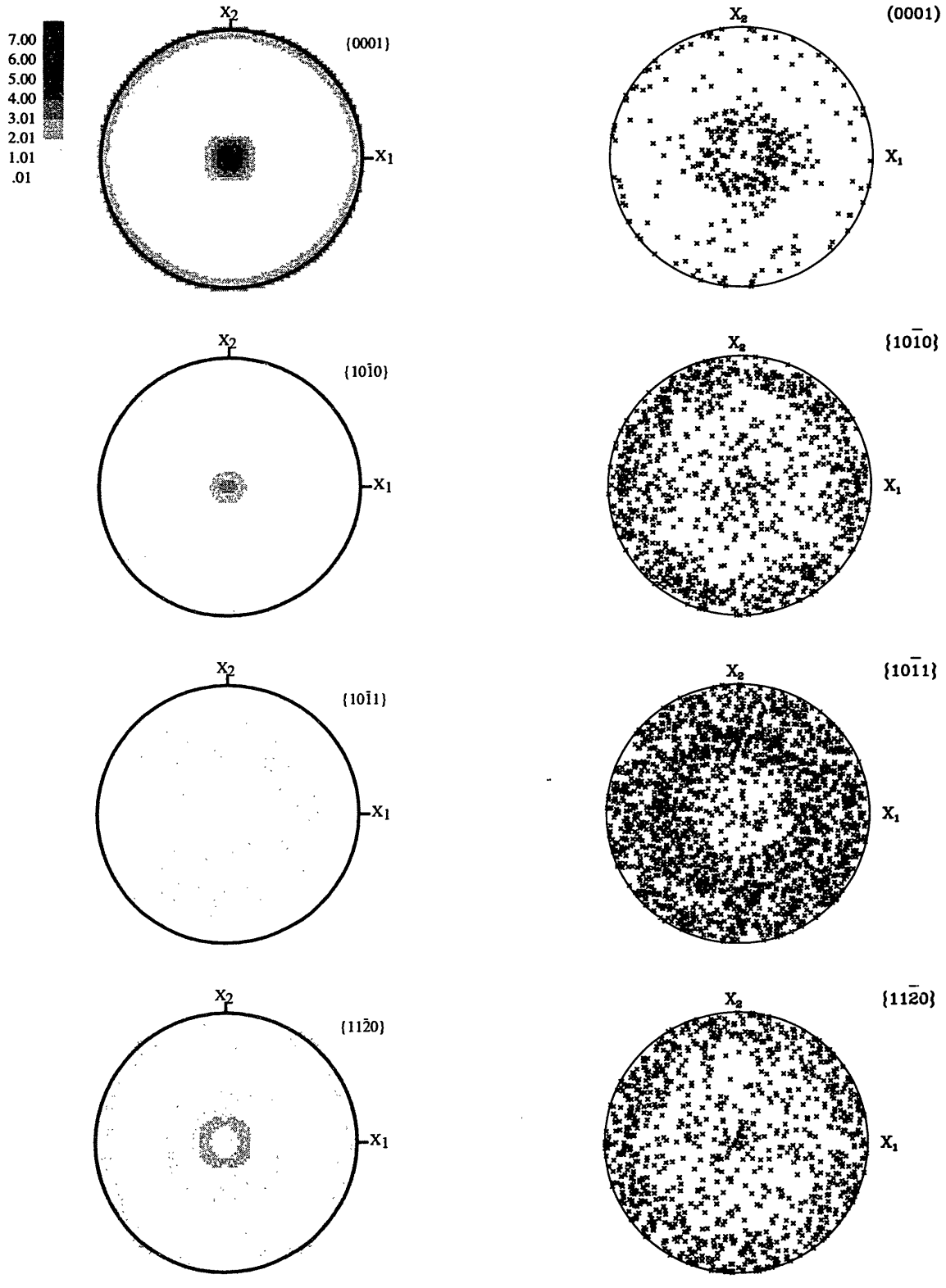


Figure D-1: FEM calculated pole figures after simple compression of h.c.p. magnesium to 100% at elevated temperature.